Cloud-Radiative Impact on the Dynamics of Extratropical Cyclones and Implications for Predictability

Zur Erlangung des akademischen Grades eines

DOKTORS DER NATURWISSENSCHAFTEN
(Dr. rer. nat.)

von der KIT-Fakultät für Physik des

Karlsruher Instituts für Technologie (KIT)

genehmigte

DISSERTATION

von

M. Sc. Behrooz Keshtgar

aus Shiraz, Iran

Tag der mündlichen Prüfung:	21.06.2024
Referentin:	Prof. Dr. Corinna Hoose
Korreferent:	Prof. Dr. Aiko Voigt

KIT
Karlsruher Institut für Technologie

Abstract

The dynamics and predictability of extratropical cyclones are strongly shaped by cloud diabatic processes. While the cloud impact due to latent heating has been the focus of many studies, little is known about the impact of cloud radiative heating (CRH) on the dynamics of extratropical cyclones. In this thesis, we investigate the impact of CRH on the dynamics of extratropical cyclones and its implications for cyclone predictability. Using the ICOsahedral Nonhydrostatic (ICON) model, we combine different modeling approaches and methods, from idealized baroclinic life cycle simulations in different model setups and hindcast simulations over the North Atlantic region to large-eddy-model simulations. The added value of such a holistic approach is that we gain a comprehensive understanding of the impact of CRH on the dynamics of cyclones.

We develop a new modeling technique that isolates the impact of CRH on idealized cyclones in an easy-to-interpret manner. Using this modeling technique, we find that CRH has a substantial impact on the dynamics of idealized extratropical cyclones. We identify a tug-of-war between the radiative impact of low-level clouds, which weaken cyclones, and high-level clouds, which strengthen cyclones. We study the impact of CRH near the surface and at upper levels near the tropopause and find that the impact of CRH is most prominent at upper levels.

To understand the impact of CRH on the upper-tropospheric circulation, we diagnose the evolution of differences in potential vorticity between a simulation with and without CRH, and we quantify through which processes these differences grow over the course of the cyclone's life cycle. We find that CRH affects the cyclone mostly via the intensification of latent heating from cloud microphysical processes and subsequent changes in the large-scale flow near the tropopause. Our results show that although CRH is comparably small in magnitude, it can affect extratropical cyclones through continuous modulation of cloud microphysical heating and subsequently the large-scale flow. Therefore it is possible that uncertainties in CRH can affect the development of cyclones and the numerical forecasts at synoptic scales.

We assess the uncertainty in CRH due to the uncertainty in the representation of the cloud field with respect to model settings over the North Atlantic. We find that while the sensitivity to model resolution is limited, the CRH changes dramatically with microphysics and convection schemes. In particular, we show that the distribution of vertical velocity and cloud ice mass mixing ratio are critical factors in modifying the modeled CRH. Our results show a clear benefit of high-resolution simulations with explicit representation of convection, which allow updrafts to interact directly with the cloud field for simulating the CRH. Following these results, we quantify sources of uncertainty in CRH due to the uncertainties in the treatment of radiative transfer within an idealized extratropical cyclone. To this

end, we combine large-eddy-model simulations with offline radiative transfer calculation over different regions of the cyclone. We find that parameterization of ice optical properties and cloud horizontal heterogeneity are the two factors contributing most to the mean uncertainty in CRH at larger spatial scales and can be more relevant for the large-scale dynamics of the cyclone. On the other hand, 3D cloud-radiative effects are much smaller on average, especially for stratiform clouds within the warm conveyor belt of the cyclone. Our analysis in particular highlights the potential to improve the simulation of CRH by better representing ice optical properties.

To bridge the gap between idealized studies and practical applications, we investigate the impact of CRH and its uncertainty on the dynamics of four North Atlantic cyclones. We find that CRH has a significant impact on the dynamics of North Atlantic cyclones. Consistent with the idealized study, CRH affects the dynamics of cyclones via changes in latent heating and subsequently the large-scale flow near the tropopause. Finally, we show that CRH uncertainties due to the radiation parameterization affect the evolution of potential vorticity near the tropopause.

The novelty of this thesis is that, for the first time, i) we shed light on the mechanism of the cloud-radiative impact on the dynamics of extratropical cyclones; ii) we systematically assess the uncertainty in the CRH in the extratropical atmosphere due to different factors; iii) we study the impact of the CRH on the dynamics of North Atlantic cyclones; and iv) we show that uncertainties in the CRH are relevant for the model predictions of extratropical cyclones.

Zusammenfassung

Die Dynamik und Vorhersagbarkeit von außertropischen Zyklonen wird stark von diabatischen Wolkenprozessen beeinflusst. Während der Einfluss der Wolken aufgrund der mit ihr verbundenen Freisetzung latenter Erwärmung im Mittelpunkt vieler Studien steht, ist über den Einfluss der „Cloud Radiative Heating" (CRH) auf die Dynamik außertropischer Zyklone wenig bekannt. In dieser Arbeit untersuchen wir den Einfluss der CRH auf die Dynamik außertropischer Zyklone und ihre Auswirkungen auf deren Vorhersagbarkeit. Mit dem ICOsahedral Nonhydrostatic (ICON) Modell, kombinieren wir verschiedene Modellierungsansätze und -methoden, von idealisierten Simulationen barokliner Lebenszyklen in verschiedenen Modell-Setups und Hindcast-Simulationen über dem Nordatlantik bis hin zu Large-Eddy-Modell-Simulationen. Der Mehrwert eines solchen ganzheitlichen Ansatzes besteht darin, dass wir ein umfassendes Verständnis der Auswirkungen von CRH auf die Dynamik von Zyklonen gewinnen.

Wir entwickeln ein neues Modellierungsverfahren, das die Auswirkungen von CRH auf idealisierte Zyklone auf eine leicht zu interpretierende Weise isoliert. Mithilfe dieses Verfahrens finden wir heraus, dass CRH einen erheblichen Einfluss auf die Dynamik idealisierter außertropischer Zyklone hat. Wir identifizieren sich kompensierende Mechanismen zwischen den Strahlungseffekten von tiefliegenden Wolken, die Zyklonen schwächen, und hochliegenden Wolken, die Zyklonen stärken. Wir untersuchen die Auswirkungen von CRH in Bodennähe und in den oberen Schichten nahe der Tropopause und stellen fest, dass die Auswirkungen von CRH in den oberen Schichten am stärksten sind.

Um die Auswirkungen von CRH auf die Zirkulation in der oberen Troposphäre zu verstehen, diagnostizieren wir die Entwicklung der Unterschiede in der potenziellen Vorticity zwischen einer Simulation mit und ohne CRH, und wir quantifizieren, durch welche Prozesse diese Unterschiede im Laufe des Lebenszyklus des Zyklons wachsen. Es zeigt sich, dass CRH die Zyklone hauptsächlich über die verstärkte Freisetzung latenter Wärme durch mikrophysikalische Wolkenprozesse und anschließende Veränderungen der großräumigen obertroposphärischen Strömung nahe der Tropopause beeinflusst. Unsere Ergebnisse zeigen, dass CRH, obwohl sie vergleichsweise gering ist, außertropische Zyklone durch kontinuierliche Modulation der mikrophysikalischen Erwärmung in Wolken und der großräumigen Strömung beeinflussen kann. Daher ist es möglich, dass Unsicherheiten in der CRH die Entwicklung von Zyklonen und die numerischen Vorhersagen auf synoptischen Skalen beeinflussen können.

Wir bewerten die Unsicherheit in der CRH über die Unsicherheit in der Darstellung des Wolkenfeldes in Bezug auf die Modelleinstellungen über dem Nordatlantik. Es zeigt sich, dass die Empfindlichkeit gegenüber der Wahl der Modellauflösung zwar begrenzt ist, die CRH sich jedoch je nach Mikrophysik und Konvektionsschemata drastisch ändert. Insbesondere zeigen wir, dass die Verteilung der Vertikal-

geschwindigkeit und das Wolkeneis-Massenmischungsverhältnis entscheidende Faktoren für die Veränderung der modellierten CRH sind. Unsere Ergebnisse zeigen einen klaren Vorteil von hochauflösenden Simulationen mit expliziter Darstellung der Konvektion, die Aufwinde direkt mit dem Wolkenfeld interagieren lassen, um die CRH zu simulieren. Im Anschluss an diese Ergebnisse quantifizieren wir die Quellen der Unsicherheiten in der CRH basierend auf Unsicherheiten bei der Behandlung des Strahlungstransfers innerhalb eines idealisierten außertropischen Zyklons. Zu diesem Zweck kombinieren wir Large-Eddy-Model-Simulationen mit Offline-Berechnungen des Strahlungstransfers über verschiedene Bereiche des Zyklons. Wir stellen fest, dass die Parametrisierung der optischen Eigenschaften des Eises und der horizontalen Heterogenität der Wolken die beiden Faktoren sind, die am meisten zur mittleren Unsicherheit in der CRH auf größeren räumlichen Skalen beitragen und die für die großräumige Dynamik der Zyklone relevanter sein können. Andererseits sind die 3D-Strahlungsantriebe durch Wolken im Durchschnitt viel kleiner, insbesondere für stratiforme Wolken innerhalb des „Warm-Conveyor-Belts" der Zyklone. Unsere Analyse zeigt insbesondere das Potenzial zur Verbesserung der Simulation von CRH durch eine bessere Darstellung der optischen Eigenschaften von Eis.

Um die Lücke zwischen idealisierten Studien und praktischen Anwendungen zu schließen, untersuchen wir die Auswirkungen von CRH und ihrer Unsicherheit auf die Dynamik von vier nordatlantischen Zyklonen. Wir stellen fest, dass CRH einen signifikanten Einfluss auf die Dynamik der nordatlantischen Zyklone hat. In Übereinkunft mit der idealisierten Studie beeinflusst CRH die Dynamik der Zyklone über Veränderungen der latenten Erwärmung und in der Folge der großräumigen Strömung in der Nähe der Tropopause. Schließlich zeigen wir, dass Unsicherheiten im CRH aufgrund der Parametrisierung der Strahlung die Entwicklung der potentiellen Vorticity in der Nähe der Tropopause beeinflussen.

Der neuartige Aspekt dieser Arbeit besteht darin, dass wir zum ersten Mal i) den Mechanismus des Einflusses der Strahlungsantriebes der Wolken auf die Dynamik außertropischer Zyklone beleuchten; ii) die Unsicherheit in der CRH in der außertropischen Atmosphäre aufgrund verschiedener Faktoren systematisch bewerten; iii) den Einfluss der CRH auf die Dynamik nordatlantischer Zyklone untersuchen; und iv) zeigen, dass Unsicherheiten in der CRH für die Modellvorhersagen außertropischer Zyklone relevant sind.

Preface

The PhD candidate confirms that the research presented in this thesis contains significant scientific contributions by himself. This thesis reuses material from the following publications:

Keshtgar, B., Voigt, A., Hoose, C., Riemer, M., and Mayer, B.: Cloud-radiative impact on the dynamics and predictability of an idealized extratropical cyclone, Weather Clim. Dynam., 4, 115–132, https://doi.org/10.5194/wcd-4-115-2023, 2023.

Voigt, A., **Keshtgar, B.**, and Butz, K.: Tug-Of-War on Idealized Midlatitude Cyclones Between Radiative Heating From Low-Level and High-Level Clouds, Geophys. Res. Lett., 50, e2023GL103188, https://doi.org/10.1029/2023gl103188, 2023.

Sullivan, S., **Keshtgar, B.**, Albern, N., Bala, E., Braun, C., Choudhary, A., Hörner, J., Lentink, H., Papavasileiou, G., and Voigt, A.: How does cloud-radiative heating over the North Atlantic change with grid spacing, convective parameterization, and microphysics scheme in ICON version 2.1.00?, Geosci. Model Dev., 16, 3535–3551, https://doi.org/10.5194/gmd-16-3535-2023, 2023.

Keshtgar, B., Voigt, A., Mayer, B., and Hoose, C.: Uncertainties in cloud-radiative heating within an idealized extratropical cyclone, Atmos. Chem. Phys., 24, 4751–4769, https://doi.org/10.5194/acp-24-4751-2024, 2024.

The candidate led the research performed in Keshtgar et al. (2023). The ICON simulations and analysis were performed solely by the candidate, who also wrote the text with contributions from Aiko Voigt, Corinna Hoose, Michael Riemer, and Bernhard Mayer. The simulation raw output is archived on the

high-performance storage system at DKRZ. Following open-science practice and FAIR data principle, the post-processed data used in the analysis along with the ICON simulation run scripts, scripts for deriving the baroclinic life cycle initial conditions, and the analysis scripts are published at the LMU open data server (`https://doi.org/10.57970/h1y02-bjv70`).

The results of Voigt et al. (2023) are based on the master thesis of Klara Butz titled "The radiative impact of clouds on idealized extratropical cyclones" (`https://ubdata.univie.ac.at/AC16593523`) supervised by Aiko Voigt and the candidate. The candidate advised the student together with Aiko Voigt on a daily basis. The master's project was carried out in parallel with the candidate's PhD project to further understand the cloud-radiative impact on extratropical cyclones. The candidate prepared the model setup and implemented the modeling approaches to study the cloud-radiative impact on cyclones. The candidate contributed to the conceptualization, model setup, analysis, and writing of the master's thesis and the published paper. The simulation output and ICON simulation and analysis runscripts are archived in the Phaidra repository for the permanent secure storage of digital assets at the University of Vienna under `https://doi.org/10.25365/phaidra.407` and `https://doi.org/10.25365/phaidra.408`.

The results presented in Sullivan et al. (2023) were generated in a nontraditional hackathon format. Over the course of 2 years, the former research group "Cloud-radiative interactions with the North Atlantic storm track" at IMKTRO, led by Aiko Voigt, met intermittently for intensive 3-day periods of data analysis and discussion. The candidate actively participated in all meetings and contributed to the conceptualization, execution, and organization of the analyses. The candidate directly contributed to the climatological analysis of cloud-radiative heating and cloud properties over the North Atlantic. Aiko Voigt led the funding acquisition and project management, and Sylvia Sullivan led the writing of the original draft. The candidate and co-authors contributed to the review and editing of the paper. The codes to reproduce figures from model output and the post-processed data are published on Zenodo at `https://doi.org/10.5281/zenodo.7847650`, and `https://doi.org/10.5281/zenodo.7236564`.

The candidate led the research performed in Keshtgar et al. (2024). The ICON simulations and offline radiative transfer calculations were performed solely by the candidate. The data analysis was performed by the candidate with contributions from Aiko Voigt, Bernhard Mayer, and Corinna Hoose. The candidate led the writing process of the paper with input from all co-authors. The simulation raw outputs are archived on the high-performance storage system at DKRZ. The post-processed data for producing the figures and the code repository containing scripts for ICON simulations, offline radiative transfer calculations, and the analysis are published on Zenodo (`https://doi.org/10.5281/zenodo.10807815`). Finally, the results presented in chapter 8 are based on a manuscript prepared by the candidate and in the process of being finalized for submission.

The candidate confirms that appropriate credit has been given within the thesis where reference has been made to the work of others. This copy has been supplied on the understanding that this is copyright material and that no quotation from the thesis may be published without proper acknowledgment.

Contents

1 Introduction

In this chapter, we explain the dynamics of extratropical cyclones and the role of latent heating in shaping their dynamics in Sect. 1.1. This section sets the stage for describing how clouds can affect extratropical cyclones through their interaction with radiation. We introduce cloud-radiative heating (CRH) as the key variable in this thesis and explain the simulation of the cloud-radiation interaction and its uncertainty in Sect. 1.2. Section 1.3 reviews the studies that highlight the importance of CRH for the dynamics of extratropical cyclones. Then, in Sect. 1.4, we explain the link between extratropical cyclones and midlatitude atmospheric predictability. Here we discuss how it is conceivable that uncertainties in the simulation of the CRH may affect the predictability of extratropical cyclones. Some parts of this chapter are adapted from Keshtgar et al. (2023, 2024). ©The Authors, CC BY 4.0 ⓒⓘ

1.1 Dynamics of Extratropical Cyclones

Extratropical cyclones, often referred to as midlatitude storms or low-pressure systems, are an important part of the atmospheric circulation in the midlatitudes. Extratropical cyclones determine midlatitude climate by transporting energy and moisture poleward. Extratropical cyclones account for more than 70% of total precipitation in Europe during winter (Hawcroft et al., 2012). These cyclones drive midlatitude weather and are responsible for strong wind gusts and heavy precipitation leading to flooding, storm surges, and significant economic losses (Roberts et al., 2014).

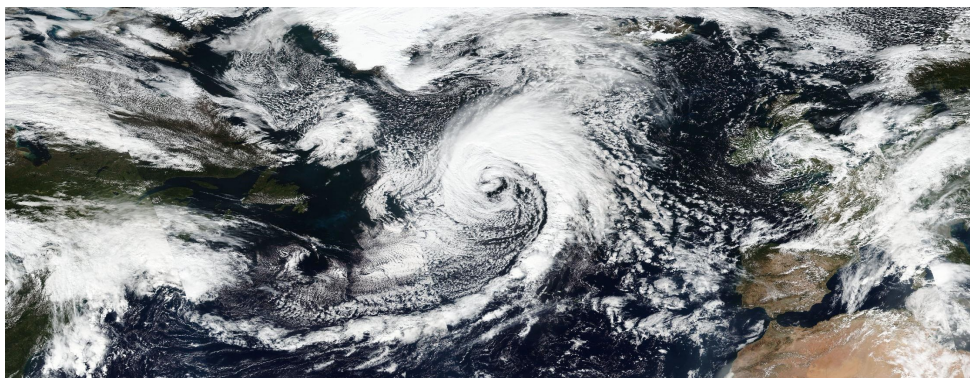Figure 1.1: Satellite image of the so-called Stalactite cyclone in the North Atlantic on 1 October 2016. The image is produced by NASA's EOSDIS Worldview program (`https://worldview.earthdata.nasa.gov/`).

Understanding the dynamics of extratropical cyclones and accurately simulating them in weather and climate models has long been a priority. Many fundamental concepts of synoptic-scale midlatitude dy-

namics, such as the formation of extratropical cyclones and the propagation of Rossby waves, were based on the discovery of quasi-geostrophic baroclinic instability in the first half of the 20th century (Charney, 1947; Eady, 1949). However, during the so-called "golden age of dry dynamics" between 1950 and 1980, research on the role of diabatic or nonconservative processes, especially due to latent heating from phase changes of water vapor during cloud formation, was limited (Wernli and Gray, 2023).

Clouds are recognized as markers of atmospheric circulation, as can be seen in any satellite image (Fig. 1.1). For example, the large comma-shaped cloud systems in the midlatitudes represent extratropical cyclones. However, clouds substantially affect the atmospheric circulation in which they are embedded. In the case of extratropical cyclones, this recognition has led to major advances in our understanding of the dynamics of extratropical cyclones and midlatitude atmospheric predictability (Wernli and Gray, 2023). Understanding the role of cloud diabatic processes has remained at the heart of this research field to this day.

Baroclinic Instability and Potential Vorticity Perspective

Looking at the history of research on extratropical cyclones makes it clear that the theory of baroclinic instability (Charney, 1947; Eady, 1949) and the potential vorticity perspective (Hoskins et al., 1985) introduced in the last century were milestones for progress in understanding the dynamics of extratropical cyclones and for numerical weather prediction (e.g., Schultz et al., 2019). These two perspectives are intricately intertwined, with baroclinic instability as the primary mechanism for the development of extratropical cyclones, and the potential vorticity perspective providing a complementary theoretical framework for analyzing the behavior of these cyclones with respect to the role of diabatic processes.

Baroclinic instability owes its existence to the meridional temperature gradient in a rotating and stratified atmosphere. The difference in solar radiative heating between the equator and the poles sets up a strong temperature gradient in the midlatitudes. This gradient drives the formation of baroclinic zones (Fig. 1.2), where pressure gradient and Coriolis forces can balance each other out in what is known as thermal wind balance. Thermal wind balance can be given by (e.g., Hoskins et al., 1978):

$$\frac{\partial u}{\partial z} \approx -\frac{g}{f\theta_0}\frac{\partial \theta}{\partial y}, \tag{1.1}$$

where u is the zonal wind, g is the gravitational acceleration, f is the Coriolis parameter, and θ is the potential temperature (θ_0 is the reference potential temperature). Equation 1.1 shows that through thermal wind balance, the temperature gradient creates a vertical wind shear (Fig. 1.2, thin black arrows on the left side of the diagram) and a situation in which the atmospheric flow is unstable to small wave perturbations, such as vorticity or temperature wave perturbations. The thermal wind balance also describes the jet streams, the westerly fast-flowing air currents at the boundary between the troposphere and the stratosphere. Jet streams are crucial for shaping weather and climate in the midlatitudes (e.g., Schneider, 2006), as disturbances can gain momentum and energy from them.
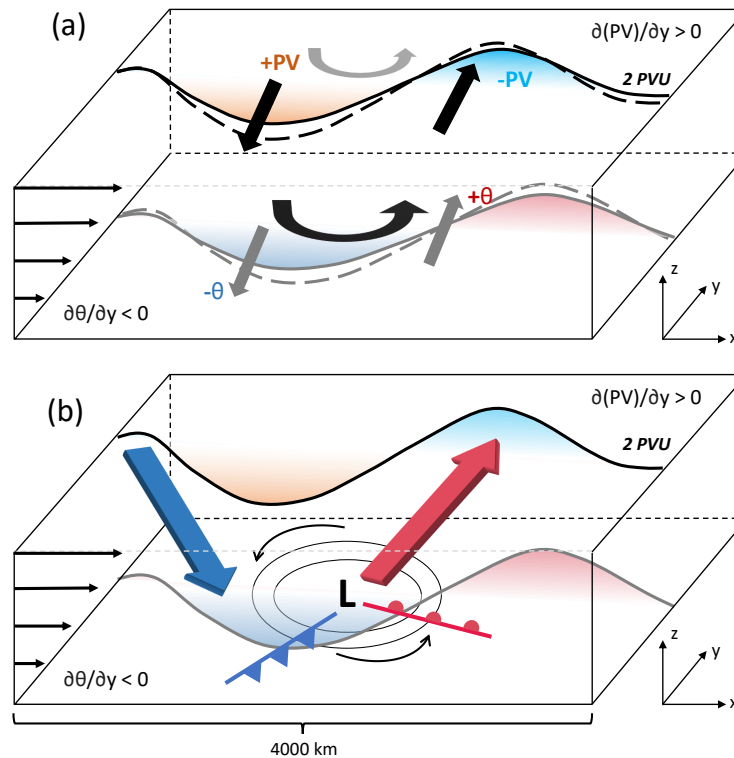
Figure 1.2: Illustration of (a) baroclinic instability and (b) cyclogenesis. Vertical wind shear is indicated by thin black arrows on the left side of the diagrams. Upper-level and surface waves are indicated by solid black and gray lines, respectively. The black and gray arrows indicate the upper-level and surface circulation, respectively, due to the PV anomalies. The black and gray circular arrows indicate the induced circulation at the surface and upper level, respectively. The black and gray dashed lines represent waves at a later time. In panel (b), "L" represents the cyclone center with warm and cold fronts. Isentropic ascent and descent are indicated by large red and blue arrows, respectively. Color shading at the upper level and surface indicates PV and temperature anomalies. 2 PVU lines mark the dynamic tropopause.

The mathematical treatment of baroclinic instability is quite challenging. Some early simplified mathematical descriptions of baroclinic instability attempted to capture the fundamental processes that drive the development of extratropical cyclones. For instance, the analytical solution of the Eady model (proposed by Eady, 1949) based on quasi-geostrophic approximation demonstrates that the fastest-growing disturbance has a wavelength of approximately 4000 km, which is the typical wavelength of surface high and low-pressure systems in the atmosphere. From these simplified models, one also obtains diagnostics that provide valuable insights into the underlying mechanisms driving baroclinic instability. For example, the "Eady growth rate" is often used to measure the baroclinicity of the atmosphere and thus the potential energy available for the growth of disturbances. The Eady growth rate can be estimated as (Lindzen and Farrell, 1980):

$$\sigma_D = 0.31 \frac{f}{N} \frac{\partial u}{\partial z}, \tag{1.2}$$

where N is the Brunt-Väisälä frequency characterizing the stability of the atmosphere. Equation 1.2 shows that disturbances grow faster in less stable environments with stronger vertical zonal wind shear or stronger meridional temperature gradient (Eq. 1.1).

Baroclinic instability based on the Eady model explains the growth of small wave perturbations or so-called normal modes. In the real atmosphere, however, there are usually wave perturbations of finite amplitude at either the upper or lower levels. These wave perturbations can arise from a variety of sources, including interactions with upper-level wave disturbances, frontal boundaries, and topographic features. The concept of the "potential vorticity perspective" (Hoskins et al., 1985) was introduced to understand atmospheric circulation in terms of interactions between different wave perturbations.

Potential vorticity (PV) is a key variable in dynamical meteorology as it captures the kinematic and thermodynamic properties of the atmospheric flow in a single quantity. PV is conserved for an adiabatic, frictionless flow. It measures the circulation of a fluid parcel and depends on the absolute vorticity and static stability of the atmosphere. The Ertel PV in height coordinates is defined by Ertel (1942):

$$PV = \frac{1}{\rho} \eta \cdot \nabla \theta, \tag{1.3}$$

where ρ is the atmospheric density, $\eta = \nabla \times \mathbf{u} + 2\Omega$ is the absolute vorticity vector, where $\nabla \times \mathbf{u}$ is the relative vorticity and 2Ω is the planetary vorticity with Ω being the Earth's angular velocity. $\mathbf{u}$ is the three-dimensional wind vector and $\nabla \theta$ is the potential temperature gradient. Potential vorticity is typically measured in Potential Vorticity Units (PVU), where 1 PVU is equivalent to $10^{-6}\,\mathrm{m^2\,s^{-1}\,K\,kg^{-1}}$. Ertel PV can also be expressed in isentropic coordinates:

$$PV = -g \frac{\partial \theta}{\partial p} (\zeta_\theta + f), \tag{1.4}$$

where p is the pressure, ζ_θ is the vertical component of the relative vorticity on isentropic surfaces, and $-g \frac{\partial \theta}{\partial p}$ represents the static stability. PV is generally higher in the stratosphere than in the troposphere because the stratosphere is characterized by strong stable stratification. The strongest increase in PV occurs in the transition zone between the troposphere and the stratosphere, i.e., the tropopause. The tropopause can be characterized as a PV surface, as it marks the boundary between high stratospheric PV and low tropospheric PV. The 2 PVU surface is commonly regarded as the dynamic tropopause (e.g., Röthlisberger et al., 2018).

Being conserved in an adiabatic, frictionless flow makes PV a unique quantity, as its rate of change can be predicted by advection:

$$\frac{DPV}{Dt} = \frac{\partial PV}{\partial t} + \mathbf{v} \cdot \nabla PV = 0, \tag{1.5}$$

where $\frac{D}{Dt}$ is the material derivative, i.e., the temporal change of the PV within an air parcel moving with the horizontal wind $\mathbf{v}$. Thus, PV anomalies represent deviations from the background state of

the atmosphere caused by the advection of air masses with lower or higher PV. Positive PV anomalies indicate regions of increased absolute vorticity or stratification, while negative PV anomalies indicate regions of decreased absolute vorticity or stratification.

One way to conceptualize baroclinic instability and the PV perspective on how a baroclinic wave develops is through the mutual interaction of two waves, one at the surface and one at upper levels near the tropopause (Fig. 1.2a; Hoskins et al., 1985). The upper-level wave can be viewed as a Rossby wave propagating westward relative to the mean flow due to meridional advection of planetary vorticity (Wirth et al., 2018). The lower-level wave can be thought of as a temperature wave perturbation with warm and cold anomalies. Each wave is associated with a wind field that operates on its own level and extends vertically to the level of the other wave. This means that the wind field advects the associated wave and the PV at the level of the other wave.

Consider an upper-level wave with positive and negative PV anomalies moving over a surface baroclinic zone. The positive PV anomaly is associated with a cyclonic circulation that advects high PV air towards the equator and low PV air towards the pole (black straight arrows in Fig. 1.2a). The upper-level wind flow related to the positive PV anomaly can extend vertically down to the surface, advecting positive vorticity and inducing cyclonic circulation at the surface (black circular arrow in Fig. 1.2a).

The induced surface cyclonic circulation advects warm air towards the pole and cold air towards the equator (gray straight arrows in Fig. 1.2a). This circulation can also induce a cyclonic circulation at the upper levels (gray circular arrow in Fig. 1.2a). The induced circulation at upper levels strengthens the initial positive PV anomaly, which, in turn, affects the lower-level wave again. As these upper and lower-level wave disturbances grow, the vertical wind shear leads to an increasing westward tilt with height between the waves. With a suitable phase shift between the two waves, the waves can become phase-locked, and the induced circulation from each wave acts optimally to amplify the amplitude of the other wave, providing a mechanism for disturbances to grow faster in a baroclinic environment. This is the essence of baroclinic instability.

Since PV is conserved under adiabatic motion, air parcels move along the isentropic surfaces. Thus, stratospheric air descends when displaced adiabatically towards the equator, while tropospheric air ascends when displaced towards the poles. During baroclinic wave development, the induced vorticity and thermal advection at lower levels alter the static stability of the atmosphere, forcing poleward-moving air associated with the positive surface temperature anomaly to ascend and equatorward-moving air associated with the negative temperature anomaly to descend (Fig. 1.2b). The isentropic ascending motion leads to the convergence of air masses near the surface and the formation of a low-pressure system.

Based on this conceptual framework, several idealized modeling studies have been conducted to investigate baroclinic growth and the basic structure of extratropical cyclones (e.g., Hoskins and West, 1979; Davies et al., 1991; Thorncroft et al., 1993). Despite the simplicity of these idealized simulations, they capture essential features of cyclone structure, such as warm and cold fronts and, in some cases, frontal occlusion. These simulations also shed light on the interaction between extratropical cyclones

and Rossby wave dynamics. For more details on the conceptual models of extratropical cyclones and cyclone classification, see Catto (2016) and Schultz et al. (2019).

Many of the early idealized modeling studies of baroclinic waves ignored atmospheric moisture in the simulations. However, within the ascending regions of the cyclone, the air undergoes adiabatic cooling due to the decrease in pressure with height (Fig. 1.2b). In the presence of atmospheric moisture, adiabatic cooling leads to condensation and the formation of clouds and precipitation, which has been shown to significantly affect the growth of baroclinic waves and extratropical cyclones.

Latent Heating

The idealized dry baroclinic life cycle simulations confirmed the essential role of baroclinicity in cyclogenesis. However, these simulations were unable to describe rapid or explosive cyclogenesis. Therefore, another mechanism has to be involved to explain rapid cyclogenesis. Some early case studies already highlighted the role of moisture in rapid cyclogenesis (e.g., Manabe, 1956; Anthes et al., 1983; Rogers and Bosart, 1986). They suggested that the latent heating associated with the formation of clouds and precipitation, in combination with baroclinic processes, can lead to the rapid deepening of cyclones. The impact of latent heating on cyclogenesis has since been demonstrated in numerous modeling and observational studies. A comprehensive review of the role of diabatic processes on extratropical cyclones, especially with respect to latent heating, is given by Wernli and Gray (2023).

As mentioned earlier, PV is a conserved quantity for frictionless adiabatic flow. Therefore, PV can serve as a tracer that indicates how the circulation is modified by diabatic processes. The diabatic modification of PV can be given by (e.g., Joos and Wernli, 2012):

$$\frac{DPV}{Dt} = \frac{1}{\rho} \eta \cdot \nabla \dot{\theta} \approx \frac{1}{\rho} \eta_z \cdot \frac{\partial \dot{\theta}}{\partial z}, \tag{1.6}$$

where $\dot{\theta}$ accounts for diabatic heating tendencies such as latent heating. Frictional processes are not considered here. It is also assumed that the vertical gradient of diabatic heating is greater than its horizontal gradient, which is generally true due to the higher variability of diabatic heating in the vertical direction (Joos and Wernli, 2012). Equation 1.6 shows that the main effect of latent heating is therefore the production of PV below the maximum of latent heating and the depletion of PV above.

From the PV perspective, the cyclone development is associated with the coupling of two anomalous waves, an upper-level PV anomaly and a surface temperature anomaly (Fig. 1.2a). When latent heating comes into play, it can enhance the mutual interaction of these two waves. Within the ascending regions of the cyclone, latent heating produces a positive PV anomaly at lower levels and a negative PV anomaly at upper levels (Fig. 1.3). These positive and negative diabatic PV anomalies intensify and maintain the growth of baroclinic waves in three ways:

1. The low-level positive PV anomaly induces cyclonic circulation at the surface and maintains and intensifies lower tropospheric cyclonic vorticity (red circular arrow in Fig. 1.3).

2. The intensified lower-level cyclonic vorticity can, in turn, induce and reinforce upper-level PV anomaly wave and its cyclonic vorticity advection (gray circular arrow in Fig. 1.3).

3. The negative PV anomaly above the maximum latent heating contributes to the downstream ridge development at upper levels, which amplifies the amplitude of the PV anomaly wave (cyan circular arrow in Fig. 1.3). However, it is now well established that ridge development due to latent heating is largely the result of its indirect impact on PV advection by altering the divergent flow, rather than its direct negative PV anomaly (Teubler and Riemer, 2021, further explanation in Sect. 1.4).

Therefore, latent heating further contributes to the westward tilt between upper- and lower-level waves, which favors rapid cyclogenesis (e.g., Stoelinga, 1996; Ahmadi-Givi et al., 2004).
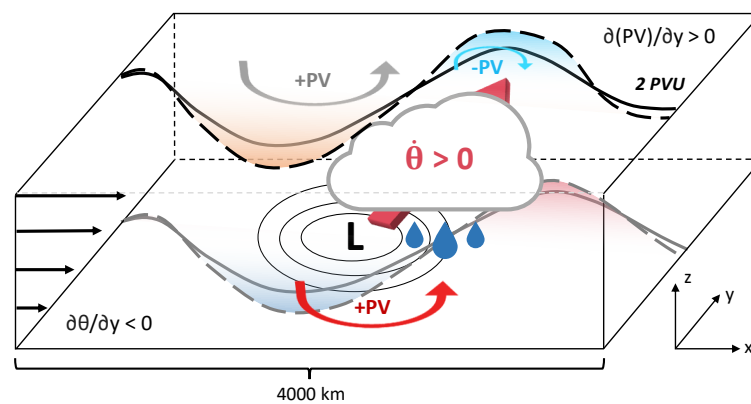
Figure 1.3: Illustration of cloud latent heating impact on baroclinic wave development. The schematic is based on the baroclinic instability diagram in Fig. 1.2, where most of the features have been explained. The red and gray circular arrows indicate the latent heating-induced cyclonic circulation at the surface and upper level, respectively. The cyan circular arrow shows the anticyclonic vorticity above the maximum latent heating.

Lorenz Energy Cycle

Another conceptual framework that explains the development of baroclinic eddies, including the impact of latent heating, is the Lorenz energy cycle (Lorenz, 1955). In the Lorenz energy cycle, energy is continuously transformed between different sources, with baroclinic eddies acting as energy conversion machines (Fig. 1.4). Here only the most important parts of the energy cycle for cyclone development are considered. For a complete list of atmospheric energy components and conversion terms, see Boer and Lambert (2008).

The main source of energy for the development of baroclinic eddies is the available potential energy of the zonal mean flow (A_Z), which owes its existence to the radiative imbalance between tropics and extratropics, i.e., the baroclinicity and can be given by (e.g., Rantanen et al., 2019):

$$\langle A_Z \rangle = \int_{p_t}^{p_b} \frac{1}{2} c_p \gamma \langle [T]''^2 \rangle \frac{dp}{g}, \tag{1.7}$$

where c_p is the specific heat capacity of dry air at constant pressure, γ is the stability parameter, and T is the temperature. The symbols $\langle\rangle$, $[]$, and $''$ represent the spatial mean over the analysis domain, the zonal mean, and the deviation from the spatial domain mean, respectively. p_b and p_t are the upper and lower bounds of the integration. The integration is done between low-levels around 900-1000 hPa and high-levels around 100-200 hPa. Note that here the dry formulation of the available potential energy of the zonal mean flow is used, which does not take into account the impact of atmospheric moisture (e.g., Stansifer et al., 2017).
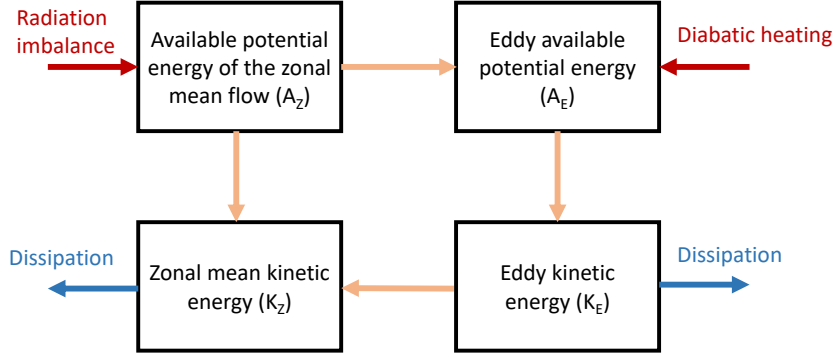
Figure 1.4: Simple diagram of the Lorenz energy cycle. Red arrows show energy sources, while blue arrows show energy sinks, e.g., by friction or turbulence. Orange arrows represent energy conversion from one source to another. The zonal mean kinetic energy refers to barotropic processes that extract kinetic energy from the eddies (Boer and Lambert, 2008).

The growing baroclinic eddies convert A_Z to the eddy available potential energy A_E:

$$\langle A_E \rangle = \int_{p_t}^{p_b} \frac{1}{2} c_p \gamma \langle T^{\star 2} \rangle \frac{dp}{g}, \tag{1.8}$$

that represents the potential energy that can be converted to eddy kinetic energy K_E:

$$\langle K_E \rangle = \int_{p_t}^{p_b} \frac{1}{2} \langle \mathbf{v}^{\star 2} \rangle \frac{dp}{g}. \tag{1.9}$$

The symbol $\star$ denotes the deviation from the zonal mean, and $\mathbf{v}$ is the horizontal wind vector. Therefore, baroclinic eddies receive potential energy from the zonal mean flow by transporting warm air poleward and cold air equatorward, i.e., cyclones act to decrease the temperature gradient in the meridional direction and increase it in the zonal direction:

$$C\left(\langle A_Z \rangle, \langle A_E \rangle\right) = -\int_{p_t}^{p_b} c_p \gamma \langle [T^{\star}v^{\star}] \frac{\partial T}{\partial y} \rangle \frac{dp}{g} - \int_{p_t}^{p_b} c_p \gamma \left(\frac{p}{p_b}\right)^k \langle [T^{\star}\omega^{\star}]'' \frac{\partial[\theta]''}{\partial p} \rangle \frac{dp}{g}, \tag{1.10}$$

where v is the meridional wind and ω is the isobaric vertical motion. A_E can be converted into eddy kinetic energy by the rising of warm air and sinking of cold air:

$$C\left(\langle A_E \rangle, \langle K_E \rangle\right) = -\int_{p_t}^{p_b} \langle \alpha^{\star}\omega^{\star} \rangle \frac{dp}{g}, \tag{1.11}$$

where α is the specific volume. Latent heating further increases the zonal temperature anomaly. It also reduces static stability and promotes stronger vertical motions. Therefore, latent heating directly increases the eddy available potential energy (Eq. 1.10), which can be converted to eddy kinetic energy. Stronger eddy kinetic energy also enhances the energy conversion between zonal mean and eddy available potential energy by the eddies. Together, these effects lead to earlier and more intense cyclone development.

To demonstrate the impact of latent heating on cyclone energetics, Fig. 1.5 shows the evolution of A_Z, A_E, and K_E for two idealized baroclinic life cycle simulations, one with 0% initial relative humidity and the other with 80% initial relative humidity. Strong latent heating in the simulation with higher initial relative humidity leads to a faster and stronger reduction of the A_Z (cf. red and blue lines in Fig. 1.5a). Consequently A_E and K_E substantially increase for simulation with higher initial relative humidity. This analysis shows that latent heating can increase cyclone intensity by almost a factor of 2 (cf. red and blue lines in Fig. 1.5c).
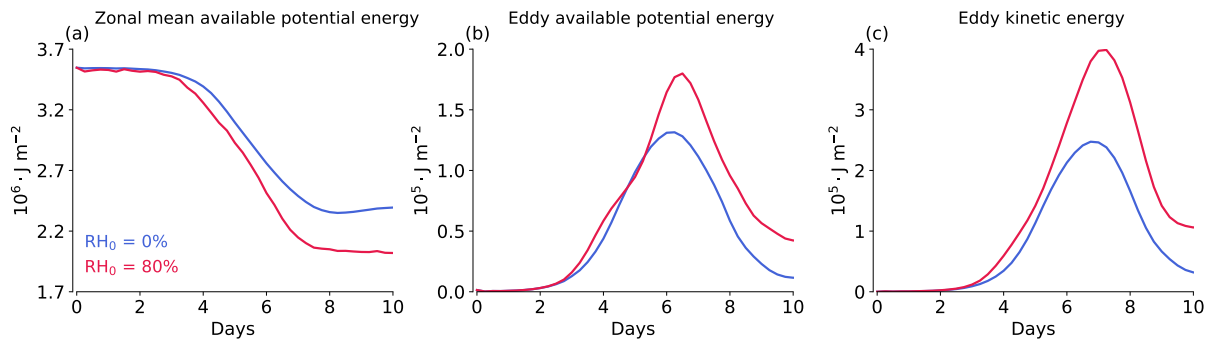
Figure 1.5: Evolution of the global mean (a) available potential energy of the zonal mean flow, (b) eddy available potential energy, and (c) eddy kinetic energy for idealized baroclinic life cycle simulations with 0% and 80% initial relative humidity. For the analysis, the data from the study of Schäfer and Voigt (2018) is used. The energy terms are vertically integrated between 100 and 900 hPa. A detailed description of the initial conditions and the model setup used for the idealized baroclinic life cycle simulations is given in Sect. 3.3.

Extensive modeling studies using various techniques have been conducted over the last decades to understand the impact of latent heating on extratropical cyclones (Wernli and Gray, 2023). In this context, an important feature of extratropical cyclones known as the warm conveyor belt (WCB) has received considerable interest in recent years. The WCB is characterized by ascending warm, moist air moving poleward ahead of the cold front and is associated with strong latent heating in cyclones (e.g., Madonna et al., 2014). It is now well established that latent heating within WCBs is important not only for the development of extratropical cyclones but also for the dynamics of upper-level Rossby waves, with consequent implications for predictability and downstream weather development (see Sect. 1.4). However, recent studies show that clouds can also affect the dynamics of extratropical cyclones through their interaction with radiation. The following section describes cloud-radiation interaction and its representation in weather and climate models.

1.2 Cloud-Radiation Interaction

Clouds play a crucial role in regulating the Earth's temperature and energy by absorbing and reflecting incoming solar radiation that would otherwise heat the atmosphere and surface. In the longwave spectrum, clouds absorb outgoing longwave radiation at their base and re-emit it at colder temperatures at their top that would otherwise cool the atmosphere and surface. Therefore, clouds affect radiative fluxes at the top-of-atmosphere (TOA) and the surface, as well as radiative heating and cooling within the atmosphere. The extent to which these warming and cooling effects occur depends on the cloud's phase and altitude. For example, low-level liquid clouds tend to have a net cooling effect at TOA, surface, and within the atmosphere. In contrast, high-level ice clouds tend to have a warming effect within the atmosphere and a cooling effect at the surface (Voigt et al., 2021).

The impact of clouds on TOA and surface radiative fluxes is quantified by the cloud radiative effects (CRE) and is calculated as the difference between all-sky and (hypothetical) clear-sky radiative fluxes. Thus, CRE measures the instantaneous cloud contribution to radiation. CRE is given by:

$$\text{CRE} = F^{all-sky} - F^{clear-sky},\tag{1.12}$$

where F is the positive downward radiative flux. CRE has units of W m^{-2} and can be decomposed into shortwave and longwave components. The difference between TOA and surface CRE gives the mass-weighted vertically integrated atmospheric CRE (Voigt et al., 2021). Many climate modeling studies use the CRE definition to emphasize the relationship between CRE and atmospheric circulation. For instance, regions dominated by ascending motion and high-level clouds are characterized by atmospheric longwave CRE warming, whereas regions dominated by descending motion and low-level clouds are characterized by atmospheric longwave CRE cooling (Voigt et al., 2021).

Clouds affect the atmospheric circulation through their interaction with radiation in two pathways. The first pathway is through cloud-radiative effects on surface temperature and is referred to as the surface pathway. The second pathway operates through changes in atmospheric temperature due to cloud-radiative heating and cooling (hereafter CRH) within the atmosphere and is referred to as the atmospheric pathway (Voigt et al., 2019). In this thesis, our focus is on the atmospheric pathway. CRH is defined as the radiative flux divergence and can be calculated at a given atmospheric level as the difference between the all-sky and clear-sky flux divergences:

$$\text{CRH} = \left.\frac{\partial T}{\partial t}\right|_{\text{radiation}}^{\text{cloud}} = \left.\frac{\partial T}{\partial t}\right|_{\text{radiation}}^{\text{all- sky}} - \left.\frac{\partial T}{\partial t}\right|_{\text{radiation}}^{\text{clear-sky}} = \frac{1}{\rho\, c_p} \cdot \frac{\partial}{\partial z}\left(F^{\text{all-sky}} - F^{\text{clear-sky}}\right).\tag{1.13}$$

CRH has units of K day^{-1} and can be decomposed into shortwave and longwave components.

Figure 1.6a shows a global view of the vertical distribution of clouds in the atmosphere. High-level clouds are most abundant along the equator due to the ascending regions associated with the intertropical convergence zone (e.g., Harrop and Hartmann, 2016). Low-level clouds dominate in the subtropics,

mainly due to lower static stability and near-surface cold advection (e.g., Li et al., 2014). Extratropical storm tracks are also characterized by high cloudiness due to the presence of deep clouds with high tops and low-level clouds associated with cyclones (e.g., Tselioudis and Jakob, 2002).

Panel b in Fig. 1.6 shows the vertical distribution of CRH in the atmosphere. High-level clouds in the tropics have a strong radiative warming effect in the middle and upper troposphere, predominantly due to the absorption of longwave radiation emitted from warmer atmospheric layers underneath (e.g., Klinger et al., 2017). The CRH from low-level clouds is characterized by a dipole of warming near the cloud base due to the absorption of longwave radiation and cooling at the cloud tops due to longwave emission at colder temperatures (e.g., Klinger et al., 2017). In the extratropics, the same CRH dipole is present in the middle and upper troposphere, with cooling at cloud tops and warming at cloud bases. These patterns of warming and cooling due to CRH have been shown to affect atmospheric circulation, both on a planetary scale and even on the scale of an extratropical cyclone (Sect. 1.3). Before discussing the impacts of CRH, the next section explains how cloud-radiation interactions are simulated in models.
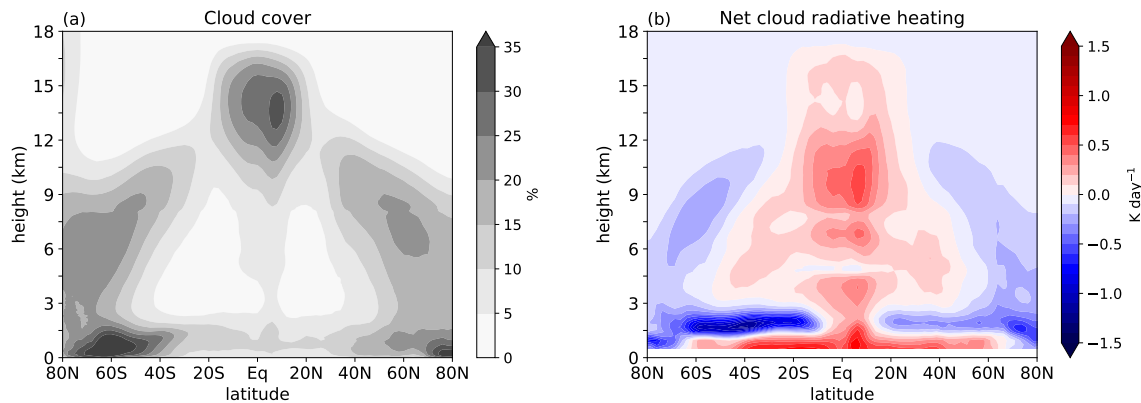
Figure 1.6: Vertical profiles of (a) zonal mean cloud cover and (b) cloud-radiative heating (CRH) averaged between 2006 and 2011 from CloudSat-CALIPSO data. Postprocessed data for cloud cover and CRH are taken from Bertrand et al. (2024) and Sullivan et al. (2023), respectively.

Simulation of Cloud-Radiation Interaction and its Uncertainty

Simulating cloud-radiation interactions is challenging and represents a persistent source of uncertainty in weather and climate models. Uncertainty in the simulation of cloud-radiative impacts can arise from uncertainty in the simulation of the cloud field as well as from uncertainty in the radiative transfer calculation of a given cloud field.

Accurate simulation of cloud-radiative impacts requires accurate simulation of both the microphysical and macrophysical properties of clouds. However, the simulation of clouds is challenging. This is because clouds are complex and their processes occur at different temporal and spatial scales, ranging from the microscale of individual cloud particles to large-scale cloud systems. Clouds are also not fully understood because some of their microphysical processes are still unknown (e.g., Grabowski et al., 2019). Even with perfect knowledge of clouds, the computational requirements to simulate all cloud properties

remain overwhelming. Therefore both the microphysical and macrophysical properties of clouds are parameterized in weather and climate models. In the context of simulating cloud-radiation interaction, these parameterizations serve several purposes. Microphysical properties such as cloud ice and liquid water content and effective particle radii provide cloud optical properties for radiation calculations. Macrophysical properties such as cloud fraction determine the spatial distribution of clouds and are therefore important for the calculation of radiative transfer between cloudy and clear-sky regions (e.g., Črnivec and Mayer, 2021).

Several studies have investigated the impact of different microphysical assumptions on cloud-radiative impacts. For example, Wang et al. (2022) showed that using the more sophisticated two-moment microphysics scheme instead of the one-moment scheme improves the simulation of cloud cover and hence the cloud radiative effects in a climate model. Wang et al. (2021) highlighted the impact of the width of the hydrometeor size distribution on CRH errors. Sullivan and Voigt (2021) identified several ice microphysical factors that influence CRH variability, such as initial ice crystal size and autoconversion rates. Other studies have found that model resolution and convection parameterization play a key role in simulating clouds and their radiative effects (e.g., Senf et al., 2020).

Another major challenge in accurately simulating the cloud-radiation interactions for a given cloud field is related to the radiation parameterization, which is limited to the vertical direction. Clouds are not homogeneous over their horizontal and vertical extents, and this spatial variability significantly affects their interactions with radiation. Cloud horizontal heterogeneity refers to the horizontal variation in cloud optical properties within a grid box. The vertical overlap determines how cloud layers are stacked on top of each other. The ability of models to account for cloud horizontal heterogeneity and vertical overlap depends primarily on their horizontal resolutions. Neglecting cloud horizontal heterogeneity increases longwave emissivity and shortwave absorption of clouds, an effect known as the plane-parallel problem of radiative transfer calculations (e.g., Črnivec and Mayer, 2019). In current weather and climate models, parameterizations are used to represent both cloud horizontal heterogeneity within grid boxes and cloud vertical overlap between adjacent grid boxes. As a result, assumptions in the parameterizations of these two sub-grid effects can lead to errors in the simulation of CRH (e.g., Wang et al., 2021).

The top row of Fig. 1.7 schematically shows different modeling approaches to simulate cloud-radiation interaction within a model column with a rather coarse horizontal resolution. A simple approach to account for cloud horizontal heterogeneity is the scaling factor method (Cahalan et al., 1994; Rossow et al., 2002), for which the cloud optical depth is multiplied by a constant factor to reduce the grid-box cloud optical depth and avoid the plane-parallel problem (Fig. 1.7a). Pincus et al. (2003) presented an alternative approach known as Monte Carlo Independent Column Approximation (McICA). In this approach, cloud horizontal heterogeneity is accounted for by generating random subgrid cloudy columns using a stochastic cloud generator, and calculating radiative transfer in each subcolumn with a random spectral band to gain computational efficiency (Fig. 1.7b). Shonk and Hogan (2008) proposed another unique method to account for cloud horizontal heterogeneity. In their algorithm, cloud layers are sep-

arated into two regions, optically thinner and thicker clouds. Together with the cloud-free region, the radiation scheme calculates radiative transfer for three regions at each model layer and is referred to as the Tripleclouds scheme (Fig. 1.7c).
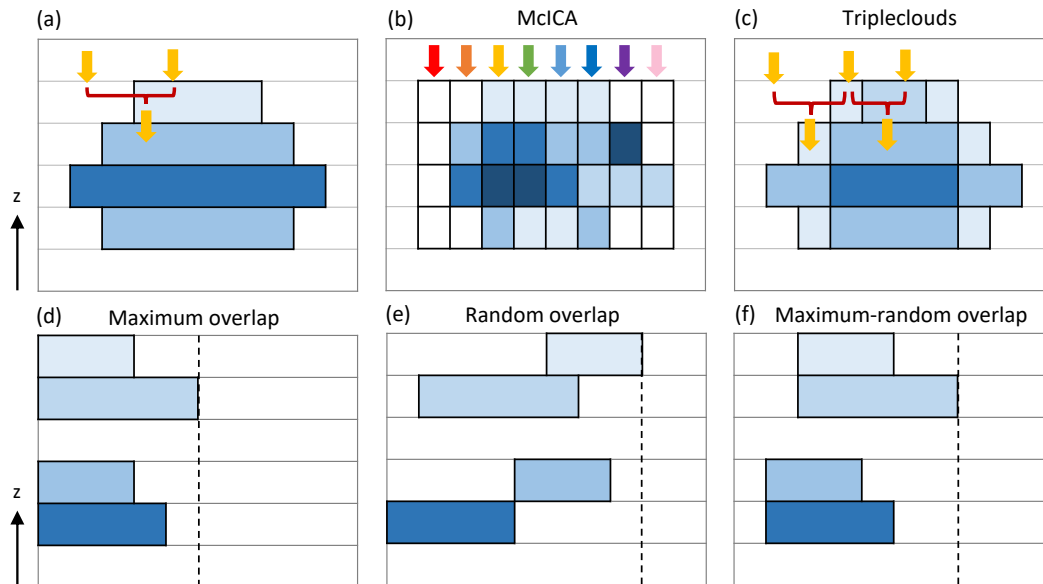
Figure 1.7: Schematic representation of cloud-radiation interaction modeling. The top row shows approaches to account for cloud horizontal heterogeneity using (a) the conventional scaling factor, (b) the Monte Carlo Independent Column Approximation (McICA), and (c) the Tripleclouds method. Yellow arrows indicate radiative fluxes and blue shading represents cloud optical depths. The rainbow-colored radiative fluxes indicate calculations in different spectral bands for the McICA method. The bottom row shows different vertical overlap assumptions: (d) maximum, (e) random, and (f) maximum-random overlap. The vertical dashed lines show total cloud cover at the surface, with higher values to the right.

The bottom row of Fig. 1.7 schematically shows different cloud vertical overlap assumptions, including maximum, random, and maximum-random. Maximum overlap assumes that all cloud layers within a model column are correlated and formed by the same process. Therefore, clouds overlap maximally in the vertical direction. As a result, the total cloud cover is reduced under the maximum overlap assumption (Fig. 1.7d). Conversely, random overlap assumes that the positions of clouds in all layers are uncorrelated and therefore overlap randomly. This assumption generally results in an increase in total cloud cover (Fig. 1.7e). The maximum-random overlap assumption combines both the maximum and random assumptions, where adjacent cloud layers overlap maximally, while clouds separated by at least one cloud-free layer overlap randomly (Fig. 1.7f). This assumption is physically justified by the fact that clouds in adjacent model layers are typically the result of the same physical process, while clouds separated by a cloud-free layer are formed independently and therefore randomly overlap with other clouds (Hogan and Illingworth, 2000). However, this is not always true, especially for cloud systems in strongly sheared environmental conditions (Giuseppe and Tompkins, 2015).

Many studies have investigated the impact of different assumptions used in the parameterization of cloud horizontal heterogeneity and vertical overlap on cloud-radiation interactions (Hogan and Bozzo, 2018; Črnivec and Mayer, 2019, 2021; Wang et al., 2021, 2022). For example, Hogan and Bozzo (2018) showed that the Triplecloud solver is a better choice than the McICA solver because it reduces uncertainty in the CRH by eliminating radiative noises associated with the Monte Carlo approach. Wang et al. (2021) demonstrate that changes in cloud vertical overlap parameters strongly affect the CRH for stratiform and tropical convective clouds.

Even in an ideal situation where clouds are perfectly known and there is no further subgrid cloud horizontal and vertical variability, the simulation of cloud-radiation interactions remains uncertain. This is due to the other uncertainty associated with the radiation parameterization. In principle, the radiative processes for a given atmospheric state are well understood. However, it is not feasible to explicitly calculate all possible radiative interactions in weather and climate models due to the enormous computational costs (Mayer, 2009). Thus, radiation schemes are simplified by calculating the radiative transfer only in the vertical direction rather than in three-dimensional space.
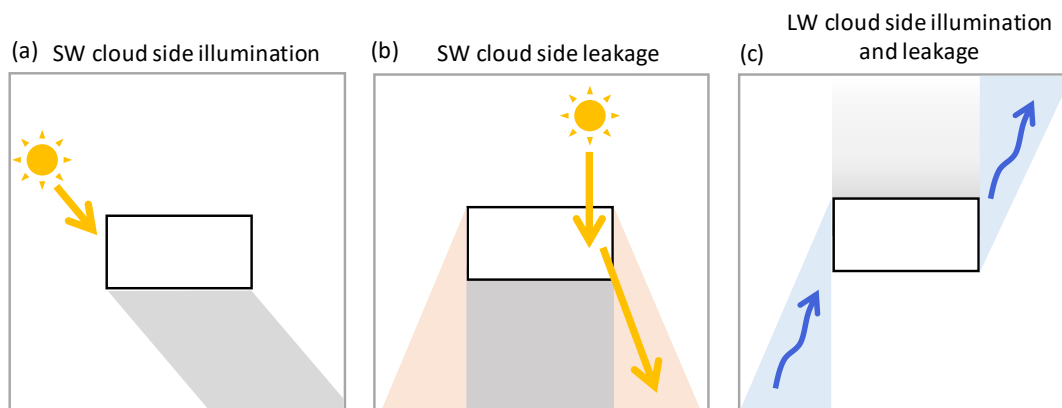
Figure 1.8: Schematic illustration of 3D cloud radiative effects that are not considered in current operational 1D radiation schemes. The gray shading in panels (a) and (b) shows the cloud shadow. Yellow and blue arrows represent photon transport in the shortwave (SW) and longwave (LW) spectrums, respectively.

Neglecting horizontal photon transport leads to significant errors in the simulation of cloud-radiative effects at the TOA, at the surface, and within the atmosphere (Jakub and Mayer, 2015; Klinger et al., 2017; Črnivec and Mayer, 2019; Singer et al., 2021). These errors are associated with 3D cloud-radiative effects. The most important 3D cloud-radiative effects relevant to the simulation of CRH are shown in Fig. 1.8. For more details on 3D radiative transfer in the cloudy atmosphere, see Mayer (2009); Hogan et al. (2016, 2019). When the sun is low in the sky, solar photons can be intercepted by cloud sides (Fig. 1.8a). This shortwave "cloud-side illumination" increases the amount of radiative flux that can be absorbed or reflected by clouds, thereby increasing shortwave CRH (e.g., Jakub and Mayer,

2015). Accounting for horizontal photon transport also accurately represents the correct position of cloud shadows in the atmosphere and at the surface, which in turn can significantly affect radiative fluxes at the surface (Črnivec and Mayer, 2019).

Solar photons can also escape through cloud-sides (Fig. 1.8b). This shortwave "cloud-side leakage" increases the amount of radiation that passes through the cloud instead of being scattered or absorbed, thereby reducing cloud reflectivity and CRH (Hogan and Shonk, 2013; Jakub and Mayer, 2016). Črnivec and Mayer (2019) demonstrated that the impact of cloud-side illumination versus cloud-side leakage on CRH depends on the solar zenith angle. When the sun is low, cloud-side illumination results in more warming, while cloud-side leakage results in cooling when the sun is high. In the longwave spectrum, photons can also be intercepted or escape through cloud sides (Fig. 1.8c). The interception of photons by cloud-sides can lead to stronger absorption and thus warming, while cloud-side leakage leads to cooling. Studies suggest that cloud-side leakage in the longwave spectrum, also known as "cloud-side cooling" (Klinger and Mayer, 2016), dominates the warming effect due to efficient emission of radiation at the cloud sides (Klinger et al., 2017, 2019).

Another simplification in radiation parameterization comes from calculating the optical properties of clouds, especially for ice crystals due to their complex shape and surface roughness. The lack of a consolidated understanding of ice crystal shapes and how they should be represented in models has created another important source of uncertainty in the simulation of cloud-radiation interactions (Zhao et al., 2018; Yi, 2022). Several ice optical parameterizations have been developed based on different assumptions of ice crystal shape, size distribution, and surface roughness (Fu, 1996; Fu et al., 1998; Yang et al., 2013; Baran et al., 2014; Baum et al., 2014). For example, Yi (2022) showed that the choice of the ice optical parameterizations significantly affects global CRE and surface temperature. Zhao et al. (2018) showed that different ice optical parameterizations largely affect the CRH and in turn the large-scale atmospheric circulation and precipitation rate.

Overall, the uncertainty associated with cloud and radiation parameterizations in the models has been translated into dramatic variability in the CRH, such that the CRH varies by a factor of 5 between different global climate models (e.g., Voigt et al., 2019). Studies also indicate that these uncertainties affect not only the dynamics of clouds (Jakub and Mayer, 2016; Klinger et al., 2019; Barekzai and Mayer, 2020), but also the circulation of the atmosphere (Zhao et al., 2018).

1.3 Cloud-Radiative Impact on Extratropical Cyclones

Section 1.1 described how latent heating due to cloud formation affects the dynamics of extratropical cyclones. However, clouds can also affect extratropical cyclones through their interaction with radiation in the atmosphere, which has received comparatively little attention.

The role of cloud-radiation interaction in determining atmospheric circulation has become an important topic in clouds and climate research (e.g., Bony et al., 2015; Voigt et al., 2021). Many climate model-

ing studies have shown that cloud-radiation interactions play a fundamental role in driving the general atmospheric circulation and its response to global warming. A comprehensive review of the radiative impact of clouds on atmospheric circulation is provided by Voigt et al. (2021). This includes studies demonstrating the importance of cloud-radiation on extratropical circulation and its response to surface warming (Grise et al., 2019; Albern et al., 2019). However, research on the radiative impact of clouds on the evolution of weather systems, particularly extratropical cyclones, is limited.

The distinction between weather and climate time scales may have led to the perception that radiation is a slow process and cannot significantly affect the circulation on weather time scales of days. However, several studies showed that radiative processes should be considered more systematically. The cyclone case studies of Chagnon et al. (2013) highlighted the importance of longwave radiative cooling for the PV structure near the tropopause. Baumgart et al. (2019) found radiation to be as important as other diabatic processes for forecast error growth on longer timescales, and Martínez-Alvarado et al. (2016) found that radiation contributes to the diabatic generation of forecast errors in WCBs and Rossby waves. With respect to cloud-radiative impacts, studies on tropical cyclones have shown that longwave absorption and emission by the anvil clouds enhance upward motion, leading to increased convective heating (Fovell et al., 2016), and Ruppert et al. (2020) found this effect to accelerate tropical cyclone development. For extratropical cyclones, however, Schäfer and Voigt (2018) were the only ones to show that CRH significantly affects the intensity of idealized cyclones. This section reviews studies that highlight the impact of CRH on extratropical cyclones.

Climate Modeling Studies

On climate time scales of years, modeling studies show that CRH affects the mean state of the tropical and extratropical circulation in the present climate and its response to climate change (Voigt et al., 2021). Of these studies, many have focused on understanding the impact of the CRH on the tropical circulation. For example, many modeling studies in the aquaplanet configuration agree that CRH strengthens the Hadley circulation and reduces mean tropical precipitation (Voigt et al., 2021). The decrease in mean precipitation is attributed to reduced latent heating in response to strong radiative warming from high clouds (Fig. 1.9, Li et al., 2015).

Other model simulations have shown a similar role for the impact of CRH on the strength and position of extratropical eddy-driven jet streams and storm tracks (Ceppi and Hartmann, 2015; Li et al., 2015; Watt-Meyer and Frierson, 2017). Li et al. (2015) investigated the impact of CRH on eddy kinetic energy in the extratropics using global atmospheric simulations with and without CRH and found that CRH increases the eddy kinetic energy (Fig. 5 of Li et al., 2015). They showed that the shift from upper tropospheric cloud-radiative heating in the tropics to cooling in the midlatitudes strengthens the meridional temperature gradient and hence baroclinicity, which is the primary source of energy for baroclinic waves (Fig. 1.9). The cloud-radiative cooling in the upper troposphere in the extratropics also weakens the at-

mospheric static stability. Both stronger baroclinicity and weaker static stability due to CRH increase the eddy growth rate (Sect. 1.1, Eq. 1.2), resulting in stronger eddy kinetic energy in the midlatitudes.

In contrast to these results, Grise et al. (2019) used a different modeling technique to study the impact of CRH on climate variability in the extratropics. They find that CRH has a small (5-10%) but statistically significant weakening impact on eddy kinetic energy in the midlatitudes, especially in the Southern Hemisphere. The weakening impact of CRH was shown to be in the lower troposphere and attributed to the cloud-radiative modification of static stability below 700 hPa. Strong cloud-radiative cooling by low-level clouds in the extratropics increases static stability at lower levels, which could lead to a weaker eddy growth rate of cyclones (Eady, 1949).

Although these studies do not agree on the sign of the CRH impact on midlatitude eddy kinetic energy, they show that CRH significantly affects the extratropical circulation and highlight the importance of properly simulating the CRH in climate models to accurately represent extratropical storm tracks and their response to climate change.
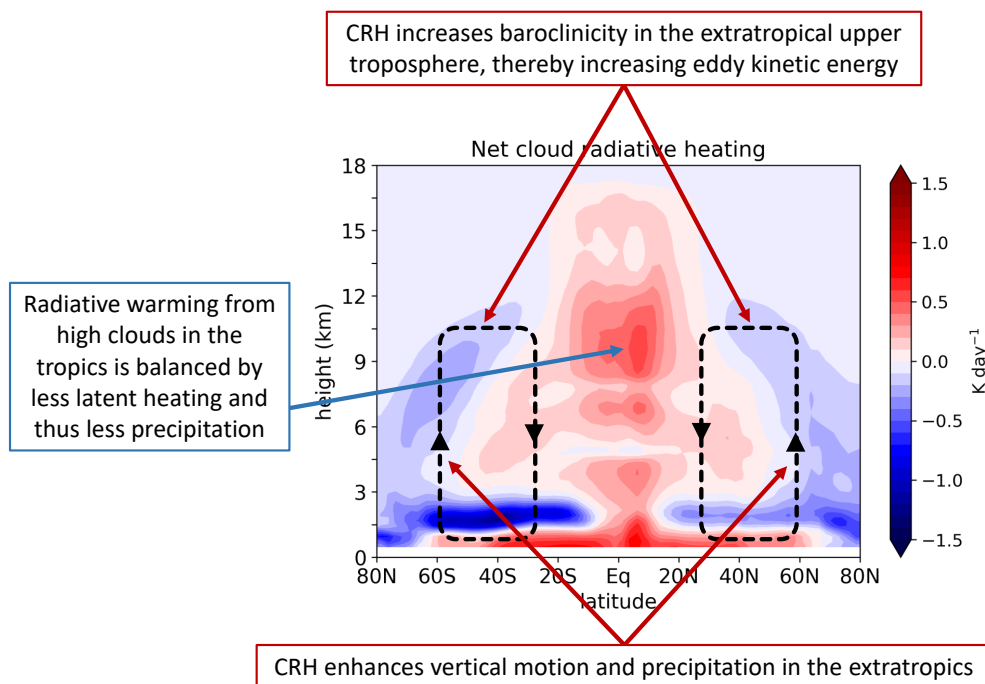
Figure 1.9: Schematic diagram summarizing the impacts of cloud-radiative heating (CRH) on zonal mean circulation in the extratropics and precipitation as described by Li et al. (2015). The color shading is the zonal mean CRH shown in Fig. 1.6.

Studies also demonstrate that CRH has a robust amplifying impact on the precipitation rate over the extratropical ocean (Voigt et al., 2021). Radiative cooling from deep cloud tops in the extratropics can enhance buoyancy and favor stronger upward motion (e.g., Fu et al., 1995). Li et al. (2015) showed that stronger baroclinicity due to CRH enhances eddy momentum fluxes through stronger eddies, which in turn enhances vertical motion in mid-to-high latitudes (40-65°N) and leads to an increase in precipitation.

Idealized Extratropical Cyclones

On weather time scales of days, the impact of CRH on extratropical cyclones is understudied. Although some studies have emphasized the importance of PV anomalies associated with radiative processes within cyclones (Spreitzer et al., 2019) and for the near-tropopause dynamics (Chagnon et al., 2013), they do not explicitly explore the role of CRH in the development of extratropical cyclones.

Schäfer and Voigt (2018) were the first to show that radiation weakens the intensity of an idealized extratropical cyclone by half and that a substantial (although not the dominant) part of the radiative weakening is due to the CRH. To illustrate this, Fig. 1.10 shows the evolution of cyclone central pressure and eddy kinetic energy for idealized baroclinic life cycle simulations with 0 and 80% initial relative humidity and different treatments of radiation (see Sect. 3.4).

Compared to the strengthening impact of latent heating on the intensity of extratropical cyclones (cf. red and blue dashed lines in Fig. 1.10), radiation substantially weakens the cyclone (cf. red or blue dashed and solid lines in Fig. 1.10). Interestingly, the impact of radiation and latent heating are comparable in magnitude, even though latent heating is about three times stronger than radiative heating and cooling in the atmosphere (Schäfer and Voigt, 2018).

A significant part of the radiative weakening is due to cloud-radiation interactions. This can be seen by comparing the intensity metrics in Fig. 1.10 between the moist simulations with all-sky and clear-sky radiation. The latter means that the clouds are made transparent to radiation and only the clear-sky radiative heating is used to step the temperature forward in time. CRH contributes to about 30% of the radiative weakening. The radiative weakening impact of clouds is consistent with the climate modeling study of Grise et al. (2019), who showed that CRH weakens the eddy kinetic energy in the midlatitude.
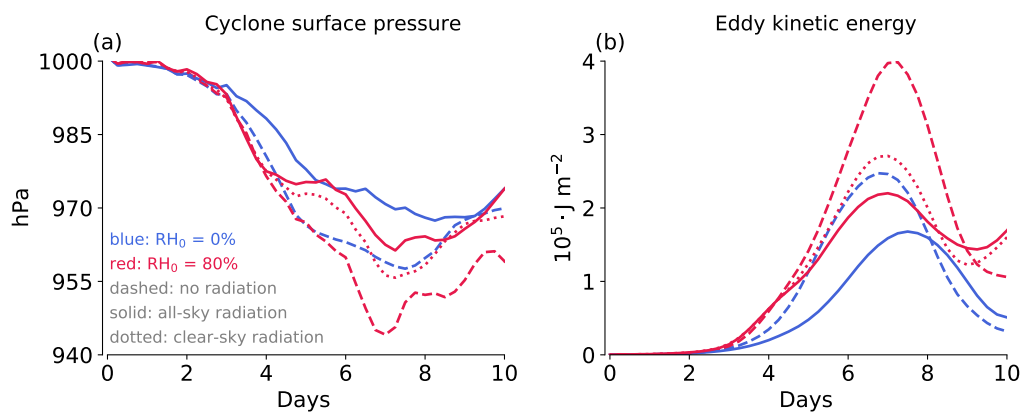
Figure 1.10: Time series of (a) cyclone central pressure and (b) global mean eddy kinetic energy for different radiation treatments in idealized baroclinic life cycle simulations. The eddy kinetic energy is vertically integrated between 100 and 900 hPa. Blue and red lines are for simulations with 0% and 80% initial relative humidity, respectively. Solid lines represent simulations with all-sky radiation, while dotted lines represent simulations with clear-sky radiation. Dashed lines show simulations with the radiation scheme turned off. For the analysis, the data from the study of Schäfer and Voigt (2018) were used. A detailed description of the initial conditions and model setup used for the idealized baroclinic life cycle simulation and modeling approaches to study cloud-radiative impact is given in Sects. 3.3 and 3.4.

Schäfer and Voigt (2018) also showed that including radiation in the simulation increases cloud cover and precipitation rate within the idealized cyclones. These results are consistent with the climate modeling study of Li et al. (2015), who showed that CRH increases cloud cover and precipitation in the midlatitudes. However, the weakening impact of CRH on cyclone intensity is inconsistent with the increased eddy kinetic energy in the study of Li et al. (2015).

However, the mechanism by which CRH affects extratropical cyclones remained unclear from the study of Schäfer and Voigt (2018). The contrasting impacts of CRH on eddy kinetic energy between studies, and the lack of a dynamical perspective on the impacts of CRH on cyclones, call for more systematic studies. The following section further emphasizes the importance of understanding the impact of CRH on cyclones for large-scale atmospheric predictability.

1.4 Extratropical Cyclones and Atmospheric Predictability

There is a strong link between extratropical cyclones and midlatitude atmospheric predictability. In this context, the role of WCBs is particularly important. Section 1.1, described how latent heating within the ascending regions of cyclones or WCBs affects upper-level downstream ridge development. This effect, also known as "diabatic outflow" refers to cross-isentropic ascent due to strong latent heating and subsequent divergent flow near the tropopause (Grams and Archambault, 2016; Wernli and Gray, 2023). The diabatic outflow with negative PV anomalies affects not only the dynamics of the associated cyclone, but also the dynamics of Rossby waves near the tropopause and downstream weather development.
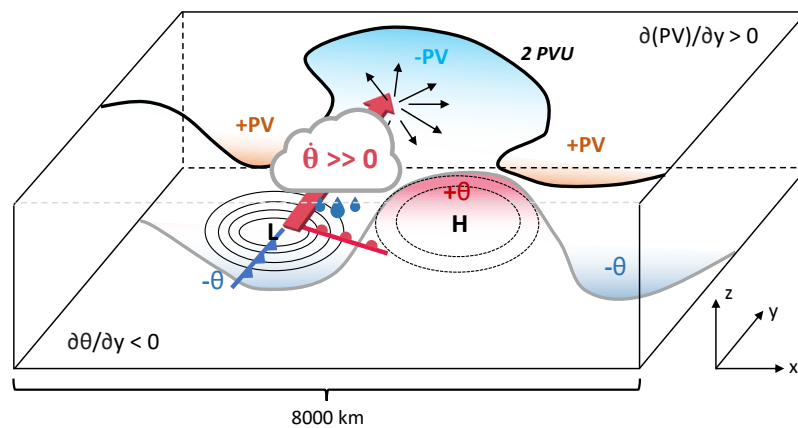
Figure 1.11: Schematic illustration of the impact of latent heating within the warm conveyor belt (WCB) of a cyclone on the tropopause wave and downstream weather development. The cyclone center is labeled "L" and the WCB is shown by the red arrow and strong latent heating. Color shading indicates PV and temperature anomalies at the upper levels and surface, respectively. The area of an upper-level ridge with a negative PV anomaly is indicated by cyan shading and the associated blocking with a positive temperature anomaly at the surface ("H"). The upper tropospheric divergent wind is indicated by thin black arrows.

Fig. 1.11 illustrates the impact of latent heating within the WCB of a cyclone on the dynamical tropopause and the downstream weather development. In some cases, strong latent heating within the WCB of

a cyclone leads to the formation of a strong ridge near the tropopause, resulting in atmospheric blocking (Wernli and Gray, 2023) and further downstream in the development of a strong cyclone (near-tropopause positive PV anomaly downstream of the ridge in Fig. 1.11). For example, the exceptional North American heat wave of June 2021 was attributed to strong ridge development by the WCB outflow of two cyclones in the North Pacific a week before the heat wave (Oertel et al., 2023b). Another example is the strong downstream ridge development in the North Atlantic associated with the tropical-extratropical transition of storm Karl in September 2016, which led to the downstream secondary cyclone formation near Norway, resulting in widespread flooding (Schäfler et al., 2018).

Many studies have focused on the impact of diabatic processes, especially latent heating within WCBs, on tropopause dynamics, which is now a well-established process (Grams and Archambault, 2016; Saffin et al., 2016; Oertel et al., 2019; Teubler and Riemer, 2021; Wernli and Gray, 2023). Other diabatic processes, such as atmospheric radiative heating and cooling, also affect the dynamics near the tropopause. Chagnon et al. (2013) showed that the contrast between the moist troposphere and the dry stratosphere produces strong longwave radiative cooling near the tropopause. The PV anomaly associated with this strong radiative cooling strongly affects the PV structure near the tropopause, and Teubler and Riemer (2021) found that this effect leads to a first-order impact on the amplitude evolution of the upper-tropospheric Rossby wave pattern.

The finding that diabatic processes associated with extratropical cyclones affect tropopause evolution and downstream weather development has led to several studies demonstrating the link between errors in simulating diabatic processes and synoptic-scale forecast error growth. Synoptic-scale forecast error growth is often associated with baroclinic instability (Zhang et al., 2007; Selz and Craig, 2015; Sun and Zhang, 2016). Baroclinic instability leads to the exponential growth of wave amplitudes (Eady, 1949). Therefore, small errors either from initial condition or physical parameterization can lead to exponential forecast error growth in the presence of baroclinic eddies.

Forecast error growth in the midlatitudes is largely attributed to errors in the simulation of WCBs (Pickl et al., 2023). The source of errors could be due to errors in the initial conditions or physical parameterization. For example, Schäfler and Harnisch (2015) showed that errors associated with moisture in the boundary layer affect the latent heating in the WCB and its forecast. Other studies showed that differences in the physical parameterization schemes such as convection, microphysics lead to forecast errors near the tropopause (Joos and Forbes, 2016; Mazoyer et al., 2021, 2023). For example, the cyclone case study of Joos and Forbes (2016) showed that changes in the microphysical parameterization affect the latent heating and outflow of the WCB, and thus the evolution of the upper-tropospheric flow.

The parameterization of the cloud-radiation interaction is a persistent source of uncertainty in weather and climate models. The uncertainty is due to many factors, such as simplified radiation schemes or poor representation of clouds in models (Sect. 1.2). Studies demonstrated that CRH affects the precipitation rate within extratropical cyclones (Schäfer and Voigt, 2018; Zhao et al., 2018). Therefore CRH uncer-

tainties may affect latent heating and act as a source of forecast error, but this possibility has not been addressed.

Dynamics of Forecast Error Growth

Baumgart et al. (2018, 2019) developed a PV error growth framework to understand the growth of PV forecast errors near the tropopause in numerical weather predictions at the synoptic-scale. The framework has led to important insights into the dynamics and multiple scales of the error growth from the convective to the synoptic or even hemispheric scale. To this end, the framework compares the near-tropopause PV tendencies between a reference analysis and a forecast simulation and quantifies the adiabatic and diabatic mechanisms that lead to the PV error growth in the forecast. Here, we explain the version of this framework that we will use in this thesis to study the impact of CRH on cyclones. For further details refer to Baumgart et al. (2018, 2019). On isentropic levels, Ertel PV tendency is given by (Baumgart et al., 2019):

$$\frac{\partial PV}{\partial t} = -\mathbf{v} \cdot \nabla_\theta PV - \dot{\theta}\frac{\partial PV}{\partial \theta} + PV\frac{\partial \dot{\theta}}{\partial \theta} + \frac{1}{\sigma}\mathbf{k} \cdot (\nabla \times \dot{\mathbf{v}}) + RES. \tag{1.14}$$

The first term on the r.h.s accounts for the PV tendency due to advection, and the remaining terms are the PV tendencies due to diabatic processes. The residual term *RES* arises from processes that can not be quantified with the available model output (e.g., numerical diffusion), from numerical errors due to the spatial and temporal discretization, and from the interpolation of model output. $\mathbf{v}$ is the horizontal wind and ∇ is the horizontal gradient, which are both calculated on isentropic levels. $\dot{\theta}$ is the diabatic heating. $\dot{\mathbf{v}}$ is the diabatic horizontal wind tendencies or nonconservative momentum tendencies.

To account for different mechanisms involved in the evolution of PV near the tropopause, the horizontal wind in Eq. 1.14 can be partitioned into contributions from rotational and divergent winds by means of Helmholtz decomposition:

$$\mathbf{v} = \mathbf{v}_{rot} + \mathbf{v}_{div}. \tag{1.15}$$

The rotational wind accounts for advective PV tendency by the (quasi-barotropic) near-tropopause flow and by the winds associated with the low-level PV anomalies (i.e., baroclinic interaction). The divergent wind contains a contribution associated with dry (balanced) dynamics and a contribution associated with moist dynamics, mostly the invigoration of upper-tropospheric divergence by latent heat release below. In the presence of prominent latent heat release, several case studies have indicated that PV advection near the tropopause by the divergent wind can be interpreted to a large extent as an indirect impact of moist processes (see e.g., discussion and references in Teubler and Riemer, 2021). Also, Baumgart et al. (2018) showed that the contribution of the lower-level winds to near tropopause PV error growth is small. Therefore, it is sufficient to restrict the analysis to a Helmholtz decomposition and avoid the intricateness of piecewise PV inversion.

The error is defined by the difference in PV between the forecast and analysis:

$$\Delta PV = PV_{\text{forecast}} - PV_{\text{analysis}}. \tag{1.16}$$

To define a positive-definite error metric, the spatial integration of the squared PV difference over a fixed domain A is considered and is referred to as potential enstrophy ($\mathscr{PV} = \frac{(\Delta PV)^2}{2}$). Thus, a positive potential enstrophy tendency is associated with error amplification and vice versa. The potential enstrophy tendency is then given by

$$\frac{d\mathscr{PV}}{dt} = \frac{1}{A} \int_A \frac{\partial}{\partial t} \frac{(\Delta PV)^2}{2} dA. \tag{1.17}$$

Based on the PV tendency equation (Eq. 1.14) and the Helmholtz decomposition (Eq. 1.15), the potential enstrophy tendency can be decomposed into different processes:

$$\frac{d\mathscr{PV}}{dt} = \mathscr{PV}_{rot} + \mathscr{PV}_{div} + \mathscr{PV}_{dia} + RES, \tag{1.18}$$

where

$$
\begin{aligned}
\mathscr{PV}_{rot} &= \frac{1}{A} \int_A -\Delta PV \Delta \mathbf{v}_{rot} \cdot \nabla_\theta \overline{PV} dA, \\
\mathscr{PV}_{div} &= \frac{1}{A} \left[\int_A -\Delta PV \Delta \mathbf{v}_{div} \cdot \nabla_\theta \overline{PV} dA + \int_A \frac{(\Delta PV)^2}{2} \nabla_\theta \cdot \overline{\mathbf{v}}_{div} dA \right], \\
\mathscr{PV}_{dia} &= \frac{1}{A} \int_A \Delta PV \left[-\Delta \dot{\theta} \frac{\partial \overline{PV}}{\partial \theta} - \overline{\dot{\theta}} \frac{\partial \Delta PV}{\partial \theta} + \Delta PV \frac{\partial \overline{\dot{\theta}}}{\partial \theta} + \overline{PV} \frac{\partial \Delta \dot{\theta}}{\partial \theta} \right. \\
&\qquad \left. + \frac{1}{\overline{\sigma}} \mathbf{k} \cdot (\nabla \times \Delta \dot{\mathbf{v}}) + \frac{1}{\Delta \sigma} \mathbf{k} \cdot (\nabla \times \overline{\dot{\mathbf{v}}}) \right] dA.
\end{aligned} \tag{1.19}
$$

The Δ symbol indicates the difference of a variable between simulations; the overbar means that the variable is averaged between the simulations. $\mathscr{PV}_{rot}$ and $\mathscr{PV}_{div}$ measure the contributions from advection by the rotational and divergent wind, respectively. The contributions from parametrized diabatic heating and nonconservative momentum are given by $\mathscr{PV}_{dia}$. For reference, the above equation is the same as Eq. 9 of Baumgart et al. (2019).

According to Eq. 1.19, the PV error growth near the tropopause can be attributed to changes in the PV advection by the rotational and divergent flow and changes in the PV by diabatic processes. Baumgart et al. (2018) focused on the amplification of pre-existing errors in the near-tropopause and found significant contributions to error growth from upper-tropospheric divergent flow associated with latent heating within WCBs of cyclones. However, the contributions of the diabatic processes and divergent flow to the PV error growth were smaller than the contribution of rotational flow associated with the nonlinear near-tropopause dynamics.

Baumgart et al. (2019) focused on the origin of error growth near the tropopause and identified distinct stages of upscale error growth. PV errors are initially dominated by diabatic heating differences from the

convection scheme within the WCBs of cyclones. These differences perturb the latent heating within the WCBs and subsequently the divergent flow near the tropopause. Differences in the upper-tropospheric divergent flow then dominate the PV error growth and subsequently lead to changes in the rotational flow. Changes in the rotational flow then dominate and further modify the evolution of the PV near the tropopause. The multi-stage mechanism of upscale error growth shows that small grid-scale errors associated with physical processes can grow to the synoptic scale, resulting in substantial forecast errors.

The PV error growth framework allows for a quantitative comparison of the impact of adiabatic and diabatic processes on extratropical cyclones. Thus, in this thesis, we use this framework to understand how CRH and its uncertainty affect the dynamics of extratropical cyclones.

2 Thesis Aim and Research Questions

The aim of this thesis is to **"investigate the impact of CRH on the dynamics of extratropical cyclones and its implication for cyclone predictability"**. In this chapter, we introduce three main research questions that we will address in this thesis. These questions are explored through detailed sub-questions.

The literature review in Ch. 1 indicates that the impact of CRH on the dynamics of extratropical cyclones is understudied. Schäfer and Voigt (2018) were the only ones to show that CRH significantly weakens the intensity of an idealized cyclone on weather time scales of days. However, a dynamical mechanism by which CRH affects cyclones remained elusive from their work. Moreover, the modeling approach used by Schäfer and Voigt (2018) does not quantify the impact of CRH on cyclones in a clean and easy-to-interpret manner. Thus, a detailed investigation of the cloud-radiative impact on extratropical cyclones is required.

In Ch. 1 we discussed that the diabatic processes associated with extratropical cyclones affect the PV near the tropopause and are therefore important for large-scale atmospheric predictability. However, the impact of CRH on near-tropopause dynamics is not well understood. CRH has been shown to destabilize clouds and their environment, thereby promoting stronger buoyancy and condensation (e.g., Fu et al., 1995; Klinger et al., 2017). Thus, CRH may indirectly affect near-tropopause dynamics through changes in latent heating and divergent flow near the tropopause (Sect. 1.4). However, these hypotheses remain to be investigated.

In Chs. 4 and 5 we investigate the impact of CRH on the dynamics of idealized extratropical cyclones by means of baroclinic life cycle simulations in different model setups and address the following research questions:

1. How does CRH affect the dynamics of idealized extratropical cyclones?

1.1. How strongly does CRH affect the intensity of extratropical cyclones?

1.2. What are the mechanisms that underlie the cloud-radiative impact?

1.3. What does this imply for the cloud-radiative impact on cyclone predictability?

These research questions are the same as those addressed in Keshtgar et al. (2023). Research questions 1.1 and 1.2 have been further evaluated by Voigt et al. (2023). In Ch. 4, we investigate the impact of CRH on the dynamics of an idealized extratropical cyclone in a channel setup and a new modeling approach that we develop to isolate the impact of CRH in the ICOsahedral Non-hydrostatic (ICON) model. In this chapter, we apply the PV error growth framework of Baumgart et al. (2018, 2019) (Sect. 1.4) to gain a process-based understanding of the CRH impact on the dynamics of the cyclone. In Ch. 5, we use the

new modeling approach to assess the impact of CRH on idealized cyclones in the global setup of Schäfer and Voigt (2018), to evaluate the robustness of the results, and to characterize differences in the radiative impact of high- and low-level clouds.

In Sect. 1.4 we discussed that due to the multiscale nature of the atmosphere, small grid-scale errors associated with physical processes within extratropical cyclones can grow to the synoptic scale, resulting in significant forecast error growth near the tropopause (e.g. Baumgart et al., 2019; Mazoyer et al., 2021). Uncertainties in CRH might act as a similar source of forecast error. CRH is uncertain in weather and climate models due to many factors, but a systematic assessment of CRH uncertainties associated with extratropical cyclones is missing.

The uncertainties in CRH arise from uncertainty in the model representation of a cloud field as well as uncertainty in the radiative treatment of a given cloud field (Sect. 1.2). With models moving to storm-resolving kilometer-scale resolutions (Satoh et al., 2019), other aspects of the radiation calculation become important compared to coarse-resolution models. For example, it is not well understood how important 3D cloud radiative effects are for extratropical cyclones, which are currently neglected in operational 1D radiation schemes (e.g., Črnivec and Mayer, 2019). Thus, assessing CRH uncertainties is essential to understand which processes contribute most to CRH uncertainties and are relevant to the dynamics of extratropical cyclones.

In Chs. 6 and 7 we investigate the uncertainty in CRH associated with extratropical cyclones and address the following research questions:

2. How large are the CRH uncertainties in the extratropical atmosphere, and which uncertainties are relevant to the dynamics of extratropical cyclones?

2.1. How does CRH change with model settings over the North Atlantic?

2.2. How does CRH change due to the uncertainties in radiation parameterization?

2.3. What is the implication of CRH uncertainties for the dynamics of extratropical cyclones?

Research question 2.1 is the same as the research question addressed in Sullivan et al. (2023), and research questions 2.2 and 2.3 are the same as those addressed in Keshtgar et al. (2024). In Ch. 6, we investigate how the simulation of CRH depends on the representation of clouds in the models. To this end, we assess the sensitivity of CRH to model resolution, convective parameterization, and microphysics schemes over the North Atlantic. For this, we analyze a series of model simulations performed during the 2016 North Atlantic Wave and Downstream impact EXperiment (NAWDEX) field campaign (Schäfler et al., 2018).

In Ch. 7 we investigate how the simulation of CRH depends on the assumptions in the parameterization of radiative processes. We quantify the uncertainty in CRH within extratropical cyclones due to four factors: 3D cloud-radiative effects, ice optical parameterization, cloud horizontal heterogeneity, and cloud vertical overlap. To this end, we study an idealized extratropical cyclone simulated at a convection-

permitting resolution of 2.5 km, and combine large-eddy model simulations at 300 m resolution with offline radiative transfer calculations.

To address the research questions outlined so far, we mostly rely on idealized baroclinic life cycle simulations. However, it is essential to test to what extent the results from idealized simulations apply to realistic weather situations. In doing so, we aim to bridge the gap between idealized simulations and practical applications and to highlight the importance of CRH uncertainties for forecast error growth. We hope that the insights gained from these efforts will help to understand if and how the representation of radiative transfer in numerical weather prediction models should be adapted. In Ch. 8, we investigate the impact of CRH on the dynamics of four different North Atlantic cyclones by performing hindcast simulations during the 2016 NAWDEX field campaign to address the following research questions:

3. How does CRH affect the dynamics of North Atlantic cyclones?

3.1. How strongly does CRH affect the dynamics of North Atlantic cyclones?

3.1. Is the mechanism underlying the CRH impact the same as for the idealized cyclone?

2.3. Do uncertainties in CRH have a measurable impact on near-tropopause dynamics?

The thesis is structured as follows. Chapter 3 describes the methods we use to address the three research questions in Chs. 4-8. Chapter 9 summarizes the main results and provides suggestions for future work that could extend the results of this thesis.

3 Methods

In this chapter, we describe the ICOsahedral Non-hydrostatic (ICON) model in Sect. 3.1 as our main tool in this thesis. In Sect. 3.2 we explain the implementation of new planar grids in ICON for idealized baroclinic life cycle simulations in a channel and limited area setups. Section 3.3 describes the model setup for idealized baroclinic life cycle simulations. Section 3.4 presents the modeling approaches we use to study the impact of CRH on extratropical cyclones. Section 3.5 describes the data sets and the method we use to assess the variability of CRH over the North Atlantic to model resolution, convection, and microphysics schemes. In Sects. 3.6 and 3.7, we explain the ICON model setup for large-eddy model simulations and offline radiative transfer calculations to quantify the uncertainties in CRH within an idealized extratropical cyclone. Finally, in Sect. 3.8, we describe the model setup for hindcast simulations during the 2016 NAWDEX field campaign. Most parts of this chapter are based on the method sections of Keshtgar et al. (2023, 2024); Voigt et al. (2023) and Sullivan et al. (2023) with some adjustments. ©The Authors, CC BY 4.0 ⓒⓘ

3.1 ICON Model

The ICON model is a unified modeling framework developed jointly by the German Weather Service (DWD), Max Planck Institute for Meteorology (MPI-M), the Deutsches Klimarechenzentrum (DKRZ), and the Karlsruhe Institute of Technology (KIT, Zängl et al., 2015; Hohenegger et al., 2023). This section provides a general introduction to the ICON model, its physical parameterizations for numerical weather prediction, and the ICON horizontal grid. Some of the information in this section is based on the ICON tutorial from the German Weather Service (Prill et al., 2023).

General Introduction

The ICON model consists of a non-hydrostatic dynamical core that solves the fully compressible non-hydrostatic equations of atmospheric motion, and packages of physical parameterizations for climate modeling, numerical weather prediction (NWP), and large-eddy model (LEM) simulations (Zängl et al., 2015; Dipankar et al., 2015; Giorgetta et al., 2018). ICON allows simulations on a global scale and in a limited-area mode with resolutions ranging from hundreds of meters to hundreds of kilometers. This is due to its unique horizontal grid that can be easily refined.

ICON uses a terrain-following geometric altitude grid in the vertical dimension and an unstructured triangular Arakawa C grid in the horizontal dimension (Prill et al., 2023). The non-hydrostatic dynamical

core of the ICON model uses the horizontal velocity component normal to the triangle edges, the vertical wind component, air density, and virtual potential temperature as prognostic variables as recommended by Gassmann and Herzog (2008). A two-time-level predictor-corrector scheme is used for time integration, which is explicit except for terms describing vertical sound wave propagation (Zängl et al., 2015). Additional packages are included in the model for physical parameterizations, which vary between NWP, LEM, and climate simulations. In this study, we use the NWP and LEM parameterization packages.

The physical parameterizations are classified into fast and slow physics. The fast-physics parameterizations are usually called every fourth or fifth dynamical core time step (Zängl et al., 2015) and include cloud microphysics, saturation adjustment, turbulent diffusion, and land/surface flux calculations. The slow-physics parameterizations are not called as frequently as the fast-physics parameterizations and include convection, cloud cover, radiation, non-orographic and orographic gravity wave drag. We briefly introduce the parameterizations used for simulating cloud processes, and for radiation in ICON, as they are crucial for studying the impact of CRH on extratropical cyclones and assessing its uncertainty in model settings. The information provided here is based on the ICON model tutorial (Prill et al., 2023).

For parametrizing **convection**, ICON uses the formulation of Tiedtke (1989) and Bechtold et al. (2008) which is a bulk mass flux convection scheme. It accounts for three convective cloud types: shallow, mid-level, and deep clouds. Each model column can only encompass one cloud type at a time, determined by a trigger function. The convection scheme undergoes three steps to determine if a grid cell exhibits convection and, if so, what type of convection. First, the grid-scale conditions are evaluated to determine if convection can be initiated within the column. Second, the changes in heat, moisture, and momentum tendencies for air parcels within the column are calculated. Finally, the intensity of the convection is determined by a cloud base mass flux closure. The cloud base mass flux closure varies for the three types of convection: deep convection utilizes a closure based on convectively available potential energy, shallow convection employs a boundary layer equilibrium closure, and mid-level convection uses a closure based on large-scale vertical velocity. Deep convection can be treated explicitly if the resolution of the model is high enough (between 1 to 3 km).

The **microphysic** schemes provide a closed set of equations to calculate the formation and evolution of condensed and frozen water in the atmosphere. ICON encompasses two microphysical schemes namely the "one-moment" (Doms et al., 2011) and "two-moment" (Seifert and Beheng, 2006) schemes. The one-moment microphysical scheme only predicts the specific mass content of different hydrometeor classes like cloud water, cloud ice, rain, and snow. The two-moment scheme additionally predicts the number concentrations of cloud particles thus providing particle size distribution, which is important information for some microphysical processes, especially for mixed-phased clouds (Seifert and Beheng, 2006). Other important parameterizations for cloud microphysical processes are saturation adjustment and turbulence. The saturation adjustment scheme removes sub- or supersaturation with respect to liquid water. It helps to establish thermodynamic equilibrium between water vapor and liquid water through condensation or evaporation of cloud droplets. This process assumes that clouds instantly relax to ther-

modynamic equilibrium. In ICON, the saturation adjustment is called twice: once before the explicit microphysical processes and once after. The second call to the saturation adjustment scheme accounts for non-equilibrium conditions arising from processes occurring between the first and second saturation adjustments, such as the turbulence scheme and any explicit microphysical processes. For example, this adjustment helps mitigate the significant heating from vapor deposition in the mixed-phase regions of clouds (Oertel et al., 2023a). The turbulent diffusion scheme also provides the sub-grid variability of water due to turbulent motions (Prill et al., 2023).

The aim of the diagnostic **cloud cover** scheme is to combine information from turbulence, convection, and microphysical parameterizations to provide the best estimate of cloud cover, cloud water, and cloud ice, as well as precipitation quantities. The cloud cover scheme in ICON is based on a probability distribution of vapor mass mixing ratios relative to saturation (Giorgetta et al., 2018).

Radiation parameterization in general consists of two parts: parameterizing the optical properties of different atmospheric components and the calculation of radiative transfer. As mentioned in Sect. 1.2, cloud optical properties such as cloud liquid and ice mass mixing ratios, which are grid-box averaged quantities, and the corresponding effective radii are needed for radiation transfer calculations. The radiation scheme uses the output from the cloud cover scheme to prepare cloud optical properties. In ICON, the effective radius of cloud ice crystals is solely a function of ice water content, and the effective radius of cloud droplets is a function of cloud water content and an externally prescribed droplet number concentration (Stevens et al., 2013). However, this formulation makes the microphysics and radiation parameterizations inconsistent (e.g., Kretzschmar et al., 2020).

The output from the radiation parameterization is radiative fluxes at the TOA, surface, and within the atmosphere. From the radiative fluxes, radiative heating and cooling are calculated, which is used for stepping the temperature forward in time. In the NWP physics package of ICON, two radiation schemes are available, the Rapid Radiative Transfer Model (RRTM; Mlawer et al., 1997) and the ecRad (Hogan and Bozzo, 2018). Both radiation schemes use the RRTM gas optics which is based on the correlated-k approach to strongly reduce the computational costs with minimal loss of accuracy (Mlawer et al., 1997). The radiative calculations are performed separately for different wavelength bands and both schemes use 16 and 14 bands in the longwave and shortwave spectrums, respectively. For the vertical overlap parameterization, both radiation schemes apply the exponential-random overlap assumption, meaning clouds with clear-sky layers in-between are uncorrelated, while the overlap in continuous cloud layers decreases exponentially with vertical distance (Shonk et al., 2010).

The ecRad and RRTM use different schemes for parameterizing cloud optical properties. In ecRad, the scheme from the Suite Of Community RAdiative Transfer codes based on Edwards and Slingo (1996) is used for liquid water droplets, and for ice crystals, one can choose between the scheme of Fu (Fu, 1996; Fu et al., 1998) and Baran (Baran et al., 2014). The scheme of Fu uses an approximate phase function and assumes a pristine hexagonal column habit for the ice crystals, whereas the ice-optical scheme of Baran allows for more complex ice particle shapes with roughened surfaces, and more complex scattering

calculations. The cloud optical properties in RRTM are parameterized based on the parameterization in the ECHAM6 climate model, in which ice crystal shapes are assumed to be spherical with an idealized size distribution (Stevens et al., 2013). Moreover, to account for cloud horizontal heterogeneity, the RRTM radiation scheme applies the scaling factor to reduce cloud optical depth whereas with ecRad it is possible to choose between the McICA (Pincus et al., 2003) or Tripleclouds (Shonk and Hogan, 2008) radiation solvers to account for cloud horizontal heterogeneity. The differences between these methods are described in Sect. 1.2.

ICON Horizontal Grids

As mentioned above, a unique feature of the ICON model is its horizontal grid. ICON uses an unstructured triangular grid based on an icosahedron consisting of 20 equilateral triangles of equal size projected onto a sphere. To achieve the target grid resolution RnBk, the triangles of the icosahedron undergo successive refinement in two steps. The first step is the root division step, where the edges of the triangles are divided into n equal segments. This division results in n^2 new equilateral triangles. The second step is the bisection step, which recursively divides each triangle into four smaller triangles, resulting in 4^k new triangles for each triangle from step one. The bisection step can be repeated iteratively to refine the grid resolution. Consequently, the root division and bisection steps together produce $n_c = 20 \cdot n^2 \cdot 4^k$ triangular cells on the sphere. Based on the area of the sphere the average grid resolution can be calculated as follows (Prill et al., 2023):

$$\overline{\Delta x} = \sqrt{\frac{4R_e^2\pi}{n_c}} = \frac{R_e}{n2^k}\sqrt{\frac{\pi}{5}} \approx 5050/(n2^k)[km], \tag{3.1}$$

where R_e is the Earth's radius. Δx can be imagined as the edge length of a square which has the same area as an equilateral triangular cell. This definition is meant to make the triangular grid comparable to a quadratic grid. Thus, the resolution can be also given by:

$$\Delta x = \sqrt{A_t} = \sqrt{\frac{\sqrt{3}}{4}\Delta l^2} \approx 0.66\Delta l, \tag{3.2}$$

where A_t represents the area of the equilateral triangular cell and Δl is triangle edge length.

After setting the resolution, the next step is to optimize the grid which can be applied during each iteration of grid refinement. The optimization is done by the so-called spring dynamics method (Prill et al., 2023). To explain spring optimization, imagine each edge of every triangle as a spring with a certain length and tension. We attach weights like tiny balls to each corner of every triangle and stick them onto the globe. Some springs will be stretched more and some less. Now we let the weights move around on the globe until they find a balance. By this procedure, we will obtain a slightly different grid of triangles which are slightly distorted and of unequal size. However, the vertices reached positions that reflect some "energy minimum". These triangles are the basis of the ICON horizontal grid and have

particularly advantageous numeric properties. A more detailed description of this method is given by Tomita et al. (2002). Finally, the geographic coordinates are mapped to the grid that can be used, for example, for visualization (Prill et al., 2023).

The ICON horizontal grid can also be created for a limited area domain. For these types of grids, an important consideration must be made, which is the specification of the grid boundary zone. The triangular cells that fall within this boundary zone are identified by unique indexes and are used to handle lateral boundary conditions.

Other types of grids can also be used in ICON, such as non-spherical planar grids like the torus grid (Fig. 3.1). The torus grid has double periodic boundary conditions and consists of equilateral triangles, thus no optimization by spring dynamics. To incorporate this geometry into ICON, the calculation of interpolation coefficients and discrete operators has been modified to use Cartesian coordinates instead of the default spherical coordinates (Dipankar et al., 2015). The Cartesian coordinates of the torus grid are $v = (x, y, 0)$, with x extending from zero to the length of the domain and y extending from zero to the width of the domain. This grid is most commonly used in LEM simulations and for the Radiative Convective Equilibrium (RCE) simulations (Dipankar et al., 2015).
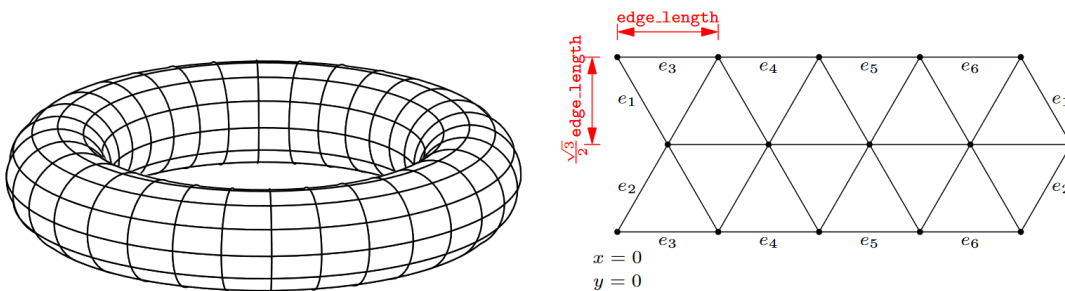
Figure 3.1: The left diagram shows the topological representation of the torus geometry. The right diagram shows the triangulation of the torus grid with double periodic boundary conditions. The edge numbers indicate shared edges between triangles at the boundaries. Figure is taken from the ICON tutorial (Prill et al., 2023).

3.2 Implementation of the new Planar Grids

In this section, we demonstrate how we build upon the implementation of the torus grid to implement two new planar grids in ICON: the planar channel grid, which allows performing idealized baroclinic life cycle simulations in the channel setup, and the ragged orthogonal grid, which allows performing simulations in the limited area mode using planar grids with open horizontal boundary conditions.

Planar Channel Grid

Model simulations using a limited area domain with periodic boundary conditions in the zonal direction and fixed boundary conditions in the meridional direction, or so-called channel simulations are a

commonly-used setup for idealized baroclinic life cycle simulations (e.g., Boutle et al., 2010; Booth et al., 2013; Tierney et al., 2018; Kirshbaum et al., 2018; Rantanen et al., 2019). In comparison to the global model setup for idealized baroclinic life cycle simulations (e.g., Polvani and Esler, 2007; Schäfer and Voigt, 2018), the channel simulations allow for more efficient and cost-effective simulations while still capturing the essential dynamics of extratropical cyclones, which is an important factor in our study. However, a channel setup is not available in ICON. As mentioned in the previous section, ICON supports planar grids such as torus grids with doubly period boundary conditions. Planar grids are also used in the ICON-Ocean component. Thus, it is possible to add specific geometry-aware calculations such as interpolation coefficients and discrete operators for the channel grid in ICON based on the routines for the torus grid and grids in the ICON-Ocean component. This requires two steps: first, the creation of the planar channel grid, and second, the integration of the geometry-aware calculation routines into the ICON model.

We create the planar channel grid with the MPI-M grid generator developed by Leonidas Linardakis[1]. The creation of the planar channel grid is based on a discrete modular Cartesian coordinate system and differs from the spherical grid creation from the icosahedron (Sect. 3.1). The triangulation of the planar channel grid and its coordinates are shown in Fig. 3.2a.
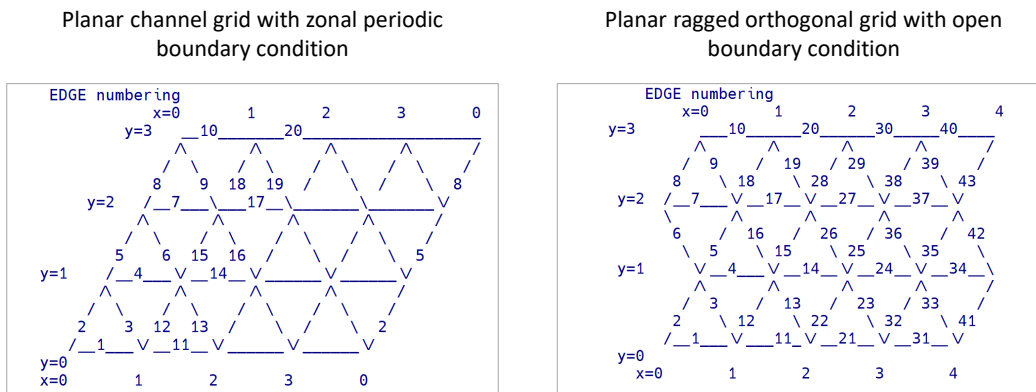

Figure 3.2: Triangulation of planar grids for use in ICON. (a) Planar channel grid with periodic boundary condition in *x* (zonal) direction and fixed boundary condition in *y* (meridional) direction. (b) Planar ragged orthogonal grid with open boundary conditions in *x* and *y* directions. Numbers on the triangle edges indicate edge indices and other numbers indicate the Cartesian coordinates of the vertices.

Each vertex, edge, and cell is uniquely identified by an index assigned by the modular coordinate system. Connectivity between vertices, edges, and cells is then established using these indices and indexing functions. Unlike the standard ICON grid, the planar grids are structured and support periodic boundary conditions. To apply a periodic boundary condition in the *x* direction (zonal), the leftmost and rightmost triangles must share the same edge as shown in Fig. 3.2a. This is like wrapping a parallelogram in the *x* direction to form a cylindrical geometry.

---

[1]see the repository https://code.mpimet.mpg.de/projects/icon-grid-generator

To create the planar channel grid, we need to specify the length, width, and resolution of the domain. This information is used to calculate the number of grid rows and columns, which in turn determines the number of triangular cells ($n_c = 2 \times rows \times columns$) on a plane. In addition, we can also specify the (artificial) geographical coordinates of the grid by assigning the latitude and longitude centers as well as their extents (on a spherical coordinate at a specific latitude) based on the length and width of the domain. Just like the torus grid (see Sect.3.1), the model does not utilize geographical coordinates for calculations. Instead, only the Cartesian coordinates are used for the interpolation coefficients and the discrete operators. However, it is important to have the geographical coordinates assigned to the grid. The geographical coordinates can be used to interpolate initial and lateral boundary conditions. They are useful for visualization and for calculating the effective solar zenith angle for the radiative transfer calculation.

The last step in preparing the grid for use in ICON is to define the grid boundary zone (Sect. 3.1). As this grid applies a fixed condition in y-direction (meridional), ICON should be configured in a limited-area mode, therefore the grid cells in the boundary zone are treated differently and must be defined. This can be done by setting a "boundary_indexing_depth" during the creation of the planar channel grid. The procedure for creating a planar channel grid is provided by Keshtgar (2023).

To implement the geometry-aware computations for the planar channel grid in ICON, we can use most of the routines implemented for the torus grid. However, we need to introduce a new function to apply periodic and fixed boundary conditions in the x- and y-directions, respectively. Mathematically, the boundary condition check for the planar channel grid can be represented by:

$$
v_1 = \begin{cases}
v_{1x} + domain\_length, & \text{if } |v_{0x} - v_{1x}| > \frac{domain\_length}{2}, \text{ and } v_{0x} > v_{1x} \\
v_{1x} - domain\_length, & \text{if } |v_{0x} - v_{1x}| > \frac{domain\_length}{2}, \text{ and } v_{0x} < v_{1x}, \\
v_{1x}, & \text{else} \\
v_{1y}, & \text{if } v_{1y} \neq v_{0y}.
\end{cases}
\tag{3.3}
$$

where, v_1 represents the coordinates of a vertex being examined, while v_0 represents the coordinates of the adjacent vertex (on the horizontal lines). The code checks whether the absolute difference between the x-coordinates of the two vertices exceeds half the domain length, thus indicating whether the vertices are on opposite sides of the domain. If this condition is true, the vertices must be wrapped in the x-direction to maintain periodic boundary conditions. Depending on the relative position of v_1 and v_0, the new x coordinate for v_1 is assigned. If the condition is not fulfilled, the coordinate remains unchanged. In the y direction, the coordinate remains unchanged as well.

Planar Ragged Orthogonal Grid

We implement another planar grid namely "Ragged Orthogonal" for use in ICON as needed for LEM simulations to quantify the uncertainty in CRH within the idealized cyclone simulated with the channel

grid (Sect. 3.6). In contrast to the planar channel grid, this grid does not apply periodic and fixed boundary conditions in the *x* and *y* directions, respectively. Instead, the grid applies open boundary conditions and allows for nudging lateral boundary conditions into and out of the domain.

The triangulation of a plane results in a parallelogram geometry (Fig. 3.2a), making it unsuitable for limited-area simulations over specific regions. However, the MPI-M grid generator allows for the creation of a planar grid that exhibits a rectangular (orthogonal) shape but with irregularities at the right and left boundaries (ragged, Fig. 3.2b). Just as in the planar channel grid, geographical coordinates are assigned according to the specified latitude and longitude centers as well as their extents. During the grid generation, the boundary zone must be defined in both *x* and *y* directions. We implement the geometry-aware calculation routines for the ragged orthogonal grid. However, for the boundary condition check, the coordinates of vertices remain unchanged in both *x* and *y* directions. The procedure for creating planar-ragged orthogonal grids is provided by Keshtgar (2024).

3.3 Idealized Baroclinic Life Cycle Simulations

We use the same initial and lateral boundary conditions for the idealized baroclinic life cycle simulations as in the global setup of Schäfer and Voigt (2018) that are adapted from the life cycle type 1 setup of Polvani and Esler (2007). The same initial condition can be used for baroclinic life cycle simulation in the channel setup (e.g., Boutle et al., 2010). This section describes the derivation of the initial conditions for the baroclinic life cycle simulations and the ICON model setups.

Initialization

The Baroclinic Life Cycle Type 1 (LC1), also known as the "anticyclonic" life cycle, is one of the baroclinic life cycle paradigms that illustrates distinct observed behaviors during the development of nonlinear baroclinic waves (Thorncroft et al., 1993). LC1 is characterized by a strong cold front and a slightly weaker warm front, forming a "T-bone" frontal structure. At upper levels, the tropopause breaks anticyclonically, resulting in the mixing of stratospheric and tropospheric air (Polvani and Esler, 2007). Schäfer and Voigt (2018) simulated the LC1 to study the impact of radiation. Here, we also use the same life cycle to study the impact of CRH on the dynamics of idealized cyclones.

Following Polvani and Esler (2007) and Schäfer and Voigt (2018), we first derive the zonal wind field and its variations with latitude (ϕ) and height:

$$u(\phi,z) = U_0 F(\phi) \left[\left(\frac{z}{z_T} \right) e^{-\frac{\left[\left(\frac{z}{z_T} \right)^2 - 1 \right]}{2}} \right], \tag{3.4}$$

where $z = H \log \frac{p_0}{p}$ is the log-pressure height, p_0 is the globally uniform surface pressure and is set to 1000 hPa. U_0 is the maximum wind speed, set to 45 m s^{-1}, occurring at height of $z_T = 14$ km. H is the scale height ($H = 7.5$ km), and $F(\phi)$ is the latitude dependence function given by:

$$F(\phi) = \begin{cases} \left[\sin\left(\pi(\sin\phi)^2\right) \right]^3 & \text{for } \phi > 0 \\ 0 & \text{for } \phi < 0. \end{cases} \tag{3.5}$$

The jet peaks at $\phi = 45°N$ by applying Eq. 3.4 (Fig. 3.3a). From the wind profile, the initial balanced temperature field through thermal wind balance can be derived as:

$$T(\phi, z) = T_r(z) - \frac{H}{R} \int_0^\phi (af + 2u\tan\phi) \frac{\partial u}{\partial z} d\phi, \tag{3.6}$$

where R is the dry gas constant, $T_r(z)$ is the reference temperature profile and a is average Earth radius. The reference temperature profile is given by:

$$T_r(z) = T_0 + \frac{\Gamma_0}{\left(z_T^{-\alpha} + z^{-\alpha}\right)^{\frac{1}{\alpha}}}, \tag{3.7}$$

where T_0 is the surface reference temperature and is set to $300\,\mathrm{K}$. Temperatures decrease with height at a constant lapse rate Γ_0 up to the height z_T. Above this height the temperature is uniform. Γ_0 is set to $6.5\,\mathrm{K\,km^{-1}}$, following the 1976 US standard atmospheric temperature profile. The sharpness of the transition between these two temperature regimes is controlled by the parameter α, which is set to 10. The integration in Eq. 3.6 can be done without numerical differentiation using the Gaussian quadratures which yields a high machine-precision accuracy (Polvani and Esler, 2007).
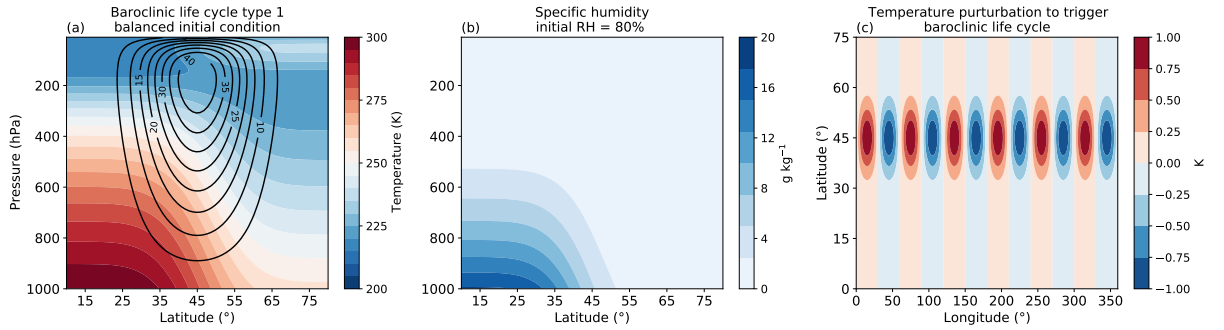

Figure 3.3: Initial conditions for idealized baroclinic life cycle simulations. (a) Balanced temperature (shaded, in K) and zonal wind (contours, in m s^{-1}). (b) Initial specific humidity and (c) temperature wave perturbation with wave number 6 and an amplitude of 1 K to trigger baroclinic development.

The initial relative humidity profile (RH) is specified by:

$$RH = \begin{cases} RH_0 \cdot \left(1 - 0.85 \cdot \frac{z}{z_{Trh}}\right)^{1.25} & \text{for } z < z_{Trh} \\ 0 & \text{for } z > z_{Trh}, \end{cases} \tag{3.8}$$

where RH_0 is the initial surface relative humidity and is set to 80% with the moisture scale height of z_{Trh} equal to $14\,\mathrm{km}$. From the RH profile, we calculate the saturation vapor pressure, and subsequently the specific humidity within the domain (Fig. 3.3b).

With the initial wind profile being baroclinically unstable, the baroclinic life cycle is then triggered by adding a sinusoidal temperature wave perturbation with an amplitude of 1 K to the temperature field (Eq. 3.6) at all levels (Fig. 3.3c). The wave perturbation has the functional form:

$$T'(\lambda, \phi) = \hat{T} \cos(m\lambda) \left[\text{sech} \left(m(\phi - \hat{\phi}) \right) \right]^2, \tag{3.9}$$

where T' is the temperature perturbation, λ is the longitude, $\hat{T}$ is the temperature wave amplitude of 1 K, m is the wave number and is set to 6, and $\hat{\phi} = 45°$N is the latitude of the jet maximum.

In the following, we discuss the ICON model setups for running idealized baroclinic life cycle simulations in both global and channel configurations.

Model Setups for Global and Channel Simulations

We use the ICON-NWP version 2.6.2.2 (Zängl et al., 2015) for idealized baroclinic life cycle simulations. We configure ICON for both limited-area channel and global simulations, which we use in Chs. 4 and 5. In both model setups, the model surface is specified as an ice-free ocean surface with no topography and time-constant sea surface temperatures that are 0.5 K cooler than the initial unperturbed temperature of the lowest model level. Our simulations therefore omit surface radiative heating and isolate the impact of atmospheric radiative heating.

The model is run with full physics including the deep and shallow convection schemes of Tiedtke (1989) and Bechtold et al. (2008), and the turbulence scheme of Raschendorfer (2001). For simulations with convection-permitting resolutions, the deep convection is treated explicitly. Cloud microphysics and grid-scale precipitation are represented by the two-ice-category one-moment scheme of Doms et al. (2011). Longwave and shortwave radiation are calculated with the Rapid Radiative Transfer Model (RRTM; Mlawer et al., 1997). A brief description of these schemes is given in Sect. 3.1. The diurnal cycle is retained and equinox conditions for the shortwave radiation calculation are used. Radiative properties of the atmosphere are set to values commonly used in aquaplanet studies (Williamson et al., 2012). Ozone is set to the values used in Williamson et al. (2012), and the atmospheric composition in terms of non-condensible trace gases are set to current values for well-mixed greenhouse gases ($CO_2 = 348$ ppmv, $CH_4 = 1650$ ppbv, $N_2O = 396$ ppbv, no CFCs).

For **global simulations**, we use the same 40 km horizontal grid resolution (R2B06 grid) and 90 vertical model levels used in Schäfer and Voigt (2018). We use the initial conditions for the baroclinic life cycle simulation described above. The baroclinic growth is induced by a wavenumber-6 temperature perturbation of 1 K amplitude at the latitude of the jet (Eq. 3.9). This results in the development of a set of six cyclones and for the analysis, we average over the six cyclones. This model setup is the same as the setup used in Schäfer and Voigt (2018), except that they used ICON version 2.0.15 for their simulations.

For **channel simulations**, we use a planar channel grid (Sect. 3.2) on a Cartesian f-plane. The channel setup allows for high horizontal resolution while keeping computational costs manageable for more

simulations. Another advantage is its perfectly uniform grid, i.e., each triangular grid cell has exactly the same area. We use a convection-permitting resolution of 2.5 km in the horizontal direction, which results in nearly 6 million grid points per level. Due to the high horizontal resolution of the grid, the deep convection scheme is disabled. In the vertical direction, we use 75 model levels. The Coriolis parameter is constant with a value for 45°N. For the domain size, we set the channel width to 9000 km and the channel length to 4000 km, which approximately equals 81 degrees in latitudinal and 51 degrees in longitudinal direction. The large meridional extent ensures that the simulated cyclone is not influenced by the meridional boundaries. Test simulations showed that the cyclone is sensitive to the domain length. For smaller lengths, the cyclone is rather weak, while for larger lengths it becomes very strong. We thus settled for a domain length of 4000 km.

The initial and lateral boundary conditions in the channel setup follow that of the global simulations except that the baroclinic life cycle initialization is done over the planar channel grid with a constant Coriolis parameter set to 45°N. Also in contrast to the global setup, baroclinic growth is triggered by a sinusoidal thermal wave with a 1 K amplitude at all levels and with a wavelength equal to the domain length (4000 km, corresponding to wave number 7). This means that a single cyclone is simulated, instead of a train of six cyclones as in the global setup. This setup has been used previously in many studies (e.g., Booth et al., 2013; Tierney et al., 2018; Kirshbaum et al., 2018).
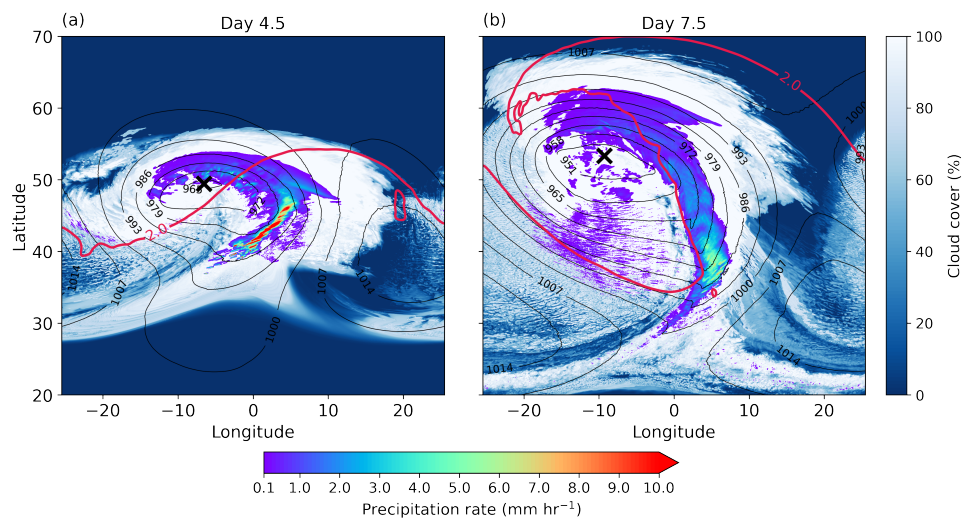

Figure 3.4: Surface pressure (black contours, hPa), total precipitation rate (colors), and cloud cover (blue shadings) for the cyclone simulation in the channel setup at (a) day 4.5 and (b) day 7.5. The red contours indicate the dynamical tropopause as given by the 2 PVU contour on the 326 K isentrope. The cross shows the position of the cyclone center given by the minimum surface pressure. The figure and the caption are adapted from Keshtgar et al. (2023). ©The Authors, CC BY 4.0 ⓒⓘ

The channel setup results in a reasonable cyclone whose structure is typical for wintertime extratropical cyclones. This is illustrated in Fig. 3.4, which shows the spatial distribution of surface pressure, cloud cover, and precipitation rate for a cyclone simulated with cloud radiation only (Sect. 3.4). For visualization and remapping purposes, the map plots from the channel simulations in this thesis use the

geographical latitude and longitude coordinates that are assigned to grid cells during the grid generation according to the Cartesian length and width of the domain (Sect. 3.2). The geographical latitude center of the grid is set to 45°N and the cyclone is initialized at 45°N. Thus, the grid extends latitudinally from 4.5 to 85.5°N. However, in all figures, the range of the latitudes is chosen to focus on the cyclone region. Nevertheless, the model computation is solely based on the Cartesian grid.

The region with the highest precipitation marks the position of the warm conveyor belt (WCB), which is located east and southeast of the cyclone center in Fig. 3.4a. The WCB moves ahead of the cold front and splits into two branches. One branch wraps cyclonically north of the cyclone center, and the other one anticyclonically towards the high-pressure region (Fig. 3.4a). The less cloudy region just behind the WCB marks the location of the descending cold, dry air. From the southwest of the cyclone center to the high-pressure center, shallow stratocumulus clouds form due to the passing of cold air over the warm sea surface (Fig. 3.4a).

The use of Cartesian instead of spherical coordinates which is employed in the global setup, results in a different, but no less realistic cyclone structure. It is well known that baroclinic waves simulated on a Cartesian geometry display stronger cyclonic flows and upper cyclonic wave-breaking during their mature phase. This is evident from the evolution of the dynamical tropopause in Fig. 3.4b, which shows that the tropopause wave rolls up cyclonically, exhibiting characteristics of the cyclonic life cycle type 2 paradigm of Thorncroft et al. (1993). Similar behavior can be achieved for a spherical geometry by adding a small cyclonic shear to the initial jet. More information on the impact of geometries on the baroclinic life cycle can be found in Balasubramanian and Garner (1997).

3.4 Modeling Approaches to Study the Cloud-Radiative Impact

Clouds affect radiative fluxes at the surface and are quantified by the cloud radiative effect (CRE). Clouds also affect radiative heating and cooling within the atmosphere and are quantified by cloud-radiative heating (CRH). Our focus in this study is on the impact of CRH on cyclones. CRH in ICON is given by:

$$\mathrm{CRH} = \left.\frac{\partial T}{\partial t}\right|_{\mathrm{radiation}}^{\mathrm{cloud}} = \left.\frac{\partial T}{\partial t}\right|_{\mathrm{radiation}}^{\mathrm{all\text{-}sky}} - \left.\frac{\partial T}{\partial t}\right|_{\mathrm{radiation}}^{\mathrm{clear\text{-}sky}} = \frac{1}{\rho\, c_v} \cdot \frac{\partial}{\partial z}\left(F^{\mathrm{all\text{-}sky}} - F^{\mathrm{clear\text{-}sky}}\right), \qquad (3.10)$$

where F is the positive downward radiative flux, T and ρ are air temperature and density, respectively. Since ICON is based on height levels, the conversion of radiative fluxes to heating rate requires the heat capacity of air at constant volume, c_v. In the idealized baroclinic life cycle simulations, the model surface is specified as an ice-free ocean surface with no topography and sea surface temperatures that are constant throughout the simulation and 0.5 K cooler than the initial temperature of the lowest model level. This allows us to exclude the effects of surface radiative fluxes and focus solely on the CRH within the atmosphere.

One modeling approach to study the impact of CRH on cyclones is the Clouds On-Off Klimate model Intercomparison Experiment (COOKIE, Stevens et al., 2012) method, which has been used extensively

in climate modeling studies to study the impact of CRH on atmospheric circulation (e.g., Li et al., 2015; Voigt et al., 2021). The COOKIE method requires two simulations: the "Clouds-On" simulation in which the radiation scheme calculates the all-sky radiative fluxes, including the radiative contributions from clouds, and the "Clouds-Off" simulation, in which clouds are set to zero in the radiative transfer calculation and only the clear-sky radiative fluxes are calculated. In other words, in the "Clouds-Off" simulation, clouds become transparent to radiation, and their impact on radiative fluxes at the surface and within the atmosphere is eliminated.

Schäfer and Voigt (2018) used the COOKIE method to study the impact of CRH on idealized cyclones. They performed three simulations with different radiative configurations: 1) No radiation, 2) all-sky radiation ("Clouds-On"), and 3) clear-sky radiation ("Clouds-Off"). The CRH impact was then estimated as the difference between the simulations with all-sky and clear-sky radiation. However, the method of Schäfer and Voigt (2018) can complicate the interpretation of results. This is because when radiation is included in the baroclinic life cycle simulations, a strong atmospheric cooling occurs in the first days of the simulations (Fig. 3.5a) due to the strong clear-sky radiative cooling. Due to this initial cooling, the atmospheric background state changes, and it is not clear whether the radiative impact on the cyclone is solely due to CRH or changes in the atmospheric background.
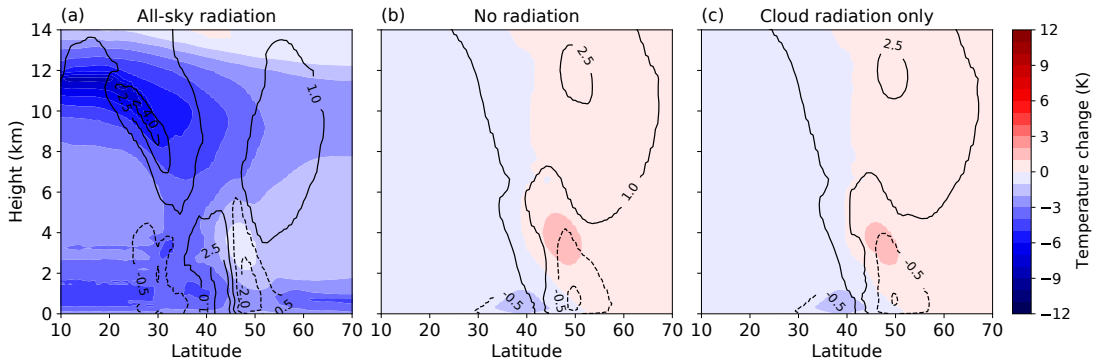

Figure 3.5: Zonal-mean changes in temperature and zonal wind (black contours, m s^{-1}) at day 3 for idealized baroclinic life cycle simulations with (a) all-sky radiation, (b) no radiation, and (c) cloud radiation only. Reprinted from Keshtgar et al. (2023). ©The Authors, CC BY 4.0

To eliminate this problem, we develop and apply a new modeling approach that isolates the impact of CRH in a clean and easy-to-interpret manner. Our new approach requires two simulations to quantify the impact of CRH: one simulation with no radiation as in Schäfer and Voigt (2018), and one simulation with only CRH. In the latter simulation, only the radiative heating from clouds, defined as the all-sky minus the clear-sky radiative heating is passed to the model's dynamical core. In terms of the thermodynamic equation, our approach is described by:

$$\left.\frac{DT}{Dt}\right|^{\text{only}}_{\text{with CRH}} = \frac{1}{c_p}\left(\frac{1}{\rho}\frac{Dp}{Dt} + \left(\left.\frac{\partial T}{\partial t}\right|^{\text{all-sky}}_{\text{radiation}} - \left.\frac{\partial T}{\partial t}\right|^{\text{clear-sky}}_{\text{radiation}}\right) + J\right), \qquad (3.11)$$

where *J* represents the heating rates from other diabatic processes. In terms of model implementation, our approach requires two calls to the radiation scheme: one call in which the scheme calculates the all-sky radiative heating rate including clouds, and one call in which clouds are set to zero, providing the clear-sky radiative heating rate. CRH is then calculated accordingly and passed to the dynamical core instead of the all-sky or clear-sky radiative heating rates. Our approach, thus, removes the initial radiative adjustment, and the cyclone forms in the same background state independent of whether CRH is active or not. This is shown in Fig. 3.5b and c.

In addition, we make our new modeling approach flexible by limiting CRH in the boundary layer or free troposphere and then passing it to the model's dynamical core. We use this technique in Ch. 5 to characterize the radiative impact of low- and high-level clouds on the dynamics of idealized extratropical cyclones.

To study the impact of CRH on North Atlantic cyclones (Ch. 8), we use the COOKIE method instead. This is because removing the clear-sky radiative heating in the hindcast simulations (Sect. 3.8) would significantly change the environmental background in which cyclones develop. This would result in simulating a different cyclone that is significantly different from reality. However, we modify the COOKIE method slightly. Since our model domain encompasses land-covered areas (Fig 3.6), eliminating the cloud-radiative impact at the surface substantially influences the surface energy fluxes and the temperature (Harrop et al., 2024). To circumvent this problem, we call the radiation scheme twice in the simulation with clear-sky radiation ("Clouds-Off"). The first call includes clouds in the radiative transfer calculation to derive all-sky surface radiative fluxes. These fluxes are then used by the model's surface scheme, preventing strong changes in surface radiative fluxes and surface temperature. In the second call, clouds are set to zero in the radiative transfer calculation and only the clear-sky radiative heating is calculated and used for stepping the temperature forward in time. In terms of the thermodynamic equation, the COOKIE method can be described as:

$$\left.\frac{DT}{Dt}\right|_{\text{with CRH}}^{\text{COOKIE}} = \frac{1}{c_p}\left(\frac{1}{\rho}\frac{Dp}{Dt} + \left(\left.\frac{\partial T}{\partial t}\right|_{\text{radiation}}^{\text{all-sky}}\right) + J\right), \tag{3.12}$$

$$\left.\frac{DT}{Dt}\right|_{\text{without CRH}}^{\text{COOKIE}} = \frac{1}{c_p}\left(\frac{1}{\rho}\frac{Dp}{Dt} + \left(\left.\frac{\partial T}{\partial t}\right|_{\text{radiation}}^{\text{clear-sky}}\right) + J\right). \tag{3.13}$$

3.5 Hindcast Simulations, Satellite, and Reanalysis Data

This section describes the model simulations and our method to assess the CRH variability to model settings over the North Atlantic Ocean in Ch. 6 (Sullivan et al., 2023).

Hindcast simulations were performed by Aiko Voigt with the ICON model version 2.1.00 during the North Atlantic Waveguide and Downstream Impact Experiment (NAWDEX) field campaign in 2016. NAWDEX was an international multi-aircraft field campaign that took place from 17 September to 22

October 2016 and that was based out of Iceland (Schäfler et al., 2018). NAWDEX studied midlatitude circulations, particularly warm conveyor belts, Rossby waves, and the North Atlantic jet stream, and the physical processes initiating and controlling them.

We use the same set of simulations as presented in Senf et al. (2020). A brief description of these runs is presented here. The ICON simulations domain extends between 23 and 80°N latitudinally and between 78°W and 40°E longitudinally (Fig. 3.6). After removing the spinup period, the ICON simulations extend over 14 d during the NAWDEX field campaign, specifically 21-25 and 30 September 2016, 1-5 October 2016, and 14-16 October 2016.
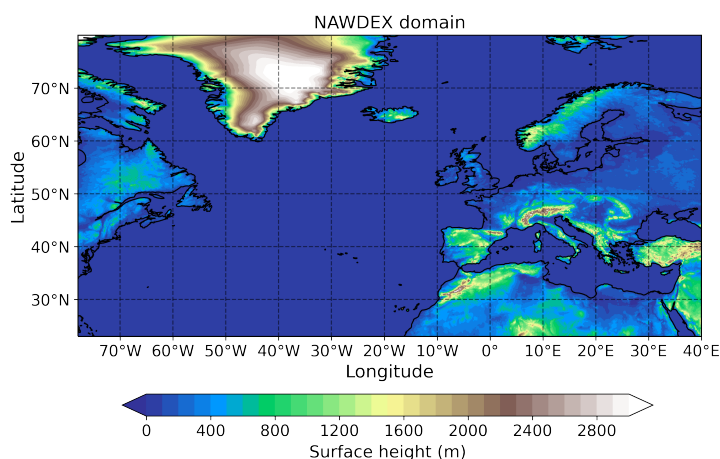

Figure 3.6: The NAWDEX simulations domain covers the entire North Atlantic, as well as the northeastern Canadian coast, Greenland, North Africa, and Europe. The domain extends from 23 to 80°N and 78°W to 40°E. The color shading shows the surface height. Figure and caption adapted from Sullivan et al. (2023). ©The Authors, CC BY 4.0 ⓒⓘ

ICON was used in NWP mode with the convection scheme of Tiedtke (1989) and Bechtold et al. (2008), used at all resolutions. For the simulations at 2.5 km resolution, the deep-convection scheme or both the deep- and shallow-convection schemes are switched off in order to investigate the effect of explicit treatment of convection. The impact of cloud microphysics is explored by switching between the one-moment microphysics of Doms et al. (2011) used in the operational NWP mode and the more sophisticated and computationally expensive two-moment microphysics of Seifert and Beheng (2006), where heterogeneous nucleation is prescribed as in Hande et al. (2015). Although the two-moment microphysics scheme was developed for convection-permitting resolutions, we use it here in combination with parameterized convection also. Longwave and shortwave radiation are calculated with the RRTM (Mlawer et al., 1997).

Finally, six different horizontal resolutions are used to span the range from typical global climate model meshes down to storm-resolving ones: 80, 40, 20, 10, 5, and 2.5 km. Across these resolutions, the number of grid cells varies by 3 orders of magnitude. In Ch. 6, the simulation with a grid spacing of *x* km is sometimes referred to simply as the *x* km simulation. In the vertical, 75 model levels are used. Lateral

boundary conditions with 3-hourly frequency and initial conditions come from the Integrated Forecast System.

We compare CRH from the NAWDEX simulations to those from the 2B-FLXHR-LIDAR data, version P2R04 from CloudSat-CALIPSO data, binned to 2.5° resolution (see Papavasileiou et al., 2020) and remapped to 0.25° resolution, over the North Atlantic domain during September and October between 2006 and 2011. Ice and liquid effective radii and water contents measured by the CloudSat cloud profiling radar and temperature and humidity profiles from the European Center for Medium-Range Weather Forecast (ECMWF) have been fed to a two-stream radiative transfer model to compute 2B-FLXHR-LIDAR heating rates by L'Ecuyer et al. (2008). We also compare heating rates from the ERA5 reanalysis of the ECMWF to the ICON NAWDEX simulations (Hersbach et al., 2020). The ERA5 reanalysis assimilates radiances from both infrared sounders, such as AIRS and IASI, and geostationary satellites, such as GOES and Meteosat. Heating rates have then been generated within the reanalysis by applying RRTM and assumptions about ice crystal effective size and cloud condensation nuclei concentrations. We download these ERA5 heating rates at 0.25° resolution over our domain from 2012 to 2016 in order to produce a climatologically representative profile.

We also present CRH profiles from other coarse-resolution, AMIP-like simulations with the ECHAM6 atmospheric component of the MPI-ESM model, the LMDz5A atmospheric component of the IPSL-CM5A model, and the ICON atmospheric model version 2.1.00 with a global R2B04 grid, corresponding to a horizontal resolution of approximately 160 km. These simulations employ climatological sea surface temperatures from the CMIP5 AMIP protocol and have been analyzed by Voigt et al. (2019). Their CRH profiles are evaluated from over 5 or more years so that we may interpret them as a North Atlantic climatology. In both the ICON NAWDEX and the AMIP-like simulations, CRH is calculated as the difference between all-sky and clear-sky flux divergences.

Cloud classes

Cloud layering strongly determines CRH, and decomposition of cloud fields into various cloud vertical structure (CVS) classes has proven to be useful in tracing the origins of atmospheric radiative warming and cooling (Oreopoulos et al., 2017; Lee et al., 2020). CVS classes build upon the International Satellite Cloud Climatology Project classification and are defined by cloud fraction thresholds at low (pressure (p) $\geq$ 680 hPa), middle (440 hPa $\leq p \leq$ 680 hPa), and high ($p \leq$ 440 hPa) altitudes. Oreopoulos et al. (2017) define a classification consisting of high, middle, low, high-middle, middle-low, high-middle-low, high-x-middle, high-low, middle-x-low, and high-x-middle-x-low clouds, as well as clear sky; altitude-1-altitude-2 denotes cloudiness at altitudinal range 1 separated by clear sky from cloudiness at altitudinal range 2, whereas altitude-1-x-altitude-2 denotes continuous cloudiness throughout altitudinal ranges 1 and 2.

Within the low-middle-high stratification, numerous possibilities exist when looking at the full cloud fraction field, as detailed in the Appendix of Oreopoulos et al. (2017). How many consecutive levels

within an altitudinal range must have cloud fractions greater than the threshold for the whole range to qualify as cloudy? Or if 20% of the cloud exists in the high altitudinal range and 80% exists in the middle altitudinal range, should it then be classified as isolated middle or high-middle?

We are mostly concerned with a general sensitivity of CRH to isolated versus deeper clouds, so we bypass some of these subtleties by employing a simplified version of the CVS classification with eight classes: isolated high, isolated middle, isolated low, high-x-middle, middle-x-low, high-low, high-x-middle-x-low, and clear sky (Fig. 3.7). To categorize cloudiness in a given grid cell, thresholds in cloud fraction are verified for the low ($p \geq 680$ hPa), middle (440 hPa $\leq p \leq 680$ hPa), and high ($p \leq 440$ hPa) ranges. These two-dimensional low, middle, and high cloud fractions are calculated over the corresponding pressure ranges from the three-dimensional cloud fraction field using the generalized overlap assumption. If, for example, a column of grid cells has more than the threshold cloud fraction in all three ranges, it is classified as high-x-middle-x-low. Or if it has only more than the threshold cloud fraction in the low altitudinal range, it is classified as low. We do not make the distinction between continuous and discontinuous layers of cloudiness. Three sets of thresholds were initially used based upon the following percentiles in the cloud fraction distribution: 60th-60th-25th, 62nd-67th-30rd, and 65th-70th-35th for high, middle, and low altitudinal ranges or cloud classes (Tab. S1 in the supplementary material of Sullivan et al., 2023). The cloud fractions associated with these percentile thresholds change by up to 1 order of magnitude; however, cloud fraction is generally larger than these threshold values when a cloud forms so that the occurrence probability of cloud classes is mostly insensitive to which thresholds are used (Fig. S1 in the supplementary material of Sullivan et al., 2023). We show results from the intermediate set of thresholds.
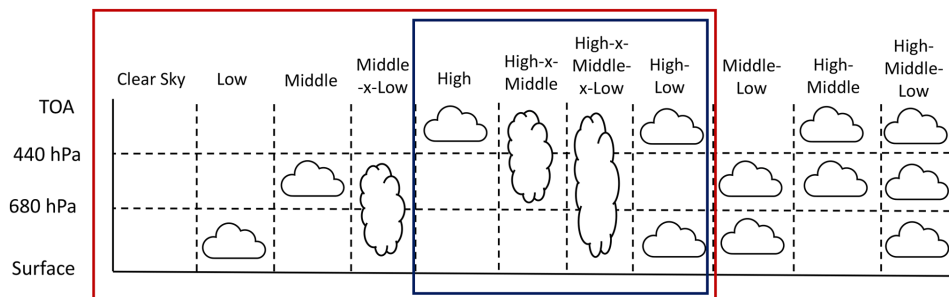

Figure 3.7: The cloud vertical structure classification of Oreopoulos et al. (2017) employs cloud fraction in three altitudinal ranges - low, middle, and high - to define 11 classes. We use a subset of these, shown in the red box, and do not distinguish between continuous and discontinuous cloud layers. We also focus on upper-tropospheric CRH influenced mostly by a smaller subset shown in the blue box. Adapted from Fig. 1 of Oreopoulos et al. (2017). Reprinted from Sullivan et al. (2023). ©The Authors, CC BY 4.0 ⓒⓘ

3.6 Large-Eddy-Model Simulations

This section describes the ICON model setup for large eddy model (LEM) simulations to quantify the uncertainty in CRH within an idealized extratropical cyclone (Ch. 7). The ICON-NWP baroclinic life

cycle simulation in the channel setup provides the initial and lateral boundary conditions for the LEM simulations. However, we repeat the ICON-NWP baroclinic life cycle simulation with some differences compared to the simulations we use in Ch. 4 and described in Sect. 3.3.

First, we use the two-moment microphysics of Seifert and Beheng (2006) instead of the one-moment scheme. Second, we use ecRad (Hogan and Bozzo, 2018), the new operational radiation scheme in ICON (Rieger et al., 2019) instead of the RRTM (Mlawer et al., 1997). The advantage of ecRad is that we can configure the offline radiative transfer setup (Sect. 3.7) in a manner that is very close to the radiative transfer setup used in ICON. From the various radiation solvers available in ecRad, we use the homogeneous solver. The solver homogenizes the cloud properties over the entire grid box, i.e., it ignores cloud fraction and does not require any assumption about cloud vertical overlap. Thus, for the purpose of radiative transfer calculation, clouds are treated as grid-box clouds. This treatment is the same as in the large-eddy-model simulations. For the cloud optical parameterization, we use the scheme from the Suite Of Community RAdiative Transfer codes (SOCRATES) based on Edwards and Slingo (1996) for liquid water droplets. For ice crystals, we use the scheme of Fu (Fu, 1996; Fu et al., 1998). Third, we use the modeling technique we developed to simulate the cyclone only with the contribution of CRH.
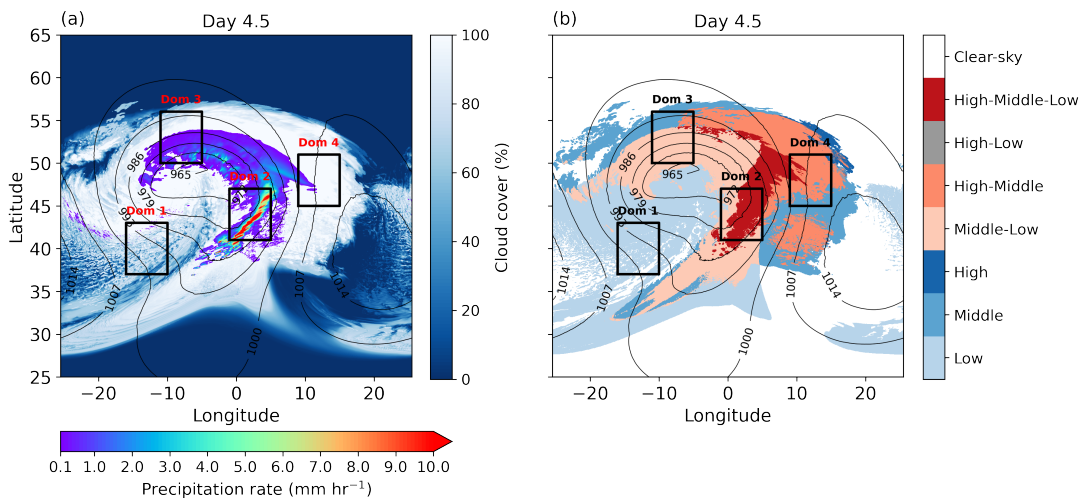

Figure 3.8: (a) Surface pressure (black contours, hPa), cloud cover, and precipitation at day 4.5 in the baroclinic life cycle simulation with ICON-NWP. Panel (b) shows cloud classes. The rectangles in both panels indicate the location of the domains for the LEM simulations. Reprinted from Keshtgar et al. (2024). ©The Authors, CC BY 4.0 ⓒⓘ

We target four different regions of the cyclone for the LEM simulations, shown by black rectangles in Fig. 3.8. To characterize the 3D structure of clouds, panel b of Fig. 3.8 shows cloud classes (Sect. 3.5). We derive the cloud classes using a 50% threshold for low-, mid-, and high-level cloud cover that are diagnosed within ICON during the model simulation. For example, if cloud cover exceeds the 50% threshold at low, middle, and high altitudes, the cloud class is high-middle-low.

Domain 1 targets low-level shallow cumulus and stratocumulus clouds southwest of the cyclone center within the cold sector. These clouds are formed by the passage of cold, dry air over the warm ocean

behind the cold front. Domain 2 targets the extensive vertical clouds within the WCB of the cyclone, where strong latent heating and precipitation occur. Domain 3 captures mid- and low-level clouds in the cyclonic branch of the WCB outflow, and Domain 4 captures mostly mid- and high-level clouds in the anticyclonic branch of the WCB outflow. In Ch. 7 We will refer to domains 1, 2, 3, and 4 as shallow cumulus, WCB ascent, WCB cyclonic outflow, and WCB anticyclonic outflow, respectively.

For the LEM simulations, we use the ICON model in a limited area setup. The LEM simulations use a planar grid with perfectly uniform triangular grid-cell areas. Unlike the planar channel grid used in the NWP simulation, the planar grid does not apply zonal periodic and fixed meridional boundary conditions (Sect. 3.2). Instead, hourly lateral boundary conditions are provided by the baroclinic life cycle simulation. The planar grid extends 471 km and 667 km in the zonal and meridional directions, respectively. This is approximately equivalent to a $6° \times 6°$ domain at $45°N$. The horizontal resolution is 300 m. We use 150 model levels with layer thicknesses increasing from 20 m near the surface to 570 m at 30 km.

As in the NWP baroclinic life cycle channel simulation, we run the LEM simulations with the two-moment microphysics scheme, the homogeneous radiation solver of ecRad, the same cloud optical parameterizations, and with only the cloud-radiative heating contribution from the radiation scheme (Sect.3.4). In contrast to the NWP simulation, we use the 3D Smagorinsky diffusion model (Smagorinsky, 1963) for the turbulence scheme and switch off the shallow convection scheme. We configure the cloud cover scheme to treat clouds as grid-scale quantities, i.e. grid boxes are either fully cloudy or clear.

We run LEM simulations for 12 hours starting on day 4.25 of the baroclinic life cycle simulation when the cyclone is in its main growth phase. We exclude the first 3 hours to remove spin-up effects. As we show in Ch. 4 between days 4 and 5, the modulation of latent heating by the CRH is strong enough to affect the dynamics of the cyclone.

3.7 Offline Radiative Transfer Calculations

This section describes the offline radiative transfer calculations we perform to quantify the uncertainty in CRH within an idealized extratropical cyclone (Ch. 7) using data from LEM simulations (Sect. 3.6). We quantify the uncertainties in the CRH due to four factors: 3D cloud-radiative effects, parameterization of ice optical properties, cloud horizontal heterogeneity, and cloud vertical overlap, as described in detail in Sect. 1.2.

For the offline radiative transfer calculations, we use the libRadtran software (Mayer and Kylling, 2005; Emde et al., 2016), which includes several radiation solvers and different cloud optical parameterizations. In order to achieve the best possible match between the offline calculations and the CRH calculated with ICON, we configure the radiative transfer setup of libRadtran as similarly as possible to ICON-LEM simulations (Sect. 3.6).

For gas absorption, we use the parameterization of Fu (Fu and Liou, 1992, 1993), which employs the correlated k-distribution method with 6 and 12 spectral bands in the solar and thermal spectra, respectively. This parameterization is optimized for use in climate models. The optical properties of cloud droplets are prescribed according to the parameterization of Hu and Stamnes (1993), which assumes spherical droplets. The optical properties of ice crystals are prescribed according to the parameterization of Fu (Fu, 1996; Fu et al., 1998), which is the same scheme used in the ICON simulations. The scheme of Fu uses an approximate phase function and assumes a pristine hexagonal column habit for the ice crystals. For the radiative transfer solver, we use the classical δ-Eddington two-stream solver (Zdunkowski, 2007), which is suitable for horizontally homogeneous clouds. This solver is similar to the ecRad homogeneous solver used in the ICON-LEM simulations.

In libRadtran, inputs are required to have normal Cartesian rectangular coordinates. Therefore, we remap the LEM simulation output from the unstructured triangular grid to a regular Cartesian grid with the same resolution using nearest neighbor interpolation. For the clear-sky background, we use pressure, temperature, density, specific humidity, and trace gas concentration from the LEM simulations. We set other inputs such as surface type, albedo, and emissivity to the same values as those used in the ICON simulations. We use the solar zenith angles used in the LEM simulations for the offline solar radiative transfer calculations.

The offline radiative transfer calculations are very time-consuming, especially the 3D Monte Carlo radiative transfer calculation (Mayer, 2009). Ideally, one would run the calculations over the entire LEM domain using the 3D cloud and clear-sky fields. However, this is not feasible because libRadtran cannot be run in parallel, and the wall-clock time of the computing nodes of the German Climate Computing Center (DKRZ) Levante supercomputer that we use for our study is limited to 8 h. To overcome the computational challenge, we divide the LEM domains into 36 $1° \times 1°$ subdomains for which we run the radiative transfer calculations individually. For each sub-domain, we use a 1D clear-sky background profile that we derive by horizontally averaging the clear-sky fields. After the radiative transfer calculations for all sub-domains are finished, we merge the results to obtain the radiative heating rate over the entire LEM domain. While this means that we neglect horizontal variability in the clear-sky background within the sub-domains, we show in Ch. 6 that this has a negligible impact, and we are able to achieve very good agreement between the CRH calculated offline with libRadtran in the reference setup using the 1D radiation calculation and online in ICON-LEM.

Partitioning of the LEM domains into sub-domains allows us to perform expensive 3D Monte Carlo radiative transfer calculations but can introduce errors in the radiative transfer calculations due to the discontinuity of the horizontal photon propagation at the lateral boundaries of the sub-domains. As an example, consider a shortwave radiative transfer calculation for a cumulus cloud near the northern boundary of a sub-domain. The shadow of this cloud should be present at the southern boundary of the sub-domain to the north of it, yet the periodic boundary conditions applied in the 3D solver mean that the shadow is placed at the southern boundary of the cloud's own sub-domain. The gravity of such an error

depends on the solar zenith angle, cloud top height, and cloud cover. We minimize this issue by making the sub-domains overlap by approximately 12 km in all directions. The overlap is sufficient for shallow cumulus clouds with a maximum height of 2 km. The overlap is too small for clouds at higher altitudes in the WCB of the cyclone, but since WCB clouds are mostly stratiform, the resulting errors tend to be small and do not affect the generality of our results.

To investigate the uncertainty in CRH, we perform several radiative transfer calculations that are listed in Tab. 3.1. For 3D cloud-radiative effects, we use the "Monte Carlo code for physically correct tracing of photons in cloudy atmospheres" (MYSTIC; Mayer, 2009). MYSTIC can also be run in independent column approximation mode (MYSTIC-ICA), which neglects horizontal photon transport between model columns and is equivalent to a 1D radiation scheme. We use the standard forward photon tracing method. The azimuth angle is set to a constant value of $180°$, which directs the solar radiation from south to north. To reduce the Monte Carlo noise, we run MYSTIC and MYSTIC-ICA with 7.2×10^6 photons for each sub-domain in the LEM domains at each time step and repeat the calculations 10 times, resulting in a total of 7.2×10^7 photons traced per sub-domain (nearly 5000 photons per LEM column). We then average these 10 calculations to derive the radiative heating in each LEM domain. Overall, the total computational time required to perform the entire set of 3D radiative transfer calculations amounts to about 1500 h on a single node of the DKRZ Levante supercomputer.

Table 3.1: List of radiative transfer calculations to quantify the uncertainty in CRH. The first column shows the purpose of the calculations, the second column the radiation solvers, and the third column the ice optical parameterization. Adapted from Keshtgar et al. (2024). ©The Authors, CC BY 4.0 ©①

Purpose	Radiation solvers	Ice optical parameterization
Reference	δ-Eddington two-stream	Fu
3D cloud radiative effects	MYSTIC	Fu
	MYSTIC-ICA	Fu
Ice optical parameterization	δ-Eddington two-stream	Baum_v36, general habit mixture
	δ-Eddington two-stream	Baum_v36, solid column
	δ-Eddington two-stream	Baum_v36, rough-aggregated
Cloud horizontal heterogeneity and overlap at 2.5 km NWP resolution (Fig. 3.9)	δ-Eddington two-stream	Fu
	δ-Eddington two-stream with maximum-random vertical overlap	Fu

To estimate the Monte Carlo noise of the MYSTIC solver in our setup, we split the 10 MYSTIC calculations for the shallow cumulus domain at a single time step into two sets of 5 calculations and average the heating rates over these two sets of 5 calculations. We then calculate the relative standard deviation of the radiative heating between these two sets at each grid box. The relative standard deviation represents the variability in the radiative heating relative to the mean values calculated from the two sets of MYSTIC calculations. The median relative standard deviations in the shortwave, longwave, and net are less than 10% for almost all grid boxes (not shown). This estimate is an upper bound, as the true

Monte Carlo noise in our calculations with 7.2×10^7 photons can be expected to be smaller. The low Monte Carlo noise of our radiation calculation allows us to calculate the CRH uncertainty due to 3D cloud-radiative effects locally at the scale of the horizontal grid resolution of the LEM domains.

To assess the impact of the ice optical parameterization, we use the more complex scheme of Baum_v36 (Yang et al., 2013; Baum et al., 2014) in addition to the scheme of Fu. The scheme of Baum includes the full phase function and three different ice habits: the general habit mixture, the solid column habit, and the rough-aggregated habit. Ice crystal surfaces are treated as severely roughened in the Baum scheme. Zhao et al. (2018) compared the radiative fluxes calculated with the schemes of Fu and Baum and showed that in the longwave spectrum, the mass absorption coefficient is smaller in the Baum scheme than in the Fu scheme, resulting in weaker longwave radiative cooling at the cloud top and weaker warming below (Fig. 1 of Zhao et al., 2018). In the shortwave spectrum, the backward scattering of radiation by ice crystals is higher in the Baum scheme due to the reduced parameterized asymmetry factor and the forward peak. This reduces the radiative flux gradient between cloudy and clear-sky layers, resulting in a weaker CRH with the ice scheme of Baum.
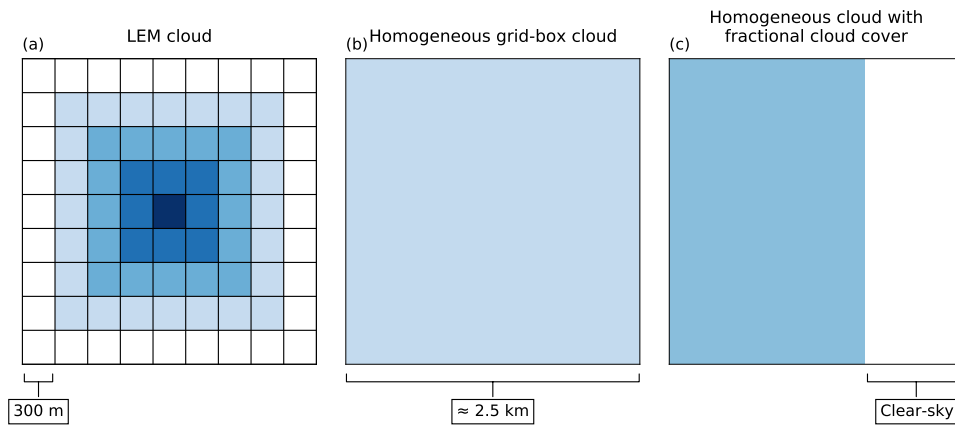

Figure 3.9: Illustration of the method used to derive homogeneous NWP clouds from LEM clouds. The plot shows a layer of grid boxes. (a) Clouds in the LEM simulation. (b) A homogeneous grid-box cloud at a resolution of 2.5 km. (c) A homogeneous cloud with fractional cloud cover at a resolution of 2.5 km. Reprinted from Keshtgar et al. (2024). ©The Authors, CC BY 4.0 ⓒⓘ

When studying the impact of cloud horizontal heterogeneity on CRH, it would be misleading to directly compare the CRH between the NWP and LEM setups since the two setups simulate different clouds. Therefore, we instead create homogeneous clouds at the 2.5 km NWP resolution by coarse-graining the LEM clouds. The method is illustrated in Fig. 3.9. We derive two types of homogeneous NWP clouds. For the first type, we average the cloud fields over all LEM grid boxes that fall within the corresponding NWP grid box with a resolution of 2.5 km. We call this type "homogeneous grid-box clouds". This type assumes that clouds are resolved at the NWP resolution so that grid boxes are either entirely cloudy or clear and that no vertical overlap assumption is needed. For the second type, we average the cloud fields only over those LEM boxes that are cloudy, and we use the number of clear-sky boxes to determine

the cloud fraction. We refer to this type as "homogeneous clouds with fractional cloud cover". This type requires an overlap assumption, for which we use the δ-Eddington two-stream solver that applies maximum-random overlap (Črnivec and Mayer, 2019).

3.8 Hindcast Simulations during the NAWDEX Field Campaign

This section describes the ICON model setup for the hindcast simulations in Ch. 8 to study the impact of CRH and its uncertainty on North Atlantic cyclones.

We use ICON-NWP version 2.6.2.2 to perform hindcast simulations during the 2016 NAWDEX field campaign (Schäfler et al., 2018). We focus on four intensive observing periods (IOPs) during NAWDEX: IOPs 3, 4, 6, and 7. These IOPs are associated with four extratropical cyclones: cyclone Valadiana during IOP 3, tropical-extratropical transitioning of cyclone Karl during IOP 4, cyclone Stalactite during IOP 6, and the so-called Frontal-wave cyclone during IOP 7.

We run two control simulations, each covering two IOPs and the evolution of two cyclones over 6 days of forecast. The first simulation starts on 22 September 2016 at 00:00 UTC and ends on 28 September 2016 at 00:00 UTC, and covers the evolution of cyclones Valdiana and Karl during IOPs 3 and 4. The second simulation starts on 30 September at 00:00 UTC and ends on 6 October at 00:00 UTC and covers the evolution of Stalactite and Frontal-wave cyclones during IOPs 6 and 7.

The ICON model setup is similar to the model setup used in Senf et al. (2020) and briefly described in Sect. 3.5. Here we provide more details and describe the differences. We configure ICON in a limited-area mode over a large domain covering the North Atlantic, as well as much of Europe and northern Africa (23°-80°N and 78°W-40°E) to ensure that simulations cover the entire temporal and spatial evolution of the cyclones (Fig. 3.6). We set the horizontal resolution to 10 km (R2B08) and in the vertical direction, we use 75 model vertical levels. For initial and lateral boundary conditions, we use the analysis and forecast data from the ECMWF Integrated Forecasting System (IFS) model at a resolution of 9 km. To ensure that simulations stay close to the actual observed large-scale synoptic situation, we update the lateral boundary data every three hours. The analysis data are available at 00:00 and 12:00 UTC, and in between we use the forecast data at 3, 6, and 9-hour lead times.

We use ICON with the NWP physics package, including the shallow and deep convection schemes of Tiedtke (1989) and Bechtold et al. (2008), the one-moment microphysics scheme based on Doms et al. (2011), and the turbulence scheme of Raschendorfer (2001).

For radiation, we use ecRad (Hogan and Bozzo, 2018), the new operational radiation scheme in ICON (Rieger et al., 2019). From different radiation solvers and cloud optical parameterizations available in ecRad, ICON is operationally configured to use the Monte-Carlo Independent Column Approximation solver (McICA; Pincus et al., 2003). For the cloud optical parameterization, we use the SOCRATES scheme based on Edwards and Slingo (1996) for liquid water and the scheme of Fu (Fu, 1996; Fu et al.,

1998) for ice crystals. In Sect. 8.2.3, we use different radiation solvers, ice-optical parameterization, and radiation schemes to assess the impact of CRH uncertainties on the predictability of cyclones.

4 Cloud-Radiative Impact on the Dynamics of an Idealized Extratropical Cyclone

In this chapter, we address research question 1: "How does CRH affect the dynamics of idealized extratropical cyclones?". In particular, we address the following questions:

1. How strongly does CRH affect the intensity of extratropical cyclones?
2. What are the mechanisms that underlie the cloud-radiative impact?
3. What does this imply for the cloud-radiative impact on cyclone predictability?

To answer these questions, we investigate the impact of CRH on the dynamics of an idealized extratropical cyclone by means of baroclinic life cycle simulations with the ICON model in the channel setup (Sect. 3.3). The simulation design is described in Sect. 4.1, and the results are presented in Sect. 4.2. The chapter closes with the discussion and conclusions in Sect. 4.3. This chapter is based on Keshtgar et al. (2023). ©The Authors, CC BY 4.0 ©①

4.1 Simulation Design

As described in Sect. 3.4, we apply our new modeling approach to study the impact of CRH on idealized cyclones. Our new modeling approach requires two simulations: one simulation with no radiation, and one simulation with only CRH. In the latter simulation, only the radiative heating from clouds, defined as the all-sky minus the clear-sky radiative heating is passed to the model's dynamical core:

$$\frac{DT}{Dt}\bigg|_{\text{with CRH}}^{\text{only}} = \frac{1}{c_p}\left(\frac{1}{\rho}\frac{Dp}{Dt} + \left(\frac{\partial T}{\partial t}\bigg|_{\text{radiation}}^{\text{all-sky}} - \frac{\partial T}{\partial t}\bigg|_{\text{radiation}}^{\text{clear-sky}}\right) + J\right). \tag{4.1}$$

To study to what extent the cloud-radiative impact is linear, we perform an additional simulation in which we multiply CRH by a factor of two before feeding it to the dynamical core (cf. Eq. 4.1). This simulation will be referenced as 2xCRH in the following. For convenience, from now on the simulations with no radiation and with cloud radiation only will be referenced as REF and CRH, respectively.

For the analysis, we use the climate data operators (Schulzweida, 2019) and first remap the model output from the triangular grid to a regular rectangular grid with the same resolution using the nearest neighbor interpolation method. We then interpolate the data to a $0.5°\times0.5°$ latitude-longitude grid using conservative interpolation. When we calculate spatial averages over the entire simulation domain, we exclude the northern and southern boundaries and perform the calculation from 10 to 80°N and 25.5°W to 25.5°E.

4.2 Results

In this section, we assess the impact of CRH on the evolution of the cyclone in terms of cyclone strength, PV, and PV tendencies from diabatic processes. To this end, we compare the REF simulation with the simulations that include CRH as given by Eq. 4.1. Using the PV error growth framework (Sect. 1.4), we investigate how CRH changes the dynamics and evolution of the cyclone. We then assess the cloud-radiative impact on cyclone predictability by disabling cloud-radiation interaction at a number of days during the cyclone growth.

4.2.1 Cloud-Radiative Impact on the Cyclone

We characterize cyclone intensity by means of eddy kinetic energy and cyclone center pressure. Eddy kinetic energy is calculated with respect to the deviation from the zonal-mean wind field at each time step. Cyclone central pressure is simply given by the minimum surface pressure within the model domain. Fig. 4.1 shows the evolution of the intensity metrics for the simulations REF, CRH, and 2xCRH.

According to the cyclone central pressure shown in Fig. 4.1a, cyclone development starts at around day 3 and peaks at around day 7. CRH has no noticeable impact on cyclone development as measured by the central pressure. However, CRH clearly strengthens the cyclone in terms of eddy kinetic energy. When CRH is taken into account, eddy kinetic energy increases after day 6 compared to the REF simulation, signaling a stronger cyclone whose peak intensity is delayed. The cloud-radiative impact is more prominent at upper levels, and weaker at lower levels (cf. Fig. 4.1b and c). This implies that CRH mostly influences the near-tropopause flow. Doubling CRH in the 2xCRH simulation further increases eddy kinetic energy, although the change between the CRH and 2xCRH simulations is smaller than that between the REF and the CRH simulations (Fig. 4.1b).

Our results are in contrast to the global simulations of Schäfer and Voigt (2018), who reported that CRH weakens idealized cyclones. Schäfer and Voigt (2018) also used the ICON atmosphere model and studied a cyclone growing from the same initial conditions. The disagreement between our finding of a strengthening CRH impact and the finding of Schäfer and Voigt (2018) of a weakening impact might seem discomforting at first sight, but in fact, it does point out the importance of model uncertainty in CRH. This is briefly described in the following. In a companion study, which was performed as a Master's thesis advised by Aiko Voigt and Behrooz Keshtgar, Butz (2022) found that the result of Schäfer and Voigt (2018) is sensitive to the version of the ICON model. Butz (2022) found a weakening CRH impact in ICON version 2.1 (which is essentially the same version as used by Schäfer and Voigt (2018), but a strengthening impact in ICON version 2.6 (which is the version used in the present study). Butz (2022) traced this difference to a difference in the simulation of low clouds, of which there are many in version 2.1 but fewer in version 2.6. The results of Butz (2022) imply that the CRH impact is not sensitive to whether a global or channel setup is used. Moreover, we have repeated our channel simulations with the two-moment microphysics scheme of Seifert and Beheng (2006) instead of the one-

moment scheme and have found that CRH impact is independent of the microphysics scheme (Fig. 4.1). Thus, the CRH impact is robust with respect to the model domain and cloud microphysics, although it can be expected to be model dependent because of model uncertainty in the simulation of CRH. In Ch. 5, we study the model dependency of CRH impact on the intensity of idealized cyclones.
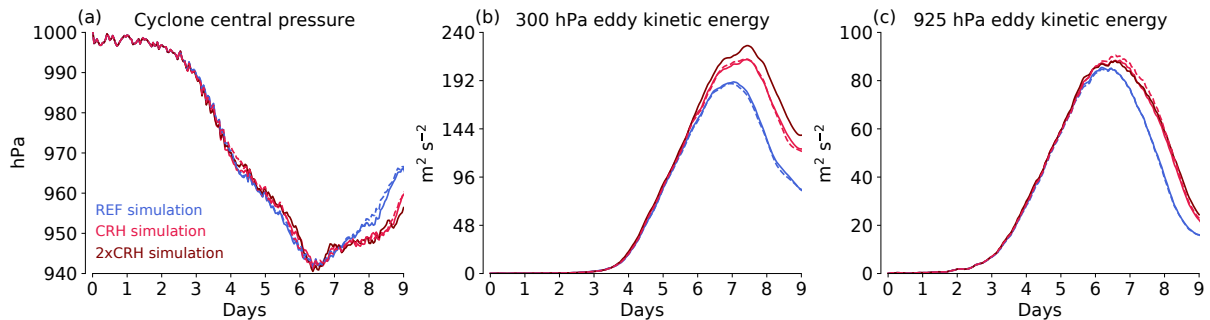

Figure 4.1: Evolution of (a) cyclone central pressure and eddy kinetic energy at (b) 300 hPa and (c) 925 hPa for simulations with no radiation (REF), cloud-radiative heating (CRH), and cloud-radiative heating increased by a factor of 2 (2xCRH). The dashed lines show additional simulations that use the two-moment instead of the one-moment microphysical scheme. Reprinted from Keshtgar et al. (2023). ©The Authors, CC BY 4.0 ©①
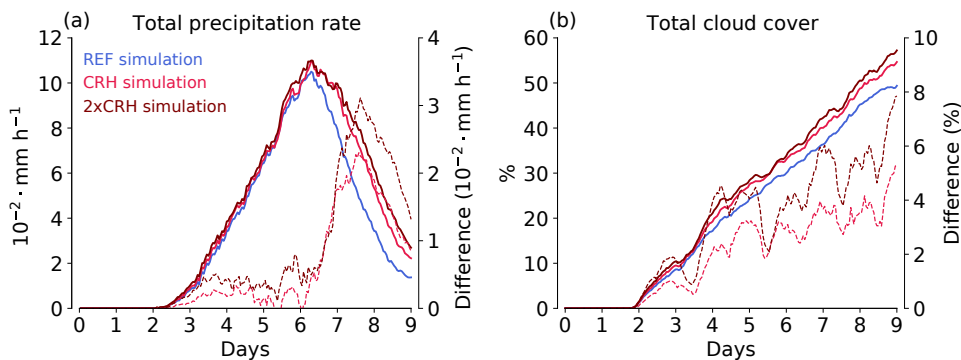
Figure 4.2: Evolution of spatially averaged (a) total precipitation rate and (b) total cloud cover for different treatments of cloud-radiative heating. The dashed lines denote the difference of the CRH and 2xCRH simulations with respect to the REF simulation. For the differences, the right y-axis is used. Reprinted from Keshtgar et al. (2023). ©The Authors, CC BY 4.0 ©①

In conjunction with the cyclone intensity metrics, Fig. 4.2 shows the evolution of spatially averaged total precipitation rate and cloud cover for the three simulations and the differences with respect to the REF simulation. The total precipitation rate is derived from hourly accumulated precipitation and includes precipitation in all forms (rain, snowfall, etc.). Precipitation starts to form around day 3 and peaks at day 6.5 for all simulations (Fig. 4.2a). Total cloud cover increases constantly during the 9 days of the simulation. When CRH is active, total precipitation rate and total cloud cover increase compared to the REF simulation (Fig. 4.2a and b). Similar to the eddy kinetic energy (Fig. 4.1), the CRH impact gets stronger with amplified CRH.

The CRH-induced increase in precipitation indicates that the cloud-radiative impact might operate via changes in condensation and latent heating, which are known to strongly affect cyclone development (Sect. 1.1). In the following subsection, we will indeed look at this point in more detail by analyzing the PV evolution.

Cloud-Radiative Impact on Potential Vorticity

PV combines dynamic and thermodynamic information and is a conserved quantity for frictionless adiabatic flow. Therefore, PV can serve as a tracer that indicates how the circulation is modified by diabatic processes (e.g. Joos and Wernli, 2012). In addition, the PV distribution on isentropic surfaces helps to characterize the synoptic-scale structure of baroclinic waves and their propagation (Hoskins et al., 1985).
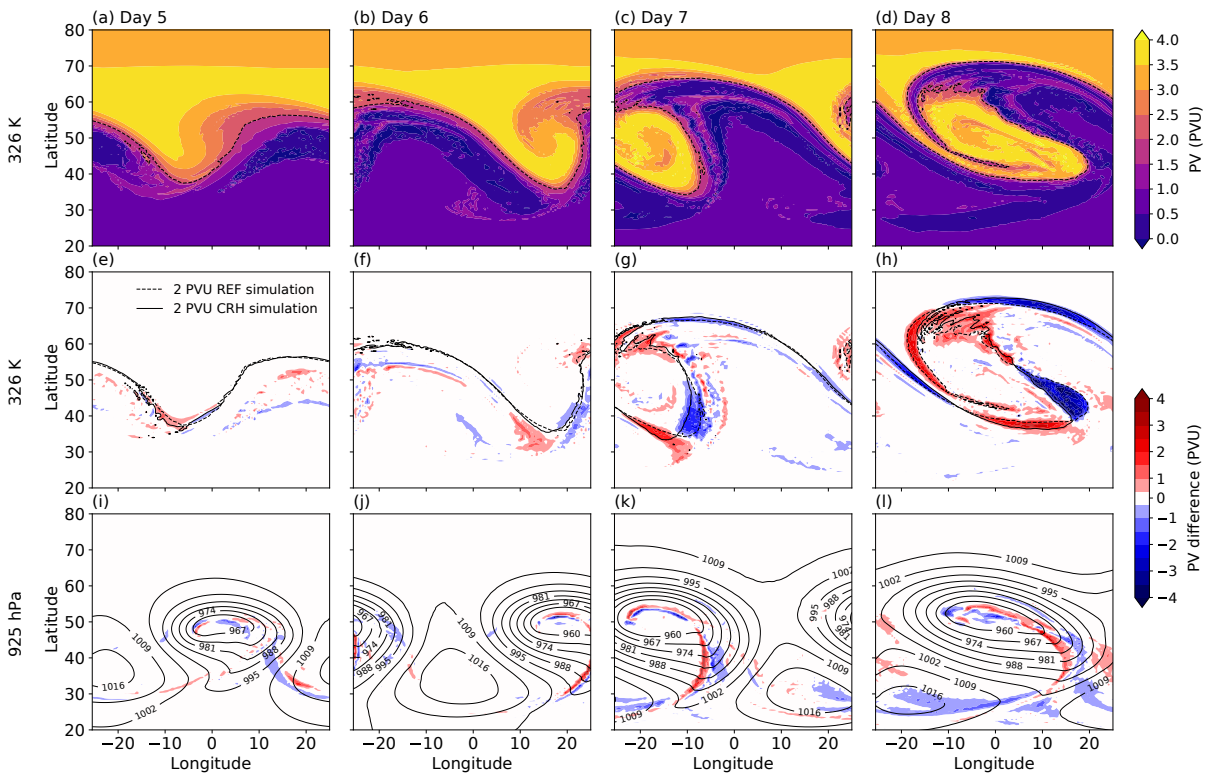
Figure 4.3: Upper-level PV evolution on the 326 K isentrope for the REF simulation from days 5 to 8 (a-d). PV differences between the CRH and REF simulations (CRH-REF) at upper levels on the 326 K isentrope (e-h) and at lower levels on the 925 hPa isobaric surface (i-l). The dynamical tropopause is shown in solid and dashed black lines for CRH and REF simulations, respectively. The thin black contours depict the surface pressure (hPa) averaged between the two simulations. Reprinted from Keshtgar et al. (2023). ©The Authors, CC BY 4.0 (cc)(i)

The first row in Fig. 4.3 shows the evolution of PV at the 326 K isentrope for the REF simulation. This isentropic level includes tropospheric air at lower latitudes and stratospheric air at higher latitudes. The tropopause is located in a region of strong PV gradients that separate tropospheric from stratospheric air masses. The dynamical tropopause is shown by the 2 PVU contour and its wave-like distortion and eventual breaking can be used to depict the development of the cyclone.

Similar to eddy kinetic energy, the wave amplitude starts to grow at around day 3 and reaches its maximum at day 7 with impending wave breaking. The wave breaking is evident from the reversal of the PV meridional gradient in the western part of the domain at day 7 (Fig. 4.3c). This is followed by the decay phase of the wave through barotropic conversion of eddy kinetic energy into zonal-mean kinetic energy (not shown).

To demonstrate the impact of CRH on the evolution of PV, the differences of PV between the CRH and the REF simulations are plotted at upper and lower levels in the second and third rows of Fig. 4.3, respectively. At the upper levels shown by the 326 K isentrope, PV differences at days 5 and 6 are small and limited to regions close to the dynamical tropopause (Fig. 4.3e and f), but grow to substantial values at days 7 and 8 (Fig. 4.3g and h). At the lower levels shown by the 925 hPa isobaric surface, PV differences are confined near the cyclone center and in the warm conveyor belt (Fig. 4.3k and j). However, lower-level PV differences are not strong enough to substantially change the eddy kinetic energy at 925 hPa during the baroclinic development (Fig. 4.1c)

The distribution of positive and negative PV differences at upper levels indicates that CRH slows the propagation of the baroclinic wave towards the east, thereby postponing the cyclonic wave-breaking, and increases the wave amplitude. These impacts can be seen from the deformation of the dynamical tropopause wave at days 7 and 8 (Fig. 4.3g and h). Higher PV east of the trough center (blue colors) and lower PV at the tip of the ridge (red colors) for the REF simulation at day 7 indicate an earlier wave-breaking and termination of the wave intensification. Positive PV differences west of the trough center (red colors) and negative PV differences on the poleward side of the ridge (blue colors in Fig. 4.3g and h) imply a deeper tropopause fold and stronger ridge for the baroclinic wave with CRH, although this is not explicitly shown in the figure.

The CRH impact is consistent with the diabatic intensification of baroclinic waves in terms of wave amplitude and growth rate. For instance, Chagnon et al. (2013) showed in their cyclone case study that the PV anomalies generated by diabatic processes help to keep the upper-level PV wave phase-locked with the surface potential temperature wave, which means that each wave component will help to increase the amplitude of the other. This mutual interaction then slows down the eastward propagation of the wave and amplifies the growth rate. Thus, including CRH helps to reinforce this impact, resulting in higher eddy kinetic energy and delayed peak time. Overall, the evolution of PV is consistent with that of eddy kinetic energy and the stronger impact of CRH at upper levels.

Potential Vorticity Tendencies from Diabatic Processes

We now investigate the modification of PV by diabatic processes and the relation to the PV differences diagnosed in the previous subsection. Diabatic processes can modify the near-tropopause PV and hence the tropopause structure. The impact can be direct through diabatically generated PV anomalies, most notably as the result of vertical gradients in diabatic heating, or indirect through changes in wind and

PV advection. For a non-conservative flow, the diabatic modification of PV is given by (e.g., Büeler and Pfahl, 2017):

$$\frac{DPV}{Dt} = \frac{1}{\rho}(\eta \cdot \nabla \dot{\theta}) + \frac{1}{\rho}(\nabla\theta \cdot \nabla \times \mathbf{F}), \tag{4.2}$$

where $\frac{D}{Dt}$ denotes the material derivative, ρ is the density, η is the absolute vorticity vector, $\dot{\theta}$ is the diabatic heating tendency, and $\mathbf{F}$ is the frictional force. The first and the second terms on the r.h.s. of Eq. 4.2 represent the PV modification due to diabatic heating tendencies and nonconservative momentum. For PV modification due to diabatic heating tendencies, one can assume that the vertical gradient of $\dot{\theta}$ dominates the PV tendency, which is typically the case. Thus, the main effect of diabatic heating is an increase of PV below the maximum of the heating and the reduction of PV above it. However, for our analysis, we derive the diabatic PV tendencies based on the three vector components of Eq. 4.2 and on model levels to benefit from the high vertical resolution. Our analysis includes all diabatic heating tendencies of the ICON model as well as the nonconservative momentum due to the parameterization of turbulence, shallow convection and non-orographic gravity waves.

The overwhelming part of the heating from cloud-radiation interaction and cloud microphysics occurs within the warm conveyor belt of the cyclone, which is characterized by extensive cloud formation and heavy precipitation. For the simulation with CRH, Fig. 4.4 shows cross-sections through the warm conveyor belt for cloud cover, CRH, and microphysical heating at day 5.5. The figure also shows the associated diabatic PV tendencies.

The two cloud bands mark the regions of ascent in the warm conveyor belt and the cyclonic branch that is located further north (Fig. 4.4a). In these regions, longwave CRH leads to strong cooling near the cloud top and modest warming below (Fig. 4.4b). In contrast, shortwave CRH warms the top of the clouds and weakly cools the cloud layer below (Fig. 4.4c). Compared to longwave CRH, shortwave CRH is small and is limited mostly to near the cloud top.

A substantial part of diabatic heating in these cloudy regions is associated with cloud microphysical processes (Fig. 4.4d). Strong microphysical heating occurs inside the cloud bands, with some cooling below. Joos and Wernli (2012) showed in their warm conveyor belt case study that the largest contribution to microphysical heating is due to the condensation of water vapor and the depositional growth of snow, and that cooling is mostly due to the evaporation of rain and snow melting.

The vertical gradients in CRH and microphysical heating lead to diabatic PV increase and reduction according to Eq. 4.2 as shown in Fig. 4.4e, f, and g. Longwave CRH mostly generates a vertical dipole of negative and positive PV tendencies near the cloud top (Fig. 4.4e). For shortwave CRH, the dipole is reversed and somewhat compensates for the longwave CRH impact. Consistent with the larger heating rates, PV tendencies associated with cloud microphysical processes are much stronger.

The relationship between cloud diabatic heating and the associated PV tendencies is further illustrated in Fig. 4.5, which shows vertical profiles of heating rates and PV tendencies averaged spatially over the entire domain and averaged between days 5 to 8. Another heating rate that is required to be considered

for the total latent heating comes from the saturation adjustment scheme. The aim of the saturation adjustment scheme is to bring the water vapor and liquid water back in equilibrium, hence this scheme accounts for the heating rates from condensation. In Fig. 4.5b, the total latent heating from the sum of cloud microphysics and saturation adjustment is shown. For comparison, the microphysical and total latent heating and their PV tendencies for the REF simulation are also plotted as dashed lines.
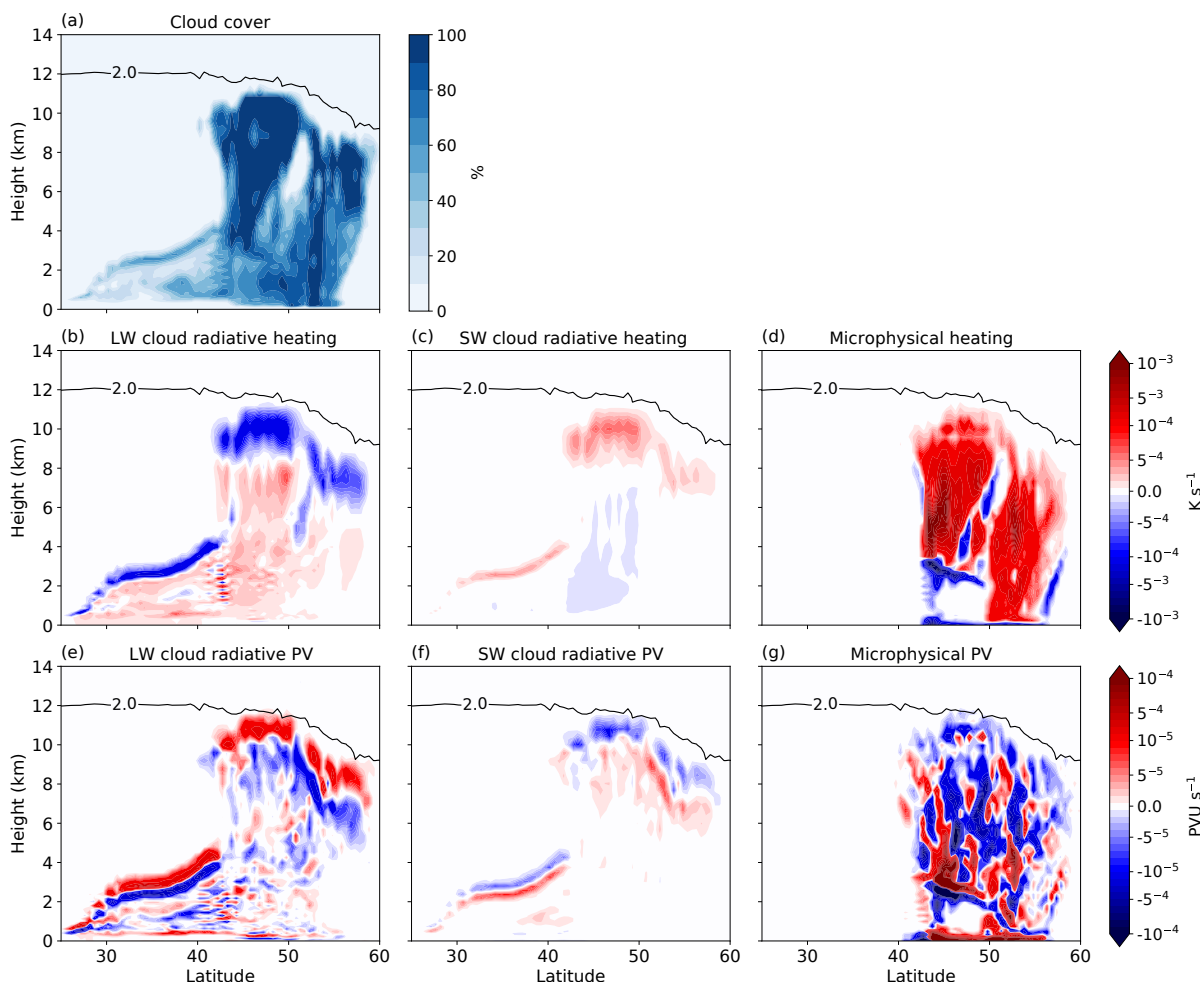

Figure 4.4: Cross-section through the warm conveyor belt at day 5.5 for the simulation with CRH. (a) cloud cover, (b) longwave CRH, (c) shortwave CRH, and (d) heating from cloud microphysical processes. Panels (e), (f), and (g) show the associated diabatic PV tendencies. Black contours show the tropopause by the 2 PVU contour. Reprinted from Keshtgar et al. (2023). ©The Authors, CC BY 4.0 ©①

On average, longwave CRH leads to a noticeable cooling at upper levels. In the boundary layer, longwave CRH cools the boundary layer top and warms the layer from below (Fig. 4.5a). Cloud microphysical processes on the other hand produce much stronger heating at mid-levels between 4-8 km (Fig. 4.5a). Saturation adjustment further increases the mid-levels heating and leads to a secondary heating maximum at 2 km (Fig. 4.5b).

Previous studies showed that the vertical dipole of PV tendencies associated with latent heating (Fig. 4.5c, d, red and dark red lines) help to increase the intensity of the cyclone (Stoelinga, 1996; Büeler and Pfahl,

2017). At lower levels, positive PV tendencies tend to form and increase the lower-tropospheric PV. The negative PV tendencies above the maximum latent heating lead to the downstream upper-level ridge amplification. This configuration supports the typical westward tilt between lower and upper-level waves, hence cyclone intensification.
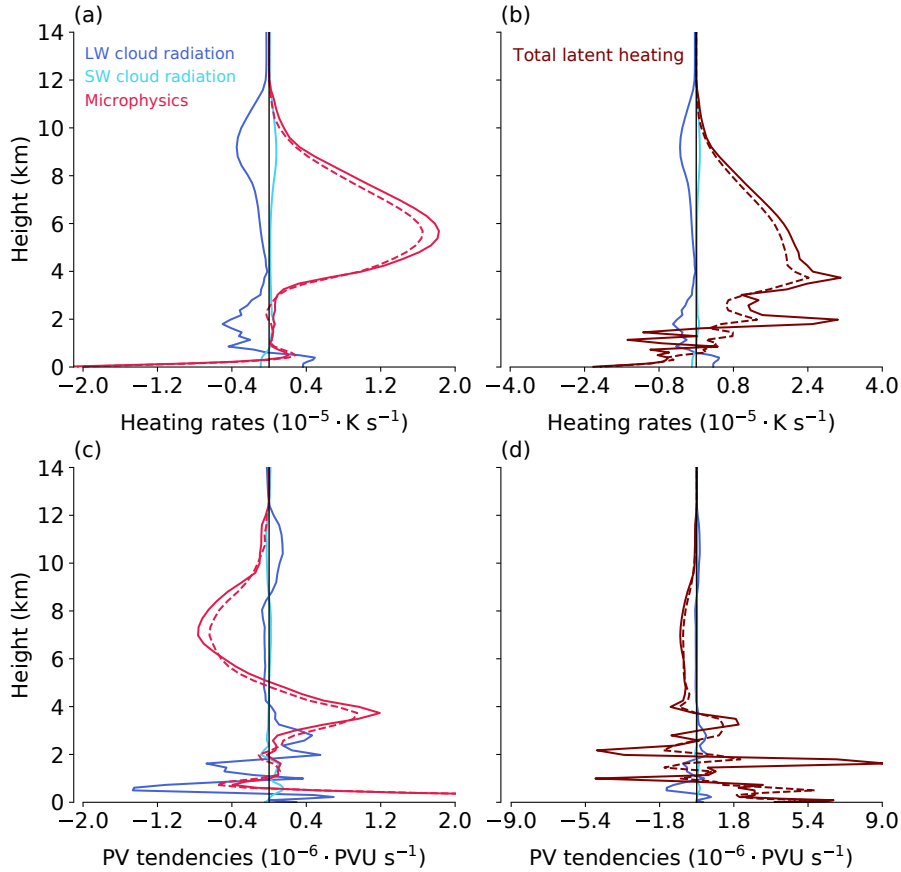

Figure 4.5: Vertical profiles of spatially averaged (a) cloud radiative and microphysical heating rates averaged between days 5 to 8. Panel (b) further shows the total latent heating calculated as the sum of cloud microphysical heating and heating from saturation adjustment. Panels (c) and (d) show the associated PV tendencies. The solid lines are for the CRH simulation, and the dashed lines are for REF simulation. Reprinted from Keshtgar et al. (2023). ©The Authors, CC BY 4.0 ⓒⓘ

PV tendencies by CRH may enhance or weaken the aforementioned PV tendencies associated with cyclone intensification. At upper levels, positive PV tendencies by longwave CRH tend to reduce the magnitude of latent heating negative PV tendency. But, at lower levels between 2-4 km, they tend to interfere positively to increase PV (Fig. 4.5c and d). CRH also amplifies the microphysical and total latent heating (Fig. 4.5a and b) and their PV tendency dipole (Fig. 4.5c and d). This is related to the destabilization of the ascent region within the cyclone by the longwave CRH dipole (Fig. 4.4b). Cloud top cooling and warming below increase the buoyancy of the layer leading to stronger ascending motion and latent heating. The stronger latent heating PV tendency dipole is in favor of cyclone intensification and hence higher eddy kinetic energy.

Moreover, the dipole of positive and negative PV tendencies by CRH in the boundary layer (Fig. 4.5c and d) suggests that the layer becomes more turbulent. Thus, CRH can impact not only the total latent heating but also other diabatic processes. To demonstrate how CRH affects diabatic PV tendencies, Fig. 4.6 shows the evolution of spatially averaged PV tendencies from individual diabatic processes. Besides CRH and total latent heating, this includes the PV tendencies from turbulence, convection, and nonconservative momentum. The convection contribution is only due to parametrized shallow convection. The PV tendencies are shown at four layers to characterize their variation with height and are shown for the CRH simulation in the first row and their differences with the REF simulation in the second row.

At upper levels (8-12 km) all diabatic processes generate negative PV tendencies except longwave CRH, which tend to damp the net negative diabatic PV tendency (Fig. 4.6a). At mid-levels (4-8 km) the negative PV tendency by total latent heating drives the total diabatic PV tendency (Fig. 4.6b). At lower levels (2-4 km) total diabatic PV tendencies are mostly controlled by opposing impacts from latent heating and turbulence (Fig. 4.6c). The opposing effect between latent heating and turbulence PV tendencies is also visible in the boundary layer (0-2 km). However, PV tendencies associated with nonconservative momentum lead to the net positive diabatic PV tendency. On average the PV tendencies associated with convection are small at all levels.
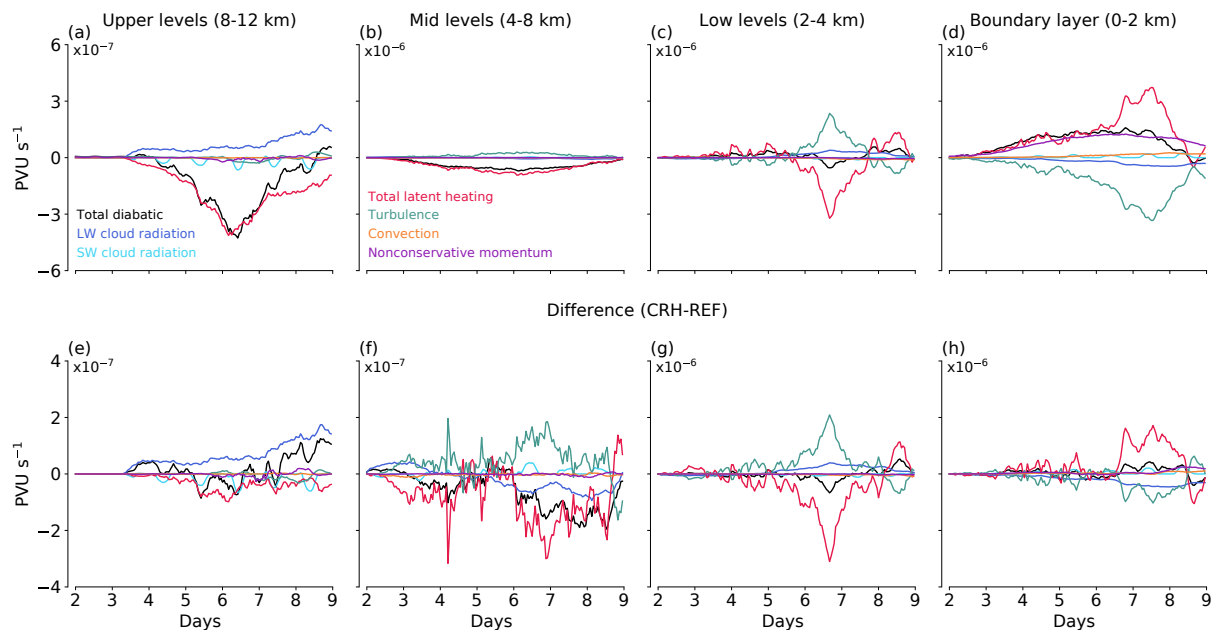

Figure 4.6: Evolution of spatially averaged and mass-weighted vertical average of diabatic PV tendencies between (a) 8-12 km, (b) 4-8 km, (c) 2-4 km, and (d) 0-2 km in the CRH simulation. Panels (e-h) show the differences between the CRH and REF simulations (CRH-REF). Note the different y axes in the panels. Total diabatic PV tendency (black line) is the sum of the individual diabatic PV tendencies shown as colored lines. Reprinted from Keshtgar et al. (2023). ©The Authors, CC BY 4.0 ©①

When CRH is included, the PV tendencies from latent heating and turbulence change at all levels. This is shown in the lower row of Fig. 4.6. In fact, the PV tendencies associated with turbulence and total

latent heating are amplified at all levels in the CRH simulation compared to the REF simulation. At upper levels, however, this amplification is more than compensated by the strong positive PV tendency from longwave CRH (Fig. 4.6e). At mid-levels, the negative PV tendency by CRH amplifies the net negative PV tendency between days 5 to 9.

Diabatic PV tendencies have a higher impact on lower-level PV than on mid- and upper-level PV. Büeler and Pfahl (2017) showed that during the cyclone maximum intensity phase, most of the PV anomalies are controlled by diabatic processes at lower levels. Thus, small changes in the net diabatic PV tendency at lower levels and boundary layer mostly due to the compensation between amplified turbulence and latent heating PV tendencies might explain the weak impact of CRH on the eddy kinetic energy at 925 hPa found in Fig. 4.1c. Near the tropopause, however, PV is strongly controlled by PV advection from the rotational and divergent flow (Riemer and Jones, 2010; Chagnon et al., 2013). Thus, changes in the diabatic PV tendencies near the tropopause (Fig. 4.6e) can not fully explain the PV differences shown in the previous subsection. Therefore, we study the impact of CRH on the PV advection and their relation to the PV differences in more detail in the following subsection.

4.2.2 Understanding the Cloud-Radiative Impact by Diagnosing the Growth of Potential Vorticity Differences

The previous section has documented a clear impact of CRH on the idealized cyclone and the evolution of PV. To understand the underlying dynamical mechanisms, we now compare the simulations with and without CRH by means of the PV error growth framework of Baumgart et al. (2018, 2019). In Sect. 1.4, we described the framework in detail. Here, we apply the framework by considering the CRH simulation as the reference analysis, and the REF simulation without radiation as the forecast:

$$\Delta PV = PV_{\text{CRH}} - PV_{\text{REF}}. \tag{4.3}$$

Because a "true" evolution of the idealized cyclone does not exist, we use the terminology of "difference" instead of "error" in the following. As described in Sect. 1.4, we calculate the potential enstrophy ($\mathscr{PV} = \frac{(\Delta PV)^2}{2}$) tendency equation:

$$\frac{d\mathscr{PV}}{dt} = \mathscr{PV}_{rot} + \mathscr{PV}_{div} + \mathscr{PV}_{dia} + RES, \tag{4.4}$$

where $\mathscr{PV}_{rot}$ and $\mathscr{PV}_{div}$ measure the contributions from changes in PV advection by the rotational and divergent wind, respectively. The contributions from changes in diabatic heating and nonconservative momentum are given by $\mathscr{PV}_{dia}$.

To compute Eq. 4.4 we linearly interpolate the model output from height-based model levels to isentropic levels that intersect the midlatitude tropopause. We choose the 326 K isentrope for the analysis and compute Eq. 4.4 on a $1° \times 1°$ grid. We have tested at which spatial resolution the diagnostic is best used. The tests were necessary because our high-resolution simulations exhibit a lot of small-scale PV

structures that could substantially affect the budget in Eq. 4.4. The tests showed that the budget is better closed when we compute Eq. 4.4 on the $1° \times 1°$ grid. In fact, for a spatial resolution close to the 2.5 km resolution of the model, Eq. 4.4 is not even approximately closed because of strong co-variability between PV and diabatic heating on small scales, which leads to large diabatic tendencies. However, this small-scale co-variability is short-lived and hence in our view is not necessarily relevant for the synoptic-scale dynamics that we are interested in. We also note that Baumgart et al. (2019) developed and tested the diagnostics with model outputs at $1° \times 1°$ grid.

Still, also on the $1° \times 1°$ grid, Eq. 4.4 is not perfectly closed. In the early stages, the difference potential enstrophy tendency on the l.h.s is larger than the sum of the individual terms on the r.h.s. This is likely due to errors in the spatial discretization. Shortly before the cyclone reaches maturity and thereafter, the l.h.s. of Eq. 4.4 becomes smaller than the r.h.s. It is reasonable to assume that this is due to a sink of difference potential enstrophy from model diffusion, discussed in detail in Baumgart et al. (2019). Their results indicated that numerical diffusion leads to a negative contribution that can be as large as the contribution from the advective tendencies. The contribution from numerical diffusion, however, cannot be quantified from our model output and means that one should in fact not expect a perfectly closed budget. The generation of PV anomalies by a numerical model's dynamical core has been also demonstrated in, e.g., Saffin et al. (2016). Nevertheless and despite these limitations, the r.h.s. of Eq. 4.4 captures the evolution of difference potential enstrophy tendency reasonably well.

Evolution of Difference Potential Enstrophy

Before studying the domain average, we look into the spatial distribution of the different contributions to the difference potential enstrophy tendency. These are shown in Fig. 4.7 for day 7.5, i.e., the time of maximum intensity of the cyclone.

Similar to the near-tropopause PV differences studied in Sect. 4.2.1, difference potential enstrophy and its contributions attain their largest values along the dynamical tropopause (Fig. 4.7). The diabatic tendencies are small and of noticeable magnitude only in the trough region (Fig. 4.7b). A further decomposition of the diabatic tendencies shows that they are dominated by total latent heating and CRH (not shown). The differences associated with CRH are mostly located in the ridge whereas differences by total latent heating are located in the trough region (not shown).

Indeed and as expected at this stage of the cyclone life cycle, advective tendencies dominate the differences in the near-tropopause PV (Fig. 4.7c and d). The rotational contribution is somewhat larger than the divergent contribution, but both are important. This result is consistent with previous findings that at synoptic scales differences in the PV evolution are governed by balanced dynamics and that the rotational tendency associated with non-linear Rossby wave dynamics controls the PV differences near the tropopause (Baumgart et al., 2018). Note that the sum of diabatic, rotational and divergent tendency does not add up to the difference potential enstrophy shown in Fig. 4.7a because of the residual term RES (see Eq. 4.4).

To show how different processes contribute to the evolution of difference potential enstrophy, we consider the time series of spatially averaged tendencies, shown in Fig. 4.8. Although Eq. 4.4 is not perfectly closed for the reasons explained in Sect. 4.2.2, the sum of the diagnosed contributions (green line) matches the actual difference potential enstrophy tendency (black line) reasonably well.
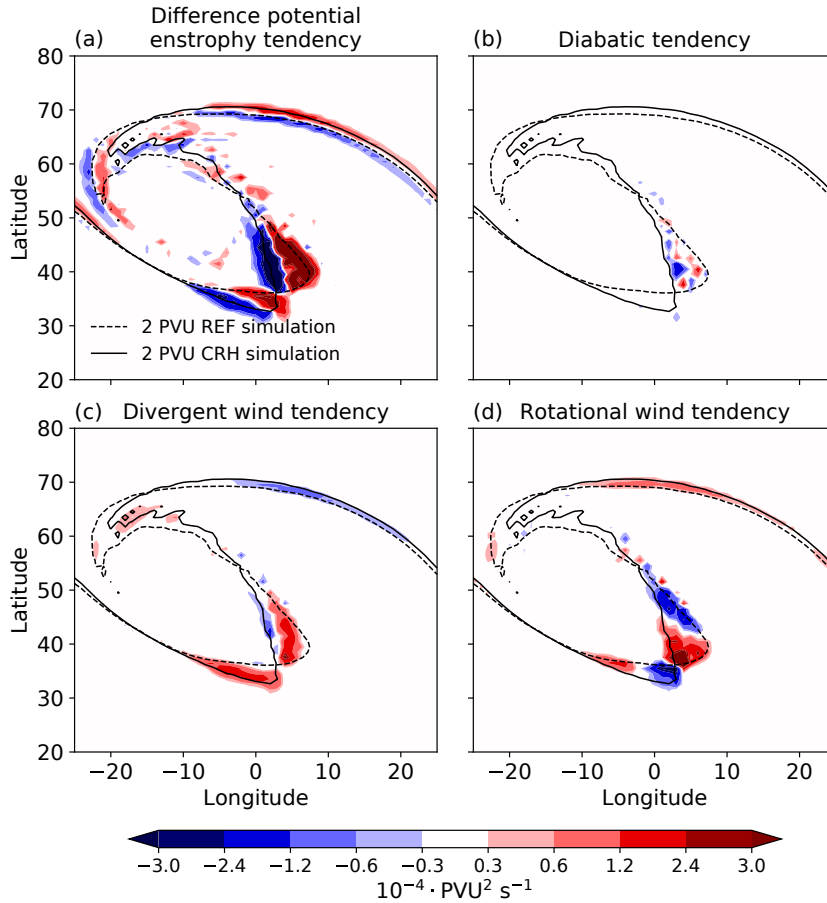

Figure 4.7: Spatial distribution of (a) difference potential enstrophy tendency and contributions from (b) diabatic processes as well as advection by the (c) divergent flow and (d) the rotational flow at day 7.5. The black contours show the dynamical tropopause for the cyclone with CRH (solid) and without CRH (dashed) on the 326 K isentrope. Reprinted from Keshtgar et al. (2023). ©The Authors, CC BY 4.0 ©①

Until day 6 the contribution from diabatic processes is almost in the same range as that from advection. However, close to the cyclone mature stage between days 6 to 8, the growth of difference potential enstrophy is dominated by advection, whose impact via the divergent and rotational flow is one order of magnitude larger compared to diabatic processes (Fig. 4.8a).

The partitioning of the diabatic tendency into the contribution from different processes in Fig. 4.8b shows that CRH and total latent heating control the diabatic impact until day 5. Thereafter, the contribution from total latent heating grows rapidly and becomes the dominant diabatic process. This means that much of the cloud-radiative impact operates via changes in latent heating: when CRH is included, latent heating amplifies between day 5 and 6.5, which in turn amplifies vertical motion and hence the divergent

flow. Following the intensification of the divergent flow, the rotational flow also increases and becomes the dominant process at the time of cyclone maximum intensity (Fig. 4.8a).

The differences in near tropopause PV during the cyclone intensification thus do not result from a direct radiative increase or decrease of PV. Instead, the CRH impact follows a multi-stage sequence of processes. From the absolute scale used in Fig. 4.8a it is difficult to infer the contributions during the first couple of days. Therefore, and similar to Baumgart et al. (2019), we also consider the relative contributions calculated as

$$\alpha = \frac{1}{\mathscr{PV}}\big(\mathscr{PV}_{rot,div,dia}\big). \tag{4.5}$$
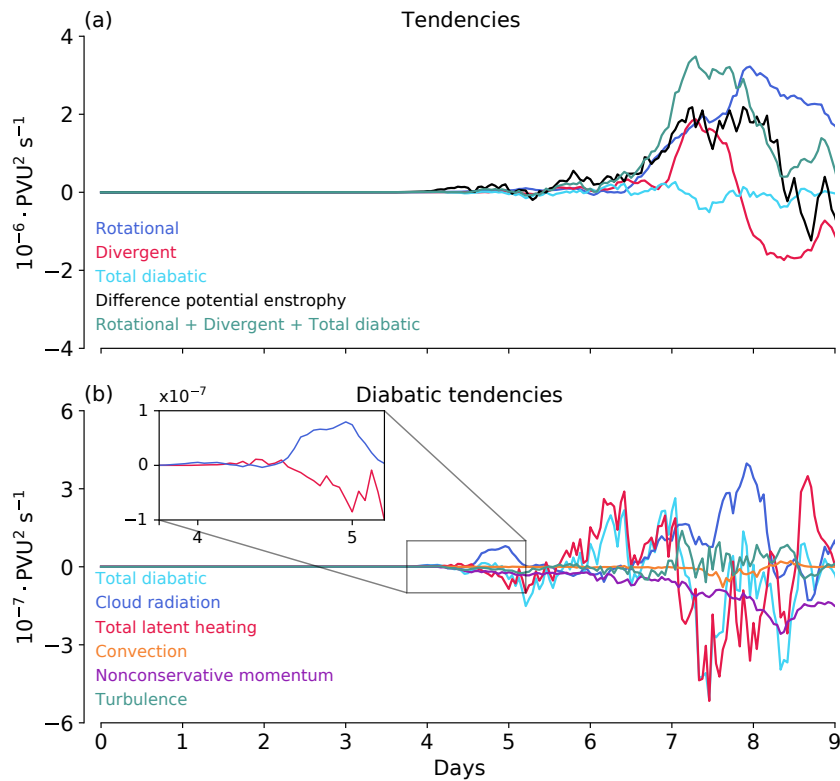
Figure 4.8: Evolution of the spatially averaged difference potential enstrophy tendency and contributions from individual processes diagnosed from the r.h.s. of Eq. 4.4. The analysis is performed around the tropopause on the 326 K isentrope. Panel (b) further decomposes the total diabatic (cyan line) contribution into the contributions from individual diabatic processes. Note the different scales in panels. Reprinted from Keshtgar et al. (2023). ©The Authors, CC BY 4.0 ⓒⓘ

Given that the only difference between the REF and the CRH simulations is the presence of cloud-radiative heating in CRH simulation, one expects that CRH initiates and dominates the differences early in the simulations. This is indeed the case. Clouds start to form at around day 2 in the lower troposphere and CRH initiates the evolution of difference potential enstrophy (Fig. 4.9a). Around the tropopause on the 326 K isentrope, the differences are dominated by the divergent flow already at day 2 (Fig. 4.9b). This

is due to the fact that most of the early CRH occurs below the tropopause level. Thus, the circulation responds quickly to the presence of CRH (Fig. 4.9) and CRH can directly impact the wind fields even in the very early stage of the cyclone growth. However, the early wind changes are small and not relevant for the PV evolution during the intensification phase, as we will further investigate in Sect. 4.2.3.
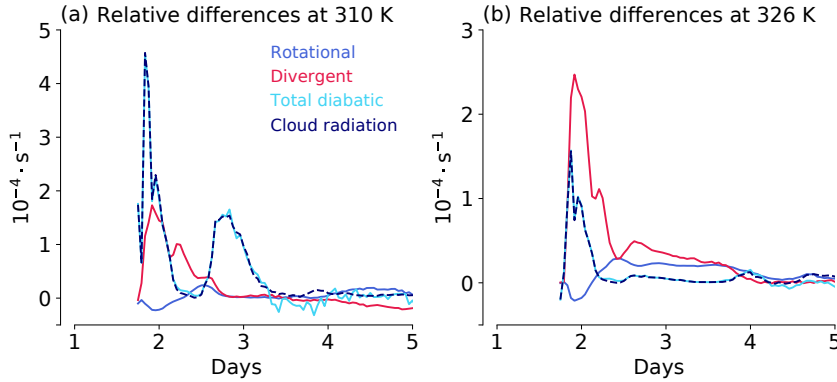

Figure 4.9: Contribution to the relative growth of difference potential enstrophy from the rotational and divergent flow as well as from total diabatic processes and cloud-radiative heating. Panel (a) is for the 310 K isentrope, which is in the lower troposphere. Panel (b) is for the 326 K isentrope, which is near the tropopause. Reprinted from Keshtgar et al. (2023). ©The Authors, CC BY 4.0 ⓒⓘ

An important finding of the above analysis is that much of the CRH impact occurs through changes in the total latent heating and that latent heating plays an important role in the up-scale growth of the differences between the CRH and REF cyclones. The physical mechanisms involved in the multi-stage growth to the synoptic scale are illustrated in Fig. 4.10 by means of latitude-longitude plots of selected processes at different days.

At day 4, considerable differences in diabatic heating between the CRH and REF simulations occur ahead of the cyclone center in the region of the warm conveyor belt. The differences are co-located with differences in precipitation (Fig. 4.10a and b). This finding is consistent with our earlier finding in Fig. 4.2a, which showed that CRH increases precipitation.

Following the changes in the total latent heating, vertical motion in the warm conveyor belt changes as well. The differences in vertical motion then lead to changes in near-tropopause divergence. This is demonstrated for day 5.5, for which differences from the near-tropopause divergent flow and differences in vertical motion are located east and southeast of the cyclone center in the warm conveyor belt (Fig. 4.10c and d). The differences in vertical motion are located slightly eastward of the differences in divergent flow. This is likely related to the westward tilt during the cyclone intensification phase (day 5.5). The vertical velocity differences are plotted on the isobaric surface at 500 hPa whereas the divergent tendency is plotted at 326 K isentrope near the tropopause. Thus, the vertical velocity differences will be advected upward to the near-tropopause level west of their position in the mid-troposphere. Finally, the CRH impact reaches the near-tropopause level, where it manifests as changes in the rotational flow that

lead to a shift in the position of the trough and the ridge. This is shown for day 7.5, for which differences in the rotational flow are dominant and control the PV differences along the tropopause (Fig. 4.10e).
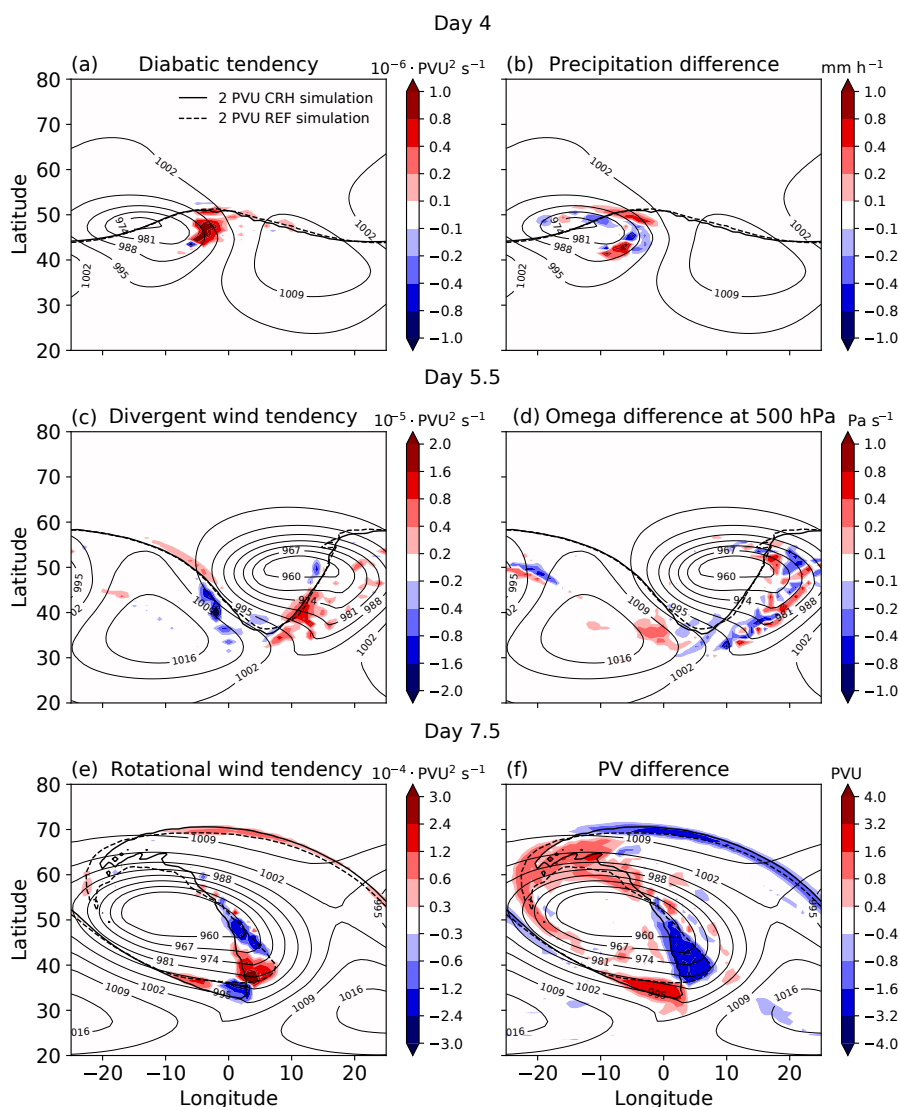

Figure 4.10: Illustration of the dominant contributions to the evolution of difference potential enstrophy during different stages of the cyclone growth (left). The right panel illustrates the underlying processes by means of fields that are closely related to the different contributions. Thick black contours show the dynamical tropopause for the REF (dashed) and CRH (solid) simulations. Thin contours show the surface pressure (hPa) averaged between the two simulations. The differences are calculated as CRH-REF. Reprinted from Keshtgar et al. (2023). ©The Authors, CC BY 4.0 ©①

4.2.3 Implications for the Cyclone Predictability

The multistage sequence of processes that underlies the CRH impact is very similar to the growth of initial state uncertainty from the convective scale to the synoptic scale (Baumgart et al., 2019). At the same time, however, our 2xCRH simulation with doubled cloud-radiative heating exhibits a substantially stronger eddy kinetic energy than the standard CRH simulation (Fig. 4.1b). This raises the question

whether the CRH impact is the result of radiative perturbations in the early phase of the cyclone life cycle that grow in a non-linear atmosphere, or whether CRH in the later phase of the cyclone is also important. The former would mean that CRH acts as a form of initial state uncertainty; the latter would mean that CRH affects the cyclone in a systematic and continuous manner during the entire life cycle.

To answer this question, we perform additional simulations in which CRH is active initially but then disabled after a certain number of days. We achieve this by restarting the model from the CRH simulation but with radiation set to zero. As a result, CRH has only interacted with the cyclone up to the restart day. We perform 4 such simulations, with CRH being deactivated at days 3, 4, 5 and 6, respectively. Fig. 4.11 characterizes the spatial pattern and magnitude of the temperature change due to CRH at the four days, where the temperature change is shown as the mass-weighted vertical average over the depth of the troposphere.
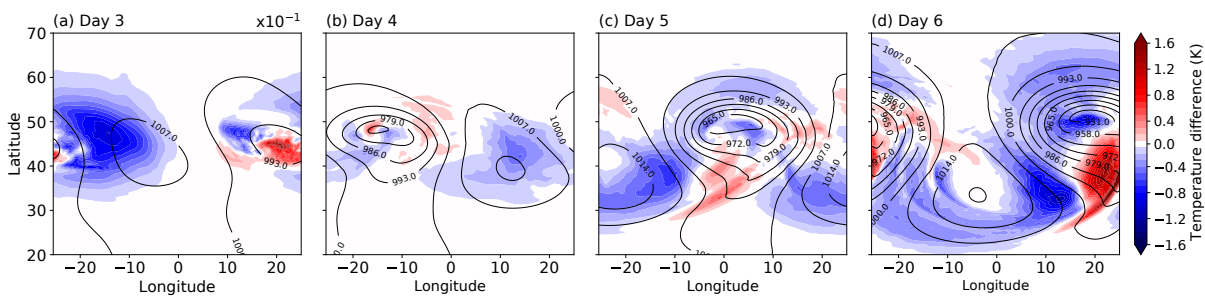
Figure 4.11: Temperature change due to cloud-radiative heating derived as the mass-weighted vertical average over the depth of the troposphere. The change is calculated as the temperature in the CRH simulation minus the REF simulation. Note that the scale of the temperature change at day 3 is ten times smaller than for the other days. Reprinted from Keshtgar et al. (2023). ©The Authors, CC BY 4.0 ©①

With clouds starting to form at around day 2 (Fig. 4.2b), small changes in temperature on the order of a few tenths of a Kelvin are already present at day 3 (Fig. 4.11a). When restarting the simulation at this time without CRH, one can think of these temperature changes as initial perturbations. The wind has also changed to some extent at day 3 due to the presence of CRH, as can be inferred from Fig. 4.9. Later in the life cycle, Fig. 4.11 shows that the temperature change grows to values more than 1 K.

The new simulations make clear that CRH has a continuous impact on cyclone intensity. This is demonstrated by the evolution of eddy kinetic energy differences with respect to the standard CRH simulation in Fig. 4.12. When CRH is disabled at day 3, eddy kinetic energy closely follows the REF simulation. The temperature and wind changes induced by CRH until day 3 are thus too small to affect the cyclone in a considerable manner. It also indicates that CRH is not affecting the cyclone by providing some small initial perturbations.

When CRH is allowed to interact with the cyclone until day 4, differences in the eddy kinetic energy decrease noticeably compared to the REF simulation. When CRH is active even longer, i.e., until day 5 or 6, the evolution of eddy kinetic energy and its maximum value more and more follow the CRH

simulation. It is further interesting that even when CRH is active until day 6, the cyclone does not reach the same peak intensity as when CRH is active throughout the entire life cycle.

As shown in Sect. 4.2.1, between days 3 to 5, CRH increases the latent heat release and precipitation rate (Fig. 4.2a) and thus affects the near-tropopause PV through divergent flow. To check this effect further, similar to Fig. 4.8 we will look into the difference potential enstrophy tendencies between the REF and the new simulations in Fig. 4.13.
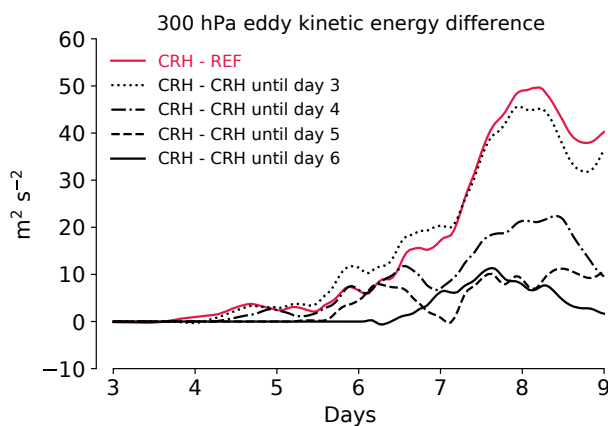
Figure 4.12: Evolution of eddy kinetic energy differences with respect to the CRH simulation at 300 hPa for the REF simulation and simulations with CRH disabled after certain days. Reprinted from Keshtgar et al. (2023). ©The Authors, CC BY 4.0 ⓒⓘ

For the simulation starting at day 3, differences caused by CRH can grow and change the near-tropopause PV. However, the PV evolution is very similar to the REF simulation during the intensification phase. Differences start to appear after the cyclone reaches its maturity (Fig. 4.13a). This is an indication of the non-linearity of the atmospheric flow caused by the CRH in the early stages of the life cycle. Letting CRH interact with the cyclone until day 4 leads to more latent heat release. This is shown by the increase in the different divergent wind tendencies, which represent an indirect impact of latent heat release near the tropopause. Compared to the simulation starting at day 3, different divergent wind tendencies are enhanced for the simulation starting at day 4 (Fig. 4.13b). With amplified divergent wind tendencies, differences in the rotational flow also increase and change the near tropopause PV during the cyclone mature stage between days 6 to 7.5. This effect becomes stronger if CRH is active until days 5 and 6 (Fig. 4.13c and d).

There is a common pattern in the evolution of tendencies and associated processes. During the cyclone mature stage, the peak of the divergent wind tendency is associated with differences in precipitation around day 7 which becomes stronger as long as CRH is active in the simulations (Fig. 4.13). Also, there are secondary smaller peaks in the divergent wind tendencies around day 6 that precede the marked increase in the rotational wind tendencies. The smaller peak is absent for the simulation with CRH disabled at day 3 (insets in Fig. 4.13). Thus, during the mature stage, the prominent growth of differences in the near-tropopause PV occurs primarily due to amplified divergent wind tendencies by CRH.
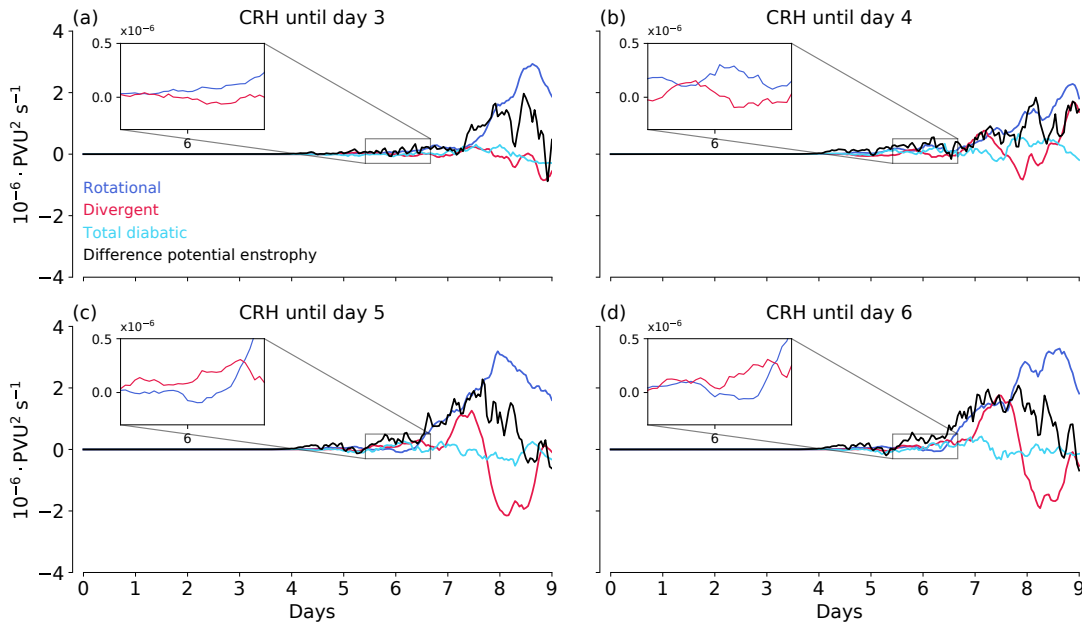
Figure 4.13: Similar to Fig. 4.8 but for tendencies calculated from the REF simulation and simulations with CRH disabled at (a) day 3, (b), day 4, (c) day 5, and (d) day 6. Reprinted from Keshtgar et al. (2023). ©The Authors, CC BY 4.0 ⓒ①

Overall, our results indicate that CRH impacts the cyclone's predictability in terms of its synoptic-scale PV evolution near the tropopause. A small part of the CRH impact indeed is due to the non-linearity of the atmospheric flow caused by small perturbations in the beginning. However, this effect does not change the cyclone near-tropopause PV during the mature phase. In fact, it is the enhanced latent heat release and the subsequent different divergent flow by CRH that leads to changes in near-tropopause PV. Thus, the CRH impact is important throughout the entire life cycle of the cyclone.

4.3 Discussion and Conclusions

We study the impact of CRH on extratropical cyclones by means of baroclinic life cycle simulations with the ICON atmosphere model. The simulations study an idealized cyclone and are run at a high resolution of 2.5 km, allowing deep convection to be modeled explicitly. In contrast to the global setup of Schäfer and Voigt (2018), we use a planar Cartesian geometry with zonal periodic boundary conditions, and we implement a new approach to isolate the impact of CRH. An important advantage of the new approach is that it facilitates the interpretation of the CRH impact because it eliminates the changes in the mean state due to strong clear-sky radiative cooling.

We find that CRH leads to substantial strengthening of the cyclone. The strengthening is most prominent at upper levels near the tropopause and weaker close to the surface. We also show that within this idealized framework CRH affects the predictability of the cyclone. Although our results are limited to a single case, we believe they allow for some general insights into how CRH affects the growth of extratropical cyclones.

Our results are in contrast to Schäfer and Voigt (2018), who found a weakening impact of CRH. As we will show in Ch. 5, the disagreement arises from changes in low-level clouds between the ICON version used in this study and an earlier model version used by Schäfer and Voigt (2018). It, therefore, seems possible - and in fact not unlikely - that other models show a different sign and magnitude of the CRH impact, and it might also be that the CRH impact depends on the cyclone case. We hence do not intend to imply that CRH strengthens all extratropical cyclones. Instead, our work highlights that CRH can have a considerable effect on extratropical cyclones, and that model uncertainty in CRH might be large enough to impact numerical forecasts at synoptic scales.

Our analysis of the evolution of PV near the tropopause shows that the presence of CRH results in a higher amplitude of the baroclinic wave and delayed cyclonic wave breaking. Both contribute to a stronger cyclone. Schäfer and Voigt (2018) suggested that the reduction in the mid-tropospheric PV by CRH could be responsible for the weakening of the cyclone. However, we show that CRH has only a small direct impact on PV. Instead, the mechanism by which CRH affects the dynamics of the cyclone operates predominantly via its influence on latent heating and near-tropopause winds.

CRH enhances total latent heat release. To elucidate the relation between CRH, increased latent heating and near-tropopause PV, we use the PV error growth framework developed by Baumgart et al. (2018, 2019). By comparing simulations with no radiation and with cloud radiation, we quantify the relative importance of diabatic and advective PV tendencies by the rotational and the divergent flows to the evolution of PV near the tropopause. We show that differences in the latent heating caused by CRH lead to differences in vertical motion in the ascending regions of the cyclone. The differences in the vertical motion then lead to changes in near-tropopause divergent flow. Following changes in the divergent flow, differences in the tropopause structure amplify with the rotational flow during the highly nonlinear stage of the baroclinic wave.

The multi-stage sequence of CRH impact on near-tropopause PV is similar to a previously identified mechanism of multi-stage upscale error growth that describes how convective-scale uncertainty may grow upscale to lead to changes at the synoptic scale. An important result of our work is that CRH is not simply affecting the cyclone by providing some kind of initial state uncertainty. Instead, CRH has a continuous effect on the cyclone. Our results show that eddy kinetic energy amplifies as long as CRH is present in the simulation. The analysis also indicates that (synoptic-scale) perturbations to the temperature field that occur early in the simulation by CRH do not project onto differences in baroclinic growth. Instead, even in our case of a growing baroclinic wave, the most prominent growth of differences is associated with modulation of moist processes by CRH and thereafter by the nonlinear tropopause dynamics.

While the direct contribution of CRH to the cyclone PV structure is small, CRH affects the cyclone by changing cloud microphysical heating and subsequently the large-scale flow. Thus, further studies are needed to look into the interaction between radiation and cloud microphysics, and whether this interaction can play a noticeable role in numerical weather predictions of extratropical cyclones. Moreover,

with models moving to storm-resolving kilometer-scale resolutions (Satoh et al., 2019), we should also consider to what extent the CRH impact might depend on an adequate representation of radiation in these models compared to low-resolution models. In Ch. 7 we do indeed investigate this by first quantifying the uncertainties in the CRH within an extratropical cyclone, and in Ch. 8 we assess the impact of the CRH and its uncertainty on the dynamics of North Atlantic cyclones.

5 Tug-Of-War on Idealized Extratropical Cyclones Between Radiative Heating From Low-Level and High-Level Clouds

In this chapter, we further investigate research question 1: "How does CRH affect the dynamics of idealized extratropical cyclones?", and focus on the following sub-questions:

1. How strongly does CRH affect the intensity of extratropical cyclones?
2. What are the mechanisms that underlie the cloud-radiative impact?

In Ch. 4, we showed that CRH strengthens an idealized extratropical cyclone. This result is in contrast to the global simulations of Schäfer and Voigt (2018), who reported that CRH weakens idealized extratropical cyclones. Therefore, in this chapter, we investigate the impact of CRH on the dynamics of idealized cyclones using baroclinic life cycle simulations with the ICON model in the same global setup of Schäfer and Voigt (2018) and our new modeling approach to isolate the impact of CRH (Sect. 3.4). The simulation design is described in Sect. 5.1. The results are presented in Sect. 5.2 and summarized in Sect. 5.3. This chapter is based on Voigt et al. (2023). ©The Authors, CC BY 4.0 ©①

5.1 Simulation Design

As described in Sect. 3.3, we run idealized baroclinic life simulations in the global setup same as Schäfer and Voigt (2018). We run the simulations with two versions of ICON. The first version is ICON2.1.00 (hereafter ICON2.1). ICON2.1 differs from the model version 2.0.15 used in Schäfer and Voigt (2018) only in terms of minor technical changes and closely reproduces the results of Schäfer and Voigt (2018) (figures in the supplementary material of Voigt et al., 2023, not shown here). The German Weather Service DWD introduced version 2.0.15 as its operational forecast model in September 2016 (Zängle and Paul, 2016).

The second version is ICON2.6.2.2 (hereafter ICON2.6) which we used for idealized channel simulations in Ch. 4. ICON2.6 differs from ICON2.1 in the correction of a major model error in the physics-dynamics coupling (Rieger et al., 2021; Zängle, 2021). In ICON2.1, the heat capacity of air at constant pressure, c_p, is used to convert the turbulent heat flux into an atmospheric temperature tendency. However, because ICON is based on height levels, the conversion requires the heat capacity of air at constant volume, c_v. The error became known as the "$c_p/c_v = 1.4$ bug" and was fixed in ICON2.6. As described in Sect. 5.2, the error results in a warmer and moister boundary layer in ICON2.1 compared to ICON2.6, and strong differences in low-level clouds and cloud-radiative heating between the two model versions.
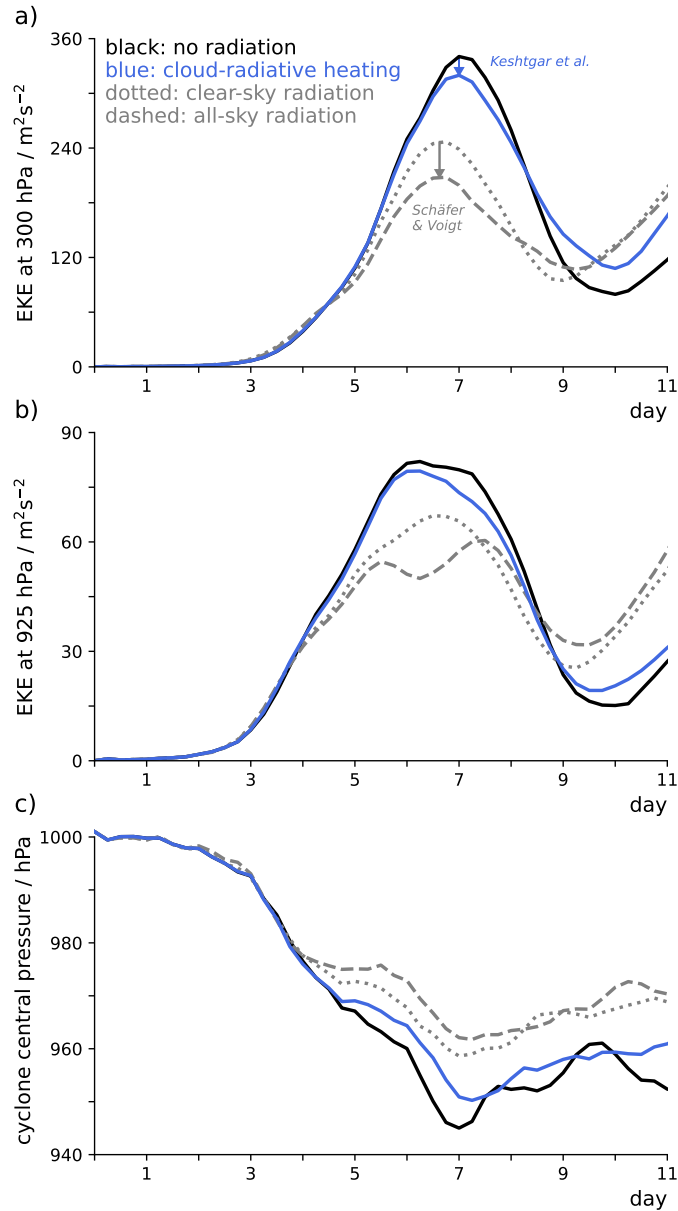
Figure 5.1: Time series of cyclone intensity metrics for different treatments of radiation in ICON2.1. Eddy kinetic energy (EKE) is averaged between 25 and 75°N, which covers the region where the cyclone is developing. The blue arrow shows the cloud-radiative impact diagnosed by the method of Keshtgar et al. (2023), and the gray arrow shows the impact diagnosed by the method of Schäfer and Voigt (2018). Note that the difference between the no-radiation and clear-sky simulations as well as the difference between the simulations with cloud-radiative heating and all-sky radiation provide an estimate of the impact of clear-sky radiative heating, which is not the topic of this study. Reprinted from Voigt et al. (2023). ©The Authors, CC BY 4.0 ⊚①

Schäfer and Voigt (2018) estimated the cloud-radiative impact from the difference between two simulations driven by all-sky and clear-sky radiation, respectively. We proposed an alternative method (Sect. 3.4) to estimate the cloud-radiative impact from the difference between a simulation with no radiation and a simulation in which cloud-radiative heating of the atmosphere is taken into account but

clear-sky radiative heating is not. This is achieved by passing the cloud-radiative heating to the dynamical core instead of the all-sky radiative heating. We used this method in Ch. 4.

Here, we focus on cyclone intensity, which we characterize in terms of eddy kinetic energy (EKE) and cyclone central pressure. EKE is defined with respect to the zonal-mean wind at a given time step. Cyclone central pressure is the minimum surface pressure within the cyclone region, where we first construct the mean cyclone by averaging over the six individual cyclones.

5.2 Results

We first show that the cloud-radiative impact on the cyclone is robust to the diagnostic method. For this purpose, we use the ICON2.1 simulations and compare the methods of Schäfer and Voigt (2018) and our new modeling approach (hereafter as Keshtgar et al. (2023) method) in Fig. 5.1. For the method of Keshtgar et al. (2023), the cyclone weakening is less pronounced in terms of EKE (Fig. 5.1a and b) but more pronounced in terms of cyclone core pressure (Fig. 5.1c). Despite these quantitative differences, both methods agree that cloud-radiative heating leads to a weaker cyclone.

Throughout the rest of the chapter, we will use the Keshtgar et al. (2023) method because it isolates the impact of cloud-radiative heating in a cleaner and easier to interpret way. In simulations using the method of Schäfer and Voigt (2018), the evolution of lower-level EKE changes from a single peak for clear-sky radiation to a double peak when cloud-radiative heating is included. This indicates qualitative changes in the dynamics of the cyclone that, while interesting, may complicate the interpretation of the cloud-radiative impact. This complication does not occur with the method of Keshtgar et al. (2023).

5.2.1 Conflicting Cloud-Radiative Impact in ICON2.1 and ICON2.6

The cloud-radiative impact is fundamentally different between ICON2.1 and ICON2.6, as shown in Fig. 5.2. While in ICON2.1 cloud-radiative heating leads to a weaker cyclone, in ICON2.6 the cyclone becomes stronger in terms of upper-level EKE when cloud-radiative heating is included (Fig. 5.2a). The EKE energy changes have the same sign throughout the troposphere (Fig. S5 in the supporting material of Voigt et al., 2023, not shown here). In ICON2.6 the cloud-radiative impact is close to zero in terms of lower-level EKE and cyclone central pressure (Fig. 5.2b and c). Further below, in Sect. 5.2.2, we will demonstrate that the conflict between the two model versions results from a robust tug-of-war between low-level and high-level clouds and model differences in the simulation of low-level clouds.

To put the cloud-radiative impact into perspective, we compare our results to previous simulations of moist baroclinic life cycles based on vertically integrated eddy kinetic energy (integrated over all model levels; Fig. S6 in the supporting material of Voigt et al., 2023, not shown here). Vertically integrated eddy kinetic energy decreases by 8% in ICON2.1 and increases by 5% in ICON2.6 due to cloud-radiative heating. While the impact of cloud-radiative heating is smaller than that of latent heating (Booth et al., 2013; Schäfer and Voigt, 2018), it is comparable to changes in the zonal wind strength by $10\,\mathrm{m\,s^{-1}}$, a

uniform warming by 6 K, or a change in the pole-to-equator temperature contrast by 10 K (Rantanen et al., 2019; Tierney et al., 2018).
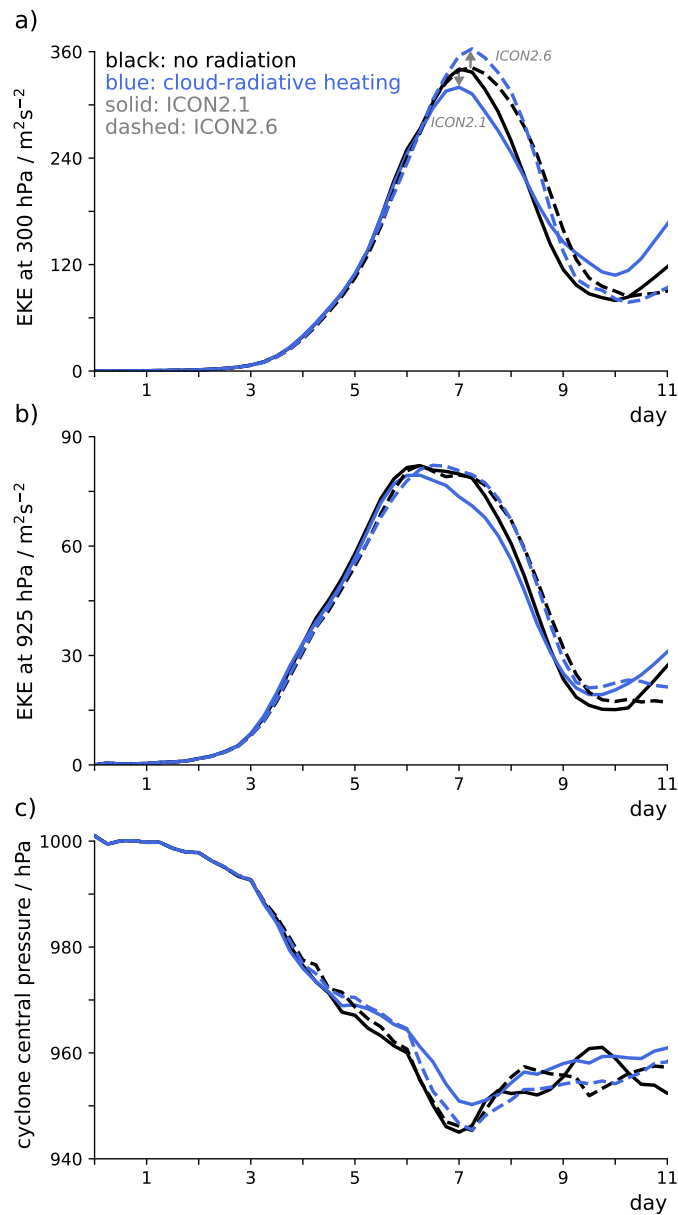

Figure 5.2: Cloud-radiative impact on the cyclone evolution in terms of (a) EKE at 300 hPa, (b) EKE at 925 hPa and (c) cyclone central pressure for ICON2.1 in solid lines and ICON2.6 in dashed lines. EKE is averaged between 25 and 75°N, which covers the region in which the cyclone develops. Reprinted from Voigt et al. (2023). ©The Authors, CC BY 4.0 ⓒⓘ

Remarkably, ICON2.1 and ICON2.6 simulate essentially the same cyclone when run without radiation. This can be seen from the time series of EKE and cyclone central pressure for the no-radiation simulations in Fig. 5.2 (black lines) and is further illustrated in Fig. 5.3. The two model versions show almost the same surface pressure pattern at day 6 (gray contours in Fig. 5.3a and b). However, they differ strongly in the cloud field that is associated with the cyclone (colored shading in Fig. 5.3a and b).

ICON2.1 simulates many more low-level clouds than ICON2.6, especially in the high-pressure region of the cyclone. Averaged over the cyclone domain from 25 to 75°N, the cloud liquid water content in the planetary boundary layer is two times higher in ICON2.1 (Fig. 5.3c), while cloud ice water content is very similar between the two model versions. The cyclones themselves, however, are not affected by the differences in boundary-layer temperature and moisture.
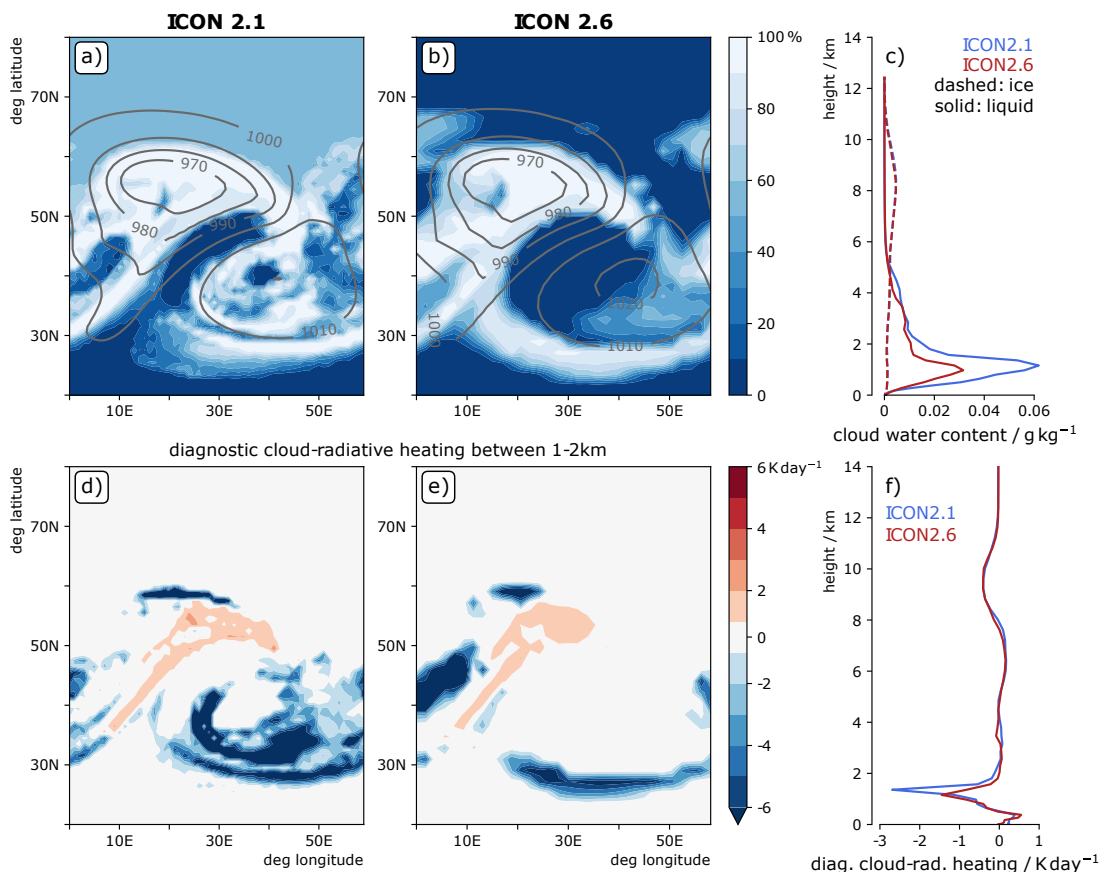

Figure 5.3: Comparison of clouds and diagnostic cloud-radiative heating in ICON2.1 and ICON2.6 for simulations without radiation on day 6. (a, b) Low-level cloud cover in percent is shown by the filled contours, surface pressure in hPa is shown by the gray contour lines. (c) Vertical distribution of cloud ice water content in dashed lines and cloud liquid water content in solid lines averaged between 25 and 75°N. (d, e) Boundary-layer diagnostic cloud-radiative heating in $K\,day^{-1}$. (f) Vertical distribution of diagnostic cloud-radiative heating averaged between 25 and 75°N. Reprinted from Voigt et al. (2023). ©The Authors, CC BY 4.0 ⓒⓘ

Panels d–f of Fig. 5.3 show the "diagnostic" cloud-radiative heating of the no-radiation cyclone. "Diagnostic" means that the cloud-radiative heating is calculated during the simulation but not given to the dynamical core of the model and hence does not affect the cyclone.

The strong differences in low-level clouds lead to very different diagnostic cloud-radiative heating in the lower troposphere. In both versions, the diagnostic heating near the top of the boundary layer is negative due to longwave radiative cooling from the tops of low-level clouds in the region of the surface high (Fig. 5.3d and e). However, because ICON2.1 simulates many more low-level clouds, the diagnostic cloud-radiative heating is twice as strong in ICON2.1 around 1.5 km altitude (Fig. 5.3f). In contrast,

the diagnostic cloud-radiative heating above the boundary layer is very similar between ICON2.1 and ICON2.6, consistent with the good agreement in cloud ice. The diagnostic cooling around 10 km is the result of longwave emission from the tops of high-level clouds that form as part of the warm conveyor belt of the cyclone (Fig. S7 in the supporting material of Voigt et al., 2023, not shown here).

The simulations with active cloud-radiative heating exhibit similar differences between ICON2.1 and ICON2.6 with respect to low-level clouds and cloud-radiative heating as the simulations without radiation. This implies that while cloud-radiation-circulation feedbacks might modify the cloud field, these feedbacks are not strong enough to override the principal differences between ICON2.1 and ICON2.6. This confirms that the diagnostic cloud-radiative heating of the no-radiation simulations is indeed useful for understanding the differences between the two model versions.

5.2.2 Tug-of-War

Figure 5.4a shows the cloud-radiative heating in the simulations with cloud-radiative heating, averaged over regions of upward motion between 40 and 60°N and between day 5 and day 6.5. Panel b shows the corresponding temperature change, and panel c the change in static stability. Static stability is calculated as the vertical gradient of potential temperature.
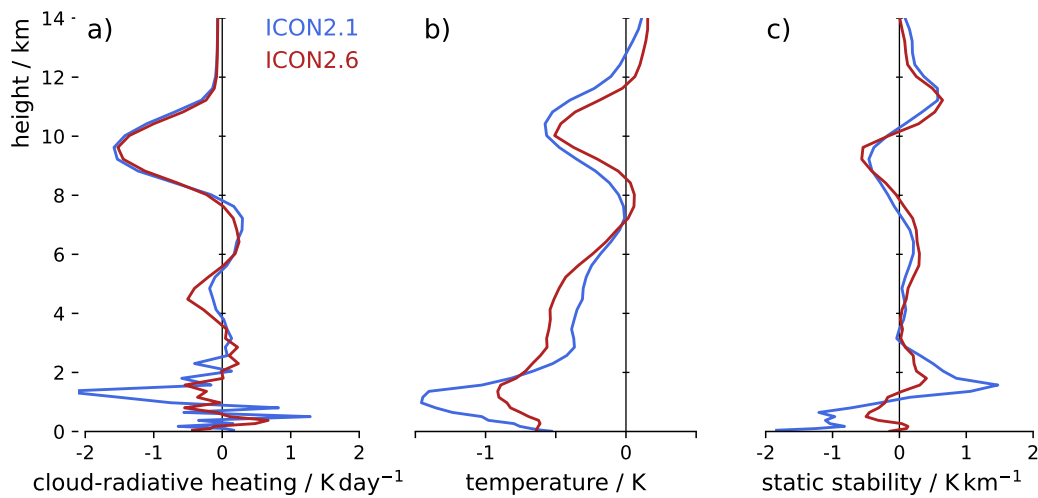

Figure 5.4: (a) Cloud-radiative heating in the simulations with active cloud-radiative heating. Panels (b) and (c) show the change in temperature and stability in simulations with cloud-radiative heating compared to simulations without radiation. All values are averaged between 40 and 6°N and day 5 and 6.5 over grid boxes with upward motion. The latter are sampled based on the pressure velocity at 5 km height. Reprinted from Voigt et al. (2023). ©The Authors, CC BY 4.0 ©①

The vertical pattern of cloud-radiative heating has two main components: radiative cooling of the upper part of the boundary layer between 1 and 2 km, and radiative cooling of the upper troposphere near 10 km. The two components result from the emission of longwave radiation from tops of low-level and high-level clouds, respectively. The vertical pattern of cloud-radiative heating leads to pronounced changes in temperature and stability in the boundary layer as well as the upper troposphere. This suggests

that cloud-radiative heating in the boundary layer and the upper troposphere might affect the cyclone in different ways.

We test this idea by performing additional simulations in which cloud-radiative heating is limited to either the boundary layer (below 2 km) or the free troposphere (above 2 km). The simulations allow us to separate the temperature and stability changes at lower and upper levels.
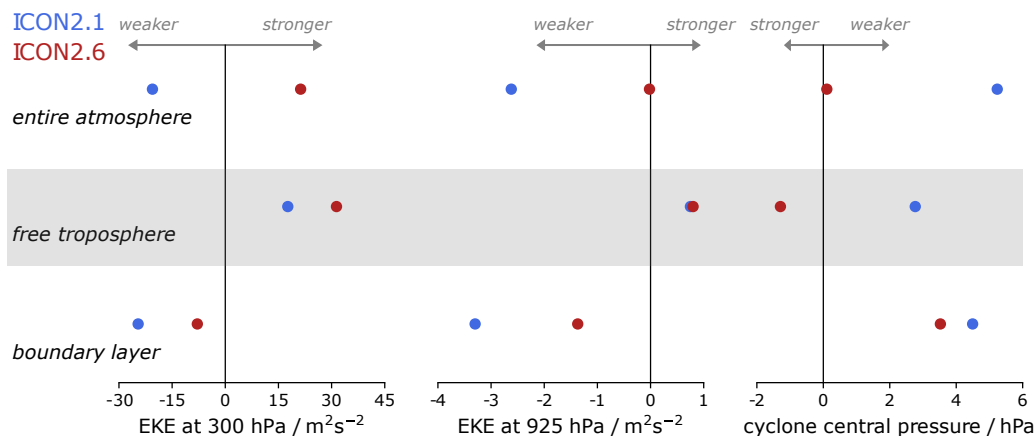

Figure 5.5: Changes in cyclone intensity due to cloud-radiative heating in the entire atmosphere (top row) and when cloud-radiative heating is limited to the free troposphere (above 2 km; middle row) and the boundary layer (below 2 km; bottom row). The change in cyclone intensity is characterized in terms of the maximum values of eddy kinetic energy (EKE) at 300 and 925 hPa and the minimum value of cyclone central pressure. EKE is averaged between 25 and 75°N. The change in cyclone intensity is calculated as the difference from the simulation without radiation. Reprinted from Voigt et al. (2023). ©The Authors, CC BY 4.0 ⓒⓘ

The simulations identify a robust tug-of-war between cloud-radiative heating in the free troposphere and the boundary layer (Fig. 5.5). When cloud-radiative heating is limited to the free troposphere, both ICON2.1 and ICON2.6 simulate a stronger cyclone in terms of EKE compared to the no-radiation setup. When only boundary-layer cloud-radiative heating is taken into account, the cyclone weakens in both model versions in terms of EKE and cyclone central pressure. Fig. 5.5 further shows that the near-zero cloud-radiative impact on lower-tropospheric EKE and cyclone central pressure in ICON2.6 results from the competing effects of cloud-radiative heating in the free troposphere and the boundary layer.

The tug-of-war also explains why cloud-radiative heating has a different impact on the cyclone in ICON2.1 and ICON2.6. In ICON2.1, the cloud-radiative impact is dominated by the weakening impact of low-level clouds. In contrast, because ICON2.6 simulates fewer low-level clouds, the cloud-radiative impact is dominated by the strengthening impact of high-level clouds.

5.2.3 Cloud-Radiative Impact on Static Stability

We now propose that the competing impacts of low-level and high-level cloud-radiative heating can be understood from changes in static stability. We start with the impact of low-level clouds and then discuss the impact of high-level clouds.

The low-level cloud-radiative cooling leads to an increase in static stability around the top of the boundary layer and a decrease below. This low-level dipole in the change of static stability is the expected response to a layer of cooling and leads to a corresponding dipole in PV (Figures S9 and S10, panels c, d, o and p in the supporting material of Voigt et al., 2023, not shown here). Based on Boutle et al. (2015), the PV increase near the top of the boundary layer is expected to weaken the coupling between the upper- and lower-levels within the cyclone and thereby reduce the growth rate of the cyclone. An additional and consistent perspective is provided by the Eady model, which predicts that increased static stability results in a weaker cyclone (Eady, 1949; Vallis, 2006).

5.3 Discussion and Conclusions

We perform global idealized baroclinic life cycle simulations to study the impact of CRH on extratropical cyclones using two versions of the ICON model that have been used in the past by the German Weather Service (DWD) for operational weather forecasting.

We show that CRH affects the dynamics and intensity of idealized extratropical cyclones. This result highlights that CRH affects the atmospheric circulation not only on long climatic timescales of years but also on short weather timescales of days to weeks.

We identify a tug-of-war between the radiative heating and cooling of low-level and high-level clouds. In line with Grise et al. (2019), we propose that changes in static stability are key to the cloud-radiative impact and the tug-of-war. Low-level clouds cool the top of the planetary boundary layer by emitting longwave radiation and create a dipole of static stability changes in the lower troposphere. Around the top of the boundary, the static stability increases, which weakens the interaction between the upper-level and lower-level waves and hence weakens the cyclone. High-level clouds also have a cooling effect at their cloud tops by emitting longwave radiation. Yet, the cooling occurs in the upper troposphere and hence decreases tropospheric stability in regions of ascent and sharpens the tropopause. The result is a stronger cyclone. The opposing effects of high-level and low-level clouds reconcile an apparent contradiction between Schäfer and Voigt (2018) and Grise et al. (2019), who concluded that cloud-radiative heating leads to weaker extratropical cyclones, and our result in Ch. 4, in which we found that extratropical cyclones become stronger due to cloud-radiative heating. The contradiction is explained as the result of differences in the simulation of low-level clouds.

Our work shows that the vertical distribution of cloud-radiative heating and cooling can affect idealized midlatitude cyclones. Future work should address how model biases and shortcomings in the representation of radiative heating from low-level and high-level clouds associated with cyclones (Bodas-Salcedo et al., 2014; Vergara-Temprado et al., 2018; Sullivan et al., 2023) might affect model representations of cyclones and storm tracks. In the following chapters, we assess the uncertainty in cloud-radiative heating in the extratropical atmosphere, and in Ch. 8 we study how uncertainties in cloud-radiative heating associated with radiation parameterization affect the dynamics of North Atlantic cyclones.

6 How Does Cloud-Radiative Heating over the North Atlantic Change with Model Resolution, Convective Parameterization, and Microphysics Scheme?

In this chapter, we address one aspect of research question 2: "How large are the CRH uncertainties in the extratropical atmosphere, and which uncertainties are relevant to the dynamics of extratropical cyclones?". In particular, we address the following question:

1. How does CRH change with model settings over the North Atlantic?

To this end, we investigate how the model simulation of CRH depends on the representation of clouds due to different model resolutions, microphysics, and convection schemes. The simulation design is described in Sect. 6.1, and results are presented in Sect. 6.2. The chapter closes with the discussion and conclusions in Sect. 6.3. This chapter is based on Sullivan et al. (2023). ©The Authors, CC BY 4.0 ©①

6.1 Simulation Design

As described in Sect. 3.5, hindcast simulations are performed with ICON during the North Atlantic Waveguide and Downstream Impact Experiment (NAWDEX) field campaign, specifically September 21-25 and 30, 2016, October 1-5, 2016, and October 14-16, 2016. Six different horizontal grid resolutions of 80, 40, 20, 10, 5, and 2.5 km were used to cover the range from typical coarse-resolution global climate models to storm-resolving models.

For the simulations at 2.5 km resolution, the deep-convection scheme or both the deep- and shallow-convection schemes are switched off in order to investigate the impact of explicit treatment of convection. The impact of cloud microphysics is explored by switching between the one-moment microphysics of Doms et al. (2011) used in the operational simulations and the more sophisticated and computationally expensive two-moment microphysics of Seifert and Beheng (2006).

In the discussion below, the simulation with a resolution of x km is sometimes referred to simply as the x km simulation. We filter out grid points corresponding to land and sea ice from the NAWDEX domain in our results below, focusing only on cloud fields over the ocean to remove differences due to surface albedo, surface temperature, or varying amounts of predicted sea ice. In addition, we compare cloud-radiative heating from the ICON simulations to those from CloudSat-CALIPSO, ERA5 reanalysis, and coarse-resolution AMIP-like simulations, as described in Sect. 3.5.

6.2 Results

In this section, we first establish the climatological representativeness of the simulated CRH and present its dependence on model settings. We investigate whether these dependencies are due to differences in the frequency of certain cloud classes, or whether the clouds in these classes have different properties. We then trace the changes in cloud class occurrence and condensate back to cloud-controlling factors.

6.2.1 Climatological Cloud-Radiative Heating in the North Atlantic

CRH profiles averaged over open ocean in the NAWDEX domain from three global climate model simulations provide a first estimate of variability in North Atlantic climatological CRH (Fig. 6.1). The most prominent intermodel differences are in the lowermost ($p \geq 800$ hPa) and uppermost ($p \leq 300$ hPa) troposphere. The atmospheric component of the IPS-CM5A model predicts by far the largest cloud-radiative cooling in the boundary layer and upper troposphere (maxima of -2.2 K day^{-1} and -1.1 K day^{-1}, respectively). These atmospheric coolings are more than 5 times the magnitude of those produced by the MPI-ESM model, while the CRH in ICON falls in between with larger boundary-layer cooling than MPI-ESM but smaller upper-tropospheric cooling. The altitudes of cloud-radiative cooling maxima also vary by about 80 hPa between the models in both the lower and upper troposphere. CRH profiles averaged over all longitudes between 23°N and 80°N mirror those over the NAWDEX domain, meaning that this midlatitude variability is not concentrated only over the North Atlantic. We also note that, on the basis of the ICON simulations, September and October are representative months for the annually averaged North Atlantic CRH (ICON full year versus ICON September–October).
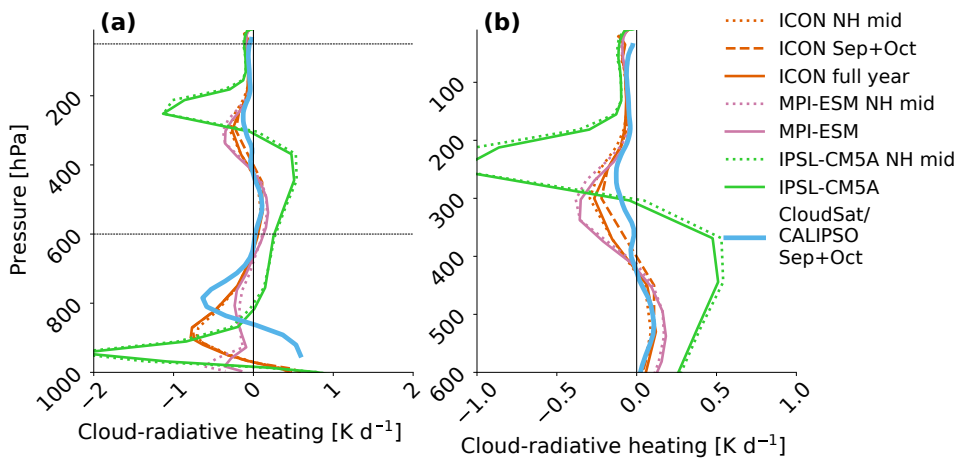

Figure 6.1: Full (a) and upper-tropospheric (b) CRH profiles averaged over the NAWDEX domain (23°N to 80°N and 78°W to 40°E) from the atmospheric components of the MPI-ESM, IPSL-CM5A, and ICON version 2.1.00 models, all with approximately 150 km horizontal resolution. The means between 23°N and 80°N over all longitudes for the three models are shown in the dotted traces denoted NH mid for Northern Hemisphere mid-latitudes. ICON profiles for both the full year and for only September and October (Sep+Oct in the dashed trace) are shown. The dashed black lines in panel (a) indicate the subset of pressures shown in panel (b). Reprinted from Sullivan et al. (2023). ©The Authors, CC BY 4.0 ⓒⓘ

The circulation effects of the differing CRH in these AMIP-like simulations have been discussed by Voigt et al. (2019); their +4 K simulations show that particularly large CRH differences with warming are concentrated in the upper troposphere. The increase of upper-tropospheric CRH with surface warming results in larger meridional temperature gradients and a poleward expansion of the Hadley cell and extratropical jets. Clear-sky radiative cooling by water vapor provides a strong constraint for upper-tropospheric cloud fraction and cloud top temperature globally (Thompson et al., 2017, 2019). This clear-sky constraint means that, if we can reliably construct the current-day upper-tropospheric CRH, we can also infer what its profile looks like under global warming. We emphasize that radiative cooling from extratropical low-level clouds has non-negligible effects on circulation, for example enhancing baroclinicity (Li et al., 2015). However, given the strong dependence of both current and future circulation on upper-tropospheric CRH, we choose to focus on the model dependencies above 5 km going forward.

We next examine the relative contribution of upper-tropospheric CRH to the total, time mean, spatial mean heating rate within our NAWDEX simulations (Fig. 6.2). This heating rate climatology for the North Atlantic is constructed from the simulations with the coarsest resolution (80 km) and includes the longwave and shortwave cloudy and clear-sky radiative heating rates, as well as dynamic, turbulent, convective, and microphysical heating rates:

$$\frac{\partial T}{\partial t} = \left(\frac{\partial T}{\partial t}\right)_{\text{CRH}} + \left(\frac{\partial T}{\partial t}\right)_{\text{Clr Sky}} + \left(\frac{\partial T}{\partial t}\right)_{\text{Dyn}} + \left(\frac{\partial T}{\partial t}\right)_{\text{Turb}} + \left(\frac{\partial T}{\partial t}\right)_{\text{Conv}} + \left(\frac{\partial T}{\partial t}\right)_{\text{Mphy}}, \quad (6.1)$$

where the largest component comes from clear-sky longwave radiative cooling (LW Clr Sky) followed by the dynamic heating (Dyn) and clear-sky shortwave radiative heating (SW Clr Sky). Thereafter, from about 9 up to 11 km, the microphysical heating and longwave cloud-radiative cooling are largest, with the latter contributing 14% to the overall budget. The three smallest components of the budget are convective heating, shortwave cloud-radiative heating, and turbulent heating at these altitudes.

The hierarchy and values of the heating rates are independent of whether we use a one- or two-moment microphysics scheme (Fig. 6.2a versus b). The longwave cloud-radiative heating profiles do differ qualitatively, however, in whether they exhibit an inflection point. While the longwave cloud component changes from cooling to heating around 7 km in the one-moment setup, it is exclusively cooling at the upper altitudes in the two-moment setup. These heating rates indicate that cloud-radiative heating, especially its longwave component, is non-negligible in the North Atlantic upper troposphere.

We first construct net CRH profiles from our NAWDEX simulations across six horizontal resolutions, with shallow convective parameterization only and explicit convection in the 2.5 km simulation and using two different microphysics schemes (Fig. 6.3). Resolution dependence is subtle. Simulations with coarser resolution exhibit larger-magnitude upper-tropospheric CRH, but profiles fall within 1 standard deviation of the 80 km profile over most of the upper troposphere. The CRH changes qualitatively with

the microphysics scheme from an S shape in the one-moment scheme (as in the AMIP-like profiles of
Fig. 6.1b) to a uniformly cooling profile in the two-moment scheme.
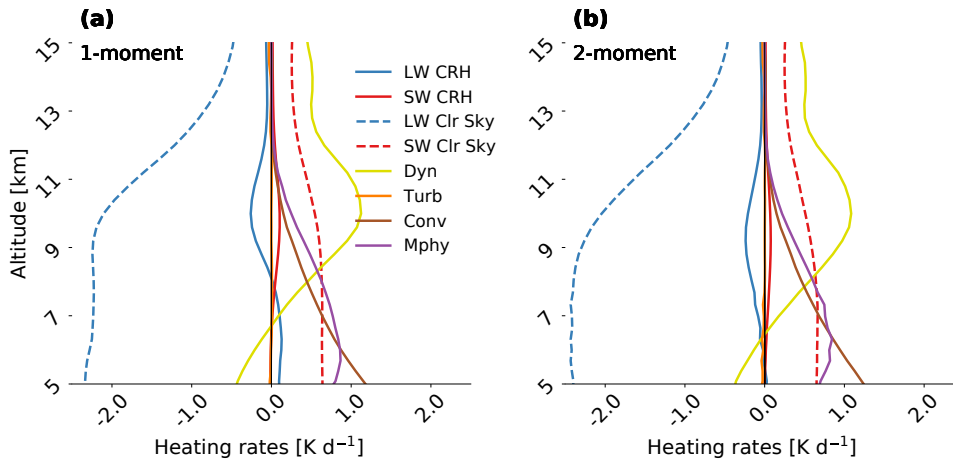

Figure 6.2: Spatial mean and time mean vertical profiles of heating-rate components at 80 km resolution in the
one- (a) and two-moment (b) microphysics schemes. LW CRH is longwave cloud-radiative heating, SW CRH is
shortwave cloud-radiative heating, LW Clr Sky is longwave clear-sky heating, SW Clr Sky is shortwave clear-sky
heating, Dyn is dynamics, Turb is turbulence, Conv is convection, and Mphy is latent heating from microphysics
and saturation adjustment. Reprinted from Sullivan et al. (2023). ©The Authors, CC BY 4.0 ⓒⓘ
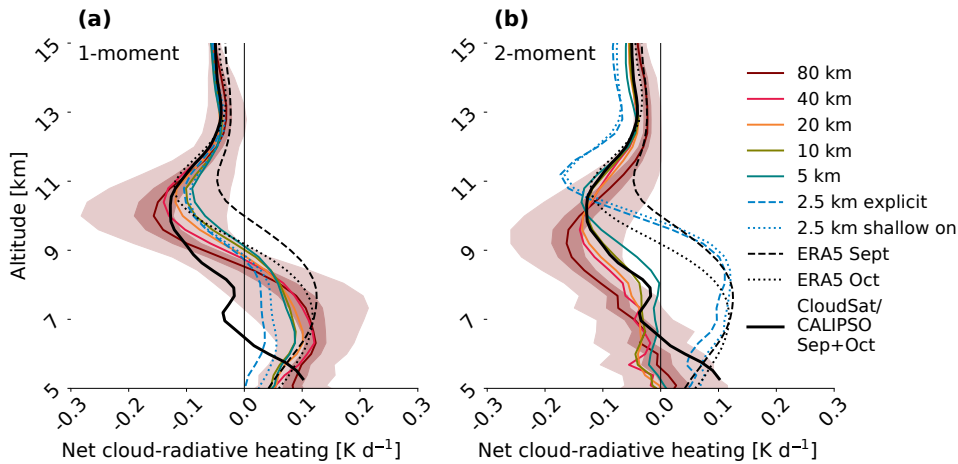
Figure 6.3: Upper-tropospheric, time mean, and area mean net cloud-radiative heating from the ICON NAWDEX
simulations at grid resolutions from 2.5 up to 80 km with a one- (a) and two-moment (b) microphysics scheme. The
2.5 km simulations either use only the shallow convection parameterization (shallow on) or explicitly represent
both shallow and deep convection (explicit). The standard deviation and standard error over daily means are
depicted as light- and dark-red shades atop the 80 km profile. Profiles from the ERA5 reanalysis in September
(dashed black) and October (dotted black), as well as the CloudSat-CALIPSO 2B-FLXHR-LIDAR product (solid
black), are also included. Reprinted from Sullivan et al. (2023). ©The Authors, CC BY 4.0 ⓒⓘ

The most dramatic change occurs in turning off the deep convective parameterization in the two-
moment microphysics simulations (Fig. 6.3). Omitting the deep convective parameterization in the
2.5 km simulations shifts the upper-tropospheric cooling peak upward by 2 km and narrows its vertical
depth relative to the other simulations. The explicit representation of convection also produces prominent

heating below 9 km, not present in the other two-moment simulations. Although these results are for the full simulation length in Fig. 6.3, they are robust for shorter durations down to a single day (Fig. S2 in the supplementary material of Sullivan et al., 2023, not shown here).

Decomposing the net CRH into its longwave and shortwave components, we find that model dependencies are not isolated within a single component (Fig. 6.4). Both the longwave and shortwave CRH change more strongly with microphysics and convective scheme than with resolution. Interestingly, while the magnitude of longwave cooling increases at coarser resolution, that of shortwave heating decreases. Because longwave cooling is about twice as large as shortwave heating, it dominates the net CRH dependence. The larger spread on the longwave profiles also shows that this component drives more of the CRH variability across days.
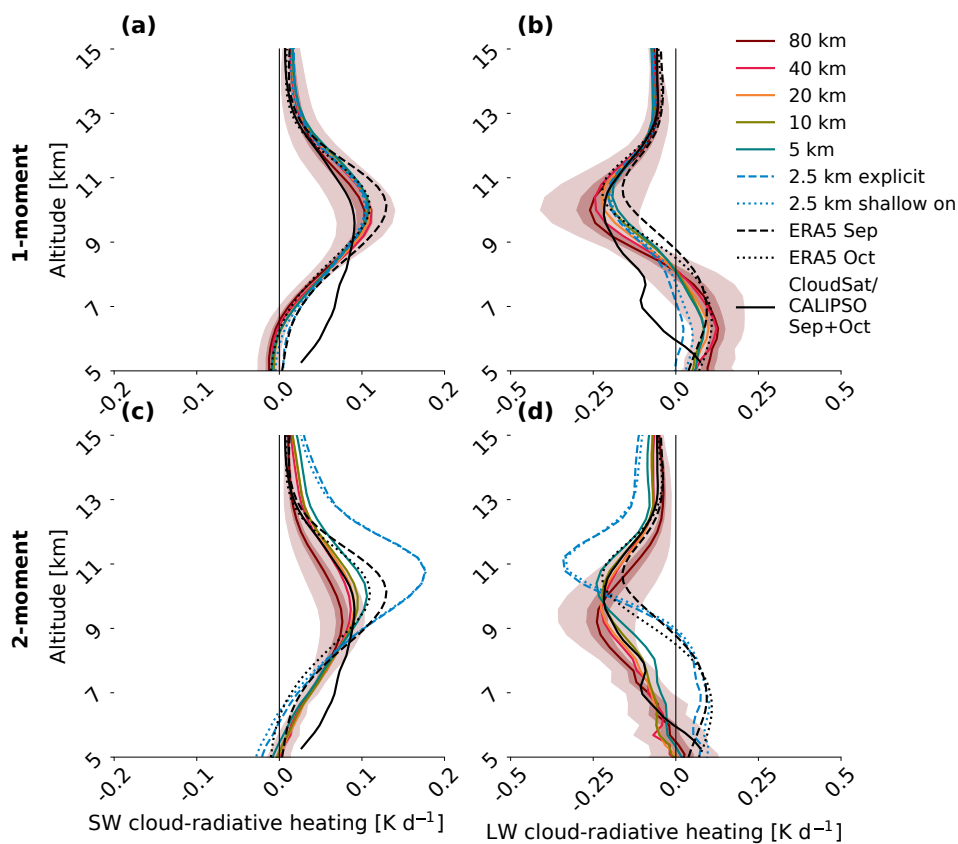
Figure 6.4: Upper-tropospheric, time mean, area mean shortwave (a, c) and longwave (b, d) cloud-radiative heating with all model settings as in Fig. 6.3. One- (a, b) and two-moment (c, d) microphysics schemes are shown, as well as profiles from the ERA5 reanalysis in September (dashed black) and October (dotted black) and the CloudSat-CALIPSO 2B-FLXHR-LIDAR product (solid black). Note the different x-axis limits on the (a, c) versus (b, d). Reprinted from Sullivan et al. (2023). ©The Authors, CC BY 4.0 ⓒⓘ

Atop the simulated CRH values - both net and decomposed into their longwave and shortwave components we overlay both ERA5 reanalysis values and a CloudSat-CALIPSO climatology over the NAWDEX domain during September and October. ERA5 assimilates observed radiances but still makes cloud microphysical assumptions within its radiative transfer calculations along the lines of a one-moment scheme

in which only cloud liquid and ice mass mixing ratios are tracked (e.g., Tiedtke, 1993; Forbes and Tompkins, 2011). The CloudSat-CALIPSO product (2B-FLXHR-LIDAR) incorporates cloud microphysical measurements into its calculation (Sect. 3.5). The ERA5 and CloudSat-CALIPSO profiles differ strongly from one another and from the simulations. The ERA5 profile has a muted version of the S shape from the one-moment simulations, whereas the CloudSat-CALIPSO profile shows uniform upper-tropospheric cooling by clouds as in the two-moment simulations.

Taking CloudSat-CALIPSO as our baseline, simulations with moderate resolution (10- or 20 km) and the two-moment microphysics compare most favorably. Using instead the ERA5 reanalysis as our baseline gives an indication of CRH with the cloud environment but not microphysics observationally constrained, and in this case, our simulations with the finest resolution (2.5 km) and two-moment microphysics compare most favorably. None of the one-moment profiles mirror the CloudSat-CALIPSO or ERA5 profiles especially well. The messy state of this evaluation highlights the following difficulty: cloud-radiative heating is not directly observed, even from satellites, and associated radiative transfer or microphysical assumptions complicate any model-measurement comparison.

6.2.2 Cloud Class Decomposition

We turn next to understanding the strong convective and microphysical scheme dependency in the upper-tropospheric CRH by breaking it down into that associated with various cloud classes. Such a decomposition allows us to determine whether CRH differences are due to variations in heating associated with a particular cloud class or variations in the probability of occurrence associated with a particular cloud class. Stated mathematically, the total CRH is the summation, over all clouds classes i, of the heating associated with a given cloud class weighted by its frequency of occurrence (f_i below):

$$\text{CRH} = \sum_i \text{CRH}_i \, f_i. \tag{6.2}$$

As detailed in Sect. 3.5, eight cloud classes are defined on the basis of cloud cover in three altitudinal ranges. Upper-tropospheric CRH is driven primarily by four of these eight cloud classes: isolated high clouds, continuous high-x-middle clouds, layered high-low clouds, and deep high-x-middle-x-low clouds (blue box in Fig. 3.7). Physically, isolated high clouds correspond to either dissipating anvil outflow cirrus or cirrus formed in situ. High-x-middle-x-low clouds represent forms of midlatitude deep convection, such as cyclones. The profiles associated with the low, middle, middle-x-low, and clear-sky regions are generally omitted, as these contribute negligibly to the CRH between 5 and 15 km (not shown).

Box plots of area-weighted occurrence frequency show negligible resolution dependence for all cloud classes (Fig. 6.5). For the classes including high clouds that are influential for upper-tropospheric CRH, the mean occurrence changes by less than 2% between the simulations with 80 and 2.5 km resolutions. Otherwise, these box plots indicate that low clouds are the most frequent, with a mean occurrence of around 30%, followed by deep clouds (H-x-M-x-L) and clear sky, both with mean occurrences of roughly

17%. Isolated middle clouds are least common, followed by high-x-middle clouds, occurring at an average of 2% and 3% of the time, respectively. Isolated high clouds also occur less frequently in this region, with only 6% coverage on average.
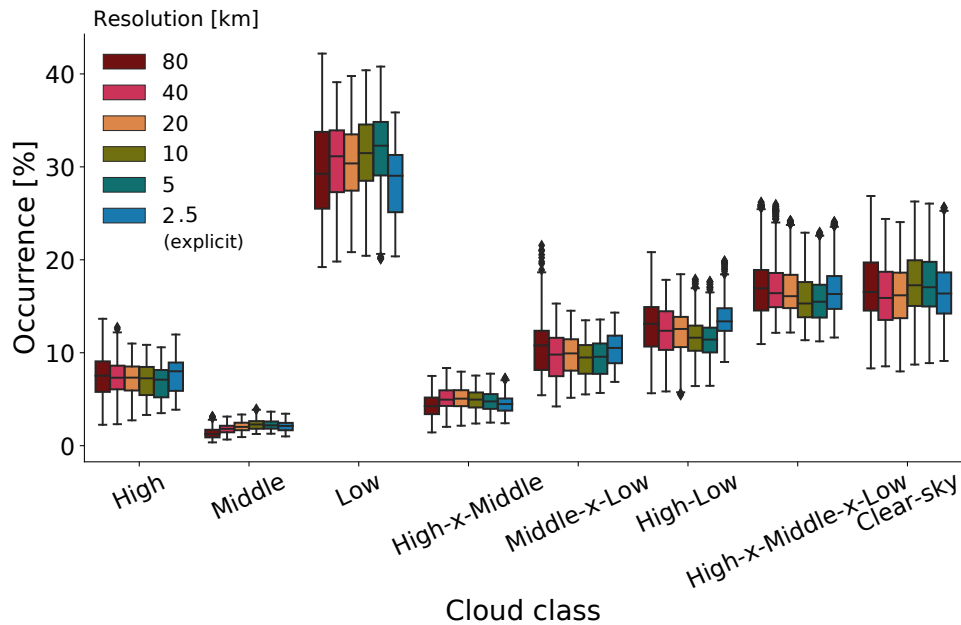

Figure 6.5: Area-weighted occurrence frequency for eight cloud classes across resolutions for the simulations with two-moment microphysics. The box shows 25th (Q1), 50th (Q2), and 75th (Q3) percentiles. The whiskers show 1.5 times the interquartile range below the first quartile up to 1.5 times the interquartile range above the third quartile, i.e., [Q1 - 1.5(Q3 - Q1), Q3 + 1.5(Q3 - Q1)]. Diamonds indicate outliers. Fig. S3 in the supplementary material of Sullivan et al. (2023) (not shown here) is the same plot for the one-moment microphysics. Thresholds of the 62nd, 67th, and 30rd percentiles of the cloud fraction distribution are used for high, middle, and low clouds, but mean occurrence is not sensitive to these thresholds (Fig. S1 in the supplementary material of Sullivan et al., 2023, not shown here). The 2.5 km simulation uses neither a deep nor shallow convective parameterization (explicit). The sum of occurrence over all classes equals 1, and the sum over all classes except clear sky equals mean cloud fraction. Reprinted from Sullivan et al. (2023). ©The Authors, CC BY 4.0 (cc)(i)

While the occurrence probabilities do not reflect the model dependencies of the net CRH, the cloud-class-filtered CRH does (Fig. 6.6). The isolated high clouds (high or high-low) uniformly radiatively heat the upper troposphere between 5 and 15 km, whereas deeper clouds (high-x-middle or high-x-middle-x-low) radiatively cool above about 8 km. Isolated high clouds absorb more outgoing longwave radiation (OLR) than clear sky, whereas deep clouds absorb this OLR in the liquid cloud at lower altitudes and re-emit it at colder temperatures from their cloud tops. For the isolated clouds, heating intensifies with finer resolution and especially with turning off the convective parameterization with the two-moment scheme. In contrast, for the deeper clouds, cooling moderates with finer resolution. But again, the largest change in the radiative-heating profile comes from turning off the convective parameterization with the two-moment scheme.

Having looked at both f_i and CRH_i from Eq. 6.2, we conclude that the latter factor drives the overall CRH dependencies. In other words, different model settings do not change the distribution of occur-

rence of various cloud classes; they only change the CRH profiles associated with these cloud classes. Additionally, these changes are not limited to a single cloud class but rather appear across all of those containing high clouds.
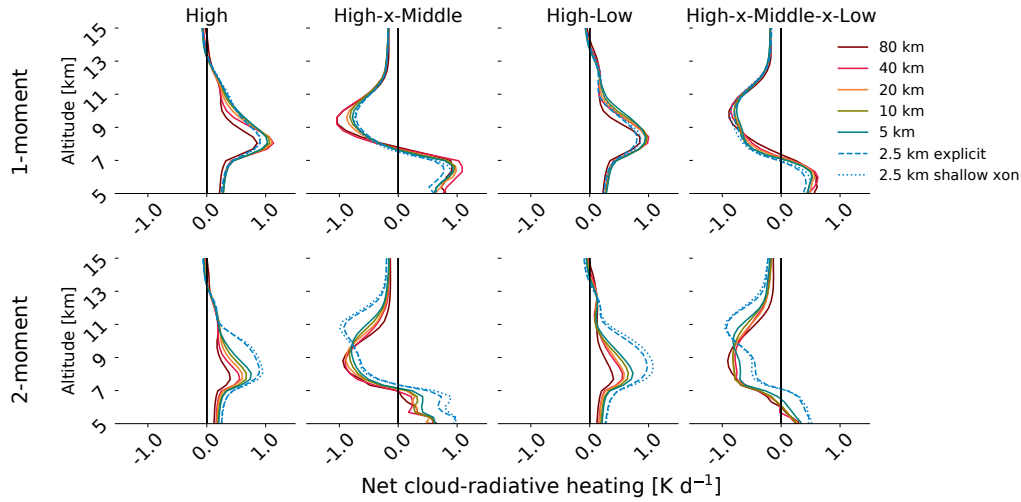

Figure 6.6: Upper-tropospheric, time mean, area mean net cloud-radiative heating for four of the eight cloud classes with all model settings as in Fig. 6.3. Reprinted from Sullivan et al. (2023). ©The Authors, CC BY 4.0 ⓒⓘ

6.2.3 Cloud Properties by Class

We have ruled out varying occurrences of different cloud classes and now turn to cloud properties – overall and within the cloud classes – as an explanation for the model dependencies of CRH. An increased magnitude of time mean and area mean cloud-radiative cooling or heating can be due either to a larger amount of condensate in the cloud, a greater coverage of the clouds, or both. We examine cloud liquid water (q_c), cloud fraction, and cloud ice mass mixing ratios (q_i) for the various simulation settings in Fig. 6.7. q_c increases slightly with finer resolution in the two-moment scheme; however, its values are insufficient to drive the model dependencies in CRH (Fig. 6.7d).

Differences in cloud fraction qualitatively mirror those in CRH for the one-moment scheme (Fig. 6.7b); specifically, cloud fraction peaks at a lower altitude and has a larger maximum in the simulations with coarser resolution, as does the cooling in its net CRH profiles. The correspondence of cloud fraction and net CRH dependence is weaker in the two-moment simulations (Fig. 6.7e). Cloud fraction is about 2% larger for the 2.5 km simulations, but otherwise there is no consistent trend with resolution or the altitude of maximum cloud fraction. This weak dependence of cloud fraction on model setting appears across the classes with high clouds (Fig. S4 in the supplementary material of Sullivan et al., 2023, not shown here).

The primary driving factor of the large CRH changes with two-moment microphysics and explicit convection is then q_i (Fig. 6.7f). The amount of cloud ice quadruples from about $5 \, \text{mg kg}^{-1}$ in the 80 km simulation to about 19 mg kg^{-1} in the two 2.5 km simulations (without shallow or any convective parameterization). The one-moment simulations show no such change in q_i with model settings (Fig. 6.7c).

As in Sect. 6.2.2, we can decompose these q_i differences into those associated with various cloud classes. Figure 6.8 illustrates that the q_i increases with resolution are somewhat larger for the deeper cloud layers - the high-x-middle and high-x-middle-x-low classes - than for the isolated high clouds but occur qualitatively across all the classes with high clouds. Likewise, the lack of resolution and convection dependence in q_i for the one-moment schemes is uniform across classes; there are no compensating differences in q_i.
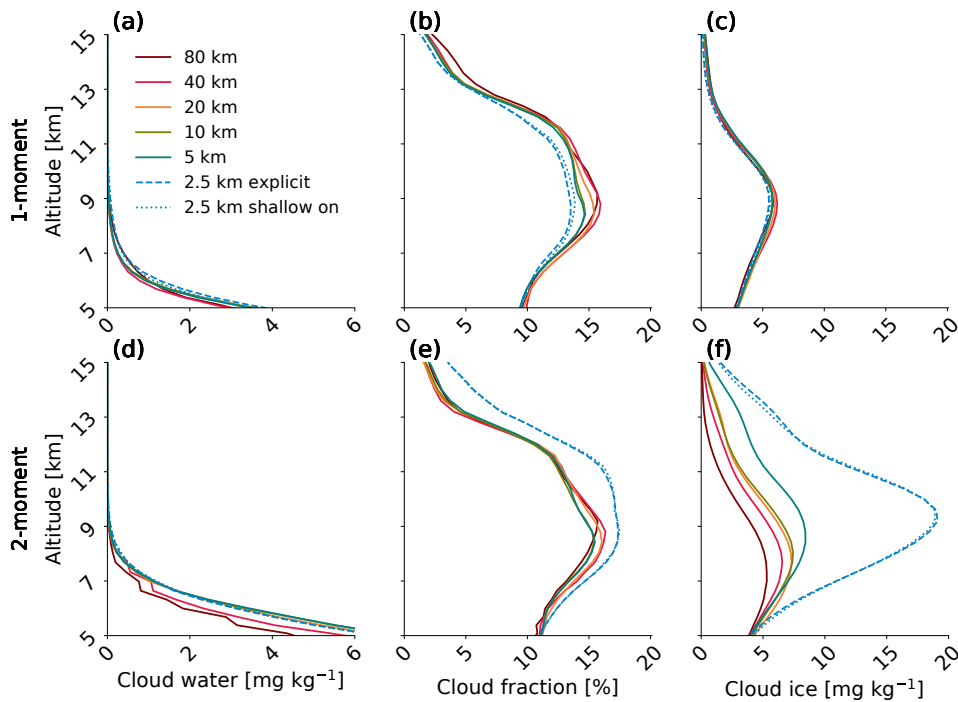
Figure 6.7: Upper-tropospheric, time mean, and area mean profiles of cloud water mass mixing ratio (panels a and d), cloud fraction (panels b and e), and cloud ice mass mixing ratio (panels c and f) for the one- (a-c) and two-moment (d-f) microphysics simulations, with all model settings as in Fig. 6.3. Reprinted from Sullivan et al. (2023). ©The Authors, CC BY 4.0 ⓒⓘ

    The model uses only condensate mass to calculate CRH. However, CRH is also physically determined by hydrometeor number, and we examine cloud ice crystal numbers (N_i) from our simulations to understand how their omission may affect CRH. N_i profiles parallel q_i ones for the two-moment microphysics simulations (Fig. 6.9, top panels). The runs without a deep convective parameterization produce more than 4 times as many ice crystals as those with a convective parameterization. Not only is more ice mass produced in the clouds, it is also distributed over many more hydrometeors. In physically accurate frameworks, larger N_i should promote multiple scattering and eventual absorption of solar radiation, enhancing the shortwave heating peak (Fig. 6.4c). Distribution of ice mass over many more crystals could also prolong cloud lifetime and enhance CRH. Our simulations permit such a cloud lifetime effect insofar as it is independent of CRH, but the cloud occurrence and cloud fraction results above indicate that it is not dominant.
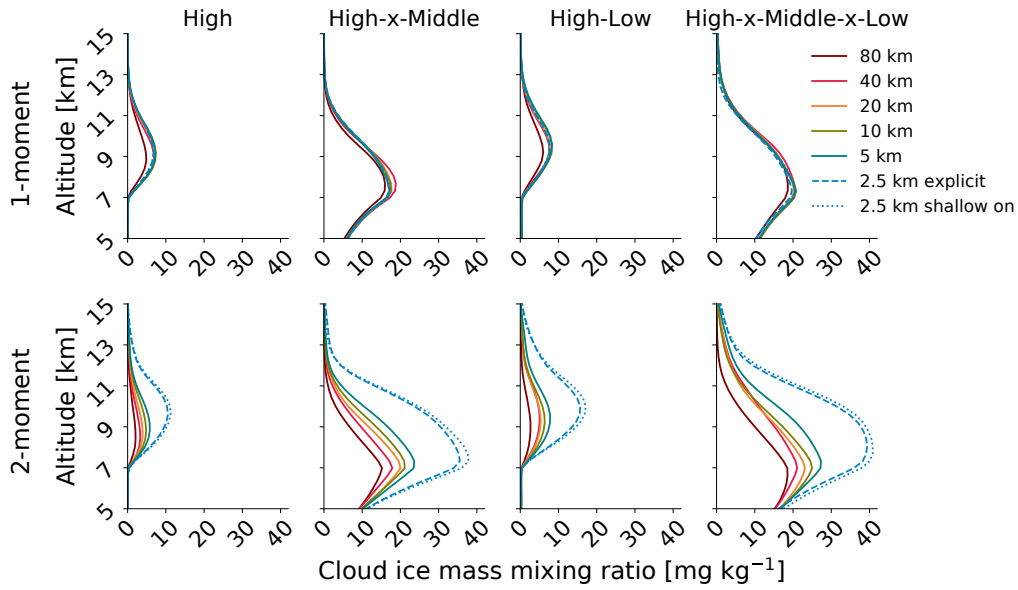
Figure 6.8: Diagnostic ice mass mixing ratios from one- (top panels) and two-moment (bottom panels) simulations for the four cloud classes that include high clouds with all model settings, as in Fig. 6.3. Reprinted from Sullivan et al. (2023). ©The Authors, CC BY 4.0 ⓒ①
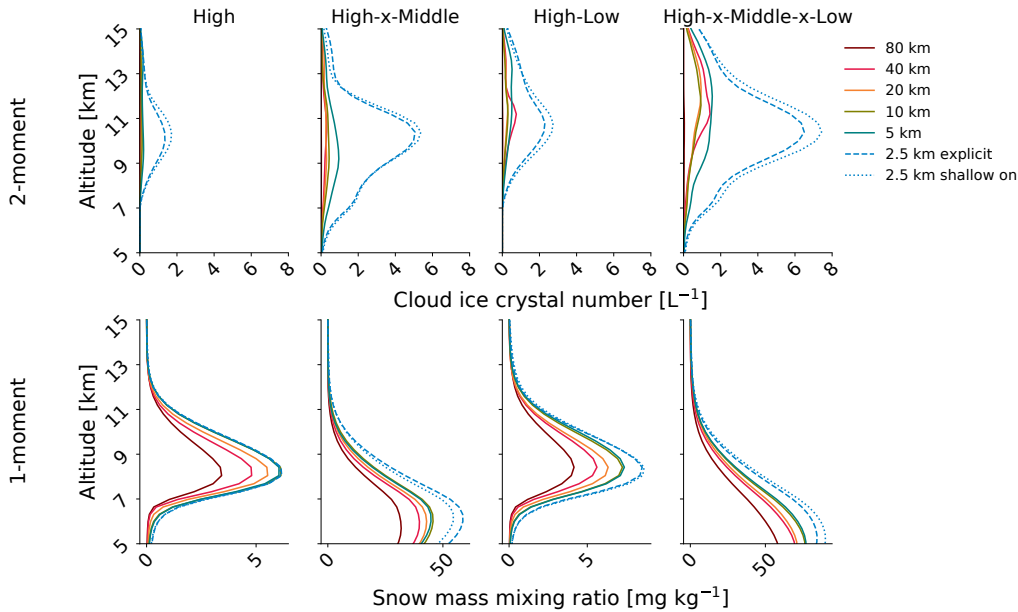

Figure 6.9: Cloud ice crystal number from the two-moment simulations (top panels) and snow mass mixing ratios from the one-moment simulations (bottom panels) for the four cloud classes that include high clouds with all model settings, as in Fig. 6.3. Reprinted from Sullivan et al. (2023). ©The Authors, CC BY 4.0 ⓒ①

Along with liquid and ice crystals, upper-tropospheric clouds may also contain snow (q_s) and graupel (q_g). Whereas q_i showed no model dependency for the one-moment simulations, the maximum in q_s changes almost 2-fold from the 80 km simulation down to the 2.5 km one without convective parameterization (Fig. 6.9, bottom). This monotonic increase in q_s appears for all cloud classes with the largest-

magnitude changes from deep clouds in the one-moment scheme. Similarly, the q_g maximum changes by 1 order of magnitude across these model settings between 5 and 15 km (Fig. S5 in the supplementary material of Sullivan et al., 2023, not shown here). It is important to note that snow and graupel do not interact with the radiative transfer scheme in ICON. This exclusion of certain hydrometeors from the radiation scheme is motivated in part by size and in part by lack of a corresponding fractional coverage variable (e.g., Xu and Randall, 1995). Graupel will tend to sediment out more rapidly than the time step used to call the radiation scheme, whereas the fractional coverage of snow, distinct from the liquid or ice cloud fraction, is not a tracked variable. We can therefore conclude that resolution dependence for the one-moment microphysics is concentrated in radiatively inactive cloud species.

6.2.4 Understanding Cloud Property Differences

As a final step, we ask why the high, high-x-middle, high-low, and high-x-middle-x-low clouds produce more ice and have slightly higher coverage in the two-moment simulations. We have advocated in the work on tropical cloud-radiative heating for process decomposition as a means of unraveling such differences (Sullivan and Voigt, 2021; Sullivan et al., 2022). This process decomposition can be done in a number of ways. Processes can be classified based upon the temperature range in which they are active to generate an altitudinally stratified recipe for CRH (Sullivan and Voigt, 2021). Processes can also be organized based upon when they occur within the cloud lifecycle to produce a temporally stratified recipe for CRH (Sullivan et al., 2022).

Here, processes are categorized as sources versus sinks of cloud ice. Then q_i variations are understood either in terms of differences in the source-sink formulations or in terms of differences in the inputs to these formulations:

$$(q_i, N_i) = \phi(\text{CPs}, \text{CCFs}) - \psi(\text{CPs}, \text{CCFs}), \tag{6.3}$$

where ϕ and ψ represent microphysical sources and sinks, respectively; CP denotes a cloud parameter like the deposition density of ice crystals; and CCF denotes cloud-controlling factors, a term for the environmental conditions that determine cloud properties (e.g., Stevens and Brenguier, 2009).

Within the two ice microphysics schemes in ICON, ice mass can be consumed by autoconversion, melting, and sedimentation. Because q_c differences are so much smaller than those in q_i, we focus on sink processes that do not involve the liquid phase, namely autoconversion and sedimentation. Ice mass can also be generated by nucleation, droplet freezing, depositional growth, and riming. Somewhat larger cloud water mixing ratios at finer resolution in the two-moment simulations may contribute to slightly stronger riming and droplet-freezing tendencies (Fig. 6.7). However, these processes cannot be the primary driver for the q_i differences of much larger magnitude. We focus instead on nucleation and growth sources.

Cloud Ice Sources and Sinks

Autoconversion is the process of converting between ice and snow, with its rate S_{auc} represented as follows in the two microphysics schemes:

$$S_{\text{auc, 1M}} = (10^3 \, s^{-1})(q_i - q_{i,0}), \tag{6.4}$$

$$S_{\text{auc, 2M}} = E_{ii} N_i q_i G(\delta_i, \theta_i), \tag{6.5}$$

where $q_{i,0}$ is a threshold ice mass mixing ratio before autoconversion initiates, set to 0 in the one-moment scheme; E_{ii} is the ice-ice collision efficiency; and G is a function of δ_i and θ_i, non-dimensional combinations of gamma distribution parameters representing the ice crystal sizes. The one-moment formulation simply transfers ice to snow over a fixed time constant. This sink is then much stronger than in the two-moment formulation, which incorporates dependence on the crystal numbers and relative sizes.

Snow and ice settle at the following terminal velocities in the one- and two-moment schemes:

$$v_{Ts,1M} = (7.37 \, \text{m s}^{-1} \, \text{kg}^{-0.125}) \, m_s^{0.125}, \tag{6.6}$$

$$v_{Ts,2M} = (8.156 \, \text{m s}^{-1} \, \text{kg}^{-0.526}) \, m_s^{0.526}, \tag{6.7}$$

$$v_{Ti,2M} = (317 \, \text{m s}^{-1} \, \text{kg}^{-0.363}) \, m_i^{0.363}, \tag{6.8}$$

where m_s is the snow crystal mass, and m_i is the ice crystal mass. Ice does not sediment in the one-moment scheme. For a range of hydrometeor masses $\sim \mathcal{O}(\, 10^{-13}$ kg up to 10^{-10} kg), the terminal settling velocity for snow in the one-moment scheme is much stronger than that for either ice or snow in the two-moment scheme. The sedimentation sink is then also much stronger in the one-moment formulation.

Heterogeneous nucleation occurs on ice-nucleating particles (INPs), represented as follows in the one- and two-moment schemes, respectively:

$$C_{\text{INP, 1M}} = (1 \times 10^2) \exp\left[-0.2(T - 273 \, \text{K})\right], \tag{6.9}$$

$$C_{\text{INP, 2M}} = \begin{cases} (4.99 \times 10^4) \exp\left[-0.2622(T - 237 \, \text{K})^{1.2044}\right] \\ (7.72 \times 10^4) \exp\left[-0.0406(T - 220 \, \text{K})^{1.4705}\right] f(\text{RH}_{\text{ice}}), \end{cases} \tag{6.10}$$

where T is subzero temperature, and RH_{ice} is the relative humidity with respect to ice. While the one-moment scheme represents only immersion nucleation (Eq. 6.9), the two-moment scheme represents both a relative humidity-dependent deposition nucleation and immersion nucleation (cases of Eq. 6.10). Both formulations predict exponential increases in INP as subzero temperature cools but with a much steeper slope in the two-moment than one-moment scheme. Conversely, the absolute INP number from the one-moment scheme is much higher (e.g., Sullivan et al., 2022, their Fig. 10a).

Finally, the rate of depositional growth S_{dep} is represented with a much more complicated temperature dependence in the two-moment scheme:

$$S_{dep,\ 1M} = (1.3 \times 10^{-5}) m_i^{1/3} (q_v - q_{sat,i}), \tag{6.11}$$

$$S_{dep,\ 2M} = \frac{4\pi C_i D_i S_i f(m_i)}{\left[\frac{RT}{p_{sat,i}\mathscr{D}} + \frac{L_{iv}}{k_i T} \left(\frac{L_{iv}}{RT} - 1 \right) \right]}, \tag{6.12}$$

where q_v is the specific humidity, $q_{sat,i}$ and $p_{sat,i}$ are the saturation specific humidity and vapor pressure with respect to ice, C_i is the crystal capacitance, $f(m_i)$ represents a mass-dependent ventilation coefficient, k_i is the thermal conductivity of ice, L_{iv} is the latent heat of sublimation, D_i is the diffusivity of vapor water, S_i is the saturation with respect to ice, and R is the gas constant. Key to both the nucleation and growth sources is the initial mass at which ice crystals are formed. The two-moment scheme initiates its crystals at 10^{-14} kg, and the one-moment scheme initiates its crystals at a much larger mass of 10^{-12} kg (e.g., Sullivan et al., 2022, their Tab. 2). While the two-moment scheme generates fewer smaller crystals, they also stay aloft longer.

Cloud-Controlling Factors by Class

Looking at the cloud ice source and sink formulations above, temperature (T), specific humidity (q_v), and vertical velocity (w) are the most important cloud-controlling factors (CCFs). T and q_v appear explicitly in Eqs. 6.9-6.12, while the influence of w is felt indirectly by determining saturation with respect to ice (RH_{ice} or S_i in Eqs. 6.10 and 6.12). The strength of w relative to v_{Ts} also determines whether ice crystals sediment. We examine these inputs across cloud classes and model settings (Fig. 6.10). Specific humidity differences from the 80 km simulation are quite small (Fig. 6.10, top row). The simulations with finer resolution are drier than the 80 km one below 10 km, but there is not a smooth trend toward lower specific humidity with finer resolution.

Profiles of temperature difference from the 80 km simulation mostly indicate a consistent trend of upper-tropospheric temperatures cooling as resolution is refined, aside from the 2.5 km simulations (Fig. 6.10, middle row). Across all classes with high clouds, the 40 km simulation is about 0.5 K cooler than the 80 km one between 5 and 11 km; the 5 km simulation is as much as 1.8 K cooler at these altitudes. These shifts toward colder temperatures below 11 km can help explain the increasing q_i there at finer resolutions. Colder temperatures will accelerate nucleation of new crystals and depositional growth of existing crystals at warmer subzero temperatures in the two-moment scheme. However, the trend does not hold for the 2.5 km simulations without convective parameterization. Variations in input temperature cannot explain the dramatic increase in q_i with explicit convection.

Vertical velocities increase systematically with refined resolution, especially for the deep cloud layers (Fig. 6.10, bottom row). Deep cloud layers - high-x-middle and high-x-middle-x-low classes - are characterized by ascent throughout, whereas the isolated cirrus - high or high-low classes - have ascending

air only above 7 km with descent below. Strengthening ascent will promote nucleation and growth in the same manner as cooling temperature. For the high-x-middle clouds, vertical velocity increases by a factor of 1.8 - from 1.2 to 2.2 m s^{-1} between 80 and 2.5 km resolutions. For the high-x-middle-x-low clouds, vertical velocity increases by a factor of 1.4 - from 2.5 to 3.5 m s^{-1} between 80 and 2.5 km resolutions.

A subtlety of vertical velocity is that a few instances of strong ascent can drive the majority of ice nucleation (e.g., Donner et al., 2016; Sullivan et al., 2016; Shi and Liu, 2016). The extreme values are more influential than the means depicted in Fig. 6.10, so we also construct the probability distribution of vertical velocities at 500 hPa from the various simulations (Fig. 6.11). We note that the ICON model uses no representation of subgrid-scale variability in vertical velocities. The variance of these resolved vertical velocity distributions becomes larger for finer resolution and without convective parameterization for both the one- and two-moment microphysics schemes. This distribution broadening indicates that vertical velocities, not only in the mean but also in the extremes, intensify at finer resolutions.
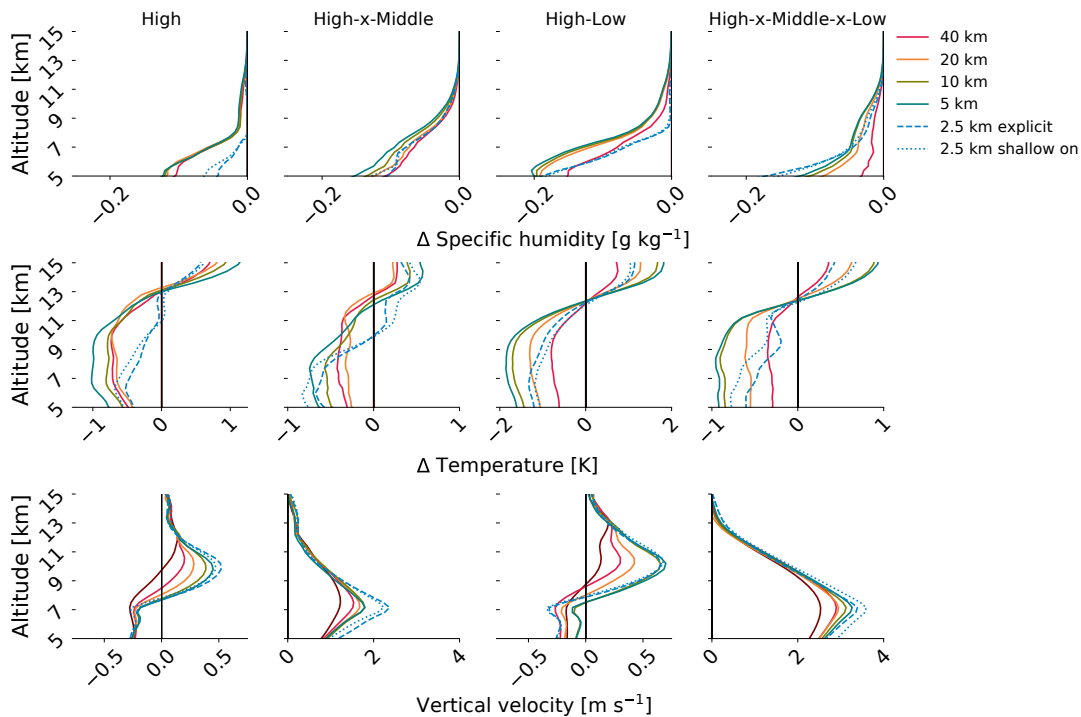
Figure 6.10: Differences in the upper-tropospheric, time mean, and area mean specific humidity (top row) and temperature profiles (middle row) from that of the 80 km simulation. Time mean and area mean vertical velocity profiles for all simulation settings (bottom row - note the different x-axis limits in the first and third panels versus the second and fourth panels). Variables associated with the four cloud classes that include high clouds are shown for the simulations with the two-moment scheme only, with all model settings as in Fig. 6.3. Reprinted from Sullivan et al. (2023). ©The Authors, CC BY 4.0 ©①

A final factor to consider is the separation of convective and grid-scale microphysics with parameterized convection. Within a convecting grid cell, when convection is parameterized, the more sophisticated formulations of Eqs. 6.4-6.12 are superseded by simpler formulations in the convective microphysics. In particular, liquid condensate is converted to ice using a linear interpolation of temperatures between 273

and 235 K. As a result, the stronger vertical velocities at higher resolutions have a particularly strong effect in the absence of convective parameterization, as they influence ice formation and growth in all grid cells, not only the non-convecting ones.

This analysis of source and sink processes and the cloud-controlling factors driving them produces a balance in favor of larger ice production within the two-moment scheme, especially with explicit convection. The most important elements in this balance are (1) weaker autoconversion and sedimentation sinks, (2) smaller initial crystal sizes, and (3) more instances of strong vertical velocity in the two-moment setup with explicit convection.
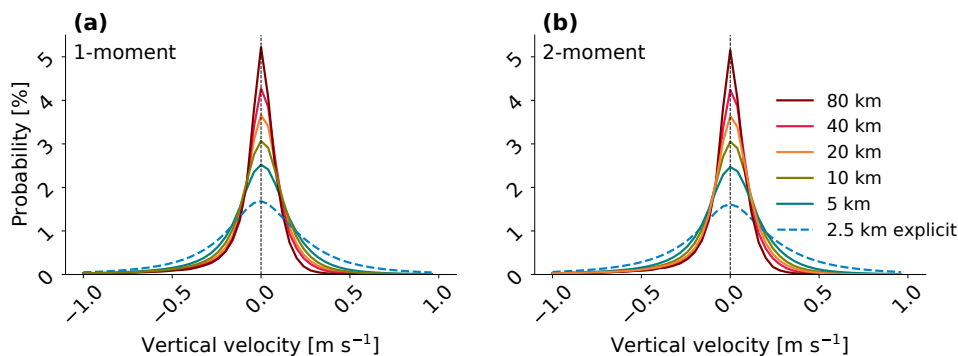
Figure 6.11: Probability distributions of vertical velocity from the simulations with the one-moment (panel (a)) and two-moment microphysics (panel (b)) with all model settings as in Fig. 6.3. Because we seek to explain the resolution dependence of q_i, these velocities are not averaged or interpolated to a uniform grid. Reprinted from Sullivan et al. (2023). ©The Authors, CC BY 4.0 ©①

6.3 Discussion and Conclusions

We have explored CRH dependencies on resolution, convective parameterization, and microphysics scheme in the ICON model. We find that the combination of parameterized versus explicit representation of convection and a one versus two-moment microphysics scheme is the most influential model setting for CRH in the ICON simulations. When we use a two-moment microphysics scheme, switching from parameterized to explicit convection has a much more dramatic effect than in the one-moment simulations. We posit that, when convection is parameterized, separation of convective and grid-scale microphysics produces a larger difference in the two-moment case. Sensitivities to resolution are more muted than those to the microphysics or convection parameterizations (Fig. 6.12). This result reflects the increased importance of constraining microphysical uncertainties as we transition toward the higher resolutions of storm-resolving models.

Strong microphysical and convective sensitivity and weaker resolution sensitivity in the CRH profiles do not appear in distributions of cloud class occurrence and appear only weakly in cloud fraction profiles. Instead, it is the cloud ice mass mixing ratio profiles that mirror the CRH dependencies most closely. We can trace these cloud ice mass mixing ratio differences back one additional step to changes in microphysical formulations and cloud-controlling factors (Fig. 6.12). Radiatively inactive frozen species, like

snow and graupel, and the initial ice crystal mass, via its effect on subsequent growth and sedimentation rates, are two influential aspects of the microphysical formulations. Within the cloud-controlling factors, the width of the vertical velocity distribution and the upper-tropospheric temperature vary systematically with model setting.
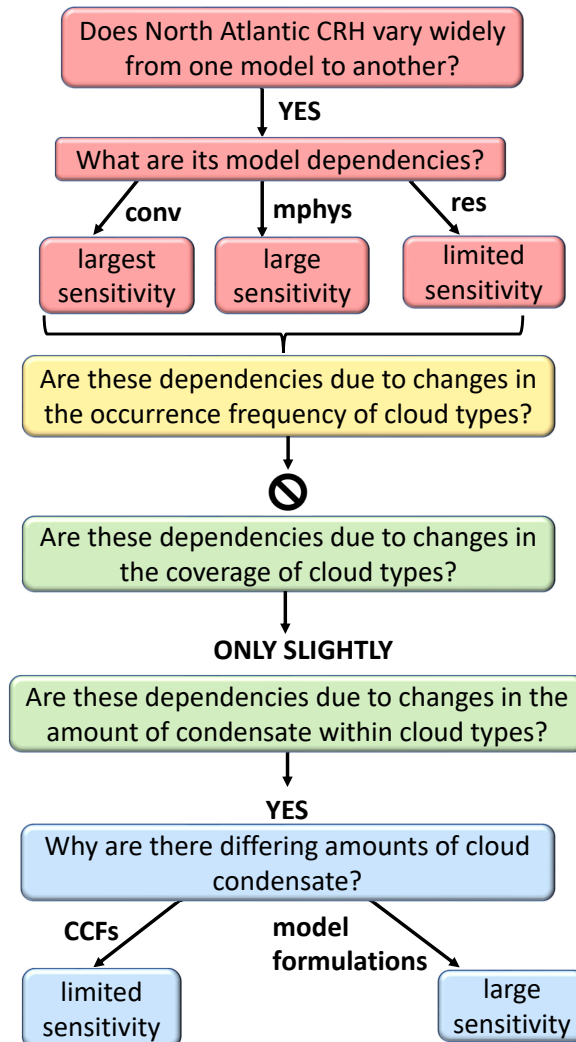

Figure 6.12: A schematic overview of our analysis. Results of Sects. 6.2.1, 6.2.2, 6.2.3, and 6.2.4 are shown in pink, yellow, green, and blue, respectively. Reprinted from Sullivan et al. (2023). ©The Authors, CC BY 4.0 ©①

Importantly, these findings are robust in relation to several factors. The dependencies affect both short-wave and longwave components of the cloud-radiative heating and occur across isolated cirrus, layered cirrus-boundary-layer cumulus, and forms of deep convection (high, high-low, high-x-middle, and high-x-middle-x-low in our decomposition). They are also not dependent on the cloud fraction thresholds used to define these cloud classes (Fig. S1 in the supplementary material of Sullivan et al., 2023, not shown here) or on the simulation duration. The resolution and scheme dependencies already emerge within a single-day simulation (Fig. S2 in the supplementary material of Sullivan et al., 2023, not shown here).

The upper-tropospheric CRH variability motivating this work also appears not only across three coarse-resolution global climate models (Fig. 6.1) but also between the ERA5 reanalysis and the CloudSat-CALIPSO 2B-FLXHR-LIDAR data (Fig. 6.3). Here, it is the more moderate resolutions and parameterized convection that agree best with the CloudSat-CALIPSO CRH (Fig. 6.3). While our analysis method could be generalized to other regions or modeling frameworks, the role of q_i and specific microphysical processes or parameters in CRH sensitivity will not necessarily generalize.

This last point highlights a challenge in further constraining atmospheric cloud-radiative heating: even our baseline contains uncertainties or assumptions. The disagreement between the ERA5 and CloudSat-CALIPSO profiles indicates that thermodynamic and wind fields are insufficient to constrain CRH. Both the one- and two-moment microphysics schemes generate quite similar distributions of cloud class occurrence despite drastically different upper-tropospheric CRH profiles (Figs. 6.5 and S3 in the supplementary material of Sullivan et al., 2023, not shown here). Stated another way, both cloud macrophysical and microphysical properties are needed to predict cloud-radiative heating. This result is consistent with other studies. For example, Sullivan and Voigt (2021) showed that CRH varies 4-fold by flipping ice microphysical schemes.

A second challenge is that different combinations of model settings may improve model-measurement agreement in top-of-atmosphere or surface radiative fluxes versus atmospheric cloud-radiative heating. Models are often tuned based upon their outgoing longwave radiation, but as we have noted throughout, it is the in-atmosphere heating that feeds back upon circulation. As an example, Senf et al. (2020) assess the top-of-atmosphere cloud-radiative flux using the same set of runs and find the best agreement with the CloudSat-CALIPSO climatology from the simulation with 2.5 km resolution and shallow convective parameterization only. Here, it is instead the more moderate resolutions and parameterized convection that agree best with the CloudSat-CALIPSO CRH (Fig. 6.3).

We highlight the benefit of high-resolution simulations in better representing cloud microphysical processes and allowing updrafts to interact directly with the cloud field. Although a better representation of the cloud field in the model can significantly reduce the bias in the simulation of CRH, uncertainties associated with the radiation parameterization can still contribute to CRH variability. In the next chapter, we will indeed consider this aspect and discuss the relative importance of CRH uncertainties to the dynamics of extratropical cyclones.

7 Uncertainties in Cloud-Radiative Heating Within an Idealized Extratropical Cyclone

In this chapter, we address another aspect of research question 2: "How large are the CRH uncertainties in the extratropical atmosphere, and which uncertainties are relevant to the dynamics of extratropical cyclones?". In particular, we address the following questions:

1. How does CRH change due to the uncertainties in radiation parameterization?
2. What is the implication of CRH uncertainties for the dynamics of extratropical cyclones?

To this end, we investigate uncertainties in CRH within an extratropical cyclone due to radiation parameterization. The simulation design is described in Sect. 7.1. We present the results in Sect. 7.2 and summarize the main conclusions with discussion in Sect. 7.3. This chapter is based on Keshtgar et al. (2024). ©The Authors, CC BY 4.0 ⓒⓘ

7.1 Simulation Design

As described in Sect. 3.6, we perform an idealized baroclinic life cycle simulation in the channel setup at the convective-permitting resolution of 2.5 km in which cloud-radiative heating of the atmosphere is taken into account but clear-sky radiative heating is not. We target four different regions of the cyclone for large-eddy-model (LEM) simulations: shallow cumulus, warm conveyor belt (WCB) ascent, WCB cyclonic outflow, and WCB anticyclonic outflow (Fig. 3.8).

The offline radiative transfer calculations require as input the 3D fields of cloud ice and liquid water content and effective particle radii from LEM simulations. We briefly characterize the clouds from the LEM simulations in Fig. 7.1, which shows domain and time averages of cloud ice contents, liquid water contents, and cloud fractions for the four LEM domains. We calculate the time average over nine snapshots that are each separated by a 30 min time interval between 12:30 and 16:30 domain local time (DLT). We use the same snapshots for the offline radiative transfer calculation. During this time interval, the solar zenith angles change from low to high values in all regions, which is an important factor for the shortwave 3D cloud-radiative effects (Sect. 7.2.2).

In the shallow cumulus region, low-level liquid clouds prevail in the boundary layer between 0 and 2 km, with cloud fraction peaking at 40% at an altitude of around 1 km (Fig. 7.1a and b). In the WCB ascent region, extensive vertical clouds contain both ice and liquid water. The liquid water content in the lower and middle levels is much higher and more variable in time than the ice water content in the upper levels (Fig. 7.1c). The decomposition of cloud fraction shows that liquid clouds are concentrated in the

lower levels between 0 and 4 km, where their cloud fraction reaches a maximum of 60% at around 1 km. Mixed-phase clouds are located at intermediate levels between 2 and 7 km. Above the boundary layer, the fraction of ice clouds increases rapidly, reaching a maximum of nearly 60% at about 8 km (Fig. 7.1d).
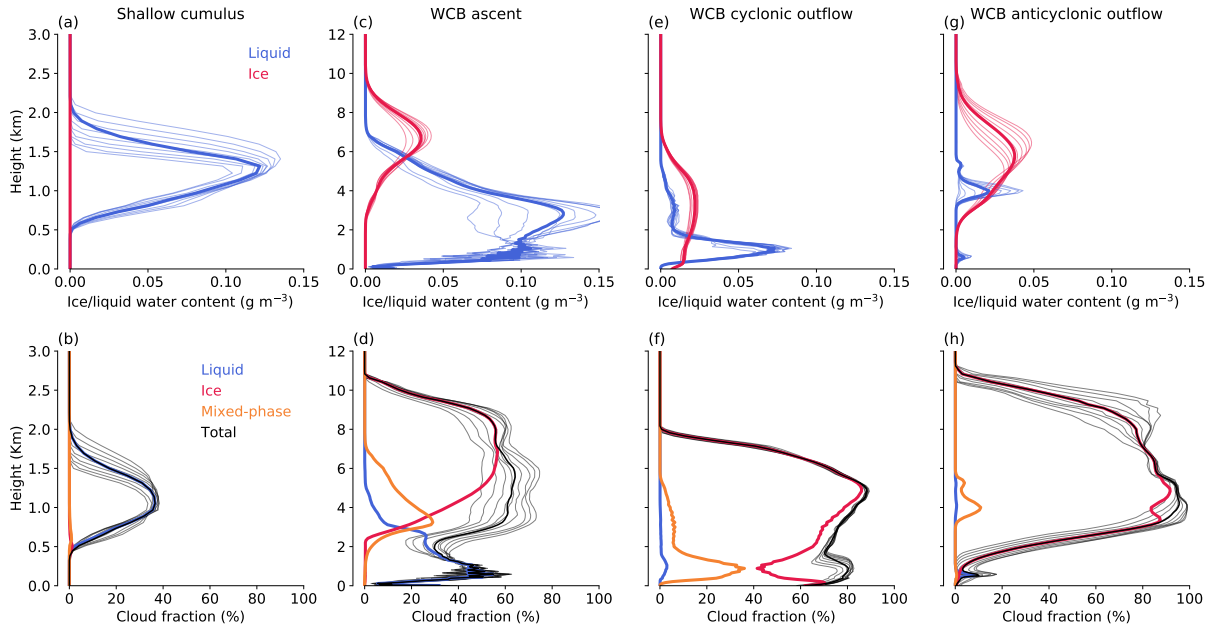

Figure 7.1: Profiles of domain-averaged cloud hydrometeor contents and total cloud fraction, decomposed into the contributions from liquid, ice, and mixed-phase clouds for all four LEM domains. Thin lines show profiles for nine snapshots between 12:30 and 16:30 DLT. The thick lines show time-averaged profiles. The threshold used to determine cloudy grid boxes for both ice and liquid water contents is $10^{-8}\,\mathrm{kg\,kg^{-1}}$ (Costa-Surós et al., 2020). Note the different y axes for panels (a) and (b). Reprinted from Keshtgar et al. (2024). ©The Authors, CC BY 4.0 ⓒⓘ

Clouds in the WCB cyclonic outflow region also contain both ice and liquid water but are located at lower altitudes compared to the WCB ascent region (Fig. 7.1e). The total cloud fraction is dominated by ice clouds and reaches nearly 90% at around 6 km. Mixed-phase clouds exist only in the boundary layer (Fig. 7.1f). In the WCB anticyclonic outflow, mid- and high-level clouds contain both ice and liquid water, with ice water content dominating over liquid water content (Fig. 7.1g). The total cloud fraction is dominated by ice clouds (Fig. 7.1h).

The WCB ascent and outflow regions are much cloudier than the shallow cumulus region. In the WCB outflow regions, stratiform ice clouds cover almost the entire domain. We quantify CRH uncertainties in the four LEM domains due to four factors: 3D cloud-radiative effects, parameterization of ice optical properties, cloud horizontal heterogeneity, and cloud vertical overlap (Tab. 3.1). The offline radiative transfer calculations are described in detail in Sect. 3.7.

7.2 Results

In this section, we assess CRH in the four regions of the cyclone. We derive CRH from all-sky and clear-sky radiative heating in the shortwave and longwave spectra for each of the radiative transfer settings (Tab. 3.1). To quantify the impact of the four factors mentioned above, we compare the time and domain averages of the CRH from the different radiative transfer calculations.

7.2.1 Average Profiles of Cloud-Radiative Heating

Figure 7.2 shows domain and time averages of longwave, shortwave, and net CRH in the four regions of the cyclone for the ICON and the reference offline radiative transfer calculations. Despite the differences in the radiative transfer setup between ICON and libRadtran, the CRH profiles agree very well (cf. dashed and solid lines in Fig. 7.2). In all four regions, longwave radiation leads to cooling at the cloud tops and weak warming at the cloud bases (Fig. 7.2; blue), resulting in radiative destabilization of the cloud. In contrast, shortwave radiation warms the cloud tops and slightly cools the lower parts of the clouds, resulting in radiative stabilization of the cloud (Fig. 7.2; red). The longwave CRH is about twice as large as the shortwave CRH. Thus, the net CRH profiles are dominated by the stronger longwave CRH (Fig. 7.2; black).
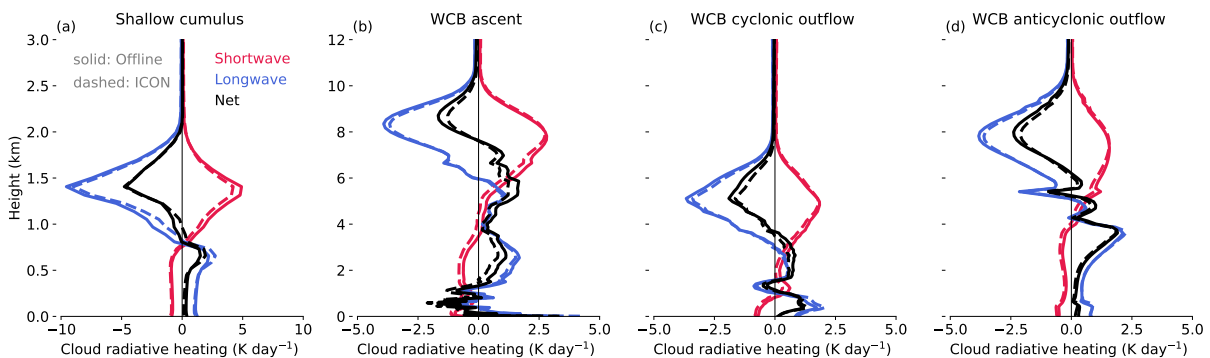
Figure 7.2: Domain and time averages of shortwave, longwave, and net CRH. Profiles are shown for (a) shallow cumulus, (b) WCB ascent, (c) WCB cyclonic outflow, and (d) WCB anticyclonic outflow regions. The ICON CRH is shown with dashed lines, and the CRH derived from the offline reference 1D radiative transfer calculation is shown with solid lines. Note the different x and y axes in panels (a) and (b–d). Reprinted from Keshtgar et al. (2024). ©The Authors, CC BY 4.0 ⓒⓘ

The CRH in the shallow cumulus region is almost twice as strong as in the WCB regions (Fig. 7.2a). Grise et al. (2019) and Voigt et al. (2023) showed that the strong cloud-radiative cooling of the boundary layer has a weakening effect on the intensity of extratropical cyclones. The CRH in WCB regions is strongly influenced by the radiative heating of the ice clouds (Fig. 7.2b-d). Although the CRH in the WCB regions is weaker than the CRH in the shallow cumulus region, previous work showed it to be important for the near tropopause dynamics of the cyclone (Li et al., 2015; Keshtgar et al., 2023; Voigt

et al., 2023). Thus, it is important to quantify CRH uncertainties in all four regions of the extratropical cyclone.

7.2.2 3D Cloud-Radiative Effects

We quantify 3D cloud-radiative effects as the difference in CRH between that calculated with the MYSTIC solver (3D; Sect. 3.7) and that with the MYSTIC solver run in the independent column approximation mode (1D). The latter is a 1D radiation scheme and neglects horizontal photon transport between model columns. To visualize the 3D cloud-radiative effects, Fig. 7.3 shows cross-sections of 3D and 1D all-sky radiative heating and their differences in shallow cumulus clouds southwest of the cyclone center at 16:30 DLT. At this location and time, the solar zenith angle is approximately 65°.
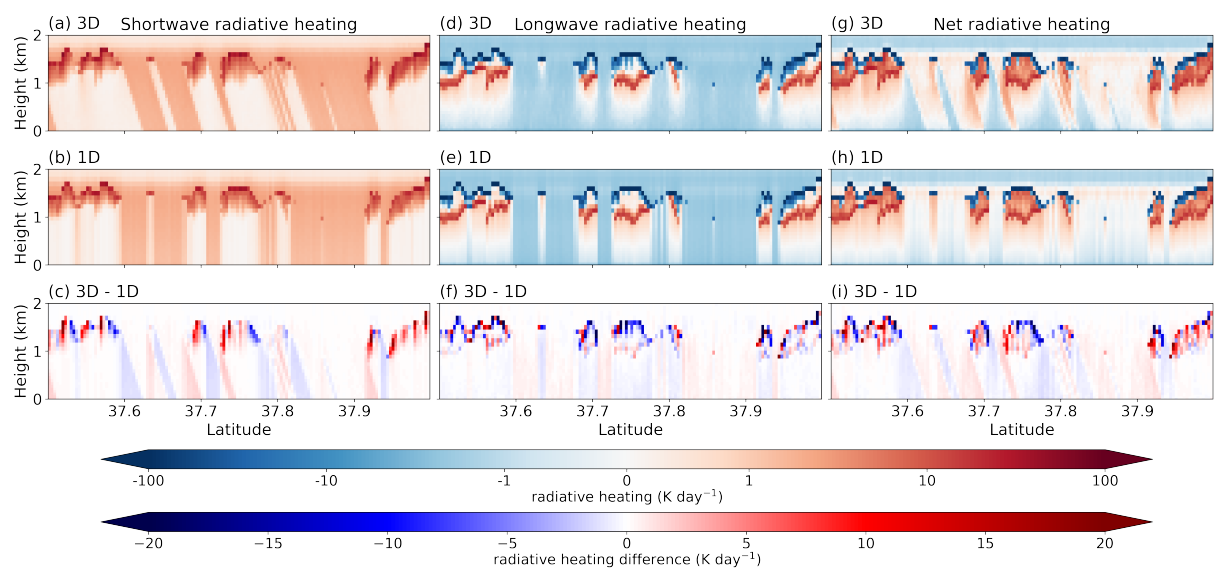
Figure 7.3: Cross-sections of shortwave, longwave, and net all-sky radiative heating visualized using a logarithmic color scale for shallow cumulus clouds southwest of the cyclone center. The upper row shows 3D calculations, the middle row shows 1D calculations, and the lower row shows the differences between the 3D and 1D calculations. The cross-sections are at 16:30 DLT and 11.5°W and between 37.5 and 38°N. The solar zenith angle is 65°. Note that the impression of a lower solar zenith angle in the figure is due to the aspect ratio of the figures. Reprinted from Keshtgar et al. (2024). ©The Authors, CC BY 4.0 ©①

In the shortwave spectrum, neglecting horizontal photon transport leads to incorrect positions of illuminated and shadowed areas in the atmosphere and on the surface (Fig. 7.3a-c). Črnivec and Mayer (2019) showed that this can have a substantial impact on surface radiative fluxes and hence the surface energy balance. However, our focus is on the 3D radiative effects of clouds within the atmosphere. In Fig. 7.3a, the southern sides of the clouds (see the shallow cumulus domain in Fig. 3.8) facing the sun receive more radiative energy in the 3D calculation than in the 1D calculation (red colors around 1.5 km in altitude in Fig. 7.3c). In some cases, the northern sides of the clouds are shadowed and receive less energy (blue colors around 1.5 km in altitude in Fig. 7.3c). The shortwave cloud-side leakage is small in this example due to the low position of the sun.

In the longwave spectrum, cloud "shadows", visible as white areas below clouds (panels d and e of Fig. 7.3), are weaker in the 3D calculation than in the 1D calculation due to the horizontal photon transport between model columns. However, the largest differences between the 3D and 1D calculations occur at the cloud–clear-sky boundaries, where horizontal emission of longwave radiation from the cloud tops and cloud sides leads to stronger radiative cooling in the 3D calculation (blue colors around 1.5 km in height in Fig. 7.3f).

In the net, most features of cloud-radiative heating and cooling within the atmosphere are present in both 3D and 1D calculations (Fig. 7.3g and h). However, due to shortwave cloud-side illumination and horizontal longwave cloud absorption and emission, large differences exist at the interface of clouds and clear-sky regions around 1.5 km in height in Fig. 7.3i and in the position of cloud shadows.

Figure 7.4 shows the average profiles of 3D cloud-radiative effects for the four regions of the cyclone. In all regions, shortwave and longwave CRH is stronger in the 3D radiation calculation due to shortwave cloud-side illumination and longwave cloud-side cooling, respectively. There is a direct relationship between cloud-side illumination and the solar zenith angle (Fig. 7.4a; thin lines). In the 3D calculation, clouds receive more radiative energy from their sides at higher solar zenith angles, which increases shortwave cloud-radiative warming. Črnivec and Mayer (2019) also showed this direct relationship between cloud-side illumination and the solar zenith angle. The magnitude of the cloud-side cooling depends on the magnitude of the longwave CRH, such that the stronger the longwave CRH, the stronger the longwave cooling from the cloud sides.
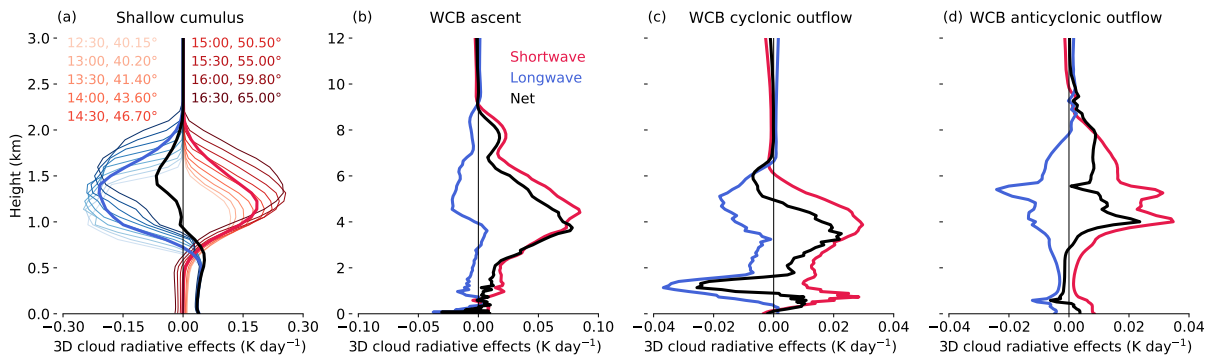

Figure 7.4: Average profiles of shortwave, longwave, and net 3D cloud-radiative effects for the four cyclone regions. The 3D cloud-radiative effects are calculated as the difference in domain mean CRH between 3D (MYSTIC) and 1D (MYSTIC-ICA) radiative transfer calculations. The thin lines in panel (a) show the 3D radiative effects for nine snapshots between 12:30 and 16:30 DLT, with the legend indicating the time and domain mean solar zenith angles for all snapshots. Note the different x axes in the panels. Reprinted from Keshtgar et al. (2024). ©The Authors, CC BY 4.0 ⓒ①

The 3D cloud-radiative effects are much weaker for WCB regions dominated by stratiform clouds than for the shallow cumulus region, which contains a lot of broken clouds (Fig. 7.4). This is expected due to the weak horizontal gradients of cloud optical properties and the small aspect ratio of the stratiform clouds in the WCB regions. For shallow cumulus clouds, the net 3D cloud-radiative effect is dominated

by cloud-side longwave cooling (Fig. 7.4a). This could lead to a stronger radiative destabilization of clouds during both day and night. In contrast, for stratiform clouds in the WCB, shortwave cloud-side illumination dominates the daytime 3D cloud-radiative effects except for shallow liquid clouds in the boundary layer of the WCB cyclonic outflow region, where longwave cloud-side cooling becomes dominant (Fig. 7.4b-d). The stronger shortwave cloud-side illumination in the WCB regions is most likely due to the higher solar zenith angle at higher latitudes compared to that of the shallow cumulus region at lower latitudes. Although the incoming shortwave radiative fluxes are weaker at higher latitudes, shortwave cloud-side warming becomes stronger at higher zenith angles.

7.2.3 Impact of Ice Optical Parameterization

We now quantify the impact of ice optical parameterization by comparing the CRH calculated with the ice optical parameterization of Fu and the more complex ice optical parameterization of Baum. The ice scheme of Baum includes three ice habits, which allows us to also assess the effect of different ice habits. We only consider clouds in the three WCB domains, where ice crystals are abundant.
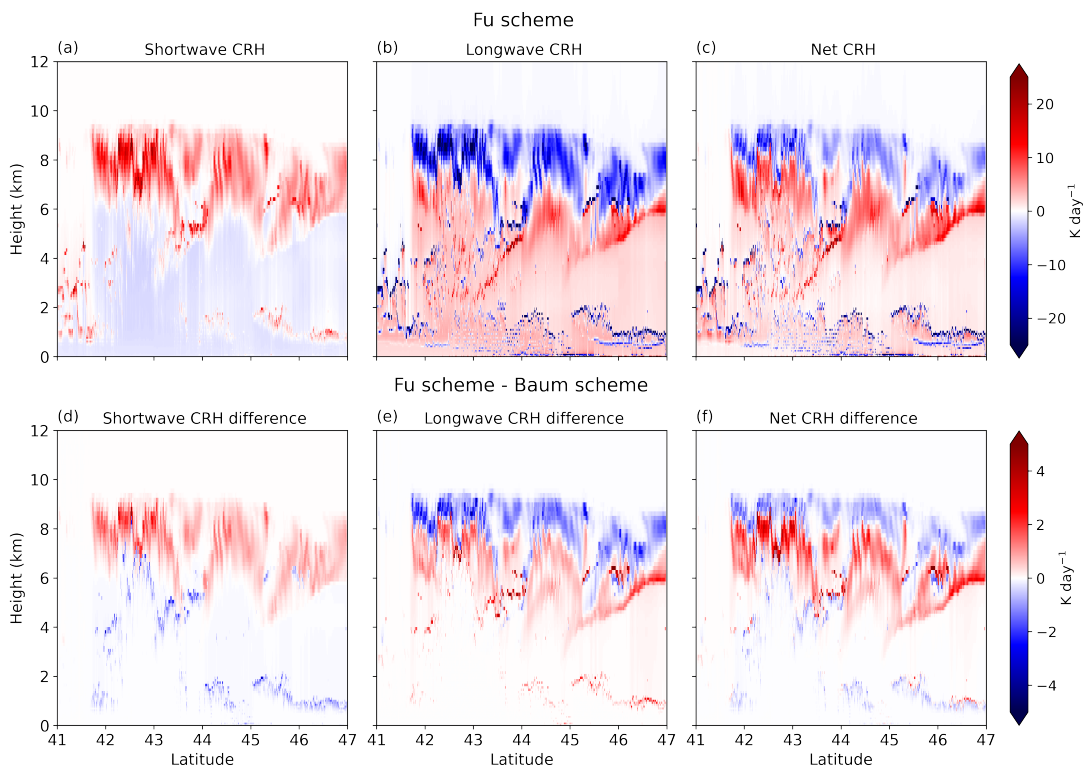
Figure 7.5: Cross-sections of (a) shortwave, (b) longwave, and (c) net CRH calculated with the ice optical parameterization of Fu in the WCB ascent region. Panels (d-f) show CRH differences between the ice scheme of Fu and the ice scheme of Baum with the general habit mixture (Fu - Baum). Cross-sections are shown at 14:30 DLT and at 3° longitude. Reprinted from Keshtgar et al. (2024). ©The Authors, CC BY 4.0 ⓒ①

The top row in Fig. 7.5 shows cross-sections of shortwave, longwave, and net CRH in the WCB ascent region for the ice scheme of Fu. The bottom row in Fig. 7.5 shows the CRH differences between the ice

schemes of Fu and Baum with the general habit mixture. Fu results in stronger longwave and shortwave CRH than Baum does (Fig. 7.5d and e), with CRH differences reaching up to 20% of the absolute values. As a result, Fu leads to stronger radiative destabilization in the longwave but stronger stabilization in the shortwave.
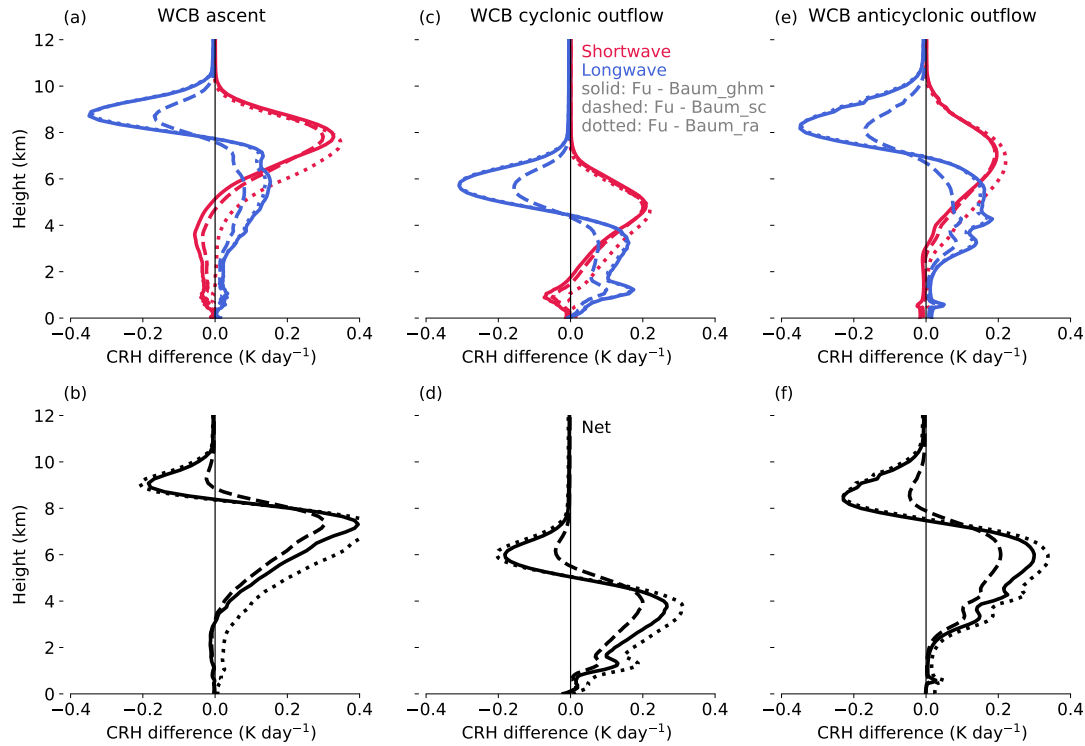

Figure 7.6: Impact of ice optical parameterization on time- and domain-averaged CRH in the three WCB regions. The CRH differences are calculated between the radiative transfer calculations and the ice schemes of Fu and Baum (Fu - Baum). The differences between Fu and Baum, along with general habit mixture (ghm), solid column (sc), and rough-aggregated (ra) habits, are shown using solid lines, dashed lines, and dotted lines as indicated in the legend. Reprinted from Keshtgar et al. (2024). ©The Authors, CC BY 4.0 ⓒⓘ

Figure 7.6 shows CRH differences between Fu and Baum. In all three WCB regions, longwave CRH and shortwave CRH are amplified in Fu compared to in Baum. The magnitude of the CRH differences depends on which ice crystal habit is chosen in the Baum scheme, with different impacts in the longwave and shortwave. In the longwave, the differences between Fu and Baum are the same for the general mixture and rough-aggregated habits but are smaller by a factor of 2 when the solid column habit is used in Baum. In the shortwave, the impact of the ice habit is much smaller. The stronger impact of the ice habit on the longwave compared to the shortwave CRH is an interesting aspect of our results.

Compared to Baum, Fu leads to stronger shortwave and longwave cloud-radiative warming in the middle and lower parts of the clouds and therefore to net cloud warming (Fig. 7.6, lower row). Although Fu leads to some increase in cloud-radiative cooling of the upper cloud parts, this suggests that the radiative destabilization of clouds within the WCB regions is smaller in Fu than in Baum.

7.2.4 Cloud Horizontal Heterogeneity and Vertical Overlap

We continue by quantifying the impact of cloud horizontal heterogeneity and vertical overlap. Both factors are not resolved at 2.5 km and therefore need to be parameterized. We calculate the CRH differences between the radiation calculations using the two types of homogeneous NWP clouds and the LEM clouds (Sect. 3.6, Fig 3.9). For homogeneous grid-box clouds, an overlap assumption is not needed. For the homogeneous clouds with fractional cloud cover, we use a maximum-random overlap assumption.

The solid lines in the first row of Fig. 7.7 show CRH differences between homogeneous grid-box clouds and the LEM clouds, decomposed into longwave and shortwave components. In all regions, the magnitude of the longwave and shortwave CRH profiles is overestimated when homogeneous grid-box clouds are used, with the longwave CRH being more strongly affected than the shortwave CRH and the largest differences occurring in shallow cumulus clouds.
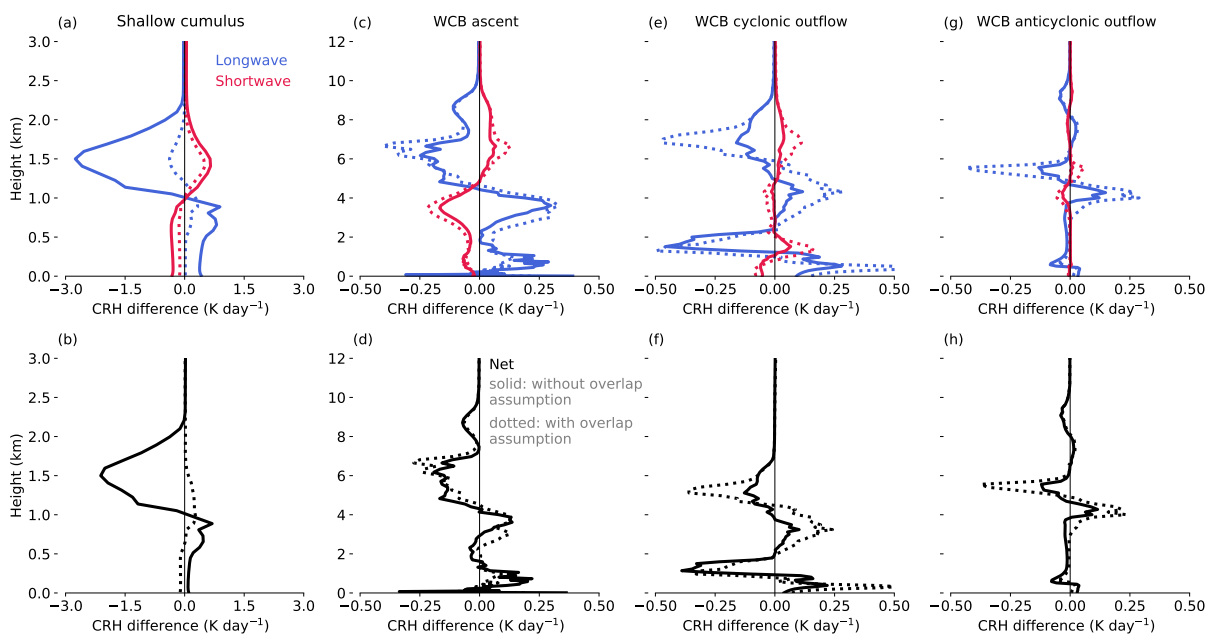
Figure 7.7: Impact of cloud horizontal heterogeneity and vertical overlap on CRH, which are not resolved at a 2.5 km horizontal resolution. The CRH differences are calculated between the LEM reference calculation and the radiative transfer calculations for the homogeneous NWP clouds (NWP - LEM), with solid lines for the homogeneous grid-box clouds (without overlap assumption) and dotted lines for the homogeneous clouds with fractional cloud cover (with overlap assumption). Note the different x and y axes for panels (a) and (b). Reprinted from Keshtgar et al. (2024). ©The Authors, CC BY 4.0 ⓒ①

The second row of Fig. 7.7 compares the impact of the two types of homogeneous clouds. When the overlap scheme is used for the homogeneous clouds with fractional cloud cover, the differences in CRH between the NWP and LEM clouds are strongly reduced in the shallow cumulus region, from 2 to 0.5 K day^{-1}. This illustrates a clear positive impact of taking into account cloud fraction and partial overlap for these clouds and that treating these clouds as grid-box clouds at a 2.5 km resolution is problematic.

In the three WCB regions, cloud vertical overlap assumption has a smaller impact on CRH because the cloud fraction is higher. However, in contrast to the shallow cumulus region, taking the cloud overlap assumption into account has a detrimental effect and in fact increases the CRH differences for shortwave, longwave, and net (Fig. 7.7c-h). This supports the idea that clouds in the WCB regions can be treated as grid-box clouds at a 2.5 km resolution for radiative purposes because there is no obvious benefit of taking into account the cloud fraction and vertical overlap assumption.

7.2.5 Relative Importance of Uncertainties

In the previous subsections, we have assessed the individual impacts of the following four factors on CRH: 3D cloud-radiative effects, ice optical parameterization, cloud horizontal heterogeneity, and cloud vertical overlap. In this subsection, we characterize the relative importance of these four factors for extratropical cyclones, with the hope that this can guide efforts to improve CRH in models. As part of this characterization, we distinguish between mean uncertainties in spatial scales of around 500 km, which is approximately the size of the LEM domain, and local uncertainties that arise on the scale of the horizontal grid resolutions. For uncertainties due to 3D cloud-radiative effects and ice optical parameterization, the scale of the horizontal grid resolution is 300 m, and for the uncertainties due to cloud horizontal heterogeneity and cloud vertical overlap, the scale of the horizontal grid resolution is 2.5 km.

For the mean uncertainties, we compute the absolute mean difference,

$$\delta CRH_{mean} = |\overline{CRH_a} - \overline{CRH_b}|, \tag{7.1}$$

where the bars represent the average over time and the domain and the subscripts a and b indicate different radiative transfer calculations. This means that the mean uncertainties are obtained from the absolute values of the figures shown in Sects. 7.2.2, 7.2.3 and 7.2.4.

For the local uncertainties, we compute the mean absolute difference by first computing the absolute CRH differences at all grid points and then averaging over time and the domain,

$$\delta CRH_{local} = \frac{1}{n \cdot t} \sum_{j=1}^{t} \sum_{i=1}^{n} |CRH_a(i, j) - CRH_b(i, j)|. \tag{7.2}$$

n is the number of horizontal grid points i at each vertical layer, and t is the number of time steps j. To derive the local uncertainties due to horizontal cloud heterogeneity and vertical overlap, we coarse-grain the LEM CRH to the same horizontal resolution as the NWP CRH.

Figure 7.8 shows mean uncertainties by means of stacked bar plots in altitude intervals of 2 km calculated based on Eq. 7.1. For shallow cumulus clouds in the boundary layer between 0 and 2 km, the largest source of mean uncertainty is cloud horizontal heterogeneity without overlap assumption (Fig. 7.8a-c; blue bars). Allowing for partial overlap of homogeneous clouds with cloud fraction significantly reduces

the mean uncertainty (cf. green and blue bars in Fig. 7.8a-c). The mean uncertainty due to 3D cloud-radiative effects is about half of the uncertainty due to cloud horizontal heterogeneity when vertical overlap is considered.

For clouds in the WCB ascent region, cloud horizontal heterogeneity has a significant impact on the mean uncertainty at all levels and dominates the CRH uncertainty in the boundary layer (Fig. 7.8d-f; blue bars). Apart from the boundary layer and in contrast to shallow cumulus clouds, considering the vertical overlap assumption increases the mean uncertainty (cf. green and blue bars in Fig. 7.8d-f). Ice optical parameterization dominates the mean uncertainty in net CRH in the middle and upper levels above 6 km in altitude (Fig. 7.8f). The 3D cloud-radiative effects contribute relatively little, except at altitudes between 2 and 6 km in the shortwave and the net.
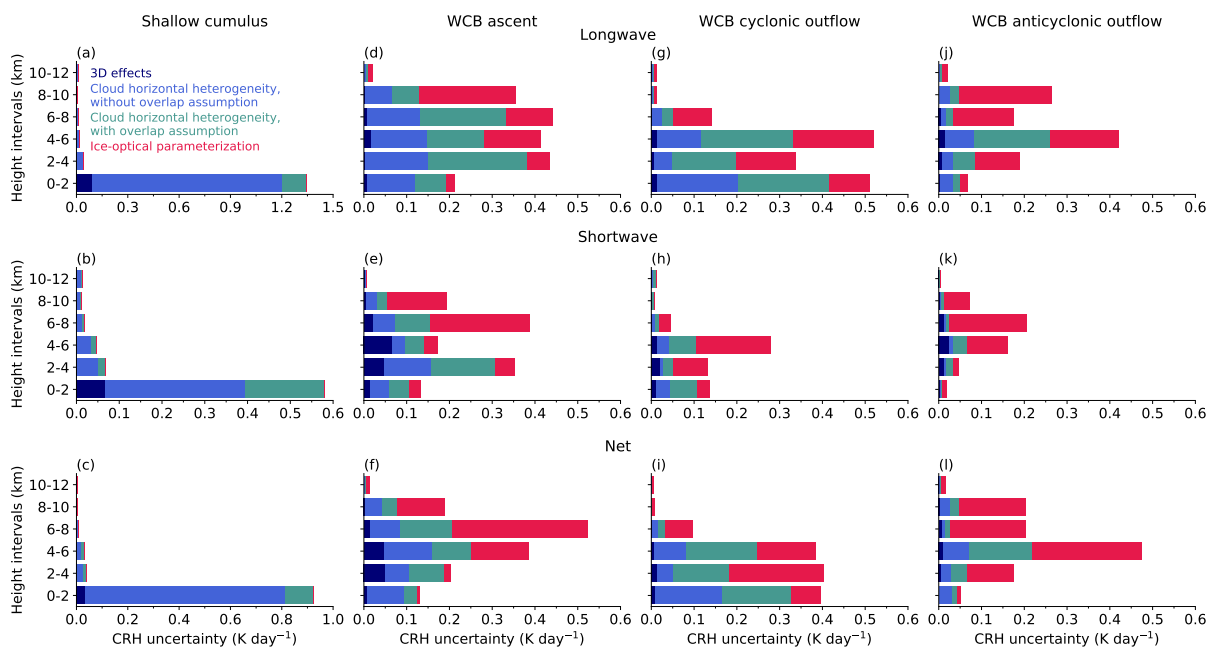
Figure 7.8: Mean uncertainties in CRH diagnosed as the absolute difference in domain and time mean CRH between different radiative transfer calculations. Uncertainties are decomposed into shortwave, longwave, and net. Uncertainties are computed as mass-weighted averages over 2 km altitude intervals. For the uncertainty due to the ice optical parameterization, the difference between the ice schemes of Fu and Baum with the general habit mixture is used. The contribution of each factor is given by the horizontal length of its colored bar. Note the different x axes in the panels. Reprinted from Keshtgar et al. (2024). ©The Authors, CC BY 4.0 ⓒⓘ

The relative importance of the four factors for the mean uncertainties in the WCB cyclonic outflow region is similar to that in the WCB ascent region (Fig. 7.8g-i). The ice optical parameterization contributes significantly to the mean uncertainty in the middle and upper levels, while cloud horizontal heterogeneity dominates the mean uncertainty in the boundary layer. The vertical overlap assumption increases the mean uncertainty, and the impact of the 3D cloud-radiative effects is small. The mean uncertainty in the WCB anticyclonic outflow region is dominated by the ice optical parameterization, and the impact of

cloud horizontal heterogeneity and vertical overlap is much weaker compared to the other regions of the cyclone, except those between 4 and 6 km in altitude (Fig. 7.8j-l).

Now we turn to local uncertainties in CRH. These are illustrated in Fig. 7.9 for net CRH. For comparison of mean and local uncertainties, Fig. 7.9 includes the mean net CRH uncertainties from Fig. 7.8 only for values larger than $0.05\,\mathrm{K\,day^{-1}}$, shown as gray-hatched bars. In contrast to the mean uncertainties, the impact of 3D cloud-radiative effects is much stronger at the scale of the horizontal grid resolution of 300 m. Except for the WCB anticyclonic domain, cloud horizontal heterogeneity dominates local uncertainties at the boundary layer between 0 and 2 km and mid-levels between 2 and 8 km in all regions of the cyclone. As for the mean uncertainties, taking into account the vertical overlap assumption reduces the local uncertainties for shallow cumulus clouds but slightly increases them for stratiform clouds in the WCB regions. Local uncertainties due to 3D cloud-radiative effects, cloud horizontal heterogeneity, and vertical overlap are much larger compared to their mean uncertainties in all four regions of the cyclone. However, the ice optical parameterization has similar impacts on local and mean uncertainties. This shows that 3D cloud-radiative effects, cloud horizontal heterogeneity, and vertical overlap have a much stronger impact on CRH locally than on the domain mean.
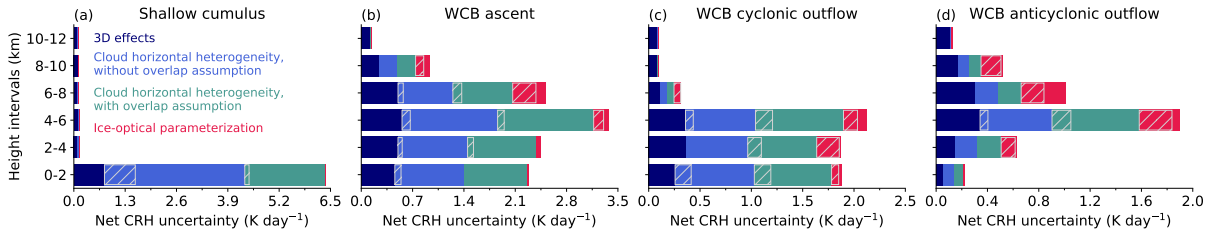

Figure 7.9: Same as Fig.7.8 but for local uncertainties in net CRH. For comparison, the mean net CRH uncertainties from Fig.7.8 are superimposed as gray-hatched bars. Mean uncertainties smaller than $0.05\,\mathrm{K\,day^{-1}}$ are not shown as they would not be visible in the plot. Note the different x axes in the panels. Reprinted from Keshtgar et al. (2024). ©The Authors, CC BY 4.0 ⓒ①

To understand the relative importance of CRH uncertainties at different horizontal spatial scales and for the dynamics of extratropical cyclones, we coarse-grain CRH from different radiative transfer calculations from their original horizontal resolution to horizontal resolutions equivalent to 2.5, 5, 10, 50, 100, and 500 km, which is approximately the spatial extent of the LEM domains. We calculate the CRH uncertainty at different spatial scales x by computing the mean absolute difference in net CRH between different radiative transfer calculations from different sets of coarse-grained CRH and average them over time and the domain,

$$\delta CRH_x = \frac{1}{n \cdot t} \sum_{j=1}^{t} \sum_{i=1}^{n} |CRH_{x,a}(i,j) - CRH_{x,b}(i,j)|. \tag{7.3}$$

Here, x is the horizontal resolution of the coarse-graining, the subscripts a and b indicate different radiative transfer calculations, n is the number of horizontal grid points i at each vertical layer for different

resolutions, and *t* is the number of time steps *j*. The CRH uncertainty calculated from Eq. 7.3 is an intermediate between the mean and the local CRH uncertainties described earlier, such that at horizontal resolutions of 300 m and 2.5 km this equation is equivalent to Eq. 7.2, and at a resolution of 500 km, the equation is equivalent to Eq. 7.1. For the shallow cumulus domain, where clouds are present only in the boundary layer, we apply a mass-weighted vertical average to the CRH uncertainties between 0 and 2 km in altitude, but for the WCB domains, we apply the average between 0 and 12 km in altitude (Fig. 7.10).
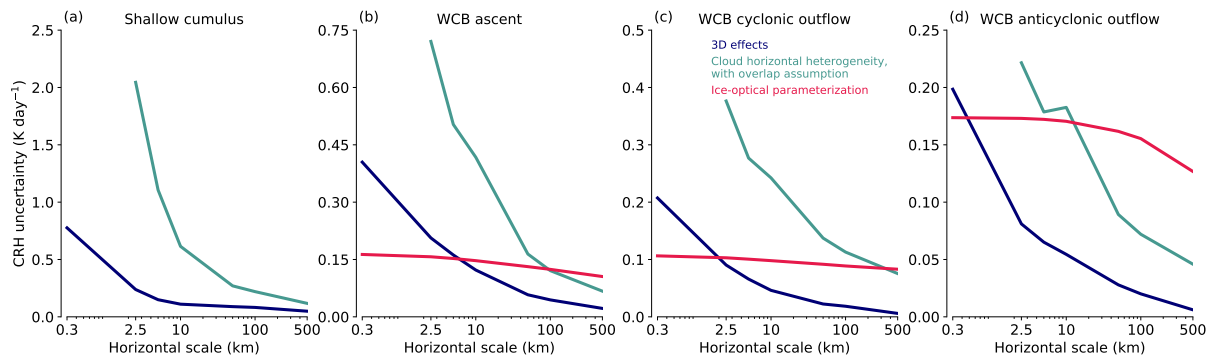
Figure 7.10: Net CRH uncertainties as a function of horizontal scale from 300 m to approximately 500 km for all LEM domains. Uncertainties are computed as mass-weighted vertical averages between 0–2 and 0–12 km altitude intervals for shallow cumulus and WCB regions, respectively. For the uncertainty due to the ice optical parameterization, the CRH difference between the ice schemes of Fu and the ice scheme of Baum with the general habit mixture is used. Note the different y axes in the panels. Reprinted from Keshtgar et al. (2024). ©The Authors, CC BY 4.0 ⓒⓘ

Figure 7.10 shows that in all regions of the cyclone, the net CRH uncertainty due to 3D cloud-radiative effects and cloud horizontal heterogeneity with overlap assumption decrease with increases in the horizontal scale. In the WCB regions, these uncertainties decrease more rapidly than the uncertainty due to the ice optical parameterization (cf. green and dark-blue lines with red lines in Fig. 7.10b-d). This analysis indicates that while the CRH uncertainty due to 3D cloud-radiative effects is large at horizontal resolutions of hundreds of meters, its spatial extent is limited and it becomes less relevant at larger spatial extents. The uncertainty due to cloud horizontal heterogeneity shows a similar pattern but is larger than the uncertainty due to 3D cloud-radiative effects. In contrast, the uncertainty due to the ice optical parameterization is more or less constant as a function of horizontal scale in the WCB regions and dominates the uncertainty at spatial scales of 100 km or more. This is due to the large-scale stratiform ice clouds that cover entire domains in the WCB region of the cyclone, and therefore nearly the same level of uncertainty occurs over the entire domain.

Our analysis suggests that large-scale changes in the dynamics of the cyclone are more susceptible to CRH uncertainties due to cloud horizontal heterogeneity (assuming resolved clouds at the horizontal resolution of the NWP model) and ice optical parameterization than due to 3D cloud-radiative effects.

7.3 Discussion and Conclusions

We study CRH and its uncertainty within an idealized extratropical cyclone. To this end, we simulate an idealized extratropical cyclone with the ICON atmosphere model at a horizontal resolution of 2.5 km and focus on CRH within four regions of the cyclone with distinct cloud patterns: shallow cumulus clouds southwest of the cyclone center, deep clouds in the ascending region of the warm conveyor belt (WCB), stratiform low- and mid-level clouds in the WCB cyclonic outflow, and high stratiform ice clouds in the WCB anticyclonic outflow. For these four regions, we perform large-eddy-model (LEM) simulations at a horizontal resolution of 300 m, which we use to drive offline radiative transfer calculations. This provides a framework, for the first time, to assess and compare uncertainty in CRH due to four factors within an extratropical cyclone: 3D cloud-radiative effects, ice optical parameterization, cloud horizontal heterogeneity, and cloud vertical overlap. Since we can assume that clouds from the LEM simulations are perfectly known for the purpose of radiative transfer calculation, we quantify the last two factors by coarse-graining the LEM clouds to a horizontal resolution of 2.5 km, that of the NWP model. We create two sets of NWP homogeneous clouds, with and without cloud fraction. By doing so, we quantify to what extent ignorance of the cloud sub-grid variability at scales below 2.5 km affects CRH.

We find that 3D cloud-radiative effects are large at the scale of the horizontal grid resolution of 300 m but negligible on larger spatial scales of hundreds of kilometers. The 3D cloud-radiative effects are also more important for shallow cumulus clouds than for clouds within the WCB. Horizontal photon transport within the cloud and from the cloud sides is small in the three WCB regions, where more uniform stratiform clouds prevail. These results are consistent with previous findings that 3D cloud-radiative effects are small for stratiform clouds (Črnivec and Mayer, 2021) but important for the dynamics of shallow cumulus clouds (Jakub and Mayer, 2016).

The uncertainty in CRH due to different ice optical parameterizations is substantial in the WCB of the cyclone. We show that using the more complex ice optical parameterization of Baum leads to weaker shortwave and longwave CRH. Our analysis shows that the ice optical parameterization is the largest source of uncertainty in spatial scales of 500 km in the upper troposphere where ice clouds prevail. The uncertainty due to ice optical parameterization is also rather uniform in space, which suggests that it can affect the cyclone by modulating large-scale radiative heating. Our findings are consistent with the results of Zhao et al. (2018), who found that the ice scheme of Baum has a weaker effect on shortwave cloud-radiative effects compared to the ice scheme of Fu. Zhao et al. (2018) showed that the Baum scheme decreases static stability and increases vertical motion in the midlatitudes. An important potential implication of this result that should be tested in future work is to what extent this might enhance latent heating in the WCB ascent region and alter the dynamics of the cyclone (Keshtgar et al., 2023). Our expectation is in line with studies showing that perturbations on a larger spatial scale are more effective for baroclinic error growth (e.g., Sun and Zhang, 2016). Recently, Lloveras et al. (2023) showed that small-scale perturbations, even with large amplitudes, have a negligible impact on the dynamics of the

cyclone and the error growth near the tropopause compared to larger-scale perturbations with smaller amplitudes.

Cloud horizontal heterogeneity contributes significantly to CRH uncertainty in all regions of the cyclone. This is consistent with previous findings that when cloud sub-grid variability is neglected, both longwave CRH and shortwave CRH are overestimated (e.g., Črnivec and Mayer, 2019). The impact is strong for shallow cumulus clouds, but it is much smaller for the stratiform clouds in the WCB. Including the vertical overlap assumption significantly improves the simulation of CRH for shallow cumulus clouds but in fact slightly degrades CRH for clouds in the WCB since the maximum-random overlap assumption misrepresents the vertical arrangement of cloud layers in sheared flows, and a more complex form of the overlap assumption would be needed (e.g., Giuseppe and Tompkins, 2015). The comparison between the impact of cloud horizontal heterogeneity and cloud vertical overlap shows that for shallow cumulus clouds, vertical overlap has a stronger impact on CRH than cloud horizontal heterogeneity. In contrast, for stratiform clouds in the WCB, vertical overlap has a weaker effect on CRH compared to cloud horizontal heterogeneity. An interesting corollary of our work is that for extratropical cyclones, treating clouds as grid-box quantities in kilometer-scale models with resolutions of around 2 km appears to be a reasonable choice because schemes for cloud cover and vertical overlap themselves can act as sources of uncertainty that are rarely quantified. This supports the approach taken by Hohenegger et al. (2023) for the ICON-Sapphire kilometer-scale model, where they decided to remove the cloud cover scheme and treat grid boxes as either entirely cloudy or entirely cloud-free.

Our study indicates that improving the representation of ice optical properties is particularly relevant for the dynamics of extratropical cyclones. This is for several reasons. First, for the baroclinic error growth, the spatial scale of the uncertainty is more important than the amplitude of the uncertainty (e.g., Lloveras et al., 2023). Although 3D cloud-radiative effects are large at the scales of LEM grid resolution and have been shown to affect the organization of subtropical low-level clouds, their spatial extent is limited. Second, cloud sub-grid variability and 3D cloud-radiative effects can be taken into account in existing state-of-the-art radiation schemes such as TripleClouds (Črnivec and Mayer, 2021) and the Speedy Algorithm for Radiative Transfer through Cloud Sides (SPARTACUS; Hogan et al., 2016). Third, the parameterization of ice optical properties represents an important source of uncertainty and dominates the CRH uncertainty at larger scales.

Although advances in radiation solvers can account for both 3D radiative effects and cloud sub-grid variability, the lack of knowledge about the shape and surface roughness of ice particles continues to introduce large variability in CRH and remains a critical challenge for better representation of ice optical properties in models. Future work in the direction of ice optical properties should also address the problem that in many current models including ICON, the ice crystal effective radii are not treated consistently in the microphysics and radiation schemes (Sullivan and Voigt, 2021), and longwave cloud scattering is neglected (Fan et al., 2023). In view of our results, in Ch. 8 we investigate the impact of ice optical parameterization on the dynamics and predictability of North Atlantic cyclones.

8 Cloud-Radiative Impact on the Dynamics of North Atlantic Cyclones

In this chapter, we fully address research question 3: "How does CRH affect the dynamics of North Atlantic cyclones?". In particular, we address all of the following questions:

1. How strongly does CRH affect the dynamics of North Atlantic cyclones?
2. Is the mechanism underlying the CRH impact the same as for the idealized cyclone?
3. Do uncertainties in CRH have a measurable impact on near-tropopause dynamics?

To answer these questions, we perform hindcast simulations during the 2016 NAWDEX field campaign (Sect. 3.8). The simulation design is described in Sect. 8.1. The results are presented in Sect. 8.2 and summarized in Sect. 8.3.

8.1 Simulation Design

As described in Sect. 3.8, we run two control simulations, each covering the development of two cyclones corresponding with two Intensive Observing Periods (IOPs) of NAWDEX. Control simulations are run for 6 days. Here, the period of each IOP corresponds to the period of one cyclone development, and we refer to cyclones by their IOP number. (Tab. 8.1). Before we explain our simulation design, we provide a brief overview of the synoptic evolution of cyclones during each IOP from our ICON simulations (top and middle rows in Fig. 8.1). We further assess our ICON simulations against the ERA5 reanalysis with respect to the evolution of the cyclone central pressure (bottom row of Fig. 8.1).

IOP 3: Cyclone Vladiana formed through the interaction between an upper-level positive potential vorticity anomaly and a stationary surface low around 50°N and 40°W in a strong baroclinic zone (Fig. 8.1a). The cyclone intensified rapidly between 22 and 23 September 2016 and formed a strong elongated upper-level ridge east of the cyclone center associated with the anticyclonic branch of the WCB (Fig. 8.1b). In the late stages of the cyclone development, the upper-level ridge broke anticyclonically, forming a PV dipole over western Europe (Oertel et al., 2020). The central pressure of cyclone Vladiana reached a minimum of 975 hPa on 23 September 2016 at 16:00 UTC based on ERA5 and 978 hPa on 24 September 2016 at 00:00 UTC in our ICON simulation (Fig. 8.1c).

IOP 4: The extratropical transitioning of storm Karl during IOP 4 was a post-tropical stage of a long-lived tropical cyclone that reached its minimum surface pressure on 15 September 2016 and remained in the tropical Atlantic for 10 days (Euler et al., 2019). The storm then moved poleward and interacted

with a preexisting jet streak around 35°N and 60°W on 25 September (Fig. 8.1d). Karl then moved northeastward and merged with another extratropical low-pressure system and transitioned rapidly into an extratropical cyclone. The advection of low-PV in the outflow of the cyclone's WCB resulted in a cyclonically wave-breaking at tropopause level (Fig. 8.1e). The downstream development of the ridge associated with Karl led to a strong jet streak on 27 September and a secondary cyclone Walpurga that led to strong poleward moisture transport and widespread floods in Norway (Schäfler et al., 2018). The central pressure of Karl reached a minimum of 968 hPa on 26 September 2016 at 18:00 UTC based on ERA5. The central pressure in the ICON simulation slightly deepens to 965 hPa and peaks a bit later (Fig. 8.1f).
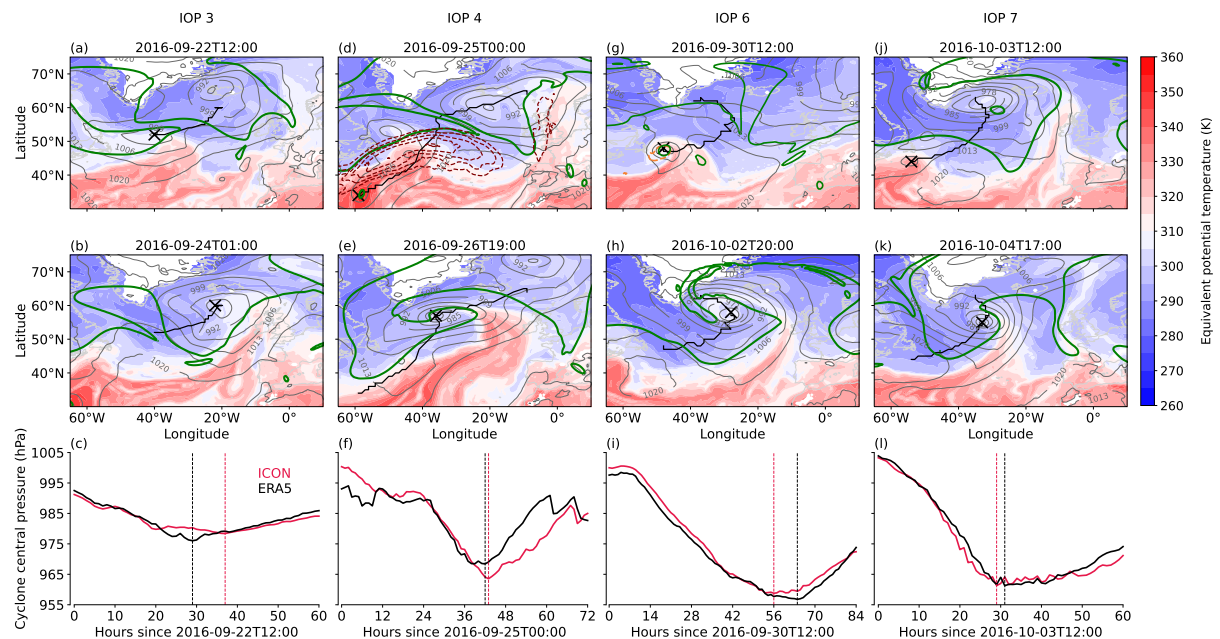
Figure 8.1: Snapshots of equivalent potential temperature at 850 hPa (color shading) and the mean sea level pressure (gray contour lines, hPa) at the start time of the cyclone development (top row) and at the time of the cyclone maximum intensity (middle row). The bottom row shows the evolution of the cyclone central pressure for ICON simulations (red) and ERA5 data (black). Results are shown during (a, b, c) IOP 3, (d, e, f) IOP 4, (g, h, i) IOP 6, and (j, k, l) IOP 7. The green contours in the map plots indicate the dynamic tropopause as given by the 2 PVU contour on the 320 K isentrope. The dark red contours in panel (d) show the wind speed at 200 hPa (every 10 m s^{-1} between 40-90 m s^{-1}). The orange contour in panel (g) shows the diabatic Rossby vortex as given by the 2 PVU contour on the 850 hPa isobaric surface. The black lines and the x markers in the map plots indicate the cyclone track and the position of the cyclone center. The vertical dashed lines in the bottom row plots indicate the maximum intensity times of the cyclones.

IOP 6: The Stalactite cyclone formed through an interaction between two vorticity maxima at low levels on 30 September 2016 at 12:00 UTC (Fig. 8.1g). The first vorticity maxima occurred due to a strong upper-level PV cut-off that was extended down to the surface similar to a Stalactite. The second vorticity maxima formed as a strong diabatic Rossby vortex, an isolated positive PV anomaly in a moist and baroclinic zone (Fig. 8.1g, orange contour). The interaction between the two vorticities led to an explosively deepening cyclone with a strong WCB and ridge building (Fig. 8.1h). In contrast to cyclone

Vladiana during IOP 3, the WCB in the Stalactite cyclone was dominated by the cyclonic branch and a cyclonically wave-breaking at the tropopause level (Fig. 8.1h). The cyclone reached a minimum central pressure of 957 hPa on 3 October 2016 based on ERA5. The cyclone reaches its maximum intensity earlier compared to ERA5 in our ICON simulation on 2 October 2016 at 20:00 UTC with a central pressure of 959 hPa (Fig. 8.1i).

IOP 7: The Frontal-wave cyclone initially developed on 2 October 2016 as a weak sea-level pressure depression in a strong baroclinic zone around $45°N$ and $60°W$ showing characteristics of a so-called diabatic Rossby wave (Boettcher and Wernli, 2013). The surface cyclone then interacted with an upper-level trough (Fig. 8.1j), and deepened strongly with a well-developed WCB east of the cyclone center. Similar to the Stalactite cyclone during IOP 6, the WCB of the Frontal-wave cyclone was associated with both cyclonic and anticyclonic outflows and the cyclonic-wave breaking during the maximum intensity of the cyclone (Fig. 8.1k). Between 4 and 5 October 2016, the anticyclonic outflow of the WCB re-enforced the ridge associated with the Stalactite cyclone during IOP 6 resulting in a long-lasting anticyclonic block Thor over Scandinavia (Maddison et al., 2019). The central pressure of the Frontal-wave cyclone in both ERA5 and our ICON simulation reached a minimum of 962 hPa around 3 October 2016 at 18:00 UTC.

Our ICON simulations capture the observed structure and evolution of the cyclones during the four IOPs (Schäfler et al., 2018). The evolution of the cyclone central pressure from our ICON simulations during each IOP also shows good agreement with the ERA5 data. Thus, we take the control simulations as references to compare them with simulations run with clear-sky radiative heating ("Clouds-off") to investigate the impact of CRH on cyclones (Sect. 3.4). Hereafter for simplicity, we refer to "Clouds-off" simulations as COOKIE simulations.

Table 8.1: The start and end times of control and COOKIE simulations.

Simulations	Start time	End time	IOPs covered
Control sim #1	22-09-2016, 00 UTC	28-09-2016, 00 UTC	3, 4
Control sim #2	30-09-2016, 00 UTC	06-10-2016, 00 UTC	6, 7
Short COOKIE #1	22-09-2016, 12 UTC	25-09-2016, 00 UTC	3
Short COOKIE #2	25-09-2016, 00 UTC	28-09-2016, 00 UTC	4
Short COOKIE #3	30-09-2016, 12 UTC	04-10-2016, 00 UTC	6
Short COOKIE #4	03-10-2016, 12 UTC	06-10-2016, 00 UTC	7
Long COOKIE #1	22-09-2016, 12 UTC	28-09-2016, 00 UTC	3, 4
Long COOKIE #2	30-09-2016, 12 UTC	06-10-2016, 00 UTC	6, 7

From the control simulations, we restart the model to perform COOKIE simulations at different times (Tab. 8.1). We run two sets of COOKIE simulations. In the first set, we run COOKIE simulations during the period of each IOP that covers the development of one cyclone. In the second set, we run longer COOKIE simulations for the entire period of each control simulation. These simulations are only relevant for the development of the cyclones during IOPs 4 and 7, since the results of the model simulations during IOPs 3 and 6 are the same between the short and the long COOKIE simulations. With

the longer COOKIE simulations, we test to what extent the dynamics of the cyclones during IOPs 4 and 7 change due to the long absence of CRH. To distinguish between different COOKIE simulations, we refer to the first set as "short COOKIE" and the second set as "long COOKIE" simulations (Tab. 8.1).

For the analysis, we use the climate data operators (Schulzweida, 2019) to remap the model output from the unstructured triangular grid to the regular 0.5°×0.5° and 1°×1° latitude-longitude grids using the conservative interpolation method. We use the 1°×1° interpolated data sets to track the central pressure of the cyclones, and for the calculation of the PV error growth diagnostic. This is consistent with our analysis approach in Ch. 4. In Sect. 4.2.2 we argued that the potential enstrophy tendency budget closes better on a 1°×1° grid. For all other analyses, we use the 0.5°×0.5° interpolated data sets.

8.2 Results

In this section, we characterize the impact of CRH on the dynamics of the four North Atlantic cyclones in terms of cyclone central pressure, changes within the ascending regions of the cyclones, and potential vorticity. To this end, we compare simulations with and without CRH. To examine the mechanism of the CRH impact, we use the potential vorticity error growth framework (Sect. 1.4). We then assess the impact of CRH uncertainties on the evolution of potential vorticity near the tropopause.

8.2.1 Cloud-Radiative Impact on the Cyclones

To assess the impact of CRH on the intensity of the cyclones, we compare the evolution of the cyclone central pressure during each IOP between the control and the short COOKIE simulations (cf. red and blue lines in Fig. 8.2). According to this metric, CRH has no significant impact on the intensity of the cyclones. However, CRH has a stronger effect when we compare the evolution of the cyclone central pressure between the control and the long COOKIE simulations, especially during IOP 4 (cf. green and red lines in Fig. 8.2b). The long absence of CRH in the COOKIE simulation leads to a significant 20 hPa weakening of the cyclone during IOP 4. In comparison, the long absence of CRH has a much smaller weakening impact on the Frontal-wave cyclone during IOP 7 (Fig. 8.2d).
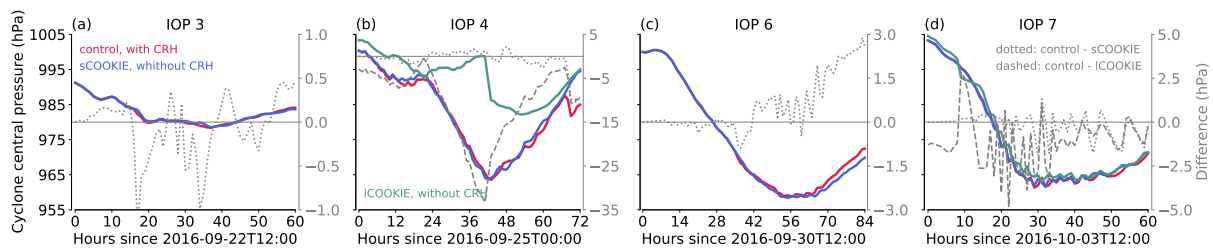

Figure 8.2: Evolution of the cyclone central pressure during (a) IOP 3, (b) IOP 4, (c) IOP 6, and (d) IOP 7 for the control simulations with CRH (red) and the short (blue) and long (green) COOKIE simulations without CRH (Tab. 8.1). Note the different second y axes: gray dotted lines show differences in cyclone central pressure between control and short COOKIE simulations, while gray dashed lines show differences between control and long COOKIE simulations.

Although the absence of CRH during IOP 3 has a negligible effect on the central pressure of cyclone Vladiana, it significantly affects the intensity of the subsequent tropical-extratropical cyclone Karl during IOP 4. During IOP 4, the ECMWF ensemble forecasts exhibited a large spread, as the extratropical transition of storm Karl was very sensitive to the location and timing of the interaction of the storm with the jet stream (Schäfler et al., 2018). Therefore, the absence of CRH prior to the development of the cyclone during IOP 4 may have changed the location and intensity of the storm, as well as the structural configuration of the upper-level jet stream. These changes, collectively, could exert a notable influence on the trajectory and the development of the cyclone during IOP 4 (Fig. 8.2b, green line).

Cloud-Radiative Impact Within the Ascending Regions of the Cyclones

We now investigate the impact of CRH on the dynamics of the cyclones at mid- and upper-levels to assess its implications for the evolution of the large-scale flow near the tropopause.

In Sect. 4.2.2 we showed that CRH affects the dynamics of the idealized cyclone mainly through changes in latent heating and vertical motion within the WCB of the cyclone. We thus examine the impact of CRH within the ascending regions of the cyclones. The ascending regions can be defined as areas with high concentrations of total column-integrated cloud hydrometeors content as they typically indicate regions of strong updrafts. For illustration, Fig. 8.3a shows a snapshot of the vertical velocity at 5 km on 4 October 2016 at 12:00 UTC. The closed green contours indicate the ascending regions using a threshold of $0.2 \, \mathrm{kg \, m^2}$ of the total column-integrated cloud hydrometeors content. The ascending regions coincide with areas of strong updraft and strong precipitation rate (blue shadings and dark red dashed contours in Fig. 8.3a).
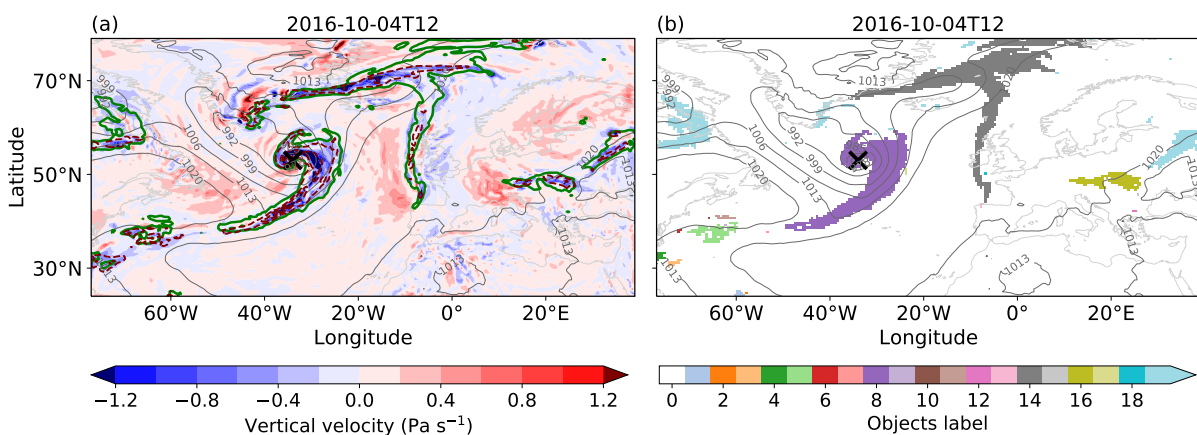
Figure 8.3: Panel (a) shows vertical velocity at 5 km (color shading) and mean sea level pressure (gray contours, hPa) on October 4, 2016 at 12:00 UTC. The green contours indicate ascending regions given by the 0.2 kg m^2 contour of the total column-integrated cloud hydrometeors content. The dark red dashed contours indicate the precipitation rate (every 2 mm hr^{-1} between 1-10 mm hr^{-1}). Panel (b) shows ascending regions from panel (a) as labeled objects, identified through connected component labeling. The x markers indicate the center of the Frontal-wave cyclone.

We use an object-based method to identify and track the ascending regions. To this end, we use the connected component labeling algorithm of the Scipy Python Package (Virtanen et al., 2020) to convert the ascending regions into objects with unique labels (Fig. 8.3b). We then track labeled objects for 1 day during the development phase of the cyclones during each IOP. For the analysis, we select objects associated with the cyclones during each IOP according to their proximity to the central pressure of the cyclone and use them as masks to spatially average variables only over the grid boxes that fall within the objects. For example, object 8 in Fig. 8.3b is associated with the ascending regions of the Frontal-wave cyclone during IOP 7.

Figure 8.4 shows the evolution of the precipitation rate within the ascending regions of the four cyclones during each IOP for the control and COOKIE simulations. CRH increases the precipitation rate for all cyclones. The long absence of CRH in the long COOKIE simulation dramatically weakens the precipitation rate for the cyclone during IOP 4, while it slightly decreases the precipitation rate for the cyclone during IOP 7 (Fig. 8.4b and d).
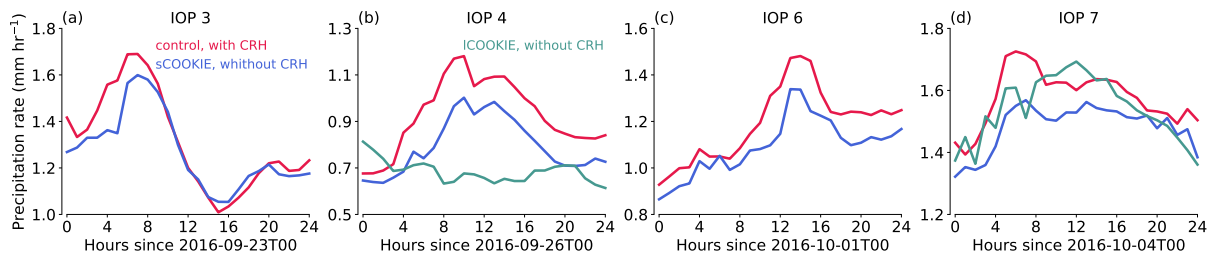
Figure 8.4: Evolution of the spatially averaged precipitation rate over the area of the ascending regions of cyclones for the control (red), short (blue), and long (green) COOKIE simulations. Results are shown for cyclones during (a) IOP 3, (b) IOP 4, (c) IOP 6, and (d) IOP 7. Note the different y axes in the panel plots.

The CRH-induced increase in precipitation rate suggests that CRH affects the microphysical properties of clouds in the ascending regions of cyclones. This can change the amount of total latent heating and alter the vertical motion. To demonstrate this, Fig. 8.5 shows vertical profiles of net radiative and microphysical heating, as well as vertical velocity within the ascending regions of cyclones for the control and COOKIE simulations. We compute the vertical profiles by averaging the variables over the time interval shown in Fig. 8.4 during each IOP. The microphysical heating is mostly due to heating from cloud microphysical processes involving ice and rain evaporation. Here we do not consider the heating rates from condensation and evaporation of vapor and liquid water, which are calculated by the saturation adjustment scheme.

Within the ascending regions of the four cyclones, CRH leads to stronger cooling at upper levels between 8-12 km and weaker cooling at mid and low levels. The stronger cooling at upper levels is due to longwave cloud-top radiative cooling, while the weaker cooling at mid- and low levels is due to longwave cloud-radiative warming in the lower part of the cloud. Both effects are absent in the COOKIE simulations (Fig. 8.5, top row). On the one hand, due to the dipole of cloud-top radiative cooling and

warming at the cloud base, clouds become more buoyant and unstable, resulting in stronger latent heating. This is shown by the enhanced cloud microphysical heating in the control simulations compared to the COOKIE simulations (Fig. 8.5, middle row). On the other hand, enhanced latent heating promotes stronger mean upward motion within the ascending regions of the cyclones (Fig. 8.5, bottom row). Both enhanced microphysical heating and vertical velocity favor stronger cyclonic vorticity.

The long absence of CRH in the long COOKIE simulation substantially weakens microphysical heating and vertical motion within the ascending regions of the cyclone during IOP 4. These responses are consistent with the strong weakening of the cyclone central pressure and precipitation rate during IOP 4 in the long COOKIE simulation (Fig. 8.2b and Fig. 8.4b). In contrast, the vertical motion gets stronger during IOP 7 in the long COOKIE simulation compared to the vertical motion in the short COOKIE simulation. This response is consistent with the higher precipitation rate in the long COOKIE simulation than in the short COOKIE simulation during IOP 7 (Fig. 8.4d).
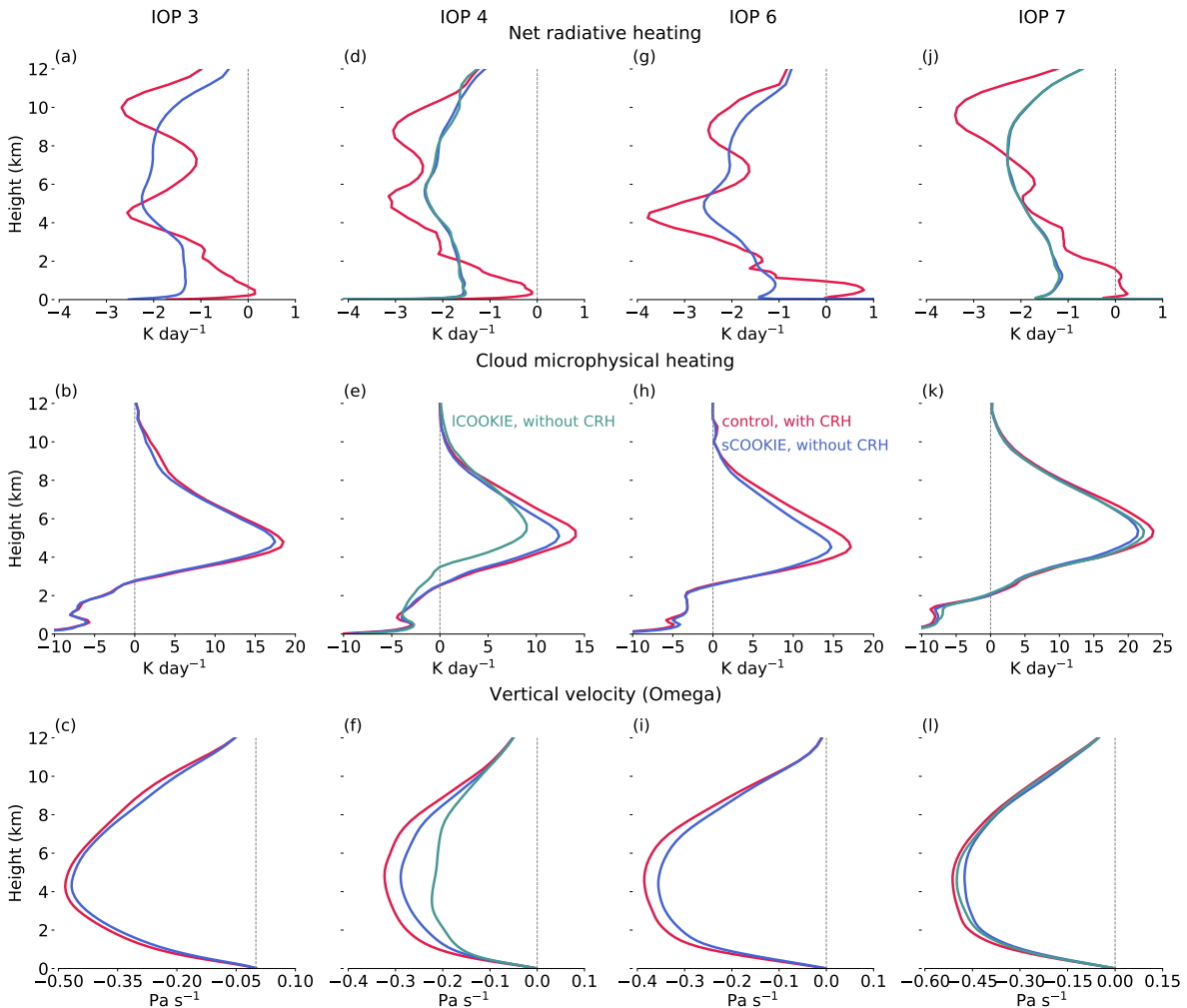
Figure 8.5: Profiles of net radiative heating (top row), microphysical heating (middle row), and vertical velocity (bottom row). The profiles are spatially averaged over the identified objects and temporally averaged over the time interval shown in Fig. 8.4. Profiles are shown for the control simulation (red) and the short (blue) and long (green) COOKIE simulations for (a, b, c) IOP 3, (d, e, f) IOP 4, (g, h, i) IOP 6, and (j, k, l) IOP 7.

Our results show a systematic and robust impact of CRH on precipitation rate, microphysical heating, and vertical motion. We observe that an increase in one of these variables corresponds to an increase in the others. Moreover, through this analysis, we can establish the importance of CRH for large-scale atmospheric circulation because changes in the upward motion within the ascending regions of the cyclones affect the divergent flow near the tropopause and the distribution of the potential vorticity. Changes in the near-tropopause potential vorticity in turn affect the dynamics of the cyclone and the development of the large-scale atmospheric circulation (Baumgart et al., 2018; Keshtgar et al., 2023).

Cloud-Radiative Impact on Potential Vorticity

To investigate the impact of CRH on large-scale atmospheric circulation, the same as the analysis for the idealized cyclone in the channel simulations (Sect. 4.2.1), we examine changes in PV near the tropopause. To demonstrate the impact of CRH on PV near the tropopause, we calculate PV differences on 320 K isentrope between the control and short COOKIE simulations at the time of the cyclone peak intensity during each IOP (Fig. 8.6).
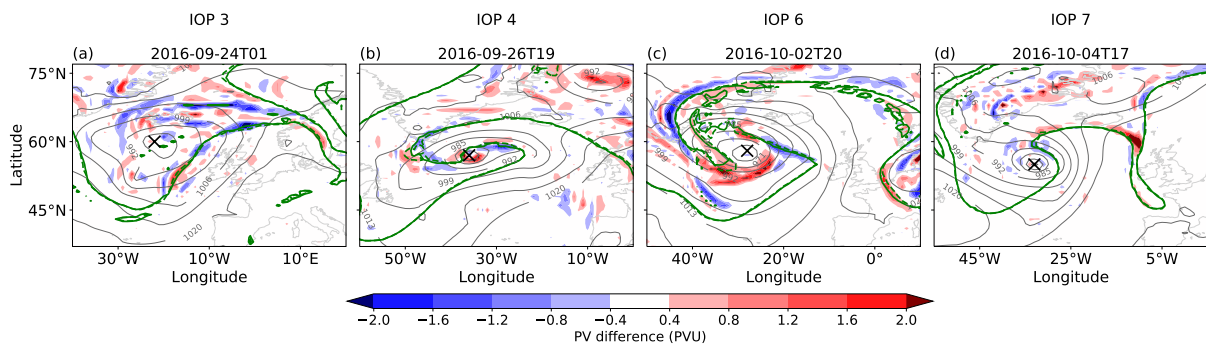
Figure 8.6: PV differences between the control and short COOKIE simulations (control-COOKIE) near the tropopause on 320 K isentrope at the time of cyclone peak intensity during (a) IOP 3, (b) IOP 4, (c) IOP 6, and (d) IOP 7. The gray contours show the mean sea level pressure (in units of hPa) for the control simulation. The solid and dashed green contours indicate the dynamical tropopause given by the 2 PVU contours for the control and short COOKIE simulations, respectively. The x markers indicate the position of the cyclone center.

PV differences between the control and short COOKIE simulations grow within a period of 1 to 2 days and reach the tropopause level during all four IOPs. PV differences are distributed both along the dynamical tropopause and within the domain (Fig. 8.6). However, PV differences do not grow to substantial values until the cyclones reach their maximum intensity, as the positions of the troughs and ridges do not change significantly.

In contrast, PV differences grow to larger values between the control and long COOKIE simulations during IOPs 4 and 7 (Fig. 8.7). The long absence of CRH results in a weaker ridge amplitude and trough near the tropopause during IOP 4. The weaker ridge is evident by the blue shadings west and north of the cyclone center, and the weaker trough by the red shadings east of the cyclone center in Fig. 8.7a. The weaker ridge and trough not only lead to the weakening of the cyclone but also delay its development

(e.g., Keshtgar et al., 2023). Both effects are evident from the evolution of the cyclone central pressure and precipitation rate during IOP 4 in the long COOKIE simulation (Fig. 8.2b and Fig. 8.4b).

The PV differences between the control and long COOKIE simulation during IOP 7 are not as large as the differences we see during IOP 4. However, the long absence of CRH results in a weaker ridge. This is evident from the blue shadings northeast of the cyclone center in Fig. 8.7b.

The comparison of the CRH impact on PV near the tropopause between the short and long COOKIE simulations shows that it takes about 4 days for CRH to significantly affect the tropopause wave. Furthermore, PV differences grow to larger values during IOP 4 than during IOP 7. These results demonstrate that the CRH impact grows over time and its magnitude depends on large-scale atmospheric conditions.
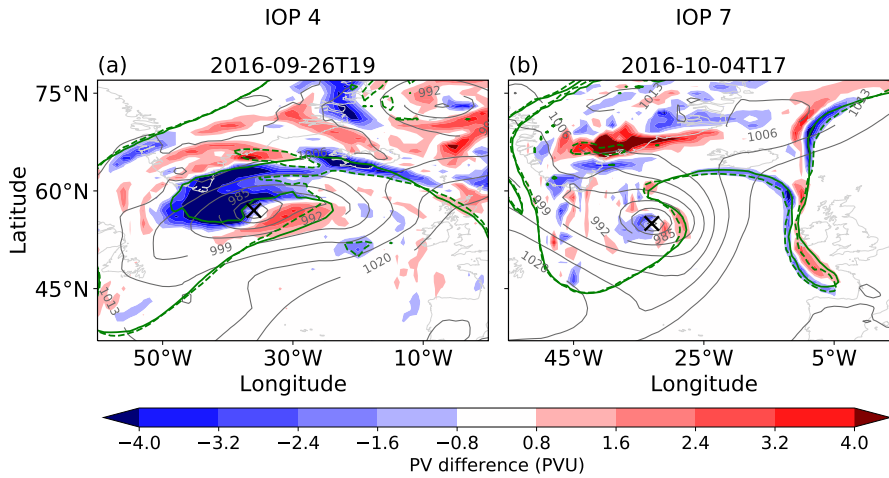
Figure 8.7: Same as Fig. 8.6 but for PV differences between the control and long COOKIE simulations at the time of cyclone peak intensity during (a) IOP 4 and (b) IOP 7.

8.2.2 Mechanism of the Cloud-Radiative Impact

To gain a process-based understanding of the impact of CRH, consistent with the analysis strategy for the idealized cyclone in the channel simulations (Sect. 4.2.2), we investigate the impact of CRH on the evolution of PV differences near the tropopause using the PV error growth framework of Baumgart et al. (2018, 2019). In Sect. 1.4 we described the framework in detail. Here, we apply the framework considering the control simulations as the reference analysis, and the COOKIE simulations as the forecast:

$$\Delta PV = PV_{\text{control}} - PV_{\text{COOKIE}}. \tag{8.1}$$

Following Baumgart et al. (2019), we calculate the potential enstrophy ($\mathscr{PV} = \frac{(\Delta PV)^2}{2}$) tendency equation:

$$\frac{d\mathscr{PV}}{dt} = \mathscr{PV}_{rot} + \mathscr{PV}_{div} + \mathscr{PV}_{dia} + BND + RES, \tag{8.2}$$

where $\mathscr{PV}_{rot}$ and $\mathscr{PV}_{div}$ measure the contributions from changes in PV advection by the rotational and divergent wind, respectively. The contributions from changes in diabatic heating and nonconservative momentum are given by $\mathscr{PV}_{dia}$. In addition, we account for the boundary effect due to PV differences being advected into or out of the analysis domain, which is between 24 to 79°N and 77°W to 39°E (*BND* term in Eq. 8.2). For reference, the full equation of the potential enstrophy tendency is shown by Eq. 9 of Baumgart et al. (2019).

Evolution of Difference Potential Enstrophy

We calculate the potential enstrophy tendency and the contributions from different processes according to Eq. 8.2 near the tropopause on 320 K isentrope during all four IOPs between the control and short COOKIE simulations. Following our analysis in Sect. 4.2.2, we first consider the time series of spatially averaged tendencies in Fig. 8.8.
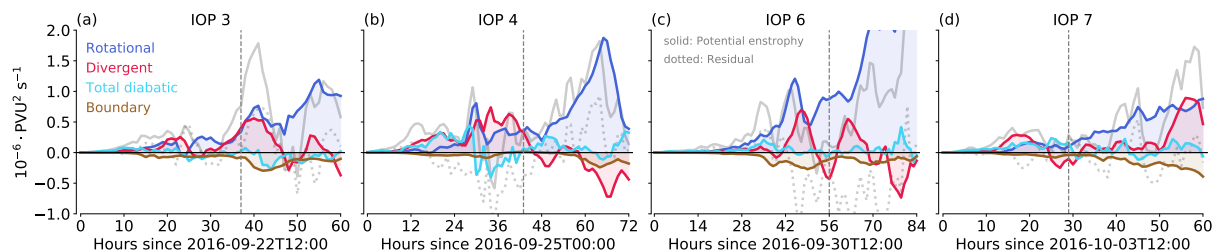
Figure 8.8: Evolution of spatially averaged potential enstrophy over the analysis domain (gray solid) and the contribution from individual processes diagnosed from the r.h.s. of Eq. 8.2 during (a) IOP 3, (b) IOP 4, (c) IOP 6, and (d) IOP 7. The dotted gray lines represent the residuals calculated as the difference between the l.h.s. and the sum of r.h.s. terms of Eq. 8.2. Vertical dashed lines indicate the maximum cyclone intensity times.

During all four IOPs, the diabatic tendencies are comparable in magnitude to the advective tendencies in the early stages of the cyclone development (cyan lines in Fig. 8.8). However, the advective tendencies quickly become larger and dominate the evolution of the potential enstrophy at the time of maximum cyclone intensity and later during the nonlinear stage of the baroclinic wave development (red and blue lines in Fig. 8.8). Thus, consistent with our results for the idealized cyclone in Ch. 4, CRH cannot substantially modify PV near the tropopause. In fact, it is the indirect impact of CRH on the divergent and rotational flows that drives substantial changes in PV.

To distinguish between the contribution of different processes to the evolution of difference potential enstrophies at different times, we consider the time series of spatially averaged relative tendencies:

$$\alpha_{rot,div,dia} = \frac{1}{\mathscr{PV}}\left(\mathscr{PV}_{rot,div,dia}\right). \tag{8.3}$$

Fig. 8.9 shows the evolution of the spatially averaged relative tendencies diagnosed from Eq. 8.3. During all four IOPs, the evolution of the difference potential enstrophy is dominated by diabatic tendencies during the first 10 hours (cyan lines in Fig. 8.9). Since the only difference between the control and

COOKIE simulations is the presence of CRH, the diabatic tendencies during this period are dominated by radiation (dark blue dashed lines in Fig. 8.9). The diabatic modification of PV then precedes further changes by the divergent tendencies as a result of latent heating modulation by CRH within the ascending regions of cyclones (red lines in Fig. 8.9). Changes in the divergent flow subsequently affect the PV advection by the rotational flow and dominate the evolution of the potential enstrophy during the highly nonlinear stage of the cyclone development (blue lines in Fig. 8.9). This multi-stage mechanism of CRH impact on near-tropopause dynamics is the same as the mechanism we identified for CRH impact on the idealized cyclone in Ch. 4.
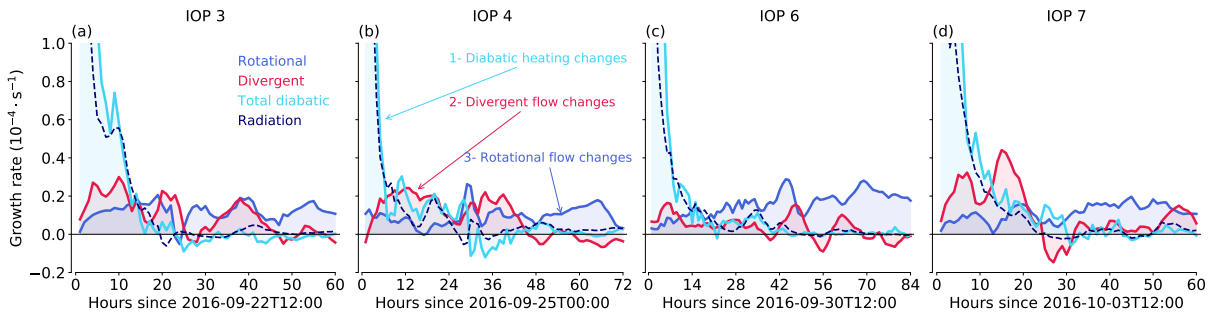
Figure 8.9: Contribution to the relative growth of spatially averaged potential enstrophy over the analysis domain from the rotational and divergent flows as well as from total diabatic processes and radiation during (a) IOP 3, (b) IOP 4, (c) IOP 6, and (d) IOP 7.

We now examine the evolution of difference potential enstrophy between the control and long COOKIE simulations (Fig. 8.10). All diagnosed tendencies from Eq. 8.2 during IOPs 3 and 6 are the same as tendencies calculated between the control and short COOKIE simulations.

The evolution of the difference potential enstrophy during IOPs 4 and 7 between the control and long COOKIE simulations differ from the tendencies calculated between the control and short COOKIE simulations (Fig. 8.10a, c). This is because PV differences between the control and long COOKIE simulations during IOPs 4 and 7 are built on top of the existing PV differences caused earlier by CRH during IOPs 3 and 6. The potential enstrophy tendency increases significantly during IOP 4 (Fig. 8.10a). The CRH-induced changes in total latent heating within the ascending regions of the cyclone during IOP 4 (red line in Fig. 8.10b) again precede the strong PV modification by the divergent flow (second peak of the divergent tendency around hour 88 in Fig. 8.10a). Substantial changes in the divergent and rotational flow (red and blue lines in Fig. 8.10a) then further enhance the potential enstrophy. This explains the weakening of the ridge and the delayed cyclonic wave breaking during IOP 4 in the long COOKIE simulation (Fig. 8.7a).

In contrast, the evolution of difference potential enstrophy does not grow substantially during IOP 7 (Fig. 8.10c). The decomposition of the diabatic tendency shows that CRH-induced changes in the total latent heating, although positive, are not as large as the changes occurring during IOP 4 (Fig. 8.10d), and differences in the divergent flow, in fact, act to dampen the growth of existing PV differences (Fig. 8.10c).

Our results show that the growth of difference potential enstrophy depends on how strongly diabatic heating changes within the ascending regions of the cyclones. During IOP 4, CRH significantly changes the amount of total latent heating and the divergent flow, which supports the amplification of difference potential enstrophy. However, the CRH-induced changes in diabatic heating and divergent flow during IOP 7 are not as strong as changes during IOP 4, and the evolution of the potential enstrophy is dictated by the near-tropopause large-scale flow. This result also explains why the long absence of CRH in the long COOKIE simulations has a stronger impact on the cyclone intensity metrics during IOP 4 than IOP 7 (Fig. 8.2 and Fig. 8.4).
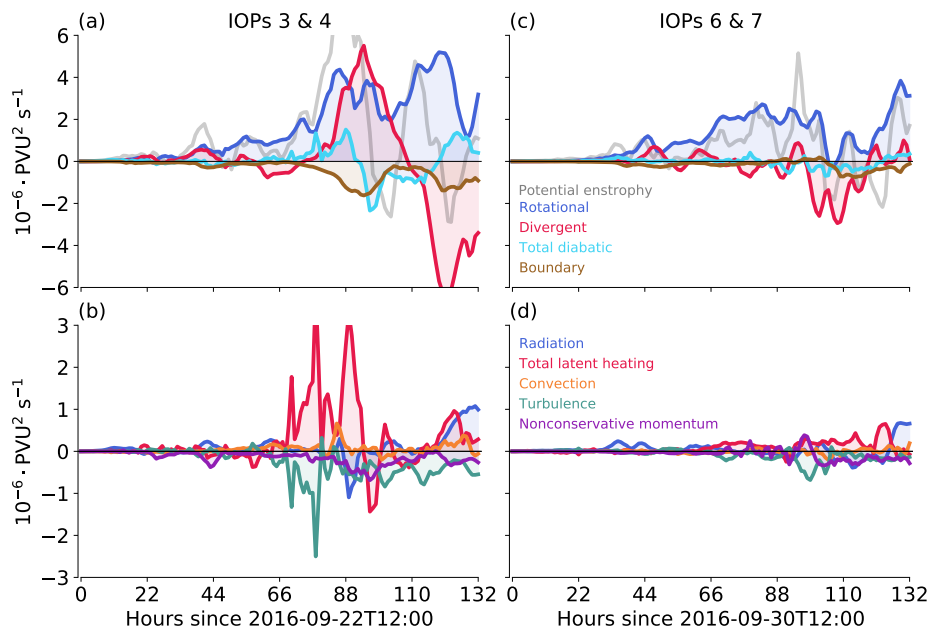
Figure 8.10: The top row shows the evolution of the spatially averaged potential enstrophy (gray solid) over the analysis domain and the contribution from individual processes diagnosed from the r.h.s. of Eq. 8.2. The bottom row shows the decomposition of the total diabatic tendency into the contributions of the individual diabatic processes. Results are shown during (a, b) IOPs 3 and 4 and (c, d) IOPs 6 and 7.

Overall, the multi-stage mechanism of the CRH impact on PV near the tropopause is the same as the mechanism we identified in our idealized study in Ch. 4. Regardless of whether PV differences initially grow upscale, or whether PV differences are amplified from existing differences at the tropopause, the impact of CRH works predominantly through the continuous modulation of latent heating within the ascending regions of the cyclones, and subsequently through changes in the divergent and rotational flows near the tropopause.

8.2.3 Impact of Cloud-Radiative Heating Uncertainties on Potential Vorticity

In this section, we examine the impact of CRH uncertainties on the evolution of potential vorticity near the tropopause to assess their implication for cyclone predictability. To this end, we repeat our control simulations (Sect.3.8) but perturb CRH instead of disabling it entirely.

Simulations with Perturbed Cloud-Radiative Heating

Many factors contribute to the uncertainty in simulating CRH in models, ranging from poor representations of clouds in models and the parameterization of the radiative transfer calculation. Here we focus on the uncertainty associated with the parameterization of radiation. In Ch. 7 we quantified uncertainties in CRH within an idealized extratropical cyclone associated with the radiation parameterization. The results suggest that uncertainties in the parameterization of ice optical properties and cloud horizontal heterogeneity may affect the dynamics and predictability of cyclones. These uncertainties significantly affect the CRH within the WCB of the cyclone, and thus may alter the latent heating. Moreover, these uncertainties affect CRH on spatial scales of 100 km and more due to the dominant large-scale stratiform clouds within the WCB of the cyclones. The latter argument is motivated by studies showing that temperature perturbations with larger spatial scales have a stronger impact on upscale error growth (e.g., Sun and Zhang, 2016; Lloveras et al., 2023).

To account for uncertainties in CRH due to the parameterization of ice optical properties and cloud horizontal heterogeneity, we run simulations with the same setup as the control simulations (Sect. 3.8), but with a different ice optical scheme, radiation solver, and radiation scheme. Table 8.2 summarizes the differences between the simulations that we use to assess the impact of CRH uncertainties on PV near the tropopause.

Table 8.2: List of ICON simulations with their radiation settings to assess the impact of CRH uncertainties on PV near the tropopause. See Chs. 1, and 3 for details and differences between ice optical schemes, radiation solvers, and radiation schemes.

Simulation name	Radiation scheme	Radiation solver	Cloud water and ice optical schemes
McICA_Fu (control)	ecRad	McICA	SOCRATES / Fu
McICA_Baran	ecRad	McICA	SOCRATES / Baran
TripleCLD_Fu	ecRad	Tripleclouds	SOCRATES / Fu
RRTM_ECHAM	RRTM	RRTM	ECHAM6

The McICA_Fu simulation is the control simulation we used in the previous sections of this chapter. In the McICA_Baran simulation, we use the ice optical scheme of Baran et al. (2014) instead of Fu (Fu, 1996; Fu et al., 1998). In the TripleCLD_Fu simulation, we change the default radiation solver in ecRad from the Monte Carlo Independent Column Approximation (McICA; Pincus et al., 2003) to the Tripleclouds solver (Shonk and Hogan, 2008). In the RRTM_ECHAM simulation, we completely switch the radiation scheme from ecRad to the Rapid Radiative Transfer Model (RRTM; Mlawer et al., 1997). To illustrate how strongly CRH changes between these simulations, Fig. 8.11 shows differences in the net radiative heating profiles between simulations with perturbed CRH and the control simulations. Profiles of net radiative heating for different simulations are derived from spatially and temporally averaged net radiative heating within the ascending regions of the cyclones (see Sect. 8.2.1).

Changing the radiation solver from McICA to Tripleclouds has a weak impact on CRH (blue lines in Fig. 8.11). However, changing the ice optical parameterization from Fu to Baran leads to stronger cloud-top radiative cooling and warming in the lower part of the cloud (green lines in Fig. 8.11). The largest difference in CRH occurs when we completely switch the radiation scheme from ecRad to RRTM. Similar to changes in the ice optical parameterization, using the RRTM radiation scheme strongly increases cloud-top radiative cooling and warming at the cloud base. We expect that stronger radiative cooling at the cloud top and warming at the cloud base result in stronger CRH-induced changes in total latent heating within the ascending regions of the cyclones and ultimately in a stronger potential enstrophy tendency near the tropopause.
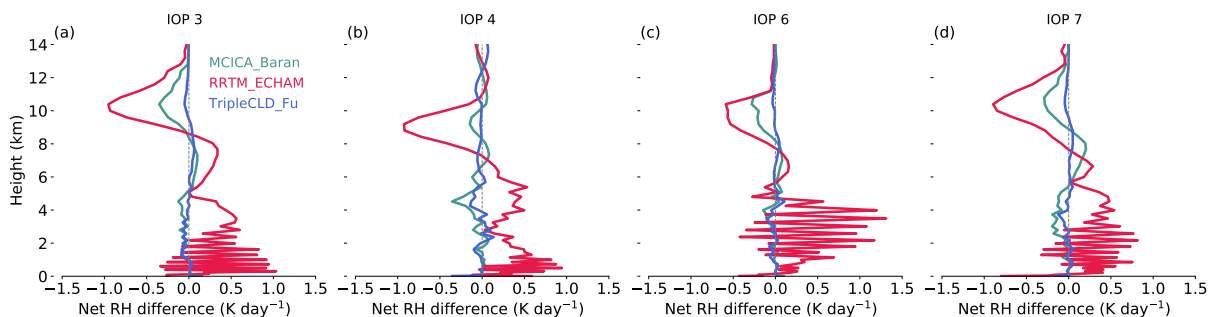
Figure 8.11: Profiles of net radiative heating (RH) differences within the ascending regions of the cyclones calculated between simulations with perturbed CRH and the control simulation during (a) IOP 3, (b) IOP 4, (c) IOP 6, and (d) IOP 7.

Evolution of Difference Potential Enstrophy

Same as the analysis in Sect. 8.2.2, we assess the impact of CRH uncertainties on PV near the tropopause by calculating the difference potential enstrophy tendencies between simulations with perturbed CRH and the control simulations. We apply the PV error growth framework considering the control simulations (McICA _Fu) as the reference and the perturbed CRH simulations as forecasts.

The first row of Fig. 8.12 shows the evolution of the difference potential enstrophy during all four IOPs. The middle and bottom rows show the contributions from the divergent and rotational tendencies, respectively. For comparison, we also include the potential enstrophy tendencies and the contribution from divergent and rotational flows calculated between the control and the long COOKIE simulations already shown in Fig. 8.10 as dotted gray lines.

CRH uncertainties affect PV near the tropopause, and the magnitude of the impact is comparable to that of CRH alone. The impact of CRH uncertainties on the potential enstrophy tendency is small during IOPs 3 and 6, but becomes larger during IOPs 4 and 7 (Fig. 8.12a, b). This is because changes in the divergent flow associated with the subsequent cyclones during IOPs 4 and 7 help to modify the rotational flow further and amplify the potential enstrophy tendency (middle and bottom rows of Fig. 8.12). Thus, CRH uncertainties affect near-tropopause dynamics in the same way as the multi-stage mechanism of the CRH impact on near-tropopause PV as we described in Sect. 8.2.2.
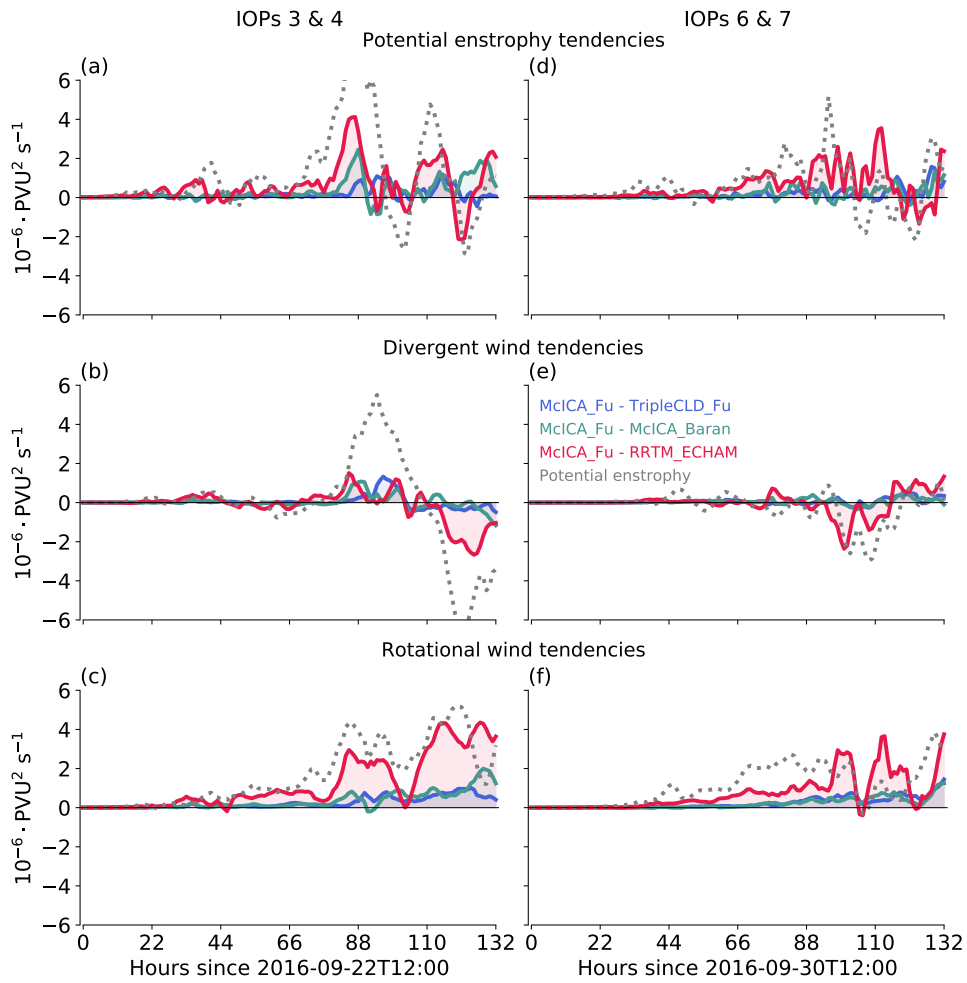
Figure 8.12: The top row shows the evolution of the spatially averaged potential enstrophy tendencies calculated between the control simulation (McICA_Fu) and simulations with perturbed CRH (Tab. 8.1). The middle and the bottom rows show the contribution from the divergent and rotational wind tendencies, respectively. The gray dotted lines in the plots are for tendencies calculated between the control and the long COOKIE simulations shown in Fig. 8.10

The impact of CRH uncertainties on the evolution of difference potential enstrophy depends on the magnitude of the CRH uncertainty, such that larger CRH uncertainties result in larger difference potential enstrophy tendencies. The largest differences in the near-tropopause PV develop between the McICA_Fu and the RRTM_ECHAM simulations. The RRTM radiation scheme leads to stronger cloud-top radiative cooling and warming from below, resulting in larger changes in total latent heating and consequently in the divergent flow (middle row in Fig. 8.12). Therefore, changes in the rotational flow are also stronger and the potential enstrophy tendencies grow to larger values (bottom row in Fig. 8.12).

8.3 Discussion and Conclusions

We perform hindcast simulations during the 2016 NAWDEX field campaign to investigate the impact of CRH, and its uncertainty, on the dynamics of North Atlantic cyclones. We focus on four IOPs during

NAWDEX: IOPs 3, 4, 6, and 7, each associated with an extratropical cyclone. To study the impact of CRH, we compare simulations with and without CRH.

We find that during the 1-2 day development phase of the cyclones, CRH has a weak impact on the cyclone central pressure. In Ch. 4 we suggested that small changes in the net diabatic PV tendency at lower levels and in the boundary layer, mainly due to the compensation between enhanced turbulence and latent heating PV tendencies, could explain the weak impact of CRH near the surface. However, we show that CRH substantially increases the precipitation rate within the ascending regions of the North Atlantic cyclones. Cloud-top radiative cooling and modest cloud-radiative warming in the lower part of the cloud, destabilize clouds within the ascending regions of the cyclones and alter the amount of latent heating. The CRH-induced increase in latent heating coincides with enhanced upward motion and changes in PV near the tropopause. These results are consistent with our findings in Ch. 4.

To investigate whether the CRH impact follows the identified mechanism of the CRH impact on the idealized cyclone, we apply the PV error growth framework of Baumgart et al. (2018, 2019). We find the same multi-stage impact of CRH on PV near the tropopause as for the idealized cyclone. CRH enhances the latent heating in the ascending regions of cyclones, leading to changes in the divergent flow near the tropopause. Following changes in the divergent flow, differences in potential vorticity are amplified by changes in the rotational flow during the highly nonlinear stage of the cyclone development.

The multi-stage mechanism of CRH impact on near-tropopause dynamics is similar to the upscale growth of initial state uncertainty from the convective scale to the synoptic scale (Baumgart et al., 2019). This might suggest that CRH acts as a random initial perturbation that grows upscale in a generic way. However, consistent with the idealized cyclone study (Sect. 4.2.3), here we also show that CRH impact works predominantly through changes in the divergent flow associated with latent heating modulation within the ascending regions of the cyclones.

An interesting result of our work is that it takes about 4 days for CRH to significantly affect the dynamics of the cyclone and the PV near the tropopause. The CRH impact also depends on the synoptic-scale configuration of the atmosphere. The 4-day absence of CRH in the simulations has a stronger impact on the dynamics of the cyclone and the PV near the tropopause during IOP 4. The predictability during the extratropical development of storm Karl was low for the eastern North Atlantic (Schäfler et al., 2018). The ECMWF ensemble forecast simulations showed a large spread during IOP 4, as the extratropical transition of Karl was shown to be very sensitive to uncertainties in the location and timing of the interaction of the storm with the upstream trough (Schäfler et al., 2018). Thus, the absence of CRH in the simulation prior to the extratropical transition of Karl leads to changes in the location and intensity of the storm, as well as in the near-tropopause dynamics, which overall significantly altered the evolution of the cyclone during IOP 4. However, this is not the case for the cyclone during IOP 7, where atmospheric predictability was high.

Our simulations with perturbed CRH show that uncertainties in CRH associated with the radiation parameterization affect the PV near the tropopause and follow the same mechanism of the CRH impact.

We find a direct relationship between the magnitude of the CRH uncertainty and the growth of the PV differences near the tropopause. We believe that future work should further investigate the impact of CRH and its uncertainties on the dynamics of more diverse cyclones and their impact on the simulation of WCBs, assessing their impact on forecast error growth.

9 Conclusions and Outlook

In this chapter, we summarize the main results and present the overarching findings to the research questions laid out in Ch. 2. We also discuss questions that arise from this thesis to give an outlook on possible future work.

Conclusions

Extratropical cyclones determine weather and climate in the midlatitudes. While baroclinicity is the main driver of extratropical cyclones, their dynamics and predictability are strongly influenced by diabatic processes. Work on diabatic impacts has mainly focused on latent heating (Wernli and Gray, 2023). In contrast, the impact of cloud-radiative heating (CRH) on the dynamics of extratropical cyclones is understudied. Schäfer and Voigt (2018) were the only ones to show that CRH significantly weakens idealized extratropical cyclones on the weather time scale of days. However, a dynamical mechanism by which CRH affects cyclones remained elusive in their work. In addition, several previous studies showed that errors in the parameterization of diabatic processes associated with extratropical cyclones can lead to significant forecast errors near the tropopause (e.g., Joos and Forbes, 2016; Baumgart et al., 2019). CRH is a persistent source of uncertainty in weather and climate models, therefore it is important to assess CRH uncertainties and their impact on the dynamics of extratropical cyclones and the near-tropopause circulation.

In this thesis, we investigated the impact of CRH on the dynamics of extratropical cyclones and its implications for cyclone predictability. We performed simulations using the ICON model in different setups and applied different methodologies. Our investigation involved idealized baroclinic life cycle simulations in both global and channel setups, as well as hindcast simulations during the 2016 NAWDEX field campaign. We developed new modeling approaches to study the impact of CRH on the dynamics of extratropical cyclones in a clean and easy-to-interpret manner. To provide a systematic assessment of CRH uncertainties, we investigated the sensitivity of CRH to model settings over the North Atlantic. We quantified uncertainties in CRH due to radiation parameterization by combining large-eddy-model simulations and offline radiative transfer calculations over different regions of an idealized cyclone. Using this multifaceted approach, we aimed to provide a comprehensive understanding of the interplay between cloud-radiation interactions occurring at the micro-scale and changes in the atmospheric circulation at the synoptic scale and to highlight the importance of accurate simulation of CRH for cyclone prediction.

In Chs. 4 and 5, we addressed research question 1 **"How does CRH affect the dynamics of idealized extratropical cyclones?"**. Our results show that CRH affects idealized cyclones in a substantial and model-dependent manner. CRH affects the dynamics of cyclones mainly through the modulation of latent heating and subsequent changes in the large-scale flow. The main findings with respect to the detailed questions are as follows:

1.1. How strongly does CRH affect the intensity of extratropical cyclones?

CRH has a substantial impact on the intensity of the idealized cyclones. We found a robust strengthening impact of CRH on cyclones in both the global and the channel setups. Moreover, we showed that the impact of CRH is most pronounced at upper levels near the tropopause and weaker near the surface. According to the vertically integrated eddy kinetic energy metric, CRH changes the intensity of idealized cyclones by more than 5%. The CRH impact is comparable to changes in the zonal wind strength by $10\,\mathrm{m\,s^{-1}}$ (Tierney et al., 2018), uniform atmospheric warming by $6\,\mathrm{K}$, or a change in the pole-to-equator temperature contrast by $10\,\mathrm{K}$ (Rantanen et al., 2019). CRH also increases the total cloud cover and precipitation rate of idealized extratropical cyclones.

1.2. What are the mechanisms that underlie the cloud-radiative impact?

To understand how CRH affects the upper-tropospheric circulation, we analyzed the evolution of potential vorticity (PV) near the tropopause between a simulation with and without CRH using the PV error growth framework of Baumgart et al. (2018, 2019). We show that CRH affects the dynamics of an idealized extratropical cyclone mainly through its impact on latent heating. Near the tropopause, direct diabatic modification of potential vorticity by intensified latent heating precedes further changes in the tropopause by the upper-tropospheric divergent flow, which represents an indirect impact of latent heating. Subsequently, differences in the tropopause structure amplify with the rotational flow during the highly nonlinear stage of the baroclinic wave. As a result, CRH increases the amplitude of the baroclinic wave and delays the wave breaking, both of which contribute to stronger cyclone development.

1.3. What does this imply for the cloud-radiative impact on cyclone predictability?

CRH affects the dynamics of the cyclone and near-tropopause PV through continuous changes in the latent heating during the growth phase of the cyclone. Our analysis shows that eddy kinetic energy and tropopause wave amplitude amplify as long as CRH is present in the simulation. This mechanism distinguishes the CRH impact from the upscale error growth mechanism, which describes how small-scale errors grow upscale and affect the synoptic-scale atmospheric circulation (Baumgart et al., 2019). Therefore, uncertainties in CRH could affect the magnitude of latent heating and may be relevant for error growth near the tropopause. In Ch. 5 we showed that differences in the vertical distribution of clouds change the sign of the CRH impact. Thus, it is possible, and

indeed not unlikely, that different model simulations of CRH can significantly affect the development of cyclones, and that the uncertainties in CRH can affect numerical forecasts at synoptic scales.

In Chs. 6 and 7, we addressed research question 2 **"How large are the CRH uncertainties in the extratropical atmosphere, and which uncertainties are relevant to the dynamics of extratropical cyclones?"**. We showed that high-resolution simulations provide a better representation of the cloud field for simulating CRH. We then found that for resolved cloud fields within an extratropical cyclone, the parameterization of ice optical properties remains an important source of uncertainty for the CRH on larger spatial scales and is therefore relevant for the large-scale dynamics of the cyclone. The main findings with respect to the detailed questions are as follows:

2.1. How does CRH change with model settings over the North Atlantic?

We showed that with the two-moment microphysics scheme, switching from parametrized to explicit convection has a stronger impact on the CRH than using the one-moment scheme. We traced the model dependency of CRH to differences in the ice mass mixing ratio, which quadruples with model resolution from 80 km to a convection-permitting resolution of 2.5 km. We showed that significant changes in the ice mass mixing ratio are due to higher ice growth and sedimentation rates in the two-moment scheme, as well as higher instances of vertical velocities at refined resolutions. These results highlight the benefit of high-resolution simulations that allow direct interaction of updrafts with the cloud field.

2.2. How does CRH change due to the uncertainties in radiation parameterization?

We showed that cloud horizontal heterogeneity and ice optical parameterization contribute more to the mean CRH uncertainty than 3D cloud-radiative effects within an idealized extratropical cyclone. The 3D cloud-radiative effects are large on the scale of the horizontal grid resolution of 300 m, but negligible on larger spatial scales of hundreds of kilometers. The 3D cloud-radiative effects are more important for shallow cumulus clouds than for clouds within the WCB. However, differences in the ice optical parameterization significantly change the mean CRH in the WCB of the cyclone. We show that the ice optical scheme of Baum leads to weaker shortwave and longwave CRH than the ice optical scheme of Fu. Neglecting cloud horizontal heterogeneity at the 2.5 km resolution also significantly affects CRH in all regions of the cyclone, resulting in an overestimation of the shortwave and longwave CRH. We show that accounting for vertical cloud overlap with the maximum random overlap assumption significantly improves the simulation of CRH for shallow cumulus clouds, but degrades CRH for clouds in the WCB.

2.3. What is the implication of CRH uncertainties for the dynamics of extratropical cyclones?

Studies show that the spatial scale of the uncertainty is more important than the amplitude of the uncertainty for baroclinic error growth (e.g., Sun and Zhang, 2016; Lloveras et al., 2023).

Therefore, CRH uncertainties with large spatial scales are more important and relevant for the dynamics of extratropical cyclones. Therefore, 3D cloud-radiative effects cannot significantly affect the dynamics of extratropical cyclones as we showed that their spatial extent is limited within extratropical cyclones. Moreover, 3D cloud radiative effects and cloud sub-grid variability can be accounted for in existing state-of-the-art radiation schemes. Thus, we argued that the uncertainty due to the ice optical parameterization is more relevant for the dynamics of extratropical cyclones. This is because we showed that not only changes in the ice optical parameterizations dominate the CRH uncertainty at larger spatial scales of 500 km in the upper troposphere, but also a lack of consolidated knowledge about the ice optical properties and how to represent them in the model continues to introduce large variability in the CRH.

In Ch. 8 we addressed research question 3 **"How does CRH affect the dynamics of North Atlantic cyclones?"**. Our results show that CRH substantially affects the dynamics of North Atlantic cyclones and the mechanism of the CRH impact is the same as the mechanism we identified for idealized cyclones. We showed that CRH uncertainties can affect the evolution of PV near the tropopause. The main findings with respect to the detailed questions are as follows:

3.1. How strongly does CRH affect the dynamics of North Atlantic cyclones?

CRH has a negligible impact on the central pressure of the four North Atlantic cyclones during their 1-2 day development phase. However, consistent with idealized studies, we show that CRH enhances the precipitation rate, latent heating, and vertical motion within the ascending regions of the cyclones. Our results demonstrate that it takes about 4 days for CRH to significantly affect the dynamics of the cyclones. In particular, the 4-day absence of CRH prior to the extratropical transition of storm Karl during IOP 4 of the NAWDEX, significantly weakened the intensity of the cyclone by 20 hPa.

3.2. Is the mechanism underlying the CRH impact the same as for the idealized cyclone?

We found the same multi-stage mechanism of the CRH impact we identified in the idealized studies. During the growth phase of the cyclones, CRH alters the latent heating and vertical motion within the ascending regions of the cyclones and subsequently the divergent flow near the tropopause. Following changes in the divergent flow, differences in the PV amplify with the changes in the rotational flow.

In addition, we showed that the magnitude of the CRH impact on PV near the tropopause depends on the large-scale configuration of the atmospheric circulation. In particular, for cyclone Karl during IOP 4 of the NAWDEX, the absence of CRH before and during the extratropical transition significantly affects the latent heating within the ascending regions of the cyclone and subsequently the divergent flow near the tropopause. This is because the extratropical transition of Karl was shown to be very sensitive to uncertainties in the location and timing of the interaction of the

storm with the upstream trough (Schäfler et al., 2018). However, the impact of CRH during IOP 7, which is associated with an explosive cyclone, is not as strong as the impact during IOP 4.

3.3. Do uncertainties in CRH have a measurable impact on near-tropopause dynamics?

We showed that uncertainties in the CRH associated with differences in radiation schemes and ice optical parameterization considerably affect the evolution of potential vorticity near the tropopause. Furthermore, we found a direct relationship between the magnitude of the CRH uncertainty and the growth of PV differences near the tropopause, such that larger CRH uncertainties lead to larger PV differences.

The research conducted in this thesis brought together expertise in high-resolution modeling, climate and atmospheric dynamics, cloud physics, and radiation, emphasizing the interactions between research at the microphysical scale of clouds and the large-scale atmospheric circulation in the midlatitudes. Together with idealized and hindcast simulations of extratropical cyclones, we made a strong case that CRH is not only important for the evolution of the large-scale circulation on climate time scales of years, but also for the dynamics of extratropical cyclones on weather time scales of days.

With models moving to storm-resolving kilometer-scale resolutions, the emerging need to reconsider and improve the treatment of radiative transfer in climate and weather models has become a priority. In this thesis, we showed for the first time how model representation of cloud-radiative interactions affects the evolution of extratropical cyclones and the large-scale flow near the tropopause. We demonstrated that uncertainties in simulations of CRH can contribute to the forecast error growth. Therefore, our results can provide insights into how the radiative transfer representation in models should be adapted to improve model predictions of cyclones.

Outlook

In this thesis, we showed that CRH has a substantial impact on the dynamics of extratropical cyclones, mainly through modulation of latent heating within the warm conveyor belts of the cyclones. We showed that the model uncertainty in clouds and CRH can be large enough to change even the sign of the CRH impact on the intensity of the cyclones. Moreover, our hindcast simulations showed that the impact of the CRH increases with time and depends on the configuration of the large-scale flow. These results warrant further studies on various aspects of the CRH impact on extratropical cyclones, as discussed below.

To gain a deeper understanding of the impact of CRH, we need to consider how different cyclones respond to the impact of CRH. Therefore, we suggest that future studies investigate the impact of CRH on an ensemble of cyclones. We also recommend investigating the impact of CRH using a combination of process-based analysis methods, such as the potential vorticity framework and Lagrangian trajectory analysis. These efforts can provide insight into how strongly CRH affects the dynamics of cyclones under

different synoptic conditions. In addition, these efforts help to identify specific synoptic conditions under which uncertainties in CRH can lead to substantial forecast error growth.

With respect to the impact of CRH uncertainties for forecast error growth, our study was limited to uncertainties due to changes in radiation schemes and ice optical parameterization. However, further investigation in this direction is required. In ICON and many other models, the effective radius of cloud crystals is solely a function of ice water content, and cloud droplet effective radius is a function of cloud water content and an externally prescribed droplet number concentration. This has created an inconsistency between cloud microphysics and radiation (Kretzschmar et al., 2020; Sullivan and Voigt, 2021). Moreover, cloud longwave scattering is not taken into account in the default radiation model setup, yet studies show that it considerably affects CRH and subsequently the meridional and vertical gradients in atmospheric temperature and the midlatitude circulation (e.g., Gu et al., 2021; Fan et al., 2023).

Our hindcast simulations in this thesis were performed with a rather coarse horizontal resolution of 10 km. However, in Ch. 6 we show that CRH varies dramatically with explicit representation of convection at the kilometer-scale resolutions and the more complex two-moment microphysics scheme. Therefore, future studies should study to what extent these uncertainties affect the evolution of cyclones and the large-scale flow near the tropopause. It would also be insightful to compare the impact of CRH uncertainties on forecast error growth with that of microphysical processes, as this allows to put the importance of CRH uncertainties into context.

Our focus in this thesis was mainly on the impact of CRH on cyclones at the synoptic scale. However, further studies are needed to understand how CRH affects cyclone characteristics at the mesoscale, such as changes in frontal structure, wind fields, and precipitation bands. We showed that changes in latent heating and cloud microphysics by CRH affect the dynamics of the warm conveyor belt and the large-scale flow. Therefore, we suggest that future studies further investigate the impact of CRH and its uncertainty on cloud microphysical processes, mesoscale circulation, and precipitation rate within extratropical cyclones.

We suggest performing simulations in the limited area mode at a convective-permitting resolution to simulate warm conveyor belts and combine them with large-eddy-model simulations. We recommend studying cyclones during the NAWDEX field campaign because their dynamics have been well studied and detailed airborne observations are available. Moreover, large-eddy-model simulations have the advantage of better simulating cloud microphysical properties and precipitation compared to models with coarser horizontal resolutions (e.g., Griewank et al., 2020; Stevens et al., 2020). Large-eddy-model simulations also allow us to prescribe the large-scale flow at the lateral boundaries and focus only on the impact of CRH uncertainties at the mesoscale. The impact of CRH uncertainties can then be assessed within warm conveyor belts to uncertainties in microphysical processes and further evaluated against NAWDEX observations.

Another powerful method to understand the interplay between cloud microphysics and CRH would be "piggybacking" (Grabowski, 2019), which allows one to isolate the impact of CRH on cloud microphysics in the absence of dynamic changes. Therefore, this approach can explicitly explore the impact of CRH on latent heating within the warm conveyor belt of a cyclone and further verify the mechanism of the CRH impact on cyclones that we identified in this thesis.

Our findings in this thesis, along with our recommendations for future research, will help to understand the potential need to adjust the representation of radiative transfer in weather and climate models. If future studies demonstrate that uncertainties in CRH have a systematic impact on the dynamics of extratropical cyclones and forecast error growth, this would strongly advocate for numerical weather prediction centers to review their approach to modeling radiative transfer calculation.

10 Bibliography

Ahmadi-Givi, F., Graig, G. C., and Plant, R. S.: The dynamics of a midlatitude cyclone with very strong latent-heat release, Q. J. R. Meteorol. Soc., 130, 295–323, https://doi.org/https://doi.org/10.1256/qj.02.226, 2004.

Albern, N., Voigt, A., and Pinto, J. G.: Cloud-Radiative Impact on the Regional Responses of the Midlatitude Jet Streams and Storm Tracks to Global Warming, J. Adv. Model. Earth Syst., 11, 1940–1958, https://doi.org/10.1029/2018ms001592, 2019.

Anthes, R. A., Kuo, Y.-H., and Gyakum, J. R.: Numerical Simulations of a Case of Explosive Marine Cyclogenesis, Mon. Weather Rev., 111, 1174–1188, https://doi.org/10.1175/1520-0493(1983)111<1174:nsoaco>2.0.co;2, 1983.

Balasubramanian, G. and Garner, S. T.: The Role of Momentum Fluxes in Shaping the Life Cycle of a Baroclinic Wave, J. Atmos. Sci., 54, 510 – 533, https://doi.org/10.1175/1520-0469(1997)054<0510:tromfi>2.0.co;2, 1997.

Baran, A. J., Hill, P., Furtado, K., Field, P., and Manners, J.: A Coupled Cloud Physics–Radiation Parameterization of the Bulk Optical Properties of Cirrus and Its Impact on the Met Office Unified Model Global Atmosphere 5.0 Configuration, J. Climate, 27, 7725 – 7752, https://doi.org/https://doi.org/10.1175/JCLI-D-13-00700.1, 2014.

Barekzai, M. and Mayer, B.: Broadening of the Cloud Droplet Size Distribution due to Thermal Radiative Cooling: Turbulent Parcel Simulations, J. Atmos. Sci., 77, 1993 – 2010, https://doi.org/10.1175/jas-d-18-0349.1, 2020.

Baum, B. A., Yang, P., Heymsfield, A. J., Bansemer, A., Cole, B. H., Merrelli, A., Schmitt, C., and Wang, C.: Ice cloud single-scattering property models with the full phase matrix at wavelengths from 0.2 to 100µm, J. Quant. Spectrosc. Radiat. Transfer, 146, 123–139, https://doi.org/https://doi.org/10.1016/j.jqsrt.2014.02.029, 2014.

Baumgart, M., Riemer, M., Wirth, V., Teubler, F., and Lang, S. T. K.: Potential Vorticity Dynamics of Forecast Errors: A Quantitative Case Study, Mon. Weather Rev., 146, 1405–1425, https://doi.org/10.1175/mwr-d-17-0196.1, 2018.

Baumgart, M., Ghinassi, P., Wirth, V., Selz, T., Craig, G. C., and Riemer, M.: Quantitative view on the processes governing the upscale error growth up to the planetary scale using a stochastic convection scheme, Mon. Weather Rev., 147, 1713–1731, https://doi.org/10.1175/mwr-d-18-0292.1, 2019.

Bechtold, P., Köhler, M., Jung, T., Doblas-Reyes, F., Leutbecher, M., Rodwell, M. J., Vitart, F., and Balsamo, G.: Advances in simulating atmospheric variability with the ECMWF model: From synoptic to decadal time-scales, Q. J. R. Meteorol. Soc., 134, 1337–1351, https://doi.org/10.1002/qj.289, 2008.

Bertrand, L., Kay, J. E., Haynes, J., and de Boer, G.: A global gridded dataset for cloud vertical structure from combined CloudSat and CALIPSO observations, Earth Syst. Sci. Data, 16, 1301–1316, https://doi.org/10.5194/essd-16-1301-2024, 2024.

Bodas-Salcedo, A., Williams, K. D., Ringer, M. A., Beau, I., Cole, J. N. S., Dufresne, J.-L., Koshiro, T., Stevens, B., Wang, Z., and Yokohata, T.: Origins of the Solar Radiation Biases over the Southern Ocean in CFMIP2 Models, J. Climate, 27, 41–56, https://doi.org/10.1175/jcli-d-13-00169.1, 2014.

Boer, G. J. and Lambert, S.: The energy cycle in atmospheric models, Clim Dyn, 30, 371–390, https://doi.org/10.1007/s00382-007-0303-4, 2008.

Boettcher, M. and Wernli, H.: A 10-yr Climatology of Diabatic Rossby Waves in the Northern Hemisphere, Mon. Weather Rev., 141, 1139 – 1154, https://doi.org/10.1175/mwr-d-12-00012.1, 2013.

Bony, S., Stevens, B., Frierson, D. M. W., Jakob, C., Kageyama, M., Pincus, R., Shepherd, T. G., Sherwood, S. C., Siebesma, A. P., Sobel, A. H., Watanabe, M., and Webb, M. J.: Clouds, circulation and climate sensitivity, Nature Geosci, 8, 261–268, https://doi.org/10.1038/ngeo2398, 2015.

Booth, J. F., Wang, S., and Polvani, L.: Midlatitude storms in a moister world: Lessons from idealized baroclinic life cycle experiments, Clim. Dynam., 41, 787–802, https://doi.org/10.1007/s00382-012-1472-3, 2013.

Boutle, I. A., Beare, R. J., Belcher, S. E., Brown, A. R., and Plant, R. S.: The moist boundary layer under a mid-latitude weather system, Bound.-Layer Meteorol., 134, 367–386, https://doi.org/10.1007/s10546-009-9452-9, 2010.

Boutle, I. A., Belcher, S. E., and Plant, R. S.: Friction in mid-latitude cyclones: an Ekman-PV mechanism, Atmos. Sci. Lett., 16, 103–109, https://doi.org/10.1002/asl2.526, 2015.

Butz, K.: The radiative impact of clouds on idealized extratropical cyclones, Master's thesis, University of Vienna, https://doi.org/10.25365/thesis.71895, 2022.

Büeler, D. and Pfahl, S.: Potential Vorticity Diagnostics to Quantify Effects of Latent Heating in Extratropical Cyclones. Part I: Methodology, J. Atmos. Sci., 74, 3567–3590, https://doi.org/10.1175/jas-d-17-0041.1, 2017.

Cahalan, R. F., Ridgway, W., Wiscombe, W. J., Bell, T. L., and Snider, J. B.: The Albedo of Fractal Stratocumulus Clouds, J. Atmos. Sci., 51, 2434–2455, https://doi.org/10.1175/1520-0469(1994)051<2434:taofsc>2.0.co;2, 1994.

Catto, J. L.: Extratropical cyclone classification and its use in climate studies, Rev. Geophys., 54, 486–520, https://doi.org/10.1002/2016rg000519, 2016.

Ceppi, P. and Hartmann, D. L.: Connections Between Clouds, Radiation, and Midlatitude Dynamics: a Review, Curr. Clim. Change Rep., 1, 94–102, https://doi.org/10.1007/s40641-015-0010-x, 2015.

Chagnon, J. M., Gray, S. L., and Methven, J.: Diabatic processes modifying potential vorticity in a North Atlantic cyclone, Q. J. R. Meteorol. Soc., 139, 1270–1282, https://doi.org/10.1002/qj.2037, 2013.

Charney, J. G.: The Dynamics Of Long Waves In A Baroclinic Westerly Current, J. Atmos. Sci., 4, 136–162, https://doi.org/10.1175/1520-0469(1947)004<0136:tdolwi>2.0.co;2, 1947.

Costa-Surós, M., Sourdeval, O., Acquistapace, C., Baars, H., Carbajal Henken, C., Genz, C., Hesemann, J., Jimenez, C., König, M., Kretzschmar, J., Madenach, N., Meyer, C. I., Schrödner, R., Seifert, P., Senf, F., Brueck, M., Cioni, G., Engels, J. F., Fieg, K., Gorges, K., Heinze, R., Siligam, P. K., Burkhardt, U., Crewell, S., Hoose, C., Seifert, A., Tegen, I., and Quaas, J.: Detection and attribution of aerosol–cloud interactions in large-domain large-eddy simulations with the ICOsahedral Non-hydrostatic model, Atmos. Chem. Phys., 20, 5657–5678, https://doi.org/10.5194/acp-20-5657-2020, 2020.

Črnivec, N. and Mayer, B.: Quantifying the bias of radiative heating rates in numerical weather prediction models for shallow cumulus clouds, Atmos. Chem. Phys., 19, 8083–8100, https://doi.org/10.5194/acp-19-8083-2019, 2019.

Črnivec, N. and Mayer, B.: Towards an improved treatment of cloud–radiation interaction in weather and climate models: exploring the potential of the Triplecloud method for various cloud types using libRadtran 2.0.4, Geosci. Model Dev., 14, 3663–3682, https://doi.org/10.5194/gmd-14-3663-2021, 2021.

Davies, H. C., Schär, C., and Wernli, H.: The Palette of Fronts and Cyclones within a Baroclinic Wave Development, J. Atmos. Sci., 48, 1666–1689, https://doi.org/10.1175/1520-0469(1991)048<1666:tpofac>2.0.co;2, 1991.

Dipankar, A., Stevens, B., Heinze, R., Moseley, C., Zängl, G., Giorgetta, M., and Brdar, S.: Large eddy simulation using the general circulation model ICON, J. Adv. Model. Earth Syst., 7, 963–986, https://doi.org/https://doi.org/10.1002/2015MS000431, 2015.

Doms, G., Förstner, J., Heise, E., Herzog, H.-J., Mironov, D., Raschendorfer, M., Reinhardt, T., Ritter, B., Schrodin, R., Schulz, J.-P., and Vogel, G.: A Description of the Nonhydrostatic Regional COSMO Model Part II : Physical Parameterization, Tech. rep., URL `www.cosmo-model.org`, 2011.

Donner, L. J., O'Brien, T. A., Rieger, D., Vogel, B., and Cooke, W. F.: Are atmospheric updrafts a key to unlocking climate forcing and sensitivity?, Atmos. Chem. Phys., 16, 12 983–12 992, https://doi.org/10.5194/acp-16-12983-2016, 2016.

Eady, E. T.: Long Waves and Cyclone Waves, Tellus, 1, 33–52, https://doi.org/10.3402/tellusa.v1i3.8507, 1949.

Edwards, J. M. and Slingo, A.: Studies with a flexible new radiation code. I: Choosing a configuration for a large-scale model, Q. J. R. Meteorol. Soc., 122, 689–719, https://doi.org/https://doi.org/10.1002/qj.49712253107, 1996.

Emde, C., Buras-Schnell, R., Kylling, A., Mayer, B., Gasteiger, J., Hamann, U., Kylling, J., Richter, B., Pause, C., Dowling, T., and Bugliaro, L.: The libRadtran software package for radiative transfer calculations (version 2.0.1), Geosci. Model Dev., 9, 1647–1672, https://doi.org/10.5194/gmd-9-1647-2016, 2016.

Ertel, H.: Ein neuer hydrodynamischer Wirbelsatz, Met. Z., 59, 277–281, 1942.

Euler, C., Riemer, M., Kremer, T., and Schömer, E.: Lagrangian Description of Air Masses Associated with Latent Heat Release in Tropical Storm Karl (2016) during Extratropical Transition, Mon. Weather Rev., 147, 2657–2676, https://doi.org/10.1175/mwr-d-18-0422.1, 2019.

Fan, C., Chen, Y.-H., Chen, X., Lin, W., Yang, P., and Huang, X.: A Refined Understanding of the Ice Cloud Longwave Scattering Effects in Climate Model, J. Adv. Model. Earth Syst., 15, e2023MS003 810, https://doi.org/https://doi.org/10.1029/2023MS003810, 2023.

Fovell, R. G., Bu, Y. P., Corbosiero, K. L., Tung, W.-w., Cao, Y., Kuo, H.-C., Hsu, L.-h., and Su, H.: Influence of Cloud Microphysics and Radiation on Tropical Cyclone Structure and Motion, Meteor. Mon., 56, 1–11, https://doi.org/10.1175/amsmonographs-d-15-0006.1, 2016.

Fu, Q.: An Accurate Parameterization of the Solar Radiative Properties of Cirrus Clouds for Climate Models, J. Climate, 9, 2058 – 2082, https://doi.org/https://doi.org/10.1175/1520-0442(1996)009<2058:AAPOTS>2.0.CO;2, 1996.

Fu, Q. and Liou, K. N.: On the Correlated k-Distribution Method for Radiative Transfer in Nonhomogeneous Atmospheres, J. Atmos. Sci., 49, 2139 – 2156, https://doi.org/https://doi.org/10.1175/1520-0469(1992)049<2139:OTCDMF>2.0.CO;2, 1992.

Fu, Q. and Liou, K. N.: Parameterization of the Radiative Properties of Cirrus Clouds, J. Atmos. Sci., 50, 2008 – 2025, https://doi.org/https://doi.org/10.1175/1520-0469(1993)050<2008:POTRPO>2.0.CO;2, 1993.

Fu, Q., Krueger, S. K., and Liou, K. N.: Interactions of Radiation and Convection in Simulated Tropical Cloud Clusters, J. Atmos. Sci., 52, 1310 – 1328, https://doi.org/10.1175/1520-0469(1995)052<1310: ioraci>2.0.co;2, 1995.

Fu, Q., Yang, P., and Sun, W. B.: An Accurate Parameterization of the Infrared Radiative Properties of Cirrus Clouds for Climate Models, J. Climate, 11, 2223 – 2237, https://doi.org/https://doi.org/10. 1175/1520-0442(1998)011<2223:AAPOTI>2.0.CO;2, 1998.

Gassmann, A. and Herzog, H.-J.: Towards a consistent numerical compressible non-hydrostatic model using generalized Hamiltonian tools, Q. J. R. Meteorol. Soc., 134, 1597–1613, https://doi.org/10.1002/ qj.297, 2008.

Giorgetta, M. A., Brokopf, R., Crueger, T., Esch, M., Fiedler, S., Helmert, J., Hohenegger, C., Kornblueh, L., Köhler, M., Manzini, E., Mauritsen, T., Nam, C., Raddatz, T., Rast, S., Reinert, D., Sakradzija, M., Schmidt, H., Schneck, R., Schnur, R., Silvers, L., Wan, H., Zängl, G., and Stevens, B.: ICON-A, the Atmosphere Component of the ICON Earth System Model: I. Model Description, J. Adv. Model. Earth Syst., 10, 1613–1637, https://doi.org/https://doi.org/10.1029/2017MS001242, 2018.

Giuseppe, F. D. and Tompkins, A. M.: Generalizing Cloud Overlap Treatment to Include the Effect of Wind Shear, J. Atmos. Sci., 72, 2865 – 2876, https://doi.org/https://doi.org/10.1175/JAS-D-14-0277. 1, 2015.

Grabowski, W. W.: Separating physical impacts from natural variability using piggybacking technique, Adv. Geosci., 49, 105–111, https://doi.org/10.5194/adgeo-49-105-2019, 2019.

Grabowski, W. W., Morrison, H., Shima, S.-I., Abade, G. C., Dziekan, P., and Pawlowska, H.: Modeling of Cloud Microphysics: Can We Do Better?, Bull. Amer. Meteorol. Soc., 100, 655–672, https://doi.org/10.1175/bams-d-18-0005.1, 2019.

Grams, C. M. and Archambault, H. M.: The Key Role of Diabatic Outflow in Amplifying the Midlatitude Flow: A Representative Case Study of Weather Systems Surrounding Western North Pacific Extratropical Transition, Mon. Weather Rev., 144, 3847–3869, https://doi.org/10.1175/mwr-d-15-0419.1, 2016.

Griewank, P. J., Heus, T., Lareau, N. P., and Neggers, R. A. J.: Size dependence in chord characteristics from simulated and observed continental shallow cumulus, Atmos. Chem. Phys., 20, 10 211–10 230, https://doi.org/10.5194/acp-20-10211-2020, 2020.

Grise, K. M., Medeiros, B., Benedict, J. J., and Olson, J. G.: Investigating the Influence of Cloud Radiative Effects on the Extratropical Storm Tracks, Geophys. Res. Lett., 46, 7700–7707, https://doi.org/10.1029/2019gl083542, 2019.

Gu, B., Ren, T., Kuo, C.-P., Yang, P., and Bowman, K.: Global Impact of Cloud Longwave Scattering in an Atmosphere-Only General Circulation Model Simulation, J. Geophys. Res.-Atmos., 126, e2020JD033 968, https://doi.org/10.1029/2020jd033968, 2021.

Hande, L. B., Engler, C., Hoose, C., and Tegen, I.: Seasonal variability of Saharan desert dust and ice nucleating particles over Europe, Atmos. Chem. Phys., 15, 4389–4397, https://doi.org/10.5194/acp-15-4389-2015, 2015.

Harris, C. R., Millman, K. J., Walt, S. J. v. d., Gommers, R., Virtanen, P., Cournapeau, D., Wieser, E., Taylor, J., Berg, S., Smith, N. J., Kern, R., Picus, M., Hoyer, S., Kerkwijk, M. H. v., Brett, M., Haldane, A., Río, J. F. d., Wiebe, M., Peterson, P., Gérard-Marchant, P., Sheppard, K., Reddy, T., Weckesser, W., Abbasi, H., Gohlke, C., and Oliphant, T. E.: Array programming with NumPy, Nature, 585, 357–362, https://doi.org/10.1038/s41586-020-2649-2, 2020.

Harrop, B. E. and Hartmann, D. L.: The role of cloud radiative heating within the atmosphere on the high cloud amount and top-of-atmosphere cloud radiative effect, J. Adv. Model. Earth Syst., 8, 1391–1410, https://doi.org/10.1002/2016ms000670, 2016.

Harrop, B. E., Lu, J., Leung, L. R., Lau, W. K. M., Kim, K.-M., Medeiros, B., Soden, B. J., Vecchi, G. A., Zhang, B., and Singh, B.: An overview of cloud-radiation denial experiments for the Energy Exascale Earth System Model version 1, Geosci. Model Dev., 17, 3111–3135, https://doi.org/10.5194/gmd-17-3111-2024, 2024.

Hawcroft, M. K., Shaffrey, L. C., Hodges, K. I., and Dacre, H. F.: How much Northern Hemisphere precipitation is associated with extratropical cyclones?, Geophys. Res. Lett., 39, L24 809, https://doi.org/10.1029/2012GL053866, 2012.

Hersbach, H., Bell, B., Berrisford, P., Hirahara, S., Horányi, A., Muñoz-Sabater, J., Nicolas, J., Peubey, C., Radu, R., Schepers, D., Simmons, A., Soci, C., Abdalla, S., Abellan, X., Balsamo, G., Bechtold, P., Biavati, G., Bidlot, J., Bonavita, M., De Chiara, G., Dahlgren, P., Dee, D., Diamantakis, M., Dragani, R., Flemming, J., Forbes, R., Fuentes, M., Geer, A., Haimberger, L., Healy, S., Hogan, R. J., Hólm, E., Janisková, M., Keeley, S., Laloyaux, P., Lopez, P., Lupu, C., Radnoti, G., de Rosnay, P., Rozum, I., Vamborg, F., Villaume, S., and Thépaut, J.-N.: The ERA5 global reanalysis, Q. J. R. Meteorol. Soc., 146, 1999–2049, https://doi.org/10.1002/qj.3803, 2020.

Hogan, R. J. and Bozzo, A.: A Flexible and Efficient Radiation Scheme for the ECMWF Model, J. Adv. Model. Earth Syst., 10, 1990–2008, https://doi.org/10.1029/2018ms001364, 2018.

Hogan, R. J. and Illingworth, A. J.: Deriving cloud overlap statistics from radar, Q. J. R. Meteorol. Soc., 126, 2903–2909, https://doi.org/10.1002/qj.49712656914, 2000.

Hogan, R. J. and Shonk, J. K. P.: Incorporating the Effects of 3D Radiative Transfer in the Presence of Clouds into Two-Stream Multilayer Radiation Schemes, J. Atmos. Sci., 70, 708 – 724, https://doi.org/ https://doi.org/10.1175/JAS-D-12-041.1, 2013.

Hogan, R. J., Schäfer, S. A. K., Klinger, C., Chiu, J. C., and Mayer, B.: Representing 3-D cloud radiation effects in two-stream schemes: 2. Matrix formulation and broadband evaluation, J. Geophys. Res.-Atmos., 121, 8583–8599, https://doi.org/https://doi.org/10.1002/2016JD024875, 2016.

Hogan, R. J., Fielding, M. D., Barker, H. W., Villefranque, N., and Schäfer, S. A. K.: Entrapment: An Important Mechanism to Explain the Shortwave 3D Radiative Effect of Clouds, J. Atmos. Sci., 76, 2123–2141, https://doi.org/10.1175/jas-d-18-0366.1, 2019.

Hohenegger, C., Korn, P., Linardakis, L., Redler, R., Schnur, R., Adamidis, P., Bao, J., Bastin, S., Behravesh, M., Bergemann, M., Biercamp, J., Bockelmann, H., Brokopf, R., Brüggemann, N., Casaroli, L., Chegini, F., Datseris, G., Esch, M., George, G., Giorgetta, M., Gutjahr, O., Haak, H., Hanke, M., Ilyina, T., Jahns, T., Jungclaus, J., Kern, M., Klocke, D., Kluft, L., Kölling, T., Kornblueh, L., Kosukhin, S., Kroll, C., Lee, J., Mauritsen, T., Mehlmann, C., Mieslinger, T., Naumann, A. K., Paccini, L., Peinado, A., Praturi, D. S., Putrasahan, D., Rast, S., Riddick, T., Roeber, N., Schmidt, H., Schulzweida, U., Schütte, F., Segura, H., Shevchenko, R., Singh, V., Specht, M., Stephan, C. C., von Storch, J.-S., Vogel, R., Wengel, C., Winkler, M., Ziemen, F., Marotzke, J., and Stevens, B.: ICON-Sapphire: simulating the components of the Earth system and their interactions at kilometer and sub-kilometer scales, Geosci. Model Dev., 16, 779–811, https://doi.org/10.5194/gmd-16-779-2023, 2023.

Hoskins, B. J. and West, N. V.: Baroclinic Waves and Frontogenesis. Part II: Uniform Potential Vorticity Jet Flows-Cold and Warm Fronts, J. Atmos. Sci., 36, 1663–1680, https://doi.org/10.1175/ 1520-0469(1979)036<1663:bwafpi>2.0.co;2, 1979.

Hoskins, B. J., Draghici, I., and Davies, H. C.: A new look at the ω-equation, Q. J. R. Meteorol. Soc., 104, 31–38, https://doi.org/https://doi.org/10.1002/qj.49710443903, 1978.

Hoskins, B. J., McIntyre, M. E., and Robertson, A. W.: On the use and significance of isentropic potential vorticity maps, Q. J. R. Meteorol. Soc., 111, 877–946, https://doi.org/https://doi.org/10.1002/qj. 49711147002, 1985.

Hoyer, S. and Hamman, J.: xarray: N-D labeled arrays and datasets in Python, Journal of Open Research Software, 5, 10, https://doi.org/10.5334/jors.148, 2017.

Hu, Y. X. and Stamnes, K.: An Accurate Parameterization of the Radiative Properties of Water Clouds Suitable for Use in Climate Models, J. Climate, 6, 728 – 742, https://doi.org/https://doi.org/10.1175/1520-0442(1993)006<0728:AAPOTR>2.0.CO;2, 1993.

Hunter, J. D.: Matplotlib: A 2D graphics environment, Comput. Sci. Eng., 9, 90–95, https://doi.org/10.1109/mcse.2007.55, 2007.

Jakub, F. and Mayer, B.: A three-dimensional parallel radiative transfer model for atmospheric heating rates for use in cloud resolving models-The TenStream solver, J. Quant. Spectrosc. Radiat. Transfer, 163, 63–71, https://doi.org/10.1016/j.jqsrt.2015.05.003, 2015.

Jakub, F. and Mayer, B.: 3-D radiative transfer in large-eddy simulations – experiences coupling the TenStream solver to the UCLA-LES, Geosci. Model Dev., 9, 1413–1422, https://doi.org/10.5194/gmd-9-1413-2016, 2016.

Joos, H. and Forbes, R. M.: Impact of different IFS microphysics on a warm conveyor belt and the downstream flow evolution, Q. J. R. Meteorol. Soc., 142, 2727–2739, https://doi.org/10.1002/qj.2863, 2016.

Joos, H. and Wernli, H.: Influence of microphysical processes on the potential vorticity development in a warm conveyor belt: A case-study with the limited-area model COSMO, Q. J. R. Meteorol. Soc., 138, 407–418, https://doi.org/10.1002/qj.934, 2012.

Keshtgar, B.: Scripts for "Cloud-radiative impact on the dynamics and predictability of an idealized extratropical cyclone", Gitlab [code], URL `https://gitlab.phaidra.org/climate/keshtgar-etal-crh-cyclone-wcd2022`, last access: 16 January 2023, 2023.

Keshtgar, B.: Scripts for "Uncertainties in cloud-radiative heating within an idealized extratropical cyclone", Gitlab [code], URL `https://gitlab.phaidra.org/climate/keshtgar-etal-2024-cyclone-crh-uncertainties`, last access: 12 March 2024, 2024.

Keshtgar, B., Voigt, A., Hoose, C., Riemer, M., and Mayer, B.: Cloud-radiative impact on the dynamics and predictability of an idealized extratropical cyclone, Weather Clim. Dynam., 4, 115–132, https://doi.org/10.5194/wcd-4-115-2023, 2023.

Keshtgar, B., Voigt, A., Mayer, B., and Hoose, C.: Uncertainties in cloud-radiative heating within an idealized extratropical cyclone, Atmos. Chem. Phys., 24, 4751–4769, https://doi.org/10.5194/acp-24-4751-2024, 2024.

Kirshbaum, D. J., Merlis, T. M., Gyakum, J. R., and McTaggart-Cowan, R.: Sensitivity of Idealized Moist Baroclinic Waves to Environmental Temperature and Moisture Content, J. Atmos. Sci., 75, 337–360, https://doi.org/10.1175/jas-d-17-0188.1, 2018.

Klinger, C. and Mayer, B.: The Neighboring Column Approximation (NCA) - A fast approach for the calculation of 3D thermal heating rates in cloud resolving models, J. Quant. Spectrosc. Radiat. Transfer, 168, 17–28, https://doi.org/10.1016/j.jqsrt.2015.08.020, 2016.

Klinger, C., Mayer, B., Jakub, F., Zinner, T., Park, S.-B., and Gentine, P.: Effects of 3-D thermal radiation on the development of a shallow cumulus cloud field, Atmos. Chem. Phys., 17, 5477–5500, https://doi.org/10.5194/acp-17-5477-2017, 2017.

Klinger, C., Feingold, G., and Yamaguchi, T.: Cloud droplet growth in shallow cumulus clouds considering 1-D and 3-D thermal radiative effects, Atmos. Chem. Phys., 19, 6295–6313, https://doi.org/10.5194/acp-19-6295-2019, 2019.

Kretzschmar, J., Stapf, J., Klocke, D., Wendisch, M., and Quaas, J.: Employing airborne radiation and cloud microphysics observations to improve cloud representation in ICON at kilometer-scale resolution in the Arctic, Atmos. Chem. Phys., 20, 13 145–13 165, https://doi.org/10.5194/acp-20-13145-2020, 2020.

L'Ecuyer, T. S., Wood, N. B., Haladay, T., Stephens, G. L., and Stackhouse Jr., P. W.: Impact of clouds on atmospheric heating based on the R04 CloudSat fluxes and heating rates data set, J. Geophys. Res.-Atmos., 113, https://doi.org/10.1029/2008jd009951, 2008.

Lee, D., Oreopoulos, L., and Cho, N.: An evaluation of clouds and radiation in a large-scale atmospheric model using a cloud vertical structure classification, Geosci. Model Dev., 13, 673–684, https://doi.org/10.5194/gmd-13-673-2020, 2020.

Li, Y., Thompson, D. W. J., Stephens, G. L., and Bony, S.: A global survey of the instantaneous linkages between cloud vertical structure and large-scale climate, J. Geophys. Res.-Atmos., 119, 3770–3792, https://doi.org/10.1002/2013jd020669, 2014.

Li, Y., Thompson, D. W. J., and Bony, S.: The Influence of Atmospheric Cloud Radiative Effects on the Large-Scale Atmospheric Circulation, J. Climate, 28, 7263 – 7278, https://doi.org/10.1175/jcli-d-14-00825.1, 2015.

Lindzen, R. S. and Farrell, B.: A Simple Approximate Result for the Maximum Growth Rate of Baroclinic Instabilities, J. Atmos. Sci., 37, 1648–1654, https://doi.org/10.1175/1520-0469(1980)037<1648:asarft>2.0.co;2, 1980.

Lloveras, D. J., Durran, D. R., and Doyle, J. D.: The Two- to Four-Day Predictability of Mid-latitude Cyclones: Don't Sweat the Small Stuff, J. Atmos. Sci., 80, 2613–2633, https://doi.org/10.1175/jas-d-22-0232.1, 2023.

Lorenz, E. N.: Available Potential Energy and the Maintenance of the General Circulation, Tellus, 7, 157–167, https://doi.org/https://doi.org/10.1111/j.2153-3490.1955.tb01148.x, 1955.

Maddison, J. W., Gray, S. L., Martínez-Alvarado, O., and Williams, K. D.: Upstream Cyclone Influence on the Predictability of Block Onsets over the Euro-Atlantic Region, Mon. Weather Rev., 147, 1277 – 1296, https://doi.org/10.1175/mwr-d-18-0226.1, 2019.

Madonna, E., Wernli, H., Joos, H., and Martius, O.: Warm Conveyor Belts in the ERA-Interim Dataset (1979–2010). Part I: Climatology and Potential Vorticity Evolution, J. Climate, 27, 3–26, https://doi.org/10.1175/jcli-d-12-00720.1, 2014.

Manabe, S.: On the Contribution of Heat Released by Condensation to the Change in Pressure Pattern, J. Meteor. Soc. Japan. Ser. II, 34, 308–320, https://doi.org/10.2151/jmsj1923.34.6_308, 1956.

Martínez-Alvarado, O., Madonna, E., Gray, S. L., and Joos, H.: A route to systematic error in forecasts of Rossby waves, Q. J. R. Meteorol. Soc., 142, 196–210, https://doi.org/https://doi.org/10.1002/qj.2645, 2016.

Mayer, B.: Radiative transfer in the cloudy atmosphere, Eur. Phys. J. Conferences, 1, 75–99, https://doi.org/10.1140/epjconf/e2009-00912-1, 2009.

Mayer, B. and Kylling, A.: Technical note: The libRadtran software package for radiative transfer calculations - description and examples of use, Atmos. Chem. Phys., 5, 1855–1877, https://doi.org/10.5194/acp-5-1855-2005, 2005.

Mazoyer, M., Ricard, D., Rivière, G., Delanoë, J., Arbogast, P., Vié, B., Lac, C., Cazenave, Q., and Pelon, J.: Microphysics Impacts on the Warm Conveyor Belt and Ridge Building of the NAWDEX IOP6 Cyclone, Mon. Weather Rev., 149, 3961–3980, https://doi.org/10.1175/mwr-d-21-0061.1, 2021.

Mazoyer, M., Ricard, D., Rivière, G., Delanoë, J., Riette, S., Augros, C., Borderies, M., and Vié, B.: Impact of Mixed-Phase Cloud Parameterization on Warm Conveyor Belts and Upper-Tropospheric Dynamics, Mon. Weather Rev., 151, 1073–1091, https://doi.org/10.1175/mwr-d-22-0045.1, 2023.

Mlawer, E. J., Taubman, S. J., Brown, P. D., Iacono, M. J., and Clough, S. A.: Radiative transfer for inhomogeneous atmospheres: RRTM, a validated correlated-k model for the longwave, J. Geophys. Res.-Atmos., 102, 16 663–16 682, https://doi.org/https://doi.org/10.1029/97JD00237, 1997.

Oertel, A., Boettcher, M., Joos, H., Sprenger, M., Konow, H., Hagen, M., and Wernli, H.: Convective activity in an extratropical cyclone and its warm conveyor belt – a case-study combining observations and a convection-permitting model simulation, Q. J. R. Meteorol. Soc., 145, 1406–1426, https://doi.org/10.1002/qj.3500, 2019.

Oertel, A., Boettcher, M., Joos, H., Sprenger, M., and Wernli, H.: Potential vorticity structure of embedded convection in a warm conveyor belt and its relevance for large-scale dynamics, Weather Clim. Dynam., 1, 127–153, https://doi.org/10.5194/wcd-1-127-2020, 2020.

Oertel, A., Miltenberger, A. K., Grams, C. M., and Hoose, C.: Interaction of microphysics and dynamics in a warm conveyor belt simulated with the ICOsahedral Nonhydrostatic (ICON) model, Atmos. Chem. Phys., 23, 8553–8581, https://doi.org/10.5194/acp-23-8553-2023, 2023a.

Oertel, A., Pickl, M., Quinting, J. F., Hauser, S., Wandel, J., Magnusson, L., Balmaseda, M., Vitart, F., and Grams, C. M.: Everything Hits at Once: How Remote Rainfall Matters for the Prediction of the 2021 North American Heat Wave, Geophys. Res. Lett., 50, e2022GL100 958, https://doi.org/10.1029/2022gl100958, 2023b.

Oreopoulos, L., Cho, N., and Lee, D.: New insights about cloud vertical structure from CloudSat and CALIPSO observations, J. Geophys. Res.-Atmos., 122, 9280–9300, https://doi.org/https://doi.org/10.1002/2017JD026629, 2017.

Papavasileiou, G., Voigt, A., and Knippertz, P.: The role of observed cloud-radiative anomalies for the dynamics of the North Atlantic Oscillation on synoptic time-scales, Q. J. R. Meteorol. Soc., 146, 1822–1841, https://doi.org/10.1002/qj.3768, 2020.

Pickl, M., Quinting, J. F., and Grams, C. M.: Warm conveyor belts as amplifiers of forecast uncertainty, Q. J. R. Meteorol. Soc., 149, 3064–3085, https://doi.org/10.1002/qj.4546, 2023.

Pincus, R., Barker, H. W., and Morcrette, J.-J.: A fast, flexible, approximate technique for computing radiative transfer in inhomogeneous cloud fields, J. Geophys. Res.-Atmos., 108, https://doi.org/10.1029/2002jd003322, 2003.

Polvani, L. M. and Esler, J. G.: Transport and mixing of chemical air masses in idealized baroclinic life cycles, J. Geophys. Res.-Atmos., 112, https://doi.org/https://doi.org/10.1029/2007JD008555, 2007.

Prill, F., Reinert, D., Rieger, D., and Zängl, G.: ICON Tutorial 2023: Working with the ICON Model, Deutscher Wetterdienst, https://doi.org/10.5676/dwd_pub/nwv/icon_tutorial2023, 2023.

Rantanen, M., Räisänen, J., Sinclair, V. A., and Järvinen, H.: Sensitivity of idealised baroclinic waves to mean atmospheric temperature and meridional temperature gradient changes, Clim Dyn, 52, 2703–2719, https://doi.org/10.1007/s00382-018-4283-3, 2019.

Raschendorfer, M.: The new turbulence parameterization of LM, COSMO Newsletter,1, 89–97, 2001.

Rieger, D., Köhler, M., Hogan, R. J., Schäfer, S. A. K., Seifert, A., de Lozar, A., and Zängl, G.: ecRad in ICON - Details on the Implementation and First Results (Technical report), URL `https://www.dwd.de/DE/leistungen/reports_on_icon/pdf_einzelbaende/2019_04.html`, last access: 19 Novmber 2019), 2019.

Rieger, D., Milelli, M., Boucouvala, D., Gofa, F., Iriza-Burca, A., Khain, P., Kirsanov, A., Linkowska, J., and Marcucci, F.: Reports on ICON 006: Verification of ICON in Limited Area Mode at COSMO National Meteorological Services, https://doi.org/10.5676/dwd_pub/nwv/icon_006, 2021.

Riemer, M. and Jones, S. C.: The downstream impact of tropical cyclones on a developing baroclinic wave in idealized scenarios of extratropical transition, Q. J. R. Meteorol. Soc., 136, 617–637, https://doi.org/https://doi.org/10.1002/qj.605, 2010.

Roberts, J. F., Champion, A. J., Dawkins, L. C., Hodges, K. I., Shaffrey, L. C., Stephenson, D. B., Stringer, M. A., Thornton, H. E., and Youngman, B. D.: The XWS open access catalogue of extreme European windstorms from 1979 to 2012, Nat. Hazard. Earth Sys., 14, 2487–2501, https://doi.org/10.5194/nhess-14-2487-2014, 2014.

Rogers, E. and Bosart, L. F.: An Investigation of Explosively Deepening Oceanic Cyclones, Mon. Weather Rev., 114, 702–718, https://doi.org/10.1175/1520-0493(1986)114<0702:aioedo>2.0.co;2, 1986.

Rossow, W. B., Delo, C., and Cairns, B.: Implications of the Observed Mesoscale Variations of Clouds for the Earth's Radiation Budget, J. Climate, 15, 557–585, https://doi.org/10.1175/1520-0442(2002)015<0557:iotomv>2.0.co;2, 2002.

Ruppert, J. H., Wing, A. A., Tang, X., and Duran, E. L.: The critical role of cloud-infrared radiation feedback in tropical cyclone development., Pnas, 117, 27 884–27 892, https://doi.org/10.1073/pnas.2013584117, 2020.

Röthlisberger, M., Martius, O., and Wernli, H.: Northern Hemisphere Rossby Wave Initiation Events on the Extratropical Jet—A Climatological Analysis, J. Climate, 31, 743–760, https://doi.org/10.1175/jcli-d-17-0346.1, 2018.

Saffin, L., Methven, J., and Gray, S.: The non-conservation of potential vorticity by a dynamical core compared with the effects of parametrized physical processes, Q. J. R. Meteorol. Soc., 142, 1265–1275, 2016.

Satoh, M., Stevens, B., Judt, F., Khairoutdinov, M., Lin, S.-J., Putman, W. M., and Düben, P.: Global Cloud-Resolving Models, Current Climate Change Reports, 5, 172–184, https://doi.org/10.1007/s40641-019-00131-0, 2019.

Schneider, T.: The General Circulation of the Atmosphere, Annu. Rev. Earth Pl. Sc., 34, 655–688, https://doi.org/https://doi.org/10.1146/annurev.earth.34.031405.125144, 2006.

Schultz, D. M., Bosart, L. F., Colle, B. A., Davies, H. C., Dearden, C., Keyser, D., Martius, O., Roebber, P. J., Steenburgh, W. J., Volkert, H., and Winters, A. C.: Extratropical Cyclones: A Century of Research on Meteorology's Centerpiece, Meteor. Monogr., 59, 16.1–16.56, https://doi.org/10.1175/amsmonographs-d-18-0015.1, 2019.

Schulzweida, U.: CDO User Guide, https://doi.org/10.5281/zenodo.3539275, 2019.

Schäfer, S. A. K. and Voigt, A.: Radiation Weakens Idealized Midlatitude Cyclones, Geophys. Res. Lett., 45, 2833–2841, https://doi.org/10.1002/2017gl076726, 2018.

Schäfler, A. and Harnisch, F.: Impact of the inflow moisture on the evolution of a warm conveyor belt, Q. J. R. Meteorol. Soc., 141, 299–310, https://doi.org/10.1002/qj.2360, 2015.

Schäfler, A., Craig, G., Wernli, H., Arbogast, P., Doyle, J. D., McTaggart-Cowan, R., Methven, J., Rivière, G., Ament, F., Boettcher, M., Bramberger, M., Cazenave, Q., Cotton, R., Crewell, S., Delanoë, J., Dörnbrack, A., Ehrlich, A., Ewald, F., Fix, A., Grams, C. M., Gray, S. L., Grob, H., Groß, S., Hagen, M., Harvey, B., Hirsch, L., Jacob, M., Kölling, T., Konow, H., Lemmerz, C., Lux, O., Magnusson, L., Mayer, B., Mech, M., Moore, R., Pelon, J., Quinting, J., Rahm, S., Rapp, M., Rautenhaus, M., Reitebuch, O., Reynolds, C. A., Sodemann, H., Spengler, T., Vaughan, G., Wendisch, M., Wirth, M., Witschas, B., Wolf, K., and Zinner, T.: The North Atlantic Waveguide and Downstream Impact Experiment, Bull. Amer. Meteorol. Soc., 99, 1607–1637, https://doi.org/10.1175/bams-d-17-0003.1, 2018.

Seifert, A. and Beheng, K. D.: A two-moment cloud microphysics parameterization for mixed-phase clouds. Part 1: Model description, Meteorol. Atmos. Phys., 92, 45–66, https://doi.org/10.1007/s00703-005-0112-4, 2006.

Selz, T. and Craig, G. C.: Upscale Error Growth in a High-Resolution Simulation of a Summertime Weather Event over Europe, Mon. Weather Rev., 143, 813–827, https://doi.org/10.1175/mwr-d-14-00140.1, 2015.

Senf, F., Voigt, A., Clerbaux, N., Hünerbein, A., and Deneke, H.: Increasing Resolution and Resolving Convection Improve the Simulation of Cloud-Radiative Effects Over the North Atlantic, J. Geophys. Res.-Atmos., 125, e2020JD032 667, https://doi.org/https://doi.org/10.1029/2020JD032667, 2020.

Shi, X. and Liu, X.: Effect of cloud-scale vertical velocity on the contribution of homogeneous nucleation to cirrus formation and radiative forcing, Geophys. Res. Lett., 43, 6588–6595, https://doi.org/https://doi.org/10.1002/2016GL069531, 2016.

Shonk, J. and Hogan, R.: Tripleclouds: An Efficient Method for Representing Horizontal Cloud Inhomogeneity in 1D Radiation Schemes by Using Three Regions at Each Height, J. Climate, 21, https://doi.org/10.1175/2007jcli1940.1, 2008.

Shonk, J. K. P., Hogan, R. J., Edwards, J. M., and Mace, G. G.: Effect of improving representation of horizontal and vertical cloud structure on the Earth's global radiation budget. Part I: Review and parametrization, Q. J. R. Meteorol. Soc., 136, 1191–1204, https://doi.org/https://doi.org/10.1002/qj.647, 2010.

Singer, C. E., Lopez-Gomez, I., Zhang, X., and Schneider, T.: Top-of-Atmosphere Albedo Bias from Neglecting Three-Dimensional Cloud Radiative Effects, J. Atmos. Sci., 78, 4053–4069, https://doi.org/10.1175/jas-d-21-0032.1, 2021.

Smagorinsky, J.: General Circulation Experiments With The Primitive Equations: I. The Basic Experiment, Mon. Weather Rev., 91, 99 – 164, https://doi.org/https://doi.org/10.1175/1520-0493(1963)091<0099:GCEWTP>2.3.CO;2, 1963.

Spreitzer, E., Attinger, R., Boettcher, M., Forbes, R., Wernli, H., and Joos, H.: Modification of potential vorticity near the tropopause by nonconservative processes in the ECMWF model, J. Atmos. Sci., 76, https://doi.org/10.1175/jas-d-18-0295.1, 2019.

Stansifer, E. M., O'Gorman, P. A., and Holt, J. I.: Accurate computation of moist available potential energy with the Munkres algorithm, Q. J. R. Meteorol. Soc., 143, 288–292, https://doi.org/10.1002/qj.2921, 2017.

Stevens, B. and Brenguier, J.-L.: Cloud-controlling factors: low clouds, in: Clouds in the perturbed climate system, edited by Heintzenberg, J. and Charlson, R., pp. 173–196, MIT Press, Cambridge, 2009.

Stevens, B., Bony, S., and Webb, M.: Clouds On-Off Klimate Intercomparison Experiment (COOKIE), https://api.semanticscholar.org/CorpusID:18485339, 2012.

Stevens, B., Giorgetta, M., Esch, M., Mauritsen, T., Crueger, T., Rast, S., Salzmann, M., Schmidt, H., Bader, J., Block, K., Brokopf, R., Fast, I., Kinne, S., Kornblueh, L., Lohmann, U., Pincus, R., Reichler, T., and Roeckner, E.: Atmospheric component of the MPI-M Earth System Model: ECHAM6, J. Adv. Model. Earth Syst., 5, 146–172, https://doi.org/https://doi.org/10.1002/jame.20015, 2013.

Stevens, B., Acquistapace, C., Hansen, A., Heinze, R., Klinger, C., Klocke, D., Rybka, H., Schubotz, W., Windmiller, J., Adamidis, P., Arka, I., Barlakas, V., Biercamp, J., Brueck, M., Brune, S., Buehler, S. A., Burkhardt, U., Cioni, G., Costa-Surós, M., Crewell, S., Crüger, T., Deneke, H., Friederichs, P., Henken, C. C., Hohenegger, C., Jacob, M., Jakub, F., Kalthoff, N., Köhler, M., van LAAR, T. W., Li, P., Löhnert, U., Macke, A., Madenach, N., Mayer, B., Nam, C., Naumann, A. K., Peters, K., Poll, S., Quaas, J., Röber, N., Rochetin, N., Scheck, L., Schemann, V., Schnitt, S., Seifert, A., Senf, F., Shapkalijevski, M., Simmer, C., Singh, S., Sourdeval, O., Spickermann, D., Strandgren, J., Tessiot, O., Vercauteren, N., Vial, J., Voigt, A., and Zängl, G.: The Added Value of Large-eddy and Storm-resolving Models for Simulating Clouds and Precipitation, J. Meteorol. Soc. Jpn., 98, 395–435, https://doi.org/10.2151/jmsj.2020-021, 2020.

Stoelinga, M. T.: A Potential Vorticity-Based Study of the Role of Diabatic Heating and Friction in a Numerically Simulated Baroclinic Cyclone, Mon. Weather Rev., 124, 849 – 874, https://doi.org/10.1175/1520-0493(1996)124<0849:apvbso>2.0.co;2, 1996.

Sullivan, S. and Voigt, A.: Ice microphysical processes exert a strong control on the simulated radiative energy budget in the tropics, Comms. Earth and Env., 2, 137, https://doi.org/10.1038/s43247-021-00206-7, 2021.

Sullivan, S., Voigt, A., Miltenberger, A., Rolf, C., and Krämer, M.: A Lagrangian Perspective of Microphysical Impact on Ice Cloud Evolution and Radiative Heating, J. Adv. Model. Earth Syst., 14, e2022MS003 226, https://doi.org/10.1029/2022ms003226, 2022.

Sullivan, S., Keshtgar, B., Albern, N., Bala, E., Braun, C., Choudhary, A., Hörner, J., Lentink, H., Papavasileiou, G., and Voigt, A.: How does cloud-radiative heating over the North Atlantic change with grid spacing, convective parameterization, and microphysics scheme in ICON version 2.1.00?, Geosci. Model Dev., 16, 3535–3551, https://doi.org/10.5194/gmd-16-3535-2023, 2023.

Sullivan, S. C., Lee, D., Oreopoulos, L., and Nenes, A.: Role of updraft velocity in temporal variability of global cloud hydrometeor number, Proceedings of the National Academy of Sciences, 113, 5791–5796, https://doi.org/10.1073/pnas.1514039113, 2016.

Sun, Y. Q. and Zhang, F.: Intrinsic versus Practical Limits of Atmospheric Predictability and the Significance of the Butterfly Effect, J. Atmos. Sci., 73, 1419–1438, https://doi.org/10.1175/jas-d-15-0142.1, 2016.

Teubler, F. and Riemer, M.: Potential-vorticity dynamics of troughs and ridges within Rossby wave packets during a 40-year reanalysis period, Weather Clim. Dynam., 2, 535–559, https://doi.org/10.5194/wcd-2-535-2021, 2021.

Thompson, D. W. J., Bony, S., and Li, Y.: Thermodynamic constraint on the depth of the global tropospheric circulation, Proc. Nat. Acad. Sci., 114, 8181–8186, https://doi.org/10.1073/pnas.1620493114, 2017.

Thompson, D. W. J., Ceppi, P., and Li, Y.: A robust constraint on the temperature and height of the extratropical tropopause, J. Clim., 32, 273–287, https://doi.org/10.1175/jcli-d-18-0339.1, 2019.

Thorncroft, C., Hoskins, B., and McIntyre, M.: Two paradigms of baroclinic-wave life-cycle behaviour, Q. J. R. Meteorol. Soc., 119, 17–55, 1993.

Tiedtke, M.: A Comprehensive Mass Flux Scheme for Cumulus Parameterization in Large-Scale Models, Mon. Weather Rev., 117, 1779 – 1800, https://doi.org/10.1175/1520-0493(1989)117<1779:acmfsf>2.0.co;2, 1989.

Tierney, G., Posselt, D. J., and Booth, J. F.: An examination of extratropical cyclone response to changes in baroclinicity and temperature in an idealized environment, Clim Dyn, 51, 3829–3846, https://doi.org/10.1007/s00382-018-4115-5, 2018.

Tomita, H., Satoh, M., and Goto, K.: An Optimization of the Icosahedral Grid Modified by Spring Dynamics, J. Comput. Phys., 183, 307–331, https://doi.org/https://doi.org/10.1006/jcph.2002.7193, 2002.

Tselioudis, G. and Jakob, C.: Evaluation of midlatitude cloud properties in a weather and a climate model: Dependence on dynamic regime and spatial resolution, J. Geophys. Res.-Atmos., 107, Aac 14–1–aac 14–10, https://doi.org/10.1029/2002jd002259, 2002.

Vallis, G. K.: Atmospheric and Oceanic Fluid Dynamics: Fundamentals and Large-scale Circulation, Cambridge University Press, Cambridge, https://doi.org/10.1017/cbo9780511790447, 2006.

Vergara-Temprado, J., Miltenberger, A. K., Furtado, K., Grosvenor, D. P., Shipway, B. J., Hill, A. A., Wilkinson, J. M., Field, P. R., Murray, B. J., and Carslaw, K. S.: Strong control of Southern Ocean cloud reflectivity by ice-nucleating particles, Proc. Natl. Acad. Sci., 115, 2687–2692, https://doi.org/10.1073/pnas.1721627115, 2018.

Virtanen, P., Gommers, R., Oliphant, T. E., Haberland, M., Reddy, T., Cournapeau, D., Burovski, E., Peterson, P., Weckesser, W., Bright, J., van der Walt, S. J., Brett, M., Wilson, J., Millman, K. J., Mayorov, N., Nelson, A. R. J., Jones, E., Kern, R., Larson, E., Carey, C. J., Polat, İ., Feng, Y., Moore, E. W., VanderPlas, J., Laxalde, D., Perktold, J., Cimrman, R., Henriksen, I., Quintero, E. A., Harris, C. R., Archibald, A. M., Ribeiro, A. H., Pedregosa, F., van Mulbregt, P., and SciPy 1.0 Contributors: SciPy 1.0: Fundamental Algorithms for Scientific Computing in Python, Nature Methods, 17, 261–272, https://doi.org/10.1038/s41592-019-0686-2, 2020.

Voigt, A. and Albern, N.: No Cookie for Climate Change, Geophys. Res. Lett., 46, 14 751–14 761, https://doi.org/10.1029/2019gl084987, 2019.

Voigt, A., Albern, N., and Papavasileiou, G.: The Atmospheric Pathway of the Cloud-Radiative Impact on the Circulation Response to Global Warming: Important and Uncertain, J. Climate, 32, 3051–3067, https://doi.org/10.1175/jcli-d-18-0810.1, 2019.

Voigt, A., Albern, N., Ceppi, P., Grise, K., Li, Y., and Medeiros, B.: Clouds, radiation, and atmospheric circulation in the present-day climate and under climate change, WIREs Clim. Change, 12, e694, https://doi.org/10.1002/wcc.694, 2021.

Voigt, A., Keshtgar, B., and Butz, K.: Tug-Of-War on Idealized Midlatitude Cyclones Between Radiative Heating From Low-Level and High-Level Clouds, Geophys. Res. Lett., 50, e2023GL103 188, https://doi.org/10.1029/2023gl103188, 2023.

Wang, H., Zhang, H., Xie, B., Jing, X., He, J., and Liu, Y.: Evaluating the Impacts of Cloud Microphysical and Overlap Parameters on Simulated Clouds in Global Climate Models, Adv. Atmos. Sci., 39, 2172–2187, https://doi.org/10.1007/s00376-021-0369-7, 2022.

Wang, X., Miao, H., Liu, Y., and Bao, Q.: Dependence of cloud radiation on cloud overlap, horizontal inhomogeneity, and vertical alignment in stratiform and convective regions, Atmos. Res., 249, 105 358, https://doi.org/10.1016/j.atmosres.2020.105358, 2021.

Watt-Meyer, O. and Frierson, D. M. W.: Local and Remote Impacts of Atmospheric Cloud Radiative Effects Onto the Eddy-Driven Jet, Geophys. Res. Lett., 44, 10,036–10,044, https://doi.org/10.1002/2017gl074901, 2017.

Wernli, H. and Gray, S. L.: The importance of diabatic processes for the dynamics of synoptic-scale extratropical weather systems—a review, preprint, https://doi.org/10.5194/egusphere-2023-2678, 2023.

Williamson, D. L., Blackburn, M., Hoskins, B. J., Nakajima, K., Ohfuchi, W., Takahashi, Y. O., Hayashi, Y.-Y., Nakamura, H., Ishiwatari, M., McGregor, J. L., Borth, H., Wirth, V., Frank, H., Bechtold, P., Wedi, N. P., Tomita, H., Satoh, M., Zhao, M., Held, I. M., Suarez, M. J., Lee, M.-I., Watanabe, M., Kimoto, M., Liu, Y., Wang, Z., Molod, A., Rajendran, K., Kitoh, A., and Stratton, R. A.: The APE atlas, Report Tn-484+str, Boulder, Colorado, USA, https://doi.org/10.5065/d6ff3qbr, 2012.

Wirth, V., Riemer, M., Chang, E. K. M., and Martius, O.: Rossby Wave Packets on the Midlatitude Waveguide—A Review, Mon. Weather Rev., 146, 1965–2001, https://doi.org/10.1175/mwr-d-16-0483.1, 2018.

Xu, K.-M. and Randall, D. A.: Impact of Interactive Radiative Transfer on the Macroscopic Behavior of Cumulus Ensembles. Part I: Radiation Parameterization and Sensitivity Tests, J. Atm. Sci., 52, 785–799, https://doi.org/10.1175/1520-0469(1995)052<0785:ioirto>2.0.co;2, 1995.

Yang, P., Bi, L., Baum, B. A., Liou, K.-N., Kattawar, G. W., Mishchenko, M. I., and Cole, B.: Spectrally Consistent Scattering, Absorption, and Polarization Properties of Atmospheric Ice Crystals at Wavelengths from 0.2 to 100 m, J. Atmos. Sci., 70, 330 – 347, https://doi.org/https://doi.org/10.1175/JAS-D-12-039.1, 2013.

Yi, B.: Diverse cloud radiative effects and global surface temperature simulations induced by different ice cloud optical property parameterizations, Sci. Rep., 12, 10 539, https://doi.org/10.1038/s41598-022-14608-w, 2022.

Zdunkowski, W. Trautmann, T. B. A.: Radiation in the atmosphere – A course in theoretical meteorology, Cambridge University Press, New York, ISBN 9780521871075, 2007.

Zhang, F., Bei, N., Rotunno, R., Snyder, C., and Epifanio, C. C.: Mesoscale Predictability of Moist Baroclinic Waves: Convection-Permitting Experiments and Multistage Error Growth Dynamics, J. Atmos. Sci., 64, 3579 – 3594, https://doi.org/10.1175/jas4028.1, 2007.

Zhao, W., Peng, Y., Wang, B., Yi, B., Lin, Y., and Li, J.: Comparison of three ice cloud optical schemes in climate simulations with community atmospheric model version 5, Atmos. Res., 204, 37–53, https://doi.org/https://doi.org/10.1016/j.atmosres.2018.01.004, 2018.

Zängl, G., Reinert, D., Rípodas, P., and Baldauf, M.: The ICON (ICOsahedral Non-hydrostatic) modelling framework of DWD and MPI-M: Description of the non-hydrostatic dynamical core, Q. J. R. Meteorol. Soc., 141, 563–579, https://doi.org/https://doi.org/10.1002/qj.2378, 2015.

Zängle, G.: Wetter und Klima - Deutscher Wetterdienst - Numerische Wettervorhersage - Operationelles NWV-System: ICON: Model configuration upgrade of ICON (Gültigkeit ab 14.04.2021), URL `https://www.dwd.de/DE/fachnutzer/forschung_lehre/numerische_wettervorhersage/nwv_aenderungen/_functions/DownloadBox_modellaenderungen/icon/pdf_2021/pdf_icon_14_04_2021.pdf`, 2021.

Zängle, G. and Paul, G.: Wetter und Klima and - Deutscher Wetterdienst - Numerische Wettervorhersage - ICON: ICON-Modellsystem mit der Einführung der Modellversion 2.0.15 (Gültigkeit ab 28.09.2016), URL `https://www.dwd.de/DE/fachnutzer/forschung_lehre/numerische_wettervorhersage/nwv_aenderungen/_functions/DownloadBox_modellaenderungen/icon/pdf_2016/pdf_icon_28_09_2016.pdf`, 2016.

Acknowledgments